

# **Design of a Bunch Shape Monitor for High Current LINACs at GSI**

DISSERTATION  
zur Erlangung des Doktorgrades  
der Naturwissenschaften

vorgelegt beim Fachbereich Physik  
der Johann Wolfgang Goethe-Universität  
in Frankfurt am Main

von  
BENJAMIN ZWICKER  
aus Bad Homburg v.d. Höhe

August 2016  
D30

vom Fachbereich Physik der  
Johann Wolfgang Goethe-Universität als Dissertation angenommen.

Dekan: Prof. Dr. Rene Reifarth

1. Gutachter: Prof. Dr. Oliver Kester

2. Gutachter: PD. Dr. Giuliano Franchetti

Datum der Disputation:

# Abstract

Within the FAIR project a prototype of a non-intercepting Bunch Shape Monitor (BSM) was developed at the heavy ion LINAC at GSI. The purpose was to obtain a dedicated diagnostics tool for bunch shape determination with a resolution below 100 ps. In addition, it was attempted to prove the feasibility of such a device for the planned proton-LINAC at FAIR (sec. 1.1) with a necessary resolution of 10 ps corresponding to  $1^\circ$  phase resolution of the foreseen 325 MHz radio frequency.

Numeric calculations of materials intercepting a 11.4 MeV/u heavy ion beam (sec. 3.2.2) indicated very high thermal stress. Therefore, a non-intercepting approach for a BSM was pursued. The design (sec. 3.3.1) utilizes secondary electrons created by rest gas ionisation and pushed out of the beam region by a homogenous E-field with up to -31 kV. The consequential formed electron beam, which carries the time information, is deflected by a 36 MHz resonance driven RF Deflector, transforming the time information into a spatial distribution. Finally detected by a micro channel plate (MCP) phosphor assembly, the electron distribution yields the bunch time structure.

After compensating for undesired effects on the primary ion beam (sec. 3.3.2), parameter studies and single macro pulse measurements proved a feasible resolution of up to  $37 \pm 6.3$  ps, corresponding to a phase resolution of below  $0.5^\circ$  for UNILAC beams (sec. 4.1.4). By manipulating the bunch length with a rebuncher, non-Gaussian profiles were obtained from 280 ps to 650 ps and were used in a feasibility study for longitudinal emittance determination. Depending on the method of analysis (sec. 4.2.1), values from  $\epsilon_{\text{Gauss}} = 1.42 \pm 0.14$  keV/u ns to  $\epsilon_{\text{SD}} = 3.03 \pm 0.33$  keV/u ns were measured. Also a finite elements-based numeric model was designed to investigate the propagation pattern of the secondary electrons within the electron optical system. The simulations showed the improper usage of the RF Deflector as an Einzel lens, as well as the time structure of the secondary electrons, while traveling to the RF Deflector. A time deviation 5.6 ps (sec. 5.2.3) was obtained with the 37 ps setup.

The BSM provides a time resolution far below 100 ps for longitudinal bunch structure measurements without any disturbing side effect on the LINAC operation. In addition, advanced measurements like emittance determination or macro pulse analysis allow deep insights into the LINAC operation. The usage of the BSM therefore proves to be a powerful diagnostics tool.

The adaption of the device for the FAIR proton-LINAC seems promising. If the phase resolution of  $0.5^\circ$  can be maintained, as the investigation of electron beam time structure has shown, that a new prototype with a resolution of 10 ps is feasible.



# Zusammenfassung

Im Rahmen des FAIR Projektes wurde ein neuartiger Prototyp eines nicht strahlzerstörenden Bunch Struktur Monitors (BSM) am GSI UNILAC entwickelt. Ziel ist es, ein zuverlässiges Diagnosegerät zu entwickeln, welches die longitudinale Struktur der Ionenbunche innerhalb des LINACs untersuchen kann. Notwendig ist hierbei eine effektive Zeitauflösung deutlich unter 100 ps, bei möglichst wenigen Makropuls Mittelungen. Nach der erfolgreichen Inbetriebnahme soll der BSM Prototyp dazu dienen, die Umsetzbarkeit eines weiteren nichtinvasiven Geräts für den geplanten Proton-LINAC bei FAIR mit einer notwendigen Zeitauflösung von 10 ps zu beurteilen.

Die numerische Simulation von Materialien, welche dem Hochstrom-Ionenstrahl ausgesetzt sind, zeigten einen sehr hohen thermischen Stress. Daher wurde der Ansatz eines nicht strahlzerstörenden Diagnosegerätes verfolgt. Das Design beruht auf der Erzeugung von Sekundärelektronen durch Strahl–Restgas Kollisionen im Strahlrohr. Durch das Anlegen eines homogenen Hochspannungspotentials innerhalb der sogenannten Feld-Box von bis zu  $-31$  kV, wird ein Elektronenstrahl erzeugt, welcher die zeitliche Struktur des Ionenbunches trägt. Die zeitliche Information des Elektronenstrahles wird beim Durchfliegen eines HF-Ablenkens, welcher resonant an die 36 MHz des Beschleunigers gekoppelt ist, in eine räumliche Intensitätsverteilung umgewandelt und auf einem bildgebenden MCP-Phosphor-Detektor durch eine CCD-Kamera detektiert. Durch die Nutzung eines ausgefeilten elektronenoptischen Systems, wird eine hohe Abbildungsgüte des Elektronenstrahles gewährleistet. Kernelemente sind fünf steuerbaren Blenden, zwei um  $90^\circ$  gebogenen gegenläufigen elektrostatische Energiespektrometer und eine elektrostatische Einzellinse. Die detektierte Elektronenverteilung wird durch eine Phasenkalibration des Ablenkens wieder in ein Zeitintervall überführt. Durch die zusätzliche Bestimmung der minimalen Abbildungsgröße des Elektronenstrahls auf dem MCP-Detektor, wird die Phasenauflösung bzw. die Zeitauflösung bestimmt.

Um eine uneingeschränkte Nutzung des BSM während des Strahlbetriebs zu ermöglichen, wurden zwei Kompensationsfelder entworfen. Für beliebige Hochspannungen werden störende Auswirkungen auf den Ionenstrahl um bis zu 99 % verringert. Das ausgefeilte, kompakte Design ermöglicht die Unterbringung der Kompensationsfelder innerhalb der knapp bemessenen Vakuumkammer des BSM. Hierdurch können jederzeit Messungen durchgeführt werden, vorausgesetzt ein Ionenstrahl ist vorhanden.

Intensive Untersuchungen der BSM Eigenschaften ergaben eine höchste Auflösung von  $37 \pm 6.3$  ps bei gleichzeitig akzeptabler Intensität auf dem MCP-Detektor. Dies entspricht einer Phasenauflösung von unter  $0.5^\circ$  bei 36 MHz. Unter anderem wurden auch stabile Einzelschussmessungen durchgeführt, welche für die Profilmessung nur einen einzelnen Makropuls benötigten, statt über typischerweise 8-32 Pulse zu mitteln.

---

Weitere Untersuchungen wurden angestellt, um den Betrieb des BSM zu optimieren. Das Hauptaugenmerk lag hierbei auf den Abhängigkeiten der Signalintensität, der Untergrundstärke und dem sich hieraus ergebenden Quotienten aus beiden Werten. Als besonders kritisch erwies sich hierbei der MCP-Phosphor-Detektor.

Spannungswerte über 1500 V führten leicht zu einem Sättigungsverhalten des Detektors, wodurch sich die Signalqualität stark verschlechterte. Störender Untergrund konnte auf die  $-31$  kV Beschleunigungsspannung der Feld-Box zurückgeführt werden, welche Tertiärelektronen beschleunigt und durch den Aufprall auf beliebige Metalloberflächen Röntgenstrahlung erzeugt.

Als Ergebnis konnten Richtwerte für die Bedienparameter des Gerätes aufgestellt werden, welche die einfache Nutzung des BSM als Diagnosegerät ohne ausführliche Einweisung ermöglicht.

Durch die Nutzung eines Einzelresonators als Rebuncher wurde die longitudinale Breite der Ionenbunche manipuliert. Es wurden durchgängig nicht gaußförmige Profile mit einer RMS Breite von 280 ps bis 650 ps gemessen. Diese systematische Profilvariation wurde genutzt, um die Durchführung einer Emittanzmessung auf der Grundlage von linearen Transformationen zu demonstrieren. Da die gemessenen Profile keiner Normalverteilung entsprachen, wurden drei Ansätze zur Profilanalyse nebeneinander verfolgt. Ein Gauß-Fit, eine logarithmische Normalverteilung und das zweite statistische Moment für beliebige Reihen. Die durch das jeweilige Analyseverfahren erhaltenen Profildauern, aufgetragen über der Fokussierstärke des Rebunchers, sollten einer parabolischen Funktion folgen. Durch die Bestimmung der Fitparameter  $a$ ,  $b$  und  $c$  der Fitfunktion  $y = a(x - b)^2 + c$  kann die Emittanz bestimmt werden. Der kleinste Emittanzwert  $\epsilon = 1.42 \pm 0.14$  keV/u ns wurde für den Gauß-Fit bestimmt, während der größte Wert  $\epsilon = 3.03 \pm 0.33$  keV/u ns durch das statistische Moment bestimmt wurde. Beide Werte verfehlen den Referenzwert von  $\epsilon = 0.85 \pm 0.14$  keV/u ns deutlich, dennoch sind die Ergebnisse zufriedenstellend, da der Referenzwert für eine völlig andere Einstellung des Beschleunigers bestimmt wurde und die gewählte Methode, über die Fitparameter die Emittanz zu bestimmen, nur für normalverteilte Bunchprofile bedenkenlos anwendbar ist.

Um ein besseres Verständnis für die Abläufe im Inneren der elektronenoptischen Struktur des BSM zu erhalten, wurde eine umfassende numerische Simulation geschrieben. Das größte Interesse galt hierbei der Zeitstruktur des Elektronenstrahles innerhalb der Elektronenoptik, da diese die Zeitauflösung verschlechtern kann. Für die Simulation wurde das Programm AMaze 3D von Field Precision LLC benutzt, welches auf einem Finite-Elemente-Code basiert. Die Simulation ist modular in verschiedene Unterprogramme gegliedert.

Zuerst wurde mit Geometer und MetaMesh ein geometrisches Modell mit der gewünschten Genauigkeit erzeugt. Zu beachten ist hierbei, dass der Gitterabstand der numerischen Stützstellen nicht unnötig klein gewählt wird, da der Rechenaufwand hierdurch stark zunimmt. Gleichzeitig muss das erzeugte 3D Gitter exakt mit den Dimensionen der elektronenoptischen Aperturen übereinstimmen.

---

Mit dem HiPhi Utility wurden die aktiven Oberflächen des 3D Modells mit einer festen elektrischen Spannung belegt. Diese Oberflächen dienten zur iterativen Berechnung der Feldverteilung zwischen den Bauelementen des BSM und sind bestimmend für elektro-optischen Eigenschaften des BSM. Für eine genügende Genauigkeit sind viele Wiederholungen bzw. Iterationen notwendig. Die Genauigkeit dieser Feldberechnung wird über das Residuum, die durchschnittliche Abweichung zwischen zwei einzelnen Punkten auf dem Gitter, bestimmt. Hierbei wurde im zeitlich verträglichen Rahmen ein Wert von  $9.7 \cdot 10^{-8}$  erreicht, welcher die empfohlenen  $1 \cdot 10^{-6}$  deutlich unterschreitet.

Mit Hilfe des HiPhiView Programms konnte die Feldverteilung graphisch dargestellt werden und visuell auf Unregelmäßigkeiten geprüft werden. Kleinere Abweichungen wurden im Bereich der Aperturen festgestellt, welche im Experiment beobachtete Verschiebungen des Elektronenstrahles erklären. Des Weiteren zeigte die Feldverteilung teilweise fehlende Abschirmung der aktiven Flächen des BSMs, da ungewollter Feld-durchgriff mehrfach festgestellt wurde.

Ein weiteres Programm, OmniTrack, importiert die von HiPhi berechnete Feldverteilung und berechnet die Bewegung einzelner Elektronen aus einem vorher definierten Ensemble. Hierbei können die Anfangs- und Endkoordinaten, die Anfangs- und Endimpulse, sowie die benötigte Laufzeit von Startpunkt zu Endpunkt ausgelesen werden.

Die Startkoordinaten wurden innerhalb eines kleinen Volumens zufällig bestimmt. Der Schwerpunkt des Startvolumens lag hierbei innerhalb des sensitiven Bereichs der Elektronenoptik, dem Analysevolumen des BSM, um einen hohen Durchsatz der Teilchen zu gewährleisten. Zusätzlich waren die Startimpulse des Ensembles null, damit die beobachteten Effekte ausschließlich auf die elektro-optischen Eigenschaften des BSM zurückgeführt werden konnten.

Da die zeitliche Struktur nur bis zur Ankunft am HF-Abklexer relevant ist, wurden die Teilchen im Zentrum des Ablenkens terminiert. Die statistische Auswertung der Laufzeiten ergab einen RMS Jitter von 5.2 ps bei einer experimentell bestimmten Auflösung von 37 ps. Hierdurch ist sichergestellt, dass die zeitliche Abweichung nur geringfügig die Auflösung beeinflusst. Spätere Rechnungen mit Startimpulsen ungleich null, welche den reell stattfindenden Prozessen bei Ion-Gasatom-Kollisionen nachempfunden sind, ergaben einen um 50 % größeren Wert, welcher ebenfalls noch nicht signifikant ist.

Weitere Untersuchungen der optischen Auflösung zeigten große Übereinstimmungen zwischen Simulation und den experimentellen Werten. Die Darstellung der Elektronentrajektorien, nach dem Passieren des als Einzellinse dienenden HF-Ablenkens, für verschiedene Parameter, zeigte dass die Einzellinse nicht optimal eingestellt werden kann.

Vertiefende Untersuchungen der Feldverteilung innerhalb der Einzellinse zeigten starke Abweichungen der Fokussierstärke um über 20 % innerhalb des von der Linsenapertur zugelassenen Bereichs. Durch diese Inhomogenität ist eine optimale Fokussierung auf den Detektor nicht möglich. Das ursprüngliche Design der Linse sieht die Nutzung einer Nadellochblende von 1 mm Durchmesser vor. Die typischen Abmessungen des divergenten Elektronenstrahles belaufen sich an der Eingangsapertur der Linse auf  $20 \times 3 \text{ mm}^2$ . Die Einzellinse wird daher deutlich außerhalb ihrer Spezifikationen betrieben. Dennoch zeigten die Feldberechnungen, dass durch die Anpassung der Aperturen an die Feld-

---

verteilung der Linse ein befriedigendes Abbildungsverhalten erreicht wird. Hierbei wird der Elektronenstrahl nicht mehr mittig durch die Linse geführt, sondern um wenige Millimeter versetzt, wodurch dieser ausschließlich durch den homogenen Bereich der Feldverteilung geleitet wird. Die Bereiche inhomogener Feldverteilungen werden komplett ausgeblendet.

Der nicht strahlzerstörende BSM liefert eine ausreichend hohe zeitliche Auflösung für detailreiche Untersuchung der longitudinalen Bunchstruktur, ohne negative Einflüsse auf den Ionenstrahl auszuüben. Fortgeschrittene Messungen, wie longitudinale Emitanzbestimmung und Makropulsanalysen, sind möglich und werden dazu beitragen die LINAC Strukturen besser zu verstehen und weiter zu optimieren.

Obwohl bei der Umsetzung des Arbeitsprinzips für den geplanten Proton-LINAC die veränderten Strahlparameter berücksichtigt werden müssen, zeigen die Ergebnisse, wie die Zeitstrukturuntersuchung und die erreichte Phasenauflösung von  $0.5^\circ$  bei 36 MHz, dass zeitliche Auflösungen bei Aufrechterhaltung der Phasenauflösung von bis zu 10 ps für einen neuen BSM Prototypen möglich sind.



# Contents

<b>1. The FAIR and GSI Facilities</b>	<b>1</b>
1.1. The FAIR Complex . . . . .	1
1.2. The Existing GSI Facility . . . . .	2
<b>2. Accelerator Physics Concepts</b>	<b>5</b>
2.1. Parameters of LINACs . . . . .	5
2.2. GSI Linear Accelerating Structures . . . . .	7
2.2.1. The Alvarez Structure . . . . .	7
2.2.2. Radio Frequency Quadrupole . . . . .	8
2.2.3. Interdigital H-mode DTL . . . . .	9
2.2.4. The Crossbar H-mode DTL . . . . .	11
2.3. Emittance . . . . .	12
2.3.1. The 6-dimensional Phase Space . . . . .	12
2.3.2. Conservation of Phase Space Density . . . . .	13
2.3.3. The Phase Space Ellipse . . . . .	14
2.3.4. Twiss Parameters and Beam Envelope Evolution . . . . .	15
2.3.5. Linear Optics . . . . .	16
2.3.6. Emittance Definition . . . . .	18
2.4. Longitudinal Beam Dynamics . . . . .	20
2.4.1. Longitudinal Stability . . . . .	20
2.4.2. Longitudinal Phase Space . . . . .	21
2.5. KONUS Beam Dynamics . . . . .	24
2.5.1. The KONUS Structure . . . . .	24
2.5.2. Zero Degree Phase Space . . . . .	24
2.5.3. Longitudinal Profile Distortions . . . . .	25
<b>3. The GSI Bunch Shape Monitor</b>	<b>27</b>
3.1. Longitudinal Parameters for Relativistic Beams . . . . .	27
3.2. Non-Relativistic Longitudinal Measurements . . . . .	29
3.2.1. Intercepting Bunch Shape Monitor . . . . .	29
3.2.2. Thin Wire in a High Power Ion Beam . . . . .	30
3.2.3. Stripline Faraday Cup . . . . .	33
3.2.4. Time-of-Flight Measurement . . . . .	34
3.3. Non-Intercepting BSM at GSI . . . . .	35
3.3.1. Working Principle . . . . .	36
3.3.2. The Field-Box . . . . .	37

3.3.3.	Electron Beam Coordinates . . . . .	42
3.3.4.	Apertures and Energy Analyzer . . . . .	43
3.3.5.	RF Deflector . . . . .	46
3.3.6.	MCP and Phosphor Assembly . . . . .	48
3.3.7.	CCD Camera . . . . .	49
<b>4.</b>	<b>BSM Measurements</b>	<b>51</b>
4.1.	BSM in Operation . . . . .	51
4.1.1.	Data Acquisition and Post Processing . . . . .	51
4.1.2.	Phase Calibration . . . . .	54
4.1.3.	Imaging Properties of the BSM . . . . .	56
4.1.4.	Phase Resolution and Absolute Time Resolution . . . . .	57
4.2.	BSM Measurements . . . . .	58
4.2.1.	Bunch Profile Measurement . . . . .	58
4.2.2.	Aperture Variation Profiles . . . . .	62
4.2.3.	Single Macro Pulse Measurements . . . . .	64
4.2.4.	Vertical Beam Profile . . . . .	66
4.3.	BSM Parameter Studies . . . . .	68
4.3.1.	Ion Beam Intensity . . . . .	68
4.3.2.	MCP Saturation Effects . . . . .	70
4.3.3.	Macro Pulse Measurement . . . . .	73
4.3.4.	Background Investigation with Absent Bunch Signal . . . . .	74
4.3.5.	Background Investigation with Bunch Signal . . . . .	76
4.4.	Choice of Parameters . . . . .	78
4.5.	Emittance Measurement . . . . .	79
4.5.1.	Experimental Setup . . . . .	79
4.5.2.	Bunch Profile Variation . . . . .	80
4.5.3.	Parabolic Fit . . . . .	83
4.5.4.	Emittance Measurements Conclusion . . . . .	86
<b>5.</b>	<b>Particle Tracking Simulations</b>	<b>87</b>
5.1.	The AMaze Modules . . . . .	87
5.1.1.	Geometer and MetaMesh . . . . .	88
5.1.2.	HiPhi . . . . .	90
5.1.3.	OmniTrack . . . . .	93
5.2.	Particle Tracking . . . . .	96
5.2.1.	Field Distribution and Cross Talk . . . . .	96
5.2.2.	SE Trajectories . . . . .	99
5.2.3.	Longitudinal Structure of the Electron Beam . . . . .	101
5.2.4.	Lens Focusing Properties . . . . .	102
5.2.5.	Lens Aberrations . . . . .	104
5.3.	An Ensemble Generated by the Ion Beam . . . . .	107

---

<b>6. Conclusion</b>	<b>113</b>
6.1. Outlook . . . . .	115
<b>References</b>	<b>116</b>
<b>A. Pictures of the BSM</b>	<b>127</b>
<b>B. Technical Drawings</b>	<b>131</b>
<b>C. Miscellaneous</b>	<b>139</b>



# List of Figures

1.1. The FAIR Facility . . . . .	2
1.2. The GSI Heavy Ion LINAC . . . . .	3
2.1. A Pair of Drift Tubes . . . . .	5
2.2. The Wideröe Concept . . . . .	7
2.3. The GSI Alvarez DTL . . . . .	8
2.4. The 4-rod RFQ . . . . .	9
2.5. Field Distribution IH-DTL . . . . .	10
2.6. The IH Prototype . . . . .	11
2.7. Field Distribution CH-DTL . . . . .	11
2.8. A Divergent Particle . . . . .	13
2.9. The Emittance Ellipse . . . . .	14
2.10. Optics of a Thin Lens . . . . .	16
2.11. A Phase Space Distribution . . . . .	18
2.12. Intrinsic Phase Focusing . . . . .	20
2.13. The Separatrix . . . . .	23
2.14. Separatrix for Different Synchronous Particles . . . . .	23
2.15. The Zero Degree Separatrix . . . . .	24
2.16. KONUS Beam Envelopes . . . . .	25
2.17. Phase Space Distortions . . . . .	26
3.1. Relativistic E-field . . . . .	28
3.2. A Phase Probe Measurement . . . . .	28
3.3. BSM with a Thin Wire . . . . .	29
3.4. Temperature Plot of a Thin Wire . . . . .	30
3.5. Contribution of the Cooling . . . . .	31
3.6. Fraction of the Cooling . . . . .	32
3.7. The Stripline Faraday Cup . . . . .	33
3.8. Time-of-Flight Setup . . . . .	34
3.9. Time-of-Flight Measurement . . . . .	35
3.10. The Non-Intercepting BSM . . . . .	36
3.11. The Field-Box . . . . .	37
3.12. E-field Distribution of the Field-Box . . . . .	38
3.13. CST Calculation Along the Beam Axis . . . . .	39
3.14. The Compensation Electrodes . . . . .	40
3.15. Final Field-Box Assembly . . . . .	41
3.16. The Electron Beam Coordinate System . . . . .	42

3.17. The XY Aperture Module Top View . . . . .	43
3.18. The XY Aperture Module Bottom View . . . . .	43
3.19. The Energy Analyzer . . . . .	44
3.20. Aperture and Energy Analyzer Assembly . . . . .	45
3.21. The RF Deflector . . . . .	46
3.22. The 36 MHz Resonance . . . . .	47
3.23. The Einzel Lens . . . . .	47
3.24. The MCP Detector . . . . .	48
3.25. The MCP Assembly . . . . .	49
3.26. The MCP Assembly . . . . .	50
4.1. Setup of the Exposure Time . . . . .	52
4.2. Data Post Processing . . . . .	53
4.3. Shift of the RF Phase . . . . .	54
4.4. The Phase Calibration . . . . .	55
4.5. Focus Width for Different Lens Settings . . . . .	56
4.6. Optimal Focuses for Different Aperture Settings . . . . .	57
4.7. A Non-Gaussian Bunch Profile . . . . .	58
4.8. Different Analyzing Methods . . . . .	60
4.9. Bunch Profiles with X Aperture Variation . . . . .	62
4.10. RMS Profile Widths . . . . .	63
4.11. Signal Intensity for Different X Apertures . . . . .	64
4.12. Single Shot Measurements . . . . .	65
4.13. The Relative Location of the Bunch Center . . . . .	65
4.14. Vertical Beam Profile Measurement . . . . .	66
4.15. Vertical Beam Profile . . . . .	67
4.16. Measurement with a Profile Grid . . . . .	68
4.17. Ion Beam Contribution without RF Power . . . . .	69
4.18. Ion Beam Contribution with RF Power . . . . .	69
4.19. Ion Beam Induced Background . . . . .	70
4.20. The MCP Signal Amplification . . . . .	71
4.21. MCP Background Amplification . . . . .	71
4.22. Signal-to-Background Ratio . . . . .	72
4.23. Macro Pulse Measurement . . . . .	73
4.24. Trafo Measurement . . . . .	74
4.25. X-ray Induced Background . . . . .	75
4.26. Pressure Induced Background with Closed Apertures . . . . .	75
4.27. Pressure Induced Background with Opened Apertures . . . . .	76
4.28. Pressure Induced Signal . . . . .	77
4.29. Pressure Induced Signal-to-Background Ratio . . . . .	77
4.30. A Single Gap Resonator . . . . .	79
4.31. Rebunched Profile Measurements . . . . .	80
4.32. RMS Profile Widths . . . . .	81
4.33. Bunch Center Fluctuations . . . . .	82

4.34. The Parabola Fit for a Gaussian Profile . . . . .	84
4.35. Parabola Fits for Three Methods . . . . .	85
5.1. The AMaze Selection Screen . . . . .	87
5.2. The Geometer Utility Program . . . . .	88
5.3. The BSM Finite-Element Model . . . . .	89
5.4. The HiPhi Utility Program . . . . .	91
5.5. The HiPhi Input File . . . . .	92
5.6. The OmniTrack Input File . . . . .	93
5.7. The OmniTrack Log File . . . . .	94
5.8. The OmniTrack Output File . . . . .	95
5.9. The Potential Distribution in the XZ Plane . . . . .	97
5.10. The Detailed XZ Plane . . . . .	98
5.11. Electron Trajectory Plot . . . . .	100
5.12. The Lens Focusing . . . . .	103
5.13. Investigation of the Focusing Properties . . . . .	105
5.14. Lens Potential Plot . . . . .	106
5.15. The Simple Ensemble Detection Pattern . . . . .	107
5.16. The Cross Section of Liberated Electrons . . . . .	108
5.17. The XYZ Correlations . . . . .	110
5.18. The Complex Ensemble Detection Pattern . . . . .	112
A.1. Field-Box Full Assembly Top View . . . . .	127
A.2. Energy Analyzer . . . . .	128
A.3. X-ray Shielding . . . . .	129
A.4. BSM in the TK5 . . . . .	130
B.1. Technical Drawing BSM . . . . .	131
B.2. Technical Drawing Field-Box . . . . .	132
B.3. Technical Drawing Compensation Electrode Front . . . . .	133
B.4. Technical Drawing Compensation Electrode Rear . . . . .	134
B.5. Technical Drawing XY Aperture Modul . . . . .	135
B.6. Technical Drawing Energy Analyzer . . . . .	136
B.7. Technical Drawing RF Deflector . . . . .	137
B.8. Technical Drawing MCP mount . . . . .	138
C.1. Python Script . . . . .	139
C.2. Cross Section 1-10 MeV H <sup>+</sup> . . . . .	140
C.3. Cross Section 100-1000 MeV H <sup>+</sup> . . . . .	141





# 1. The FAIR and GSI Facilities

The Facility for Anti-Proton and Ion Research (FAIR) with its tremendous and unprecedented performance goals will extend Darmstadt as a place of world-class accelerator experiments with the highest scientific standards. The FAIR project will extend and complement the 1969 founded GSI Helmholtz Center for Heavy Ion Research, which was, for decades, a leader in demonstrating the synthesis of super heavy elements like Hassium<sup>108</sup> or Darmstadtium<sup>110</sup>. As a result, GSI left its mark in scientific history. Most likely FAIR will continue this story of success with its research on exotic nuclei and antimatter experiments with unprecedented beam intensities and beam quality. For a quick and successful commissioning of the facility, dedicated tools, such as a Bunch Shape Monitor (BSM), are crucial. The performance and feasibility of such a device will be presented as subject of this thesis.

## 1.1. The FAIR Complex

In 2014, the construction of the largest accelerator complex within Europe started (see fig. 1.1). The complex, FAIR, will host more than 3000 scientists from over 50 countries. The first ion beam at this facility is scheduled for 2021 [1]—a Herculean task, which is only possible with the support and supervision of the whole GSI staff. The most prominent section of the FAIR is the SIS100—a 1083.6 m long superconducting synchrotron, capable of accelerating ions from protons up to uranium with a peak energy of 30 GeV or 2.7 GeV/u, respectively [2]. Housed in a tunnel almost 20 m beneath the ground, this machine will be the main accelerator for FAIR. The SIS100 will be the very first step in a 6-part modularized start version of FAIR [3]. After the SIS100, the experimental hall (CBM/HADES) and then the Super Fragment Separator (Super-FRS) will be built. Finally, the proton-LINAC (p-LINAC) will be commissioned, as a high energy proton injector for the SIS100 and SIS18, respectively [4].

The p-LINAC is planned as a Cross Barr H-mode Drift Tube LINAC (CH-DTL). It is expected the commissioning of the p-LINAC will occur quickly due to the use of a BSM. The basic working principles of a CH-DTL will be discussed in section 2.2.4.

The Super-FRS will be a very powerful separator for rare isotopes of all elements and exotic nuclei [5]. Those isotopes can be produced and spatially separated within a few hundred nanoseconds. As a large-acceptance fragment separator, the Super-FRS serves different experimental areas like the Collector Ring (CR) and the new High Energy Storage Ring (HESR). The Collector Ring (CR) is a stochastic precooling storage ring for anti-protons and secondary rare isotopes.

The HESR will allow the investigation of the hadron structure by spectroscopy using

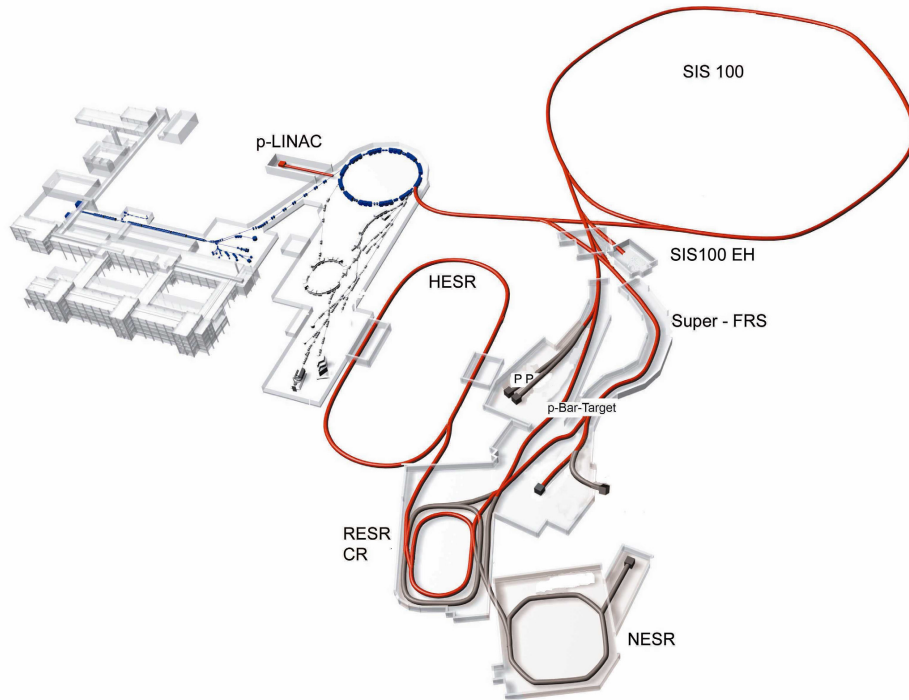


Figure 1.1.: Sketch of the FAIR and GSI Facility. Red areas indicate the sections built in the first phase of the modularized start. Blue areas belong to the GSI injector section for FAIR [6].

anti-protons with unprecedented accuracy. Electron and stochastic cooling will ensure excellent beam quality for experiments [7] like the anti-proton experiment PANDA [8]. The FAIR project will be completed by the New Experimental Storage Ring (NSR), the Recuperated Experimental Storage Ring (RESR) [9] and finally the SIS300, which will be housed directly above the SIS100. These projects will be not realized in the modularized start version, but will be part of the complete FAIR facility. It is also of great importance to upgrade the existing GSI facility, which will work as the injector for FAIR.

## 1.2. The Existing GSI Facility

The GSI Helmholtz Center for Heavy Ion Research, founded 1969 as Gesellschaft für Schwerionenforschung (GSI) [10], will play a key role for FAIR. In particular, the GSI heavy ion accelerator (UNILAC) and the GSI heavy ion synchrotron SIS18 will serve as injectors for the SIS100 [11].

The GSI UNILAC (see fig. 1.2) is the workhorse of the existing GSI facility. Almost every ion beam used for experiments is accelerated by the UNILAC. The UNILAC is not a single module, it consists of different sections. At the front end, there are the

ion sources. The most prominent are the Penning Ionization Gauge (PIG) [12, 13], the MUlti Cusp Ion Source (MUCIS) [12, 14] and the MEtal Vapor Vacuum Arc Ion Source (MEVVA) [12, 15]. The extraction voltage is 10-50 kV. MEVVA and MUCIS have a typical duty cycle of 5 Hz and 1 ms duration [16] for a pulsed beam and 50 Hz and 5 ms for the PIG ion source.

The Low Energy Beam Transport (LEBT) [17] guides the low charged ions into the Radio Frequency Quadrupole (RFQ) [18] which is responsible for the necessary bunching and further acceleration of the distributed ions. As a pulsed machine, the RFQ is a resonator for the given radio frequency (RF) of 36.136 MHz. Further explanation of some basic alternating voltage acceleration principles will follow in section 2.2.2. The energy range is 2.2 - 120 keV/u and the average particle transmission is 89% after the 2009 upgrade [19].

The following Super Lens, another RFQ with enlarged apertures, acts as a 3-dimensional focusing lens into the two Inter-Digital H-Structure Drift Tube LINACs (IH-DTL) [20]. The IH structures are based on KONUS (Kombinierte NULL grad Struktur see sec. 2.5) beam dynamics, which allows higher field gradients and higher power efficiency, than in conventional designs. The beam however is operated in a critical state, leading to instabilities which have to be intercepted with additional focusing elements within the accelerating structure and by limiting the overall structure length. Still, unwanted side effects remain, like longitudinal bunch deformation [21]. The achievable beam energy is 1295 keV/u with a transmission of almost 100% for both structures [22]. This whole section of the facility is called the High Current Injector (HSI).

When leaving the HSI, the beam has a low charge ( $U^{4+}$  or  $Xe^{4+}$ ) and is stripped of further electrons by a gas target (Gasstripper) ( $U^{28+}$  or  $Xe^{21+}$ ) [23]. It is also possible to bypass the HSI and the Gasstripper by using the High Charge State Injector (HLI)[24], consisting of the ECR, an RFQ and another IH-DTL working with a RF of 108.408 MHz. The energy range is 1360 keV/u for the HLI.

The Poststripper section of the UNILAC consists of Alvarez DTLs [25, 26] and Single Gap Resonators (ER) [25]. The Alvarez tanks accelerate the ions up to 11.4 MeV/u. The Beam power now exceeds 1221 kW and the beam intensities reach up to 12.6 mA

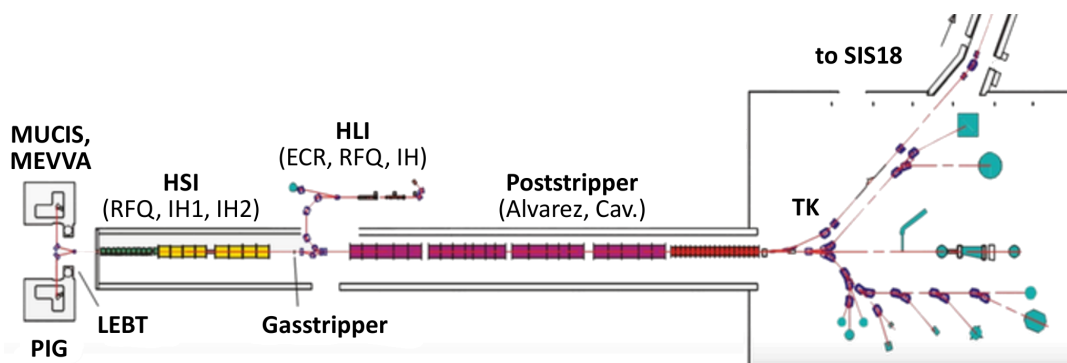


Figure 1.2.: Sketch of the GSI UNILAC and its sections [27].

which has tremendous destructive power for any material put into the ion beam (see sec. 3.2.2). The ER can be used to further increase the beam energy (13.5 MeV/u for U) or manipulate the longitudinal bunch structure for a better injection into the following SIS18.

The SIS18 is connected through the 100 m long Beam Transfer Line (TK) [28]. The TK is responsible for good beam transportation and can be used for different non-destructive beam experiments or providing drift space for effective beam bunching. The prototype BSM is also located in the middle of TK, 50 m in front of the SIS entrance. By traveling through the TK, the beam quality slowly degrades and a fraction of the beam is lost before reaching the SIS18. Before injecting into the SIS18 with an injection efficiency of 80%, the ion beam has to meet the transverse and longitudinal emittance requirements [29]. The SIS18 can accelerate  $10^{10}$  uranium ions per cycle up to 1000 MeV/u. For further usage, the ions are extracted to the Schwerionen-Speicherring (ESR) [30] for storing the beam or to the fragment separator. The beam can also be forwarded into the different high energy experiment sites. Different upgrades are foreseen to match the FAIR requirements of the SIS18 [31].

The proper operation of all these machines strongly depends on the capabilities of the operating crew, which needs information of the status of the machine and the beam. These operating information are mostly provided by sophisticated beam diagnostics, like Beam Position Monitors, Current Transformers or Profile Grids. A Bunch Shape Monitor, as it is subject of this thesis, is a rather new type of diagnostic tool due to the challenging access to the longitudinal beam parameters. A widely available Bunch Shape Monitor will be a key part of near future accelerator physic developments as the growing demand for these diagnostics already demonstrates.

## 2. Accelerator Physics Concepts

A BSM will be a vital new diagnostics tool for future accelerator applications at FAIR, especially for LINAC operations. Therefore, this chapter is mostly dedicated to LINAC related concepts.

### 2.1. Parameters of LINACs

Modern Radio Frequency (RF) LINACS, except for RFQs, consist of drift tubes and gaps embedded in a cavity. The edges of a pair of drift tubes are at different potentials, accumulating charges of different polarity thereby creating a longitudinal electric field  $\vec{E}$  which is responsible for acceleration. On the beam z-axis, the field can be expressed as:

$$E_z = E(0, z) \cos(\omega t(z) + \phi) \quad (2.1)$$

where  $t(z) = \int_0^z dz/v$  is the time when the particle with the velocity  $v$  is at the position  $z$ .

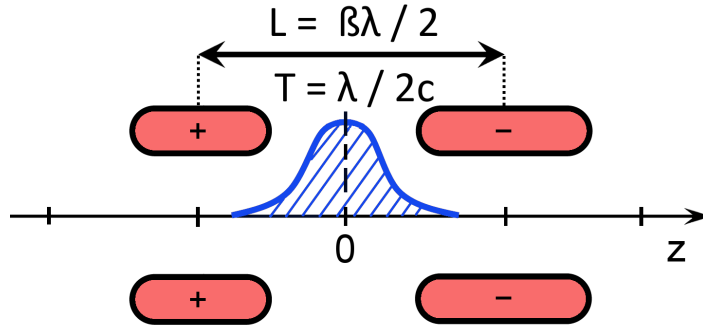


Figure 2.1.: A Pair of Drift Tubes

If for  $t = 0$  the particle is in the middle of the gap, then  $\phi$  is the RF phase of the particle. By crossing the gap, the particle gains the energy  $\Delta W$  as follows:

$$\Delta W = q \int_{-l/2}^{l/2} E(0, z) \cos(\omega t(z) + \phi) dz \quad (2.2)$$

which is usually shown as [32]

$$\Delta W = qV_0 T \cos(\phi). \quad (2.3)$$

$V_0$  is the RF gap voltage and  $T$  is the Transit Time Factor. The Transit Time Factor adjusts the energy gain, due to sinusoidal modulation of the amplitude and the finite time a particle needs to travel through the gap with respect to the DC voltage  $V_0$ . The quality of the accelerating cavity is expressed by the resonance width  $\Delta f$  at the  $-3$  dB value from the maximum  $f_0$ . A more intuitive approach is the ratio between the stored energy  $W$  and the dissipated RF power. The quality factor  $Q$  can be expressed as:

$$Q = \frac{f_0}{\Delta f}(-3 \text{ dB}) = \frac{\omega W}{P}. \quad (2.4)$$

Another quite important parameter of a room temperature cavity is the Shunt Impedance per unit length, which is independent from the excitation of the cavity. The Shunt Impedance  $Z$  is defined as the capability of generating longitudinal voltage for a given dissipated power. The Shunt Impedance reflects the capability of a cavity to generate axial fields in dependence of the applied RF power. It also relates the voltage in the cavity to the dissipated power like in a resistor. The Shunt Impedance per unit length has a typical unit of  $M\Omega/m$  and is expressed as follows:

$$Z = \frac{\left( \int_0^l |E(0, z)| dz \right)}{P \cdot l} \quad (2.5)$$

where  $l$  is the cavity length. While designing an accelerator, it is of great importance to maximize the net energy gain per dissipated power, obtaining a high efficiency of the accelerator. By relating the Transit Time Factor  $T$  to the Shunt Impedance, one obtains the Effective Shunt Impedance per unit length, which is expressed as:

$$Z_{\text{eff}} = ZT^2 \cdot \cos^2 \bar{\phi} \quad (2.6)$$

where  $\bar{\phi}$  stands for the averaged RF phase. Starting from the expressions shown above, it is easy to prove the following relations:

$$P \propto f^{-1/2}, \quad (2.7)$$

$$Q_0 \propto f^{-1/2}, \quad (2.8)$$

$$ZT^2 \propto f^{-1/2}, \quad (2.9)$$

$$\frac{ZT^2}{Q} \propto f. \quad (2.10)$$

Usually, the operating frequency together with the energy range are the most important parameters to describe any accelerating structure and are therefore the most prominent characteristics. Still other defined parameters such as the Shunt Impedance are convenient when viewing different cavity designs to assess the advantages and disadvantages of these specific designs.

## 2.2. GSI Linear Accelerating Structures

As the scientific field evolved, so too did the GSI facility and its accelerating structures. The first systematic investigation of the atomic nucleus became possible with early electrostatic accelerators like Van-de-Graaff-Accelerator or Cockcroft-Walton-Generator in the thirties. Those first accelerators reached energies of a few MeV and high continuous particle currents of several mA [33].

Soon the limitations of the electrostatic design became obvious, due to maximum applicable electric voltage. Based on the work of G. Ising, R. Wideröe suggested the use of alternating voltage for acceleration by using several cylindrical, tube-like electrodes (drift tubes). By adapting the length of the drift tubes to the particle velocity, the drift tubes work as a Faraday cage and shield the particle from the decelerating field induced by the alternating voltage. This introduces the concept of synchronous particle and is considered as the first Drift Tube LINAC (DTL). The following section will introduce the most prominent LINAC concepts used at GSI at present.

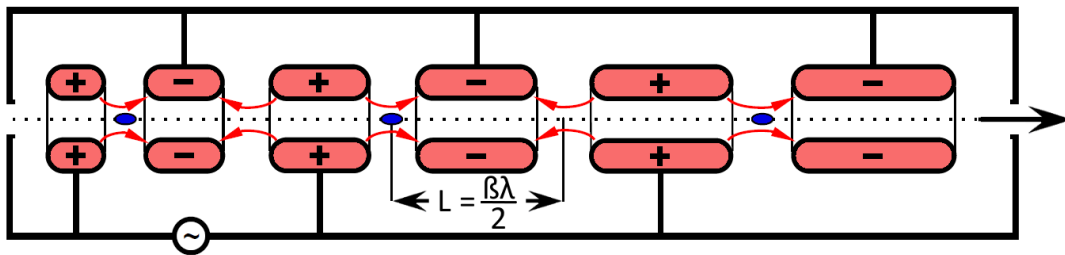


Figure 2.2.: Sketch of the Wideröe concept.

### 2.2.1. The Alvarez Structure

The basic idea of Wideröe was further developed by Luis Alvarez in the forties [34]. Instead of applying simply alternating voltage, an electromagnetic wave is used to induce the high electric fields within a cavity resonator.

Due to the increasing availability of RF amplifiers, in particular the klystron, this approach became more and more common. Typically the cavity length is matched to  $\lambda/2$  of the applied RF in order to form a standing wave within the cavity or one cell of the cavity. The cavity structure features only longitudinal E-field components ( $TM_{010}$ ). This rather simple field distribution contributes to the robustness of the design.

To gain energy, the particle has to be injected within the right phase and with enough velocity to pass the gap in time (synchronous particle), much before the amplitude of the standing wave inverted its sign.

If only a single anti-node fits into the vacuum structure, it is called a Single Gap Resonator (SGR). If consecutive gaps within one vacuum structure are used, suitable drift tubes have to be mounted into the structure, comparable to Wideröe.

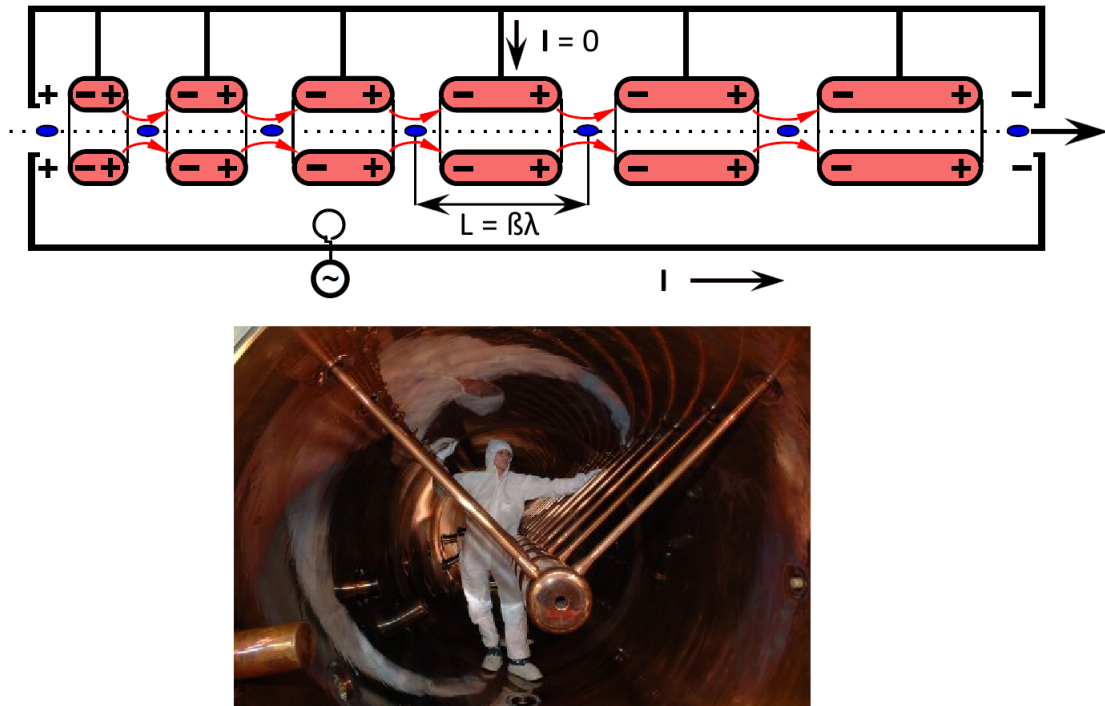


Figure 2.3.: Sketch of an Alvarez and below a picture of the GSI Alvarez DTL [35].

As long as the decelerating phase prevails, the particle is shielded within the drift tube without losing any energy and arrives at the next gap in time to be accelerated again. As the particle progresses along the LINAC, the gap between the drift tubes has to match the particle velocity to maintain the phase synchronization.

Typical SGRs are driven in  $\pi$ -mode, whereas the Alvarez structure is driven in  $2\pi$ -mode. In the case of  $\pi$ -mode, the subsequent gap phase is decelerating—meaning the particle should arrive within a half period for proper acceleration. For  $2\pi$ -mode, all cavities have the same phase and the particle should arrive within a full period. This leads to longer drift space, but allows the omission of the cell walls between the gaps, due to the cancellation of the wall currents in  $2\pi$ -mode. The energy lies between 50 MeV and 200 MeV. For protons, this corresponds to  $\beta = 0.55$  or 55% of the speed of light. Alvarez structures are used all over the world because of their easy handling. Nevertheless they are outclassed by more sophisticated, but also more complicated and therefore less robust designs.

### 2.2.2. Radio Frequency Quadrupole

The Radio Frequency Quadrupole (RFQ) represents a unique structure within the family of LINACs. Similar to the Alvarez DTL, it is also driven by RF fields, but in contrast, longitudinal and transverse field components are used together.

The longitudinal field is responsible for the acceleration and bunching, whereas the



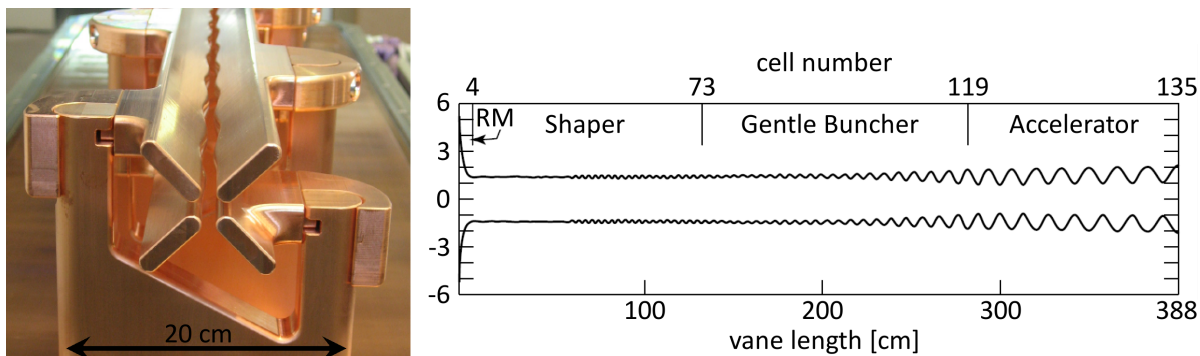


Figure 2.4.: Picture of a 4-rod RFQ (left) [37]. Scheme of a typical RFQ electrode modulation (right), with the elongation of the cell length and stronger modulation [38]. Both parameters determine whether a cell is primary focusing, bunching or accelerating.

transverse is responsible for the focusing of the initial ion distribution [36], typically provided by an ion source. The RFQ bunching process is adiabatic and therefore almost 100% effective in contrast to conventional designs, which dump the majority of the particles.

The design is based on four electrodes, with an  $x$  plane pair and a  $y$  plane pair. The pairs' electrode surface is modulated with a sinusoidal function. The modulation of the pairs is shifted to each other: the convex part of the  $x$ -electrodes fits into the concave part of the  $y$ -electrodes and vice versa.

An accelerating cell consists of one full sine modulation and changes its geometric properties with longitudinal progression—adapting to the changing requirements due to beam acceleration. The modulation amplitude is responsible for the longitudinal, accelerating field component. A high modulation amplitude leads to high acceleration and low transverse focusing (focusing through quadrupole shape).

While propagating through the RFQ, the ions are further focused transversely and bunched in longitudinal direction. By leaving the RFQ, the ion beam is prepared to be accepted by conventional DTL structures for further acceleration. The achieved energies are between 0.3 and 5 MeV per nucleon.

### 2.2.3. Interdigital H-mode DTL

The Interdigital H-mode Drift Tube LINAC (IH-DTL) is a very sophisticated DTL and was first introduced by J.P. Blewett at the CERN Symposium in 1956 [39]. Today the IH cavity is considered as standard for velocities below  $\beta = 0.1$ .

The structure is driven by a parallel and antiparallel high frequency magnetic field in beam direction [42]. In contrast to an Alvarez structure which is excited in the Transverse Magnetic Mode (TM), the IH cavity is excited in the Transverse Electric Mode (TE). This indicates the absence of longitudinal electric field components in the cavity.

The accelerating component is generated by field distortion caused by the drift tube stems (see figure 2.5). In order to understand the field distribution of an IH cavity, one should use the Maxwell Equations for a cylindrical, empty resonator with radius  $R$  and length  $L$ . If the resonator is excited in the  $H_{111}$ -mode one obtains the following equations [40]:

$$B_z = B_0 J_1 \left( 1.841 \frac{r}{R} \right) \cos \theta \sin \frac{\pi z}{l} e^{i\omega t} \quad (2.11)$$

$$B_r = \frac{\pi}{l} B_0 J_1 \frac{R}{1.841} \left( 1.841 \frac{r}{R} \right) \cos \theta \cos \frac{\pi z}{l} e^{i\omega t} \quad (2.12)$$

$$B_\theta = -\frac{\pi}{l} \frac{R^2}{1.841^2 r} B_0 J_1 \left( 1.841 \frac{r}{R} \right) \sin \theta \cos \frac{\pi z}{l} e^{i\omega t} \quad (2.13)$$

$$E_r = i\omega \frac{R^2}{1.841^2 r} B_0 J_1 \left( 1.841 \frac{r}{R} \right) \sin \theta \sin \frac{\pi z}{l} e^{i\omega t} \quad (2.14)$$

$$E_\theta = i\omega \frac{R}{1.841} B_0 J_1' \left( 1.841 \frac{r}{R} \right) \quad (2.15)$$

$$E_z = 0 \quad (2.16)$$

where the resonance frequency for an empty cavity is given by

$$\omega = \frac{c}{\sqrt{\frac{1.841^2}{R^2} + \frac{\pi^2}{l^2}}}. \quad (2.17)$$

The drift tube itself disturbs the field distribution by its significant additional contribution to the capacitance of the cavity. For example the CERN IH-DTL (LINAC3) tank 2 has a diameter of 335 mm and a length of 1549 mm [41]. The resonance frequency for an undisturbed  $H_{111}$ -mode is 535.3 MHz in strong contrast to the measured one of 202.56 MHz [41]. Due to this extra capacitance, the IH structure is highly efficient with a high Shunt Impedance but has high demands on the beam dynamics and is used in the mid and low energy range ( $\beta \leq 0.3$ ,  $\leq 200$  MHz) [42].

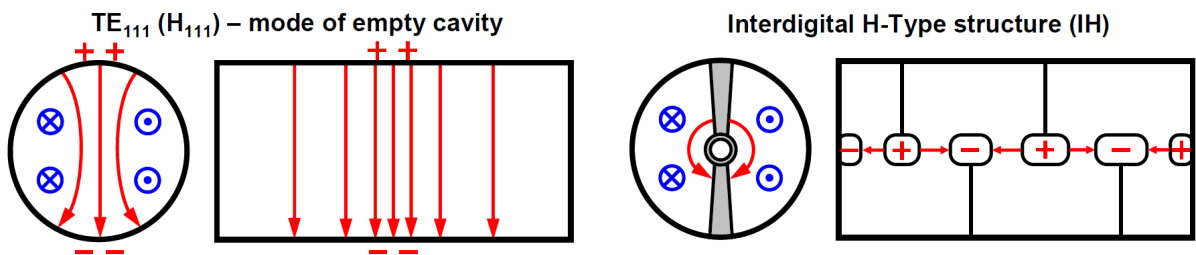


Figure 2.5.: Field distribution in an empty cavity and with interdigital drift tubes. Due to the stem-induced field distortions, an H-mode acceleration is possible [43].

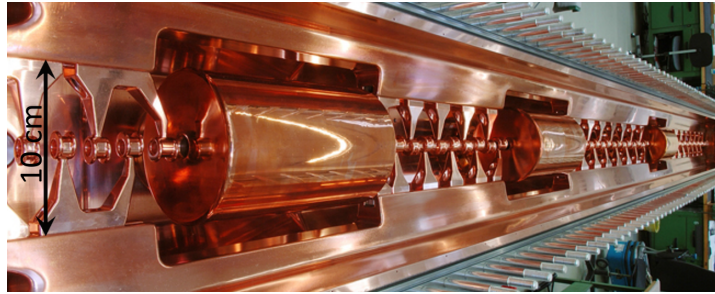


Figure 2.6.: IH prototype at GSI [43].

### 2.2.4. The Crossbar H-mode DTL

For higher frequencies than 200 MHz, the IH design is getting far too demanding on the manufacturing tolerances of the cavity. At a higher frequency, for example 325 MHz, a different approach should be considered.

A Crossbar H-mode DTL (CH-DTL) excites higher H-modes,  $H_{n11}$  (with  $n = 2, 3, 4..$ ). Following Faraday's, law more stems in the cavity increase the magnetic flux which leads to a decrease of the Shunt Impedance. It is obvious to choose the  $H_{211}$ -mode which is by far the easiest to build. Like for the IH-cavity, the accelerating field component is created by currents flowing across the stems to the drift tubes (see picture 2.7).

It is also clear that the stems carry the highest current density. The stems' geometry significantly affects the cavity's efficiency and its mechanical robustness due to capacitive load and to thermal stress. It is also intended to locally tune the CH cavity. The local gap voltage can be changed up to  $\pm 20\%$  by changing the cavity capacitance [44]. This is already demonstrated for IH cavities. The CH-DTL allows designs up to some GHz with an energy from 3 to 150 MeV [45]. For lower energies, the IH alternative is far more effective due to capacitive load between the stems which reduces RF efficiency. Due to these promising properties, the CH-DTLs are chosen as the main structure for the FAIR p-LINAC, especially after the successful test of a 2:1 scaled CH model in 2007 [46].

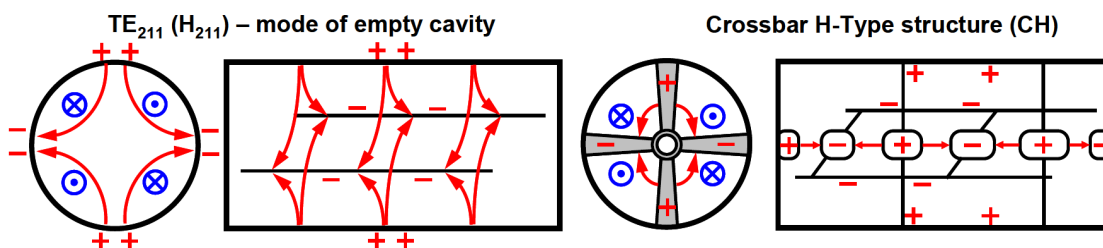


Figure 2.7.: Field distribution in an empty cavity and with crossbar drift tubes. Again the stems induce field distortions, but in contrast to the IH-DTL, a suitable distribution is less demanding with respect to the surface quality [47].

## 2.3. Emittance

All of the previously presented designs were based on the concept of synchronous particle which travels on an ideal trajectory through the whole accelerating structure. The investigation of the dynamics of particle distribution is the subject of the following section.

### 2.3.1. The 6-dimensional Phase Space

In a 3-dimensional space three spatial coordinates and three momentum coordinates are necessary for a complete description of the particle motion. Together these six coordinates define a phase space. Usually the center of gravity lies in the origin of the ordinates and the particle trajectory points in the direction of the  $z$ -axis. One particle is described by  $f_6(x, y, z, p_x, p_y, p_z)$ . Typically the occupied area in phase space looks like a hyper-ellipsoid with the half-axis  $a_i$

$$\sum_{i=1}^6 = a_i k_i^2 \text{ for } k_i = (x, y, z, p_x, p_y, p_z). \quad (2.18)$$

By integration of the function  $f_6$  for all  $k_j \neq k_i$  for  $i = 1, \dots, n < 6$  one obtains the distribution of the subspaces in order to separate transverse and longitudinal movement.

This is appropriate if only linear forces (no scattering, no space charge, energy conservation) are taken into account and therefore, there is no coupling between these two subspaces. Now one has the 4-dimensional transverse emittance  $f_4(x, y, p_x, p_y)$  and the 2-dimensional longitudinal emittance  $f_2(z, p_z)$ , thereby  $f_2(x, p_x)$ ,  $f_2(y, p_y)$  and  $f_2(z, p_z)$  applies to

$$f_2(x, p_x) = \int \int \int \int f_6 \, dy dp_y dz dp_z \quad (2.19)$$

$$f_2(y, p_y) = \int \int \int \int f_6 \, dx dp_x dz dp_z \quad (2.20)$$

$$f_2(z, p_z) = \int \int \int \int f_6 \, dx dp_x dy dp_y \quad (2.21)$$

These integrations correspond to the projection of the 6-dimensional phase space into its low dimensional subspaces. Usually it is suitable to determine the angles  $x'$  and  $y'$  between the trajectory and the beam axis (see figure 2.8) as  $p_x$  and  $p_y$  cannot be directly measured.

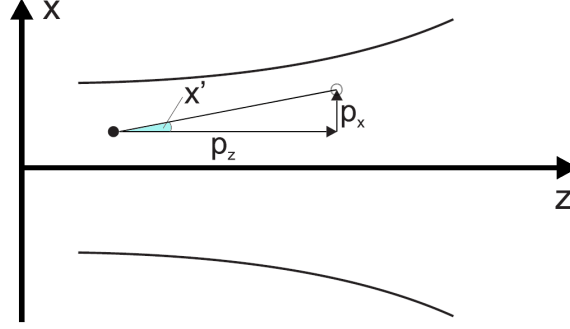


Figure 2.8.: A particle with a diverging beam envelope. The trajectory and the z-axis enclose the angle  $x'$ .

### 2.3.2. Conservation of Phase Space Density

After the description of one particle in phase space, it is necessary to introduce a formalism for an ensemble of particles. Considering a 3-dimensional Hamiltonian system with coordinates  $q_i$  for  $i = (x, y, z)$  and the conjugate momenta  $p_i$  for  $i = (x, y, z)$ , one can pick a phase space vector  $\vec{x} = (\vec{q}, \vec{p})$  and use the Hamiltonian equations (see [48])

$$\dot{\vec{x}} = (\dot{\vec{q}}, \dot{\vec{p}}) = \left( \frac{\partial H}{\partial \vec{p}}, -\frac{\partial H}{\partial \vec{q}} \right). \quad (2.22)$$

By using  $\text{div} := \left( \frac{\partial}{\partial \vec{q}}, \frac{\partial}{\partial \vec{p}} \right)$  on  $\dot{\vec{x}}$  one obtains:

$$\text{div } \dot{\vec{x}} = \left( \frac{\partial^2 H}{\partial \vec{p} \partial \vec{q}} - \frac{\partial^2 H}{\partial \vec{q} \partial \vec{p}} \right) = 0. \quad (2.23)$$

This applies due to the symmetry of second derivatives, which allows the interchanging order of partial derivatives. With the help of the continuity equation one obtains:

$$\frac{\partial f}{\partial t} + \text{div}(f \cdot \dot{\vec{x}}) = 0 \quad (2.24)$$

$$\frac{\partial f}{\partial t} + \frac{\partial}{\partial \vec{q}} (f \dot{\vec{q}}) + \frac{\partial}{\partial \vec{p}} (f \dot{\vec{p}}) = 0 \quad (2.25)$$

$$\frac{\partial f}{\partial t} + f \underbrace{\left( \frac{\partial^2 H}{\partial \vec{p} \partial \vec{q}} - \frac{\partial^2 H}{\partial \vec{q} \partial \vec{p}} \right)}_{\text{div } \dot{\vec{x}} = 0} + \dot{\vec{q}} \frac{\partial f}{\partial \vec{q}} + \dot{\vec{p}} \frac{\partial f}{\partial \vec{p}} = 0 \quad (2.26)$$

$$\text{with } f(\vec{q}, \vec{p}, t) \Rightarrow \frac{df}{dt} = 0 \quad (2.27)$$

Which basically means that the phase space density is conserved or, in other words, if the particles are compressed in spatial domain, they are decompressed in momentum

space which means their momenta distribution increases. This principle is also known as Liouville's theorem and allows predictions of the beam behavior for any location if its emittance has once been determined.

### 2.3.3. The Phase Space Ellipse

In order to gain a qualitative representation of the emittance of an ion beam, it makes sense to further separate the emittance in its  $x$  and  $y$  transverse components. This is only true if the phase spaces are not coupled with each other. For example, this is not the case in solenoids, but holds true for most emittance measurement locations.

In the following the phase space distribution  $\epsilon$  for  $x$  and  $p_x$  (denoted by  $x'$ ) will be shown as the area of a phase space ellipse with the half-axis  $a$  and  $b$  (see fig. 2.9). For the half-axis we apply  $\frac{x^2}{a^2} + \frac{x'^2}{b^2} = 1$  in Cartesian coordinates. The ellipse can also be obtained in different tilt angles, depending on the point of reference.

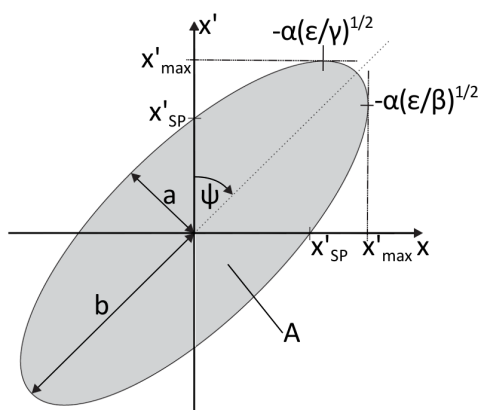


Figure 2.9.: Sketch of an emittance ellipse and its most important points: intersections with the axis, maximum displacement and the tilt angle  $\Psi$  [49].

More important than the half-axis are the Twiss Parameters  $\alpha, \beta, \gamma$ , which link the ellipse with its projection on the axis  $x$  and  $x'$ , the beam width and the maximum momentum. Typically these parameters are easy to measure for the transverse case. In accordance to [50], the Twiss Parameters are defined as

$$\alpha = \left( \frac{a^2 - b^2}{ab} \right) \cos \Psi \sin \Psi, \quad (2.28)$$

$$\beta = \frac{b}{a} \sin^2 \Psi + \frac{a}{b} \cos^2 \Psi, \quad (2.29)$$

$$\gamma = \frac{b}{a} \cos^2 \Psi + \frac{a}{b} \sin^2 \Psi. \quad (2.30)$$

With the aid of these three parameters and the emittance  $\epsilon$ , the ellipse is defined as

$$\epsilon = \frac{A}{\pi} = \gamma \cdot x^2 + 2\alpha \cdot xx' + \beta \cdot x'^2, \quad (2.31)$$

$$\text{with the normalization } \beta\gamma - \alpha^2 = 1. \quad (2.32)$$

Hence, we just showed that the emittance is the product of the two half-axes and not, as it can easily be confused, the area of the ellipse. The emittance has the dimension m, but is usually discripted as mm · mrad.

### 2.3.4. Twiss Parameters and Beam Envelope Evolution

The Twiss Parameter  $\alpha$  is dimensionless and depends on the correlation of  $x$  with  $x'$ . The parameter  $\alpha$  is negative for divergent beams and positive for convergent beams. Hence, it is zero in the beam focus.

The parameter  $\beta$  is always greater than zero ( $\beta > 0$ ) and has the inverse dimension of  $\beta$  ( $\frac{\text{m}}{\text{rad}}$ ). The parameter  $\gamma$  is also positive ( $\gamma > 0$ ) and has the inverse dimension with radiant per length ( $\frac{\text{rad}}{\text{m}}$ ). In addition, it depends on  $\alpha$  and  $\beta$ :

$$\gamma = \frac{1 + \alpha^2}{\beta}, \text{ for } \gamma > 0. \quad (2.33)$$

The correlation between the Twiss Parameters and the emittance  $\epsilon$  can be shown as:

$$\alpha = -\overline{xx'}/\epsilon, \quad (2.34)$$

$$\beta = \overline{x^2}/\epsilon, \quad (2.35)$$

$$\gamma = \overline{x'^2}/\epsilon. \quad (2.36)$$

Furthermore, the following applies to the Twiss Parameters and the most prominent points and parameters of the emittance ellipse:

$$\Psi = \frac{1}{2} \arctan \left( \frac{2\alpha}{\gamma - \beta} \right), \quad (2.37)$$

$$\pm x_{\max} = \pm \sqrt{\beta \cdot \epsilon}, \quad (2.38)$$

$$\pm x'_{\max} = \pm \sqrt{\gamma \cdot \epsilon}, \quad (2.39)$$

$$\pm x_{\text{inter}} = \pm \sqrt{\epsilon/\gamma}, \quad (2.40)$$

$$\pm x'_{\text{inter}} = \pm \sqrt{\epsilon/\beta}. \quad (2.41)$$

For better understanding, picture 2.10 depicts the connection between the beam envelope traveling through a thin lens and the emittance ellipse for certain points of recording. It also shows the correlation between a divergent beam and the Twiss Parameters.

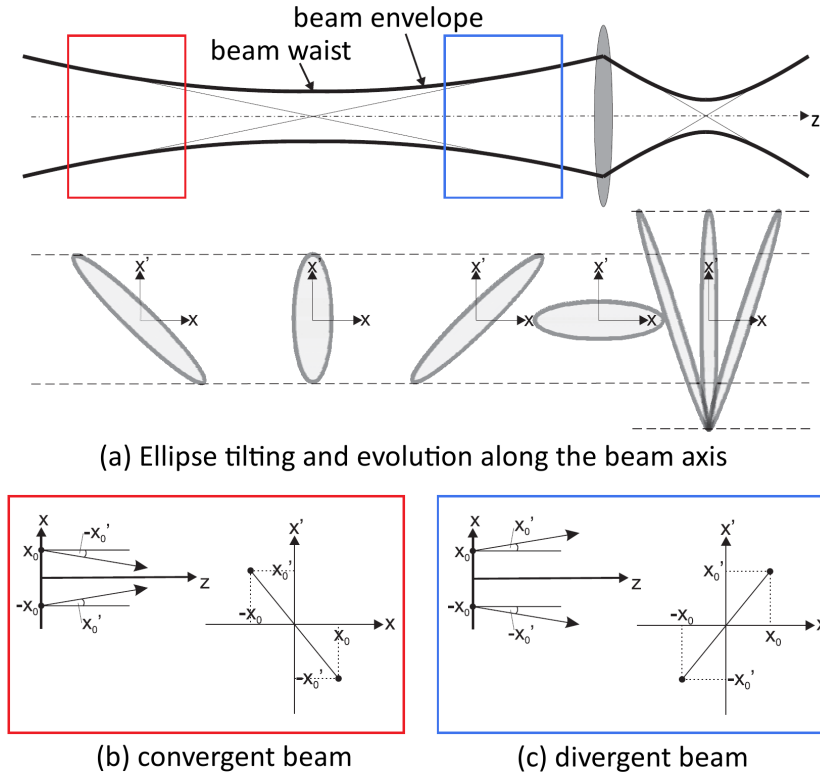


Figure 2.10.: Depicted is the evolution of an emittance ellipse along an optical system with a thin lens. From the left to the middle the beam is convergent, the ellipse is tilted to the left. In the beam waist the ellipse is upright. Here, the projection on the  $x$ -axis is minimal. Moving forward, the ellipse is now tilted to the right, the beam is divergent. The process is repeated after the thin lens with a different ellipse shape, but the occupied phase space area is conserved (figure from [51]).

### 2.3.5. Linear Optics

With the absence of non-linear forces and by the use of matrix algebra the progression of any particle can be calculated and predicted. First, the initial arbitrary particle parameters have to be defined with a 6-dimensional vector  $\vec{x}$  analog to the emittance:

$$\vec{x} = \begin{pmatrix} x_1 \\ x_2 \\ x_3 \\ x_4 \\ x_5 \\ x_6 \end{pmatrix} = \begin{pmatrix} x \\ x' \\ y \\ y' \\ l \\ \delta \end{pmatrix} = \begin{pmatrix} \text{horizontal location} \\ \text{horizontal angle} \\ \text{vertical location} \\ \text{vertical angle} \\ \text{longitudinal location} \\ \text{longitudinal momentum spread} \end{pmatrix} \quad (2.42)$$

With the knowledge of the transportation  $6 \times 6$  matrix  $\mathbf{R}$  the resulting vector  $\vec{x}(s)$  at location  $s$  can be obtained as follows:

$$\vec{x}(s) = R(s)\vec{x}(0) \quad (2.43)$$



In full representation,  $\mathbf{R}$  has the following appearance:

$$\mathbf{R} = \begin{pmatrix} R_{11} & R_{12} & R_{13} & R_{14} & R_{15} & R_{16} \\ R_{21} & R_{22} & R_{23} & R_{24} & R_{25} & R_{26} \\ R_{31} & R_{32} & R_{33} & R_{34} & R_{35} & R_{36} \\ R_{41} & R_{42} & R_{43} & R_{44} & R_{45} & R_{46} \\ R_{51} & R_{52} & R_{53} & R_{54} & R_{55} & R_{56} \\ R_{61} & R_{62} & R_{63} & R_{64} & R_{65} & R_{66} \end{pmatrix} \quad (2.44)$$

For a decoupled  $x$ ,  $y$  and longitudinal plane the matrix can be simplified to:

$$\mathbf{R} = \begin{pmatrix} R_{11} & R_{12} & 0 & 0 & 0 & 0 \\ R_{21} & R_{22} & 0 & 0 & 0 & 0 \\ 0 & 0 & R_{33} & R_{34} & 0 & 0 \\ 0 & 0 & R_{43} & R_{44} & 0 & 0 \\ 0 & 0 & 0 & 0 & R_{55} & R_{56} \\ 0 & 0 & 0 & 0 & R_{65} & R_{66} \end{pmatrix} \quad (2.45)$$

and can be separated into submatrices to obtain the resulting vector  $\vec{x}(s)$  as follows:

$$\begin{pmatrix} x(s) \\ x'(s) \end{pmatrix} = \begin{pmatrix} R_{11} & R_{12} \\ R_{21} & R_{22} \end{pmatrix} \begin{pmatrix} x(0) \\ x'(0) \end{pmatrix}, \quad (2.46)$$

$$\begin{pmatrix} y(s) \\ y'(s) \end{pmatrix} = \begin{pmatrix} R_{33} & R_{34} \\ R_{43} & R_{44} \end{pmatrix} \begin{pmatrix} y(0) \\ y'(0) \end{pmatrix}, \quad (2.47)$$

$$\begin{pmatrix} l(s) \\ \delta(s) \end{pmatrix} = \begin{pmatrix} R_{55} & R_{56} \\ R_{65} & R_{66} \end{pmatrix} \begin{pmatrix} l(0) \\ \delta(0) \end{pmatrix}. \quad (2.48)$$

This representation offers the advantage to present many beam guiding elements in a very simple manner and allows quick and easy computation of particle properties. The most prominent elements in the matrix formalism are:

A drift of the length  $L$ :

$$\mathbf{R}_x = \mathbf{R}_y = \begin{pmatrix} 1 & L \\ 0 & 1 \end{pmatrix}. \quad (2.49)$$

A thin lens with the focal length  $f$ :

$$\mathbf{R}_x = \mathbf{R}_y = \begin{pmatrix} 1 & 0 \\ 1/f & 1 \end{pmatrix}. \quad (2.50)$$

And an accelerating tube for a constant gradient [52]:

$$\mathbf{R}_x = \mathbf{R}_y = \begin{pmatrix} 1 & L_{\text{eff}} \\ 0 & p_1/p_2 \end{pmatrix}, \quad L_{\text{eff}} = L \frac{p_1 c}{E_1 - E_2} \ln \frac{p_2 c + E_2}{p_1 c + E_1}. \quad (2.51)$$

If instead of a single particle the phase ellipse is used, the matrix entries use now their phase ellipse counterparts:

$$\boldsymbol{\sigma}_x = \begin{pmatrix} \sigma_{11} & \sigma_{12} \\ \sigma_{21} & \sigma_{22} \end{pmatrix}, \quad (2.52)$$

$$\sigma_y = \begin{pmatrix} \sigma_{33} & \sigma_{34} \\ \sigma_{43} & \sigma_{44} \end{pmatrix}, \quad (2.53)$$

$$\sigma_l = \begin{pmatrix} \sigma_{55} & \sigma_{56} \\ \sigma_{65} & \sigma_{66} \end{pmatrix}. \quad (2.54)$$

### 2.3.6. Emittance Definition

It is of great importance to introduce different emittance definitions, because in the scientific community there are several designation for the emittance. Among the most used designations for emittance are:

- actual occupied phase space
- effective emittance
- rms emittance
- normalized emittance
- 90% emittance

#### Actual Occupied Phase Space

In the case of nonlinear forces the occupied area in phase space is not necessarily an ellipse. Usually particles tend to oscillate around the beam axis with a constant angular velocity and return to their initial position after one turn. For nonlinear forces, particles further away from the axis receive a higher angular velocity. Hence, they will not return to their initial position. This leads to typical s-shapes in phase space (see fig. 2.11).

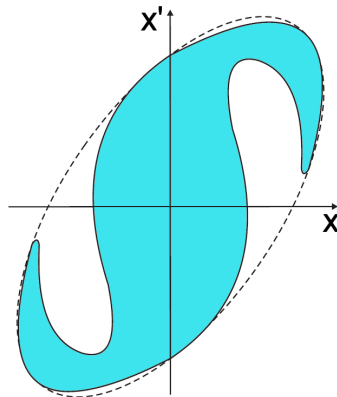


Figure 2.11.: Typical s-shape of the actual phase space distribution for the presence of nonlinear forces and the effective emittance as surrounding ellipse.

### Effective Emittance

The effective emittance describes the smallest area in phase space which can be bordered by an ellipse (see fig. 2.11), therefore the following applies  $\epsilon_{\text{occ}} \leq \epsilon_{\text{eff}}$ . If the nonlinear effects increase, the effective emittance will increase, but the actual occupied phase space stays constant. Nevertheless, the effective emittance is a crucial parameter, because all the accelerator structures have to be matched to the effective emittance [53].

### Root-Mean-Square Emittance

The RMS emittance serves as a tool to compare beams with different charge distributions. It does not only consider the occupied phase space area, but it also includes the density distribution within the occupied area. Therefore, the second order statistical moment is taken into account. With  $x$  as coordinate,  $x'$  as angle,  $\rho$  as the density in each phase space element and with  $N$  for the particle number, the RMS emittance is defined as:

$$\epsilon_{\text{eff}} = \sqrt{\overline{x^2} \cdot \overline{x'^2} - \overline{xx'^2}} \text{ with} \quad (2.55)$$

$$\overline{x^2} = \frac{1}{\rho_{\text{ges}}} \sum \rho_i x_i^2, \quad (2.56)$$

$$\overline{x'^2} = \frac{1}{\rho_{\text{ges}}} \sum \rho_i x_i'^2, \quad (2.57)$$

$$\overline{xx'^2} = \left[ \frac{1}{\rho_{\text{ges}}} \sum \rho_i x_i x_i' \right]^2. \quad (2.58)$$

### Normalized Emittance

Beam acceleration (increasing longitudinal momentum) leads to an emittance reduction, called adiabatic damping. By using a normalization the dependance of the emittance of the beam energy is terminated. It is defined as:

$$\epsilon_n = \beta_z \cdot \gamma_z \cdot \epsilon \text{ for} \quad (2.59)$$

$$\beta_z = v_z/c \text{ and} \quad (2.60)$$

$$\gamma_z = 1/\sqrt{1 - \beta_z^2} \quad (2.61)$$

## 2.4. Longitudinal Beam Dynamics

### 2.4.1. Longitudinal Stability

As mentioned in 2.1, particles have to match the RF phase between the drift tubes in order to achieve proper acceleration. The synchronous particle  $s$  has the energy  $W_s$  at the entrance of the structure and the phase  $\phi_s$ . For the actual experienced accelerating field  $U_{\text{eff}}$  the following applies:

$$U_{\text{eff}} = U_0 \cdot \cos(\phi_s) = E_0 \cdot T \cdot \cos(\phi_s). \quad (2.62)$$

Where  $U_0$  is the maximum energy gain,  $E_0$  the maximum field strength and  $T$  the Transition Time Factor (see sec. 2.1). This condition must also apply for all the other gaps. The maximum energy gain will be achieved for  $\phi_s = 0^\circ$ , but it is not possible to accelerate all particles at the same phase. Mostly the particles are closely distributed around the synchronous particle and form a bunch. For  $\phi_s = 0^\circ$  the bunch will defocus due to the unsuited energy gain and most particles will be lost. To avoid total beam loss, a different phase  $\phi_s \neq 0^\circ$  must be utilized.

For longitudinal stability, a negative phase  $\phi_s < 0^\circ$  is suitable. If the synchronous particle passes the gap while the field strength is still increasing, stability is attained. Particles which enter the gap earlier will gain less acceleration, therefore allowing the synchronous particle to catch up. Particles which have less energy, will experience a higher accelerating field  $E_z(t)$ , therefore catching up to the synchronous particle. Figure 2.12 depicts the phase focusing and it shows that phase focusing only holds true for

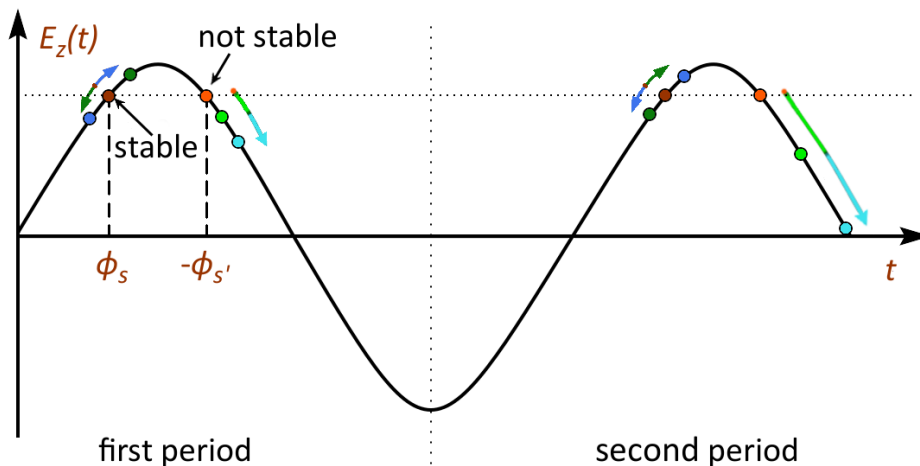


Figure 2.12.: Schematic of an accelerating amplitude and synchronous particle (dark red) with negative phase  $\phi_s = -30^\circ$  and non stable synchronous particle (red)  $\phi_{s'} = +30^\circ$ . The blue and green particles change position (oscillate) around the stable particle, where blue and green next to the unstable particle are losing pace and will get lost.

$\phi_s < 0^\circ$  and  $\phi_s > -180^\circ$ . Many structures work at  $\phi_s \leq -30^\circ$  and allow stable longitudinal movement, while the other particles oscillate around the synchronous particle.

### 2.4.2. Longitudinal Phase Space

For a better understanding of the longitudinal dynamics, some mathematical considerations have to be taken into account which are based on the following assumptions (section 2.4.2 in based on [54]):

- Particles are only accelerated within the center of the gaps (thin gap approximation)
- Particles drift force-free from one gap to another
- The distance  $L_n$  between two gaps  $n$  and  $n - 1$  is defined as  $L_n = N \cdot \beta_{n,s} \cdot \lambda$

For  $n =$  number of the cell,  $N = 1$  for a Alvarez (IH-DTL  $N = 1/2$ ),  $i =$  index of particle,  $s =$  index of synchronous particle, therefore for the energy gain per cell applies:

$$W_{n,s} = q \cdot U_{\text{eff},n} \cdot \cos(\phi_{n,s}), \quad (2.63)$$

$$W_{n,i} = q \cdot U_{\text{eff},n} \cdot \cos(\phi_{n,i}). \quad (2.64)$$

It is shown that the energy difference only depends on the phase, therefore for the energy difference between a particle and the synchronous particle the following applies:

$$\Delta(W_i - W_s) = q \cdot U_{\text{eff},n} \cdot (\cos(\phi_{n,s}) - \cos(\phi_{n,i})). \quad (2.65)$$

As for the phase difference of a non synchronous particle the following applies:

$$\begin{aligned} \frac{\Delta\phi_{n,i}}{2\pi} &= \frac{\beta_{n-1,s}}{\beta_{n-1,i}}; L_{n-1} = \beta_{n-1,s} \cdot \lambda, \\ \Delta\phi_{n,i} &= 2\pi \cdot \frac{\beta_{n-1,s}}{\beta_{n-1,i}} = 2\pi \cdot \frac{\beta_{n-1,s} \cdot \lambda}{\beta_{n-1,i} \cdot \lambda} = 2\pi \cdot \frac{L_{n-1}}{\beta_{n-1,i} \cdot \lambda}. \end{aligned} \quad (2.66)$$

In addition for a synchronous particle the following applies:

$$\Delta\phi_{n,s} = 2\pi \cdot \frac{L_{n-1}}{\beta_{n-1,s} \cdot \lambda} = 2\pi. \quad (2.67)$$

By using equation 2.66 and 2.67 one obtains equation 2.68 for the relative phase in relation to the synchronous particle:

$$\Delta(\phi_i - \phi_s) = 2\pi \frac{L_{n-1}}{\lambda} \left( \frac{1}{\beta_{n-1,i}} - \frac{1}{\beta_{n-1,s}} \right) = -2\pi \frac{\Delta\beta}{\beta_{n-1,s}}, \quad (2.68)$$

$$\text{with } \frac{1}{\beta_{n-1,i}} - \frac{1}{\beta_{n-1,s}} = \frac{1}{\beta_{n-1,s} + \Delta\beta} - \frac{1}{\beta_{n-1,s}} \approx -\frac{\Delta\beta}{(\beta_{n-1,s})^2}, \Delta\beta \ll 1.$$

By substituting the relativistic work,

$$\Delta W = A \cdot m_o \cdot \gamma^3 \cdot c^2 \cdot \beta \cdot \Delta\beta$$

into equation 2.68, the equation becomes:

$$\Delta(\phi_i - \phi_s)_n = -2\pi \frac{W_{n-1,i} - W_{n-1,s}}{A \cdot m_o \cdot c^2 \cdot \gamma_{n-1,s}^3 \cdot \beta_{n-1,s}^2}. \quad (2.69)$$

Now it is switched from a discrete to a continuous description. The accelerating fields now act as mean force along the beam z-axis. This allows equation 2.65 and 2.69 to be depicted as total derivative.

$$\frac{d(W_i - W_s)}{dz} = q \cdot E_0 \cdot T \cdot (\cos(\phi_i) - \cos(\phi_s)) \quad (2.70)$$

with

$$\frac{d(\phi_i - \phi_s)}{dz} = \frac{\Delta(\phi_i - \phi_s)}{L_{n-1}} = \frac{\Delta(\phi_i - \phi_s)}{\beta_{n-1} \cdot \lambda},$$

equation 2.69 yields:

$$\frac{d(\phi_i - \phi_s)}{dz} = -2\pi \frac{W_i - W_s}{A \cdot m_o \cdot c^2 \cdot \gamma_s^3 \cdot \beta_s^2}. \quad (2.71)$$

Through deriving equation 2.71 and by substituting 2.70 in 2.71 one obtains a second-order differential equation from two coupled first-order differential equations:

$$\frac{d^2}{dz^2}(\phi_i - \phi_s) = \frac{-2\pi}{Am_o c^2 \gamma_s^3 \beta_s^3 \lambda} \cdot \frac{d}{dz}(W_i - W_s) = \frac{-2\pi q E_0 T}{Am_o c^2 \gamma_s^3 \beta_s^3 \lambda} \cdot (\cos(\phi_i) - \cos(\phi_s)). \quad (2.72)$$

By multiplying both sides with  $\frac{d(\phi_i - \phi_s)}{dz}$ , whereby  $\frac{d(\phi_i - \phi_s)}{dz} = \frac{d(\phi_i)}{dz}$  and by integration of  $dz$  with the aid of a substitution one obtains:

$$\int \frac{d(\phi_i - \phi_s)}{dz} \cdot \frac{d^2(\phi_i - \phi_s)}{dz^2} dz = \int \frac{-2\pi q E_0 T}{Am_o c^2 \gamma_s^3 \beta_s^3 \lambda} \cdot (\cos(\phi_i) - \cos(\phi_s)) \cdot \frac{d(\phi_i)}{dz} dz, \quad (2.73)$$

$$\frac{1}{2} \left( \frac{d(\phi_i - \phi_s)}{dz} \right)^2 = \frac{-2\pi q E_0 T}{Am_o c^2 \gamma_s^3 \beta_s^3 \lambda} \cdot (\cos(\phi_i) - \cos(\phi_s)) \cdot d\phi_i, \quad (2.74)$$

With the aid of equation 2.71 the left expression is converted. The right expression is integrated. Finally one obtains the equation for the phase space motion:

$$\frac{\pi(W_i - W_s)^2}{Am_o c^2 \gamma_s^3 \beta_s^3 \lambda} + q E_0 T \cdot (\sin(\phi_i) - \phi_i \cdot \cos(\phi_s) + C) = 0. \quad (2.75)$$

The quadratic equation 2.75 is solved by:

$$(W_i - W_s) = \Delta W = \pm \sqrt{\frac{1}{\pi} Am_o c^2 \gamma_s^3 \beta_s^3 \lambda \cdot q E_0 T \cdot (\phi_i \cdot \cos(\phi_s) - \sin(\phi_i) - C)}. \quad (2.76)$$

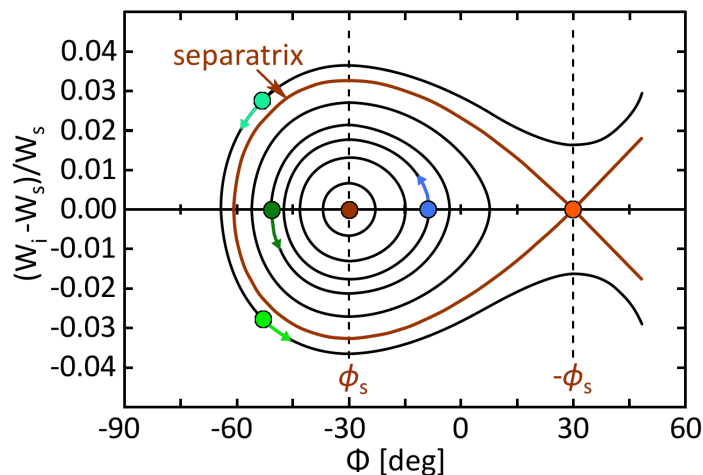


Figure 2.13.: Different trajectories in the  $\Delta\phi, \Delta W$  phase space and the separatrix with particle movement indicated.

Equation 2.76 describes oscillations of the particles in the  $\Delta\phi, \Delta W$  phase space. Figure 2.13 shows the stable (closed orbits) and non-stable (opened orbits) trajectories in phase space. The stable and non-stable domain are separated by the separatrix (see fig. 2.13), which is defined by the phase of the synchronous particle. The trajectory through  $-\phi_s$  is the upper limit for stable movements. The inside of the separatrix is called RF bucket or longitudinal acceptance. The shape and area of the RF bucket change with the phase of the synchronous particle. For  $\phi_s = -90^\circ$  is the area at a maximum, but there is no acceleration. For  $\phi_s = 0^\circ$ , at maximum acceleration, the separatrix completely vanishes (see fig. 2.14), therefore no stable particle movement is possible. It should be noted that the separatrix is only closed for  $\beta_s, \gamma_s = const$ . In a LINAC the separatrix is opened and the enclosed area decreases with the acceleration, but it is possible to trap and confine the particles within the RF bucket.

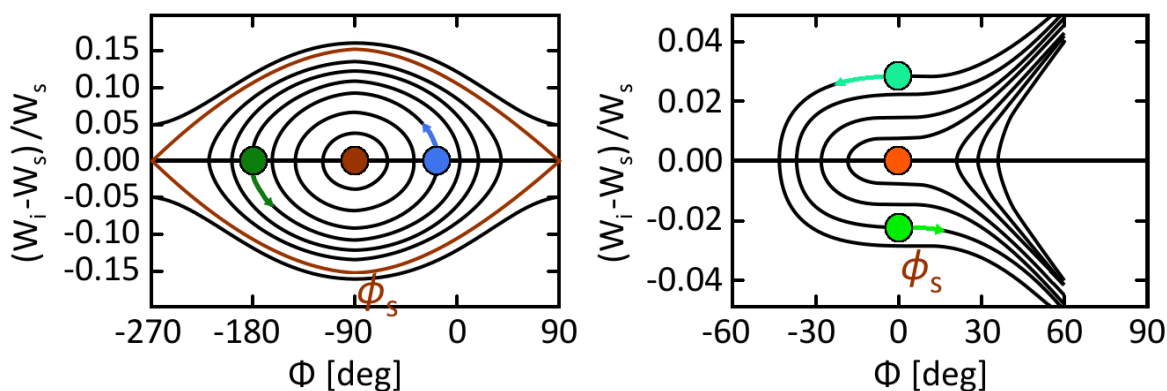


Figure 2.14.:  $\Delta\phi, \Delta W$  phase space trajectories for different synchronous particles ( $\phi_s = -90^\circ$  and  $\phi_s = 0^\circ$ ) with particle movement indicated.

## 2.5. KONUS Beam Dynamics

Section 2.4.2 explained basic longitudinal beam dynamics and made a clear statement for the non-stable case  $\phi_s = 0^\circ$ , where section 2.2 introduces the H-mode cavities and showed the advantages over conventional designs (high efficiency, short structures). To even better benefit from the H-mode structures, a synchronous particle phase of zero degree is highly desirable. To operate an H-mode structure at zero degree and to guarantee stable particle movement, a new beam dynamics concept has been developed.

The KONUS (German for combined zero degree structure) beam dynamics ensures stable acceleration, high efficiency of the applied RF. Initially developed by Professor Ratzinger and extensively described here [55], this chapter will only talk about the key characteristics of KONUS and the consequences for the beam operation.

### 2.5.1. The KONUS Structure

A KONUS structure differs from the conventional design. Transverse and longitudinal focusing is separated. Due to  $\phi_s = 0^\circ$  transverse defocusing is far less a problem, transverse focusing for each gap can be neglected. Typically 10 up to 20 gaps at  $\phi_s = 0^\circ$  are put in series and a succeeding powerful transverse focusing section is put into the cavity, mostly a quadrupole-triplet. Hereafter 3 up to 7 gaps are for the longitudinal bunching at  $\phi_s = -30^\circ$  used. These 3 sections compose one KONUS period. It is possible to put more than one period into one vacuum tank (see fig. 2.6).

### 2.5.2. Zero Degree Phase Space

The previous section introduced the three compartments of a KONUS period. The first is operating at zero degree, therefore no longitudinal phase focusing will occur, but prevention of debunching is still necessary. The fundamentally different approach is to distinguish the synchronous particle and the center of the particle distribution (bunch

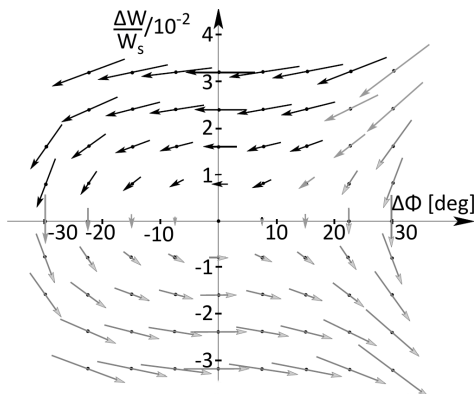


Figure 2.15.: Particle trajectories of  $\Delta\phi$ ,  $\Delta W$  phase space for a zero degree synchronous phase. The black arrows indicate the usable area by KONUS [55].



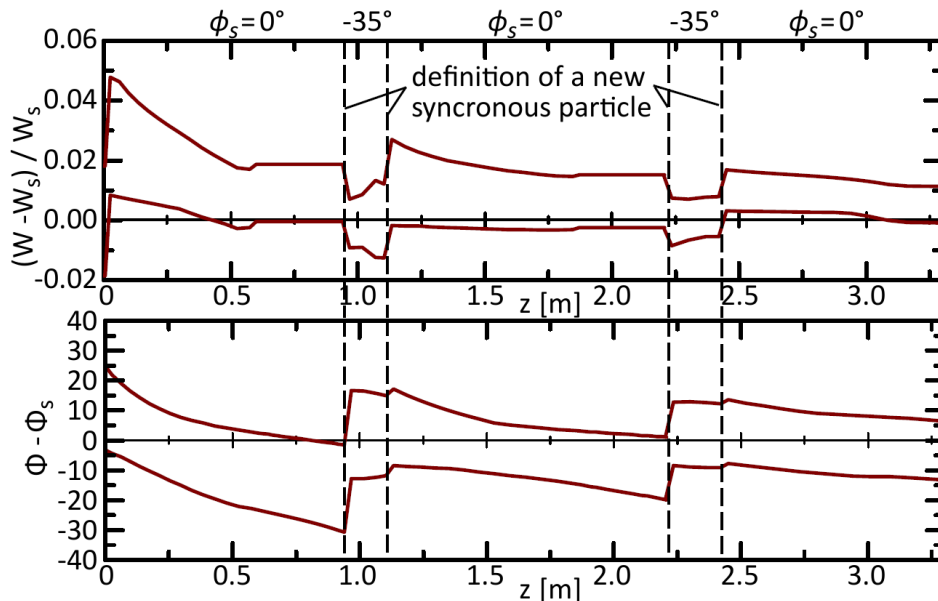


Figure 2.16.: Progression of the beam envelopes of  $\Delta W/W_s$  and  $\phi - \phi_s$  for the IH-structure at the GSI-HLI [55].

center). In conventional designs they are identical. In KONUS dynamics the bunch is injected too late into the structure in respect to the synchronous particle. In addition the bunch carries higher momentum than the synchronous particle. Gap after gap, the bunch catches up with the synchronous particle until it completely loses the additional momentum. Typically it takes a quarter phase oscillation. Figure 2.15 depicts the suitable phase space district for asynchronous injection of a bunch.

After the  $0^\circ$  section the particles are transversely focused, mostly through a quadrupole-triplet. In longitudinal space the focusing section acts as a drift and therefore it should be as short as possible. The bunch leaves this section in longitudinal divergence. A rebunching, phase focusing section (see section 2.4.1), with  $\phi_s = -35^\circ$  of typically 3 up to 7 gaps completes the KONUS period. It is possible to continue with another period within the same vacuum structure, as figure 2.16 indicates. The phase jumps shown in figure 2.16 are artificial and can be eliminated by depicting the center of the particle distribution instead of the synchronous particle.

### 2.5.3. Longitudinal Profile Distortions

In most discussions about longitudinal beam dynamics, it is assumed that the beam profile follows a Gaussian distribution or at least the initial beam at the section entrance. If this is not true, profile distortions will manifest, if they do not already exist. This is mostly treated under the topic of emittance growth because phase space observations are a powerful tool to investigate or even trace back the source of any disturbance.

In the ideal case (only linear forces), the trajectories in phase space are closed and the particle distribution is conserved (see 2.3.2), although it is subject to synchrotron

oscillations. If the ion distribution leaves an area with a defined phase and enters another, a phase matching error is the result. The trajectories in phase space change, as the profile will, too. Obviously the deformation depends on the magnitude of the phase mismatch and the acceleration section's longitudinal dynamic or on its separatrix shape. Once the distortion manifests, it will continue to travel or grow through the entire accelerator until the particles in the deformed parts are dumped and therefore are completely lost. Even more susceptible are structures with no separatrix because phase space trajectories are not closed. These structures also rely on phase jumps to compensate for the absence of the separatrix which increases the probability and magnitude of a phase matching error. But also good-natured structures as the Alvarez are capable of strong longitudinal deformations, if the initial ion distribution, even Gaussian, does not meet the structure's initial phase space demands. This was shown within the HIPPI collaboration [56], where strong emittance fragmentation emerged due to an not matched initial emittance.

Figure 2.17 depicts the beam evolution while propagation through the CH2-tank of the planned proton-LINAC at FAIR. Although the initial bunch profile looks Gaussian, besides the long tail, the phase space distribution reveals a fragmentation. While progressing, the phase space distribution will continue to fray out through different angular velocities.

After the first bunching section, the bunch profile is smoothed. After the second bunching section, the profile shows another tail in the opposite direction and the phase space distribution is already strongly fragmented. This leads to a separation of the profile into two distributions at the exit of the CH2-tank. This shows that by the means of longitudinal beam dynamics, it is almost impossible to stop further beam degradation without dumping the detached particles. In a best case scenario, it could be possible to contain the beam degradation, but the initial distortions will travel through all the succeeding structures. Good longitudinal matching of the accelerating structures with a dedicated tool, like a BSM, is essential for proper commissioning of the CH-mode DTLs.

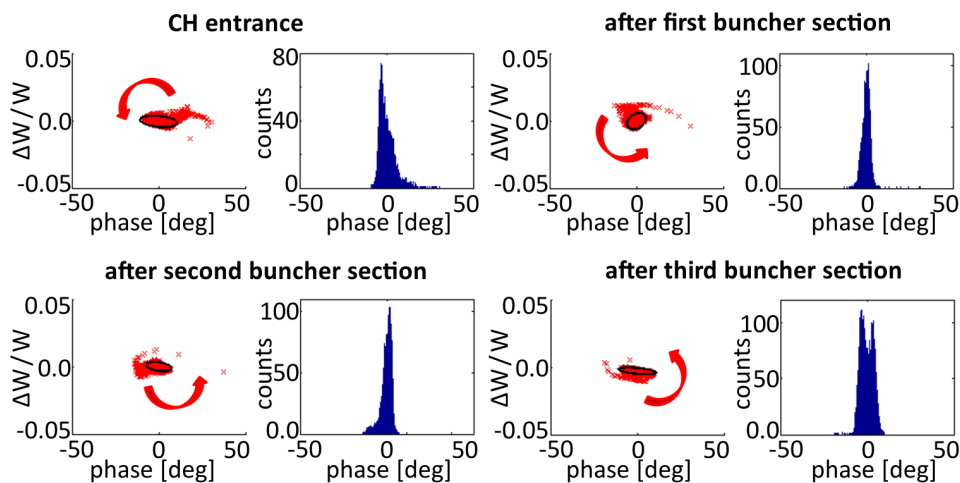


Figure 2.17.: Progression of the phase space distribution and the bunch profile along the CH2-tank of the p-LINAC for FAIR [57].

# 3. The GSI Bunch Shape Monitor

The preceding chapter introduced basic concepts and Linear Accelerator principles. Together with KONUS dynamics it was shown how and why the determination of longitudinal parameters are gaining more and more importance in accelerator facilities, especially for FAIR. This chapter introduces different approaches to measure longitudinal parameters. Furthermore the different approaches serve as demonstration why a non-intercepting BSM was designed in its present form. Finally a detailed description of the non-intercepting BSM is given. Section 3.1 is based on [58].

## 3.1. Longitudinal Parameters for Relativistic Beams

For many applications the easiest way to perform a longitudinal parameter determination is to observe the electric field of the ion distribution with a capacitive pick-up. Considering the dependence of the field distribution on the velocity of the ions, due to the finite speed of light, the electric field  $E_{\parallel}$  in beam direction for a single charge  $q = e$  in the resting lab-frame [59] is calculated as follows:

$$E_{\parallel}(t) = -\frac{e}{4\pi\epsilon_0} \cdot \frac{\gamma\beta ct}{[R^2 + (\gamma\beta ct)^2]^{3/2}} \quad (3.1)$$

whereby  $R$  is the closest approach to the charge and  $\gamma$  is the Lorentz factor. For  $E_{\perp}$  applies:

$$E_{\perp}(t) = \frac{e}{4\pi\epsilon_0} \cdot \frac{\gamma R}{[R^2 + (\gamma\beta ct)^2]^{3/2}} \quad (3.2)$$

The formulas are valid for a single particle in free space. For a correct calculation of an ion distribution one has to integrate over all the particles and furthermore due to the boundary conditions for the surface of the beam pipe or a capacitive pick-up the formulas are further modified [60]. For low velocities the obtainable field distribution does not represent the particle distribution, the electric field precedes the particle with the speed of light. For higher  $\beta$  the occupied volume by the electric field is far smaller, therefore the distribution is compressed, the field around the particles increases. Figure 3.1 illustrates this issue for different  $\beta$ .

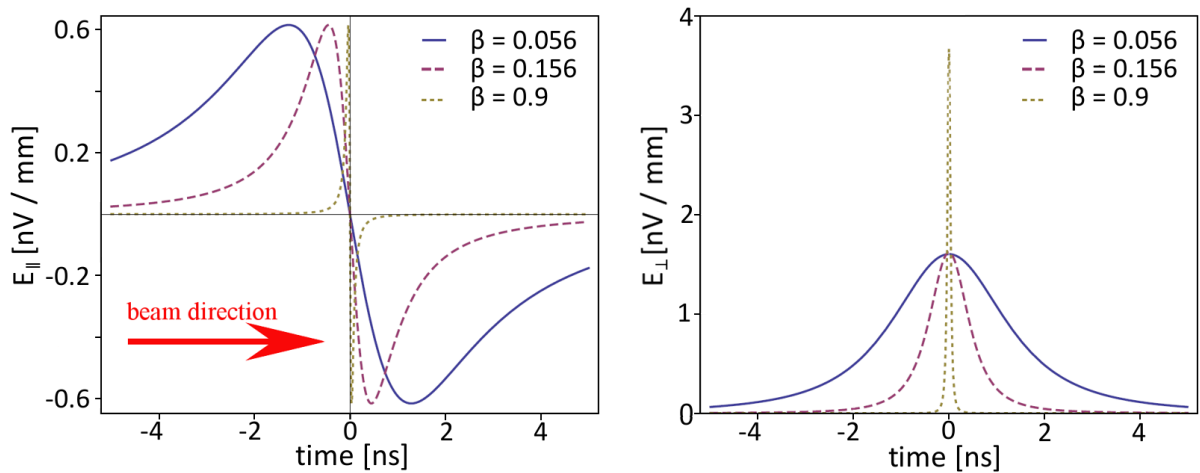


Figure 3.1.: E-field distribution for different  $\beta$  in beam direction (left) and perpendicular (right) for the identical point-like charge [61].

The left side in figure 3.1 depicts for  $t = 0$  zero-crossing for the E-field, where the single particle passes the point of observation. This indicates the option to determine the center of gravity for an ion distribution as well. This parameter is crucial for the longitudinal matching of different accelerating structures and its determination is even possible at low energies. Figure 3.2 depicts an obtained capacitive pick-up signal at GSI for a low energy of 1.4 MeV/u with the bunch positions.

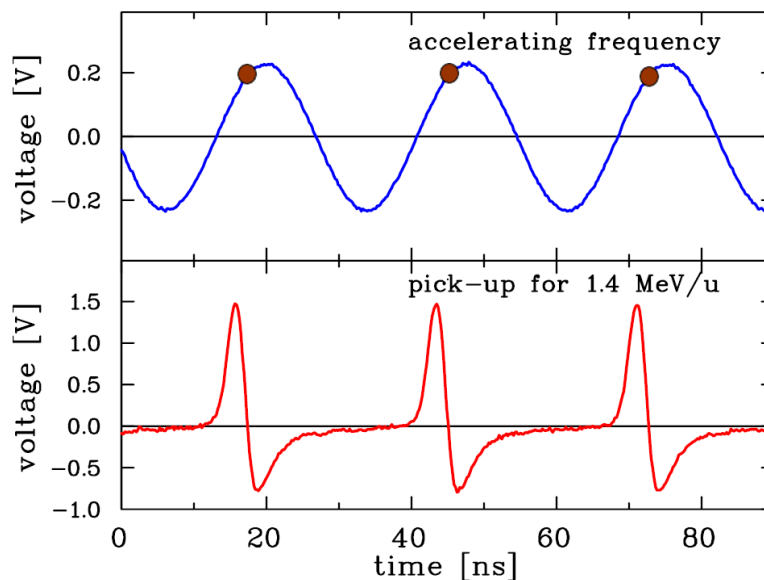


Figure 3.2.: Bunch center (red dot) indicated by zero-crossing of the pick-up signal in correlation to driving RF of the LINAC module [62].

## 3.2. Non-Relativistic Longitudinal Measurements

As pointed out in section 3.1 for beam velocities  $\beta < 0.9$  it is not possible to reconstruct the longitudinal bunch profile by measuring the E-field distribution. As a  $\beta$  below 0.9 is the case for most LINACs, different more invasive approaches are necessary.

### 3.2.1. Intercepting Bunch Shape Monitor

The secondary electron based intercepting Bunch Shape Monitor [63] is an established and reliable device for the bunch structure observation. A thin conductive wire (made of carbon or tungsten) is put in the beam (see fig. 3.3).

The ion impact liberates secondary electrons which are accelerated by a voltage of typically  $-10$  kV applied to the wire. Through a thin slit the fast electrons exit the beam tube and travel through the capacitive end (two plates) of a  $\lambda/4$  resonator matched to the accelerator RF or a higher harmonic. This leads to a specific angle of deflection for the electron's time of arrival, therefore the resonator works as a time-to-space-converter (analog to an oscilloscope). After a drift of about 0.5 m the deflected electrons are detected with a Faraday cup or an electron multiplier with a front slit. To analyze the whole bunch the deflector HF phase has to be swept for several degrees, with the result of observing different parts of the bunch structure in correlation with the RF phase. This method requires several beam pulses to obtain the full bunch shape.

For proper imaging quality, the electron beam has to be focused by an electrostatic Einzel lens via the deflector. Also the influence of beam induced space charge effects has to be estimated.

The thin wire can be moved, allowing measurements for different horizontal locations

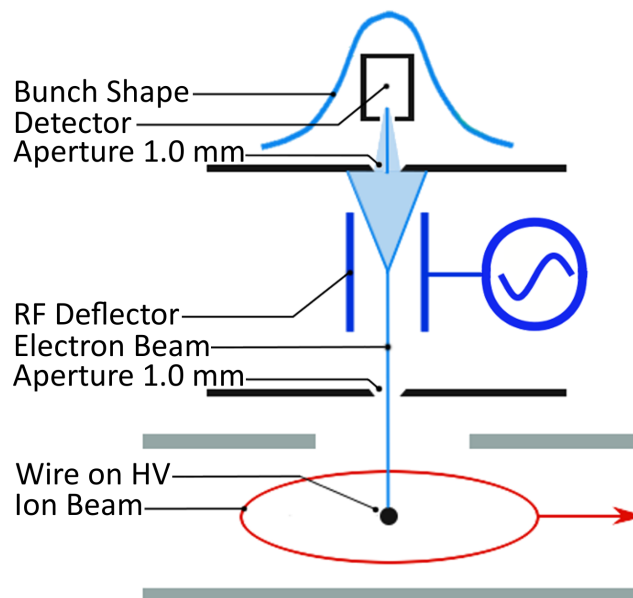


Figure 3.3.: Sketch of secondary electron BSM with a thin wire.

and avoiding wire damage for high beam powers by moving it into the beam edges. The resolution of the device is higher than  $1^\circ$  in phase and it is also known that the fast process of secondary electrons has a jitter of below 6 ps [64], therefore much faster than required. For accelerators with a high RF, a high phase resolution leads to a high time resolution. For example for p-LINAC at Fair, working at 325 MHz, a phase resolution of  $1^\circ$  corresponds to 8.5 ps.

### 3.2.2. Thin Wire in a High Power Ion Beam

The GSI LINAC has a beam peak power of 1221 kW at 11.4 MeV/u and  $I_{\max} = 12.6$  mA [65]. Even only a fraction of this huge power can vaporize many materials with a single macro pulse. To investigate the thermal behavior of a thin wire with  $\varnothing 100 \mu\text{m}$  a simple numerical simulation of a 10 mm wide segment in the wire center has been done. The simulation code only takes energy deposition by the beam and heat dissipation into account. Phase transitions are neglected because close to a transition the mechanical stress would be too much for a reliable operation of a wire.

A  $\text{U}^{73+}$  beam with an energy of 11.4 MeV/u has, due to its high charge and mass, a rather low penetration depth in tungsten of  $31 \mu\text{m}$  with a quite uniform energy deposition in the material. For a carbon wire the penetration is about  $98 \mu\text{m}$  according to SRIM calculations. This indicates that not all bunch ions are stopped in a carbon wire. A good approximation gives the comparison of the wire cross section area with the square of the penetration depth. This leads to 81% absorption in carbon for the ions. For both materials it can be considered that the beam heats the material uniformly until the maximum penetration depth is reached. One possibility for heat dissipation is thermal conduction which can be described by Fourir's law [66] as follows:

$$\dot{Q} = \frac{\lambda}{d} A (T_1 - T_2) \quad (3.3)$$

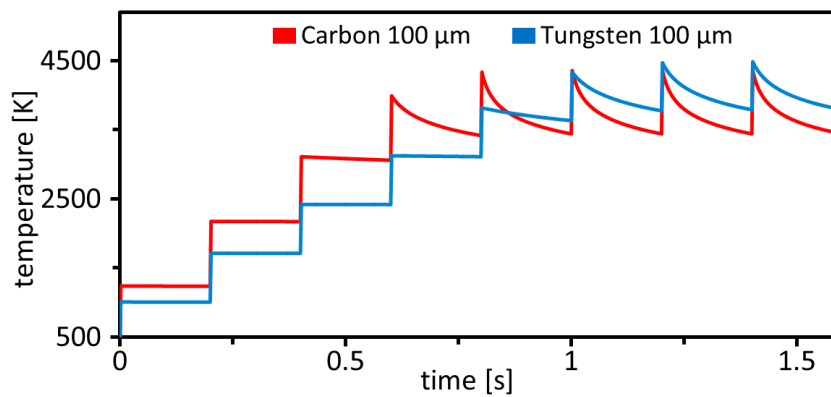


Figure 3.4.: The temperature of a tungsten and carbon wire heated by the ion beam. Within one second a temperature above 4000 K is reached. Beam parameter: 11.4 MeV/u,  $\text{U}^{73+}$ ,  $I = 5.0$  mA, pulse length  $\tau = 2$  ms, repetition rate 5 Hz, transverse RMS width  $\pm 5$  mm.

The thermal power  $\dot{Q}$  is proportional to the flow area  $A$ , the thermal conductivity  $\lambda$ , the temperature difference  $T_1 - T_2$  and it is inversely proportional to the distance  $d$ . The induced heat can be transported either deeper into the wire cross section or into flanking wire segments. By following equation 3.3 the amount of heat transported deeper into the wire is greater by a factor of 20000 than the heat transported to the other segments. The amount of transported heat out of the segment can be neglected, but the distribution within the cross-section is fast enough to ensure an almost uniform temperature within the regarded wire segment for tungsten. The carbon wire is evenly heated anyway due to the 98  $\mu\text{m}$  penetration depth.

Another process is radiation cooling. Every body, to some extent, behaves like a black radiator and radiates thermal energy. The black body radiation is described by the Stefan–Boltzmann law [67] as follows:

$$\dot{Q} = \epsilon\sigma AT^4 \quad (3.4)$$

Here the radiated thermal power  $\dot{Q}$  scales with  $T^4$  and is proportional to the wire surface  $A$ , Stefan’s constant  $\sigma$  and the emission factor  $\epsilon < 1$ . This implies a strong dependence on the temperature, but rather high temperatures ( $T > 2000$  K) are necessary for significant heat dissipation. The emissivity  $\epsilon$  is a material property.

The third and last process is thermionic emission. This means electrons with enough energy to overcome the material’s work function to escape. The thermionic emission is described by Richardson’s Law [68]

$$\dot{Q} = W \cdot A \cdot J = W \cdot A \cdot A_G \cdot T^2 \cdot e^{-\frac{W}{kT}} \quad (3.5)$$

Where  $J$  is the current density,  $W$  the work function,  $A$  the emitting surface,  $A_G$  the Richardson constant and  $e^{-\frac{W}{kT}}$  the Boltzmann factor. The thermionic emission is usually not taken into account, due to its small contribution at low energies, but with a heavy ion beam it is the mayor factor for cooling, due to enormous amounts of escaping electrons at high temperatures ( $T > 3000$  K).

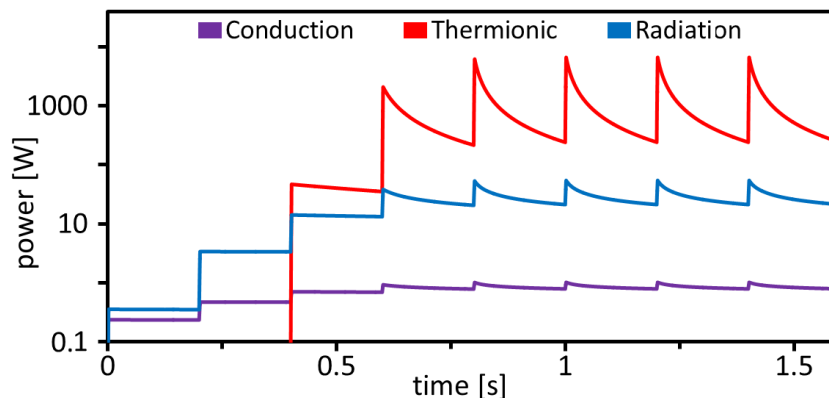


Figure 3.5.: The three components of the cooling process for an irradiated carbon wire are depicted. The thermionic emission is clearly dominating, but for  $T < 2000$  K there is no thermionic contribution (drop to zero  $t < 0.4$  ms).

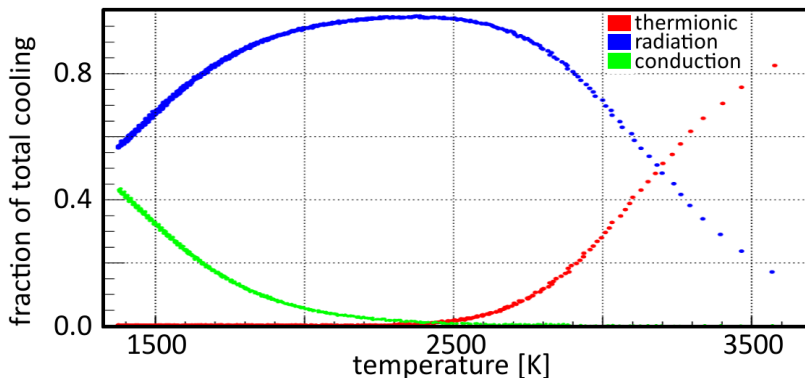


Figure 3.6.: The specific fractions of the three cooling processes of the cooling are depicted (picture from [69]). At  $T = 3200$  K the thermionic emission is dominating.

For the calculation, the following beam parameters are taken: 11.4 MeV/u,  $U^{73+}$  beam,  $I = 5.0$  mA, macro pulse length  $\tau = 2$  ms, repetition rate 5 Hz, vertical and horizontal beam RMS width  $\pm 5$  mm. The kinetic energy of a macro pulse is about 27 kJ or 60 mJ per bunch. Therefore the energy deposited per bunch is 2.06 mJ for a tungsten wire or 1.67 mJ for a carbon wire.

The calculations show the occurrence of a virtual thermodynamic equilibrium (no transition) within one second. After five pulses the carbon wire reaches  $T_{\max} = 4360$  K. The tungsten wire needs 7 pulses to reach  $T_{\max} = 4487$  K, due to its higher thermal capacity.

Figure 3.4 shows the temperature behavior over time. The melting point of tungsten is 3695 K, where as carbon does not have a fixed melting point. It sublimates directly above 4125 K. Both materials do not withstand the thermal stress when put into the heavy ion beam at GSI.

Figure 3.5 depicts the distribution of the heat dissipation allocated to its three components: thermionic emission, thermal radiation and thermal conduction. It is seen that the thermionic cooling contributes the most with 76% at 3100 K with 46 W in contrast to 13.8 W thermal radiation. For higher temperatures this percentage increases almost up to 100%, but those temperatures have no physical meaning. Furthermore, the thermionic current is massive at 3100 K with about 10 A for several milliseconds. On the other hand the convection stays even for high temperature of 4000 K below 1 W, indicating that neighbor segments do not contribute to cooling process in short terms. Therefore it can be completely neglected.

If the qualitative results of the cooling process are compared with a more detailed investigation published at the BIW'12 [69], the results are similar. Although using a more precise mathematical description of the specific heat dissipation, like a thermal conductivity  $\lambda(T)$  which changes with the temperature  $T$  and the consideration of reabsorbed electrons of the thermionic emission, the quantitative results do not differ much.

At  $T = 3500$  K 80% (see fig. 3.6) of the cooling power is induced by thermionic



emission in comparison with the obtained thermionic contribution at  $T = 3500$  K of 90% according to fig. 3.5. The contribution of the heat conduction is in both cases at  $T > 2500$  K below 10% and decreasing. Both approaches indicate that the most resistant materials will not withstand high power heavy ion beams.

### 3.2.3. Stripline Faraday Cup

Faraday cups are well known diagnostic tools for measuring small beam currents [70]. With a sufficiently high analyzer bandwidth, a coaxial Faraday cup can even be used to determine the longitudinal profile of a bunch without being susceptible to space charge effects. For a 1.4 MeV/u bunch with 1 ns duration,  $\sim 2$  GHz is the absolute minimum according to the Nyquist theorem [71]. For signal shape analysis 10 GHz bandwidth is necessary.

While the bunch ions themselves hit the metallic cup surface and create a current (beam is completely destroyed), there is also an undesirable contribution to the signal by the bunch's preceding electric field and the emitted SEs from the surface. With the help of a suppression grid to shield the cup from the electric field, these effects can be avoided. The recommendations for the electric chain are still high in the sense of the impedance tolerance and the high bandwidth as well which is rather demanding. Conventional designs are limited to 1 GHz bandwidth.

For frequencies above 10 GHz the electric circuit has to be improved. A promising

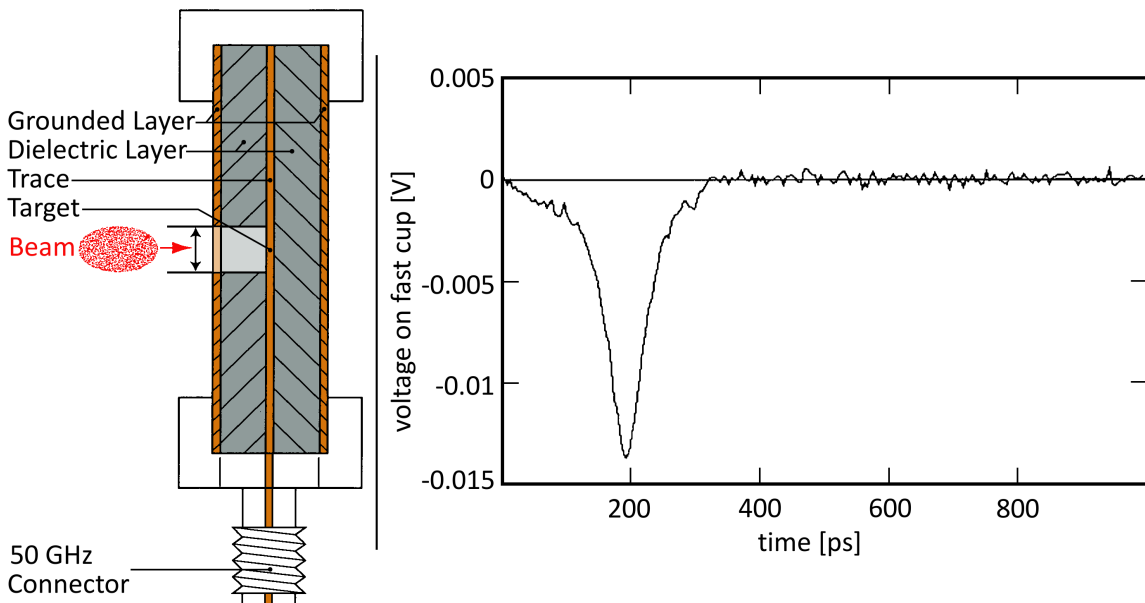


Figure 3.7.: Cross section of the stripline circuit (left) (image from [72]). Red indicates the incoming ion beam, gray marks the dielectric, orange the conductor path and orange-striped the grounded plates. A signal measured with the Stripline Faraday Cup with 20 GHz bandwidth [72].

approach is the microstrip or stripline design, which can be seen as a flattened coaxial cable. In case of a stripline circuit the conducting material is completely surrounded by a dielectric material which strongly forms the resulting impedance. The dielectric is put between two grounded plates. A microstrip circuit is only shielded on one side of the conductor. Due to the design millimeter wave frequencies are used in a TE mode which allows high bandwidths. The stripline design is more resistant to radiation noise from the environment and from itself, but more cost-intensive compared to a microstrip circuit. Used close to an accelerator the noise resilience is the decisive factor, although a microstrip circuit has a faster signal propagation. The Spallation Neutron Source (SNS) was able to demonstrate a successful measurement with a stripline Faraday cup of a bunched beam of 130 ps FWHM with a bandwidth of 20 GHz (see figure 3.7). The proposed bandwidth leads to a 50 ps time resolution, which is still not sufficient for future applications at FAIR. The authors from SNS claim even bandwidths up to 100 GHz might be possible [72], allowing a resolution of up to 10 ps. Although promising this approach is beam destroying and does not allow any further use of the analyzed beam, even if a 100 GHz device would be feasible.

### 3.2.4. Time-of-Flight Measurement

Particle detectors are also suited for longitudinal profile measurements. Hit by a single particle the response time of the detector can be less than 1 ns with a rise time below 100 ps corresponding to a timing bandwidth of 20 GHz. Well suited detectors are synthetic diamonds and Micro-Channel-Plates with a  $50 \Omega$  anode geometry.

By using a thin target foil and observing a specific angle a high beam attenuation of  $10^{-8}$  is reached and a set of collimators (see fig. 3.8) ensures single particle analyzation per bunch. The counted events are plotted over their time of arrival in relation to the RF phase, the longitudinal profile is obtained (see fig. 3.9). A high target mass is preferred to minimize the additional energy spread of the particles caused by the electronic

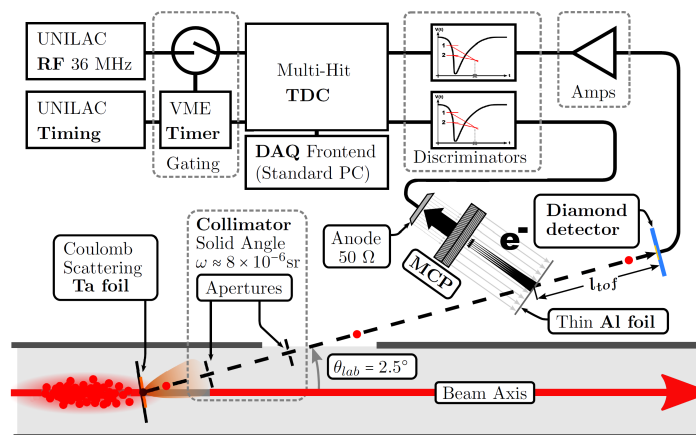


Figure 3.8.: Sketch of a TOF based particle detector capable of measuring the bunch structure and the longitudinal emittance (image from [73]).

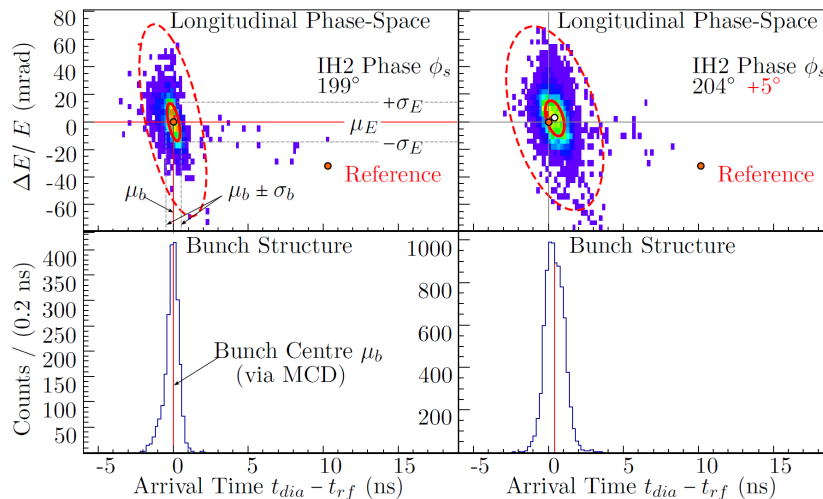


Figure 3.9.: Example of a two different bunch structures obtained at the GSI Heavy Ion LINAC through cavity manipulation [73].

stopping power. The output pulse is converted into a logic pulse with the precise timing information. For the GSI device a resolution of 50 ps is achieved, corresponding to  $0.65^\circ$  of 36 MHz. With the help of a second detector (see fig. 3.8), the energy of each particle can be measured. A different foil is moved into the path of the scattered ions. Secondary electrons are generated and driven to the second particle detector, the MCP. With the timing information of both detectors the particle velocity and therefore the energy can be calculated. With the determination of the time of arrival and energy the longitudinal phase space can be sketched now, as shown in figure 3.9.

The Time-of-Flight measurement is a powerful device to directly obtain the longitudinal emittance or just to determine the longitudinal profile length. But it is a destructive process and the further extension of the time resolution above 50 ps is not effortless which will be imperative for the application for DTLs with higher RF values.

### 3.3. Non-Intercepting BSM at GSI

The preceding section made clear statements about the thermal stress, which is expected for any intercepting material put into the LINAC beam at GSI. It is recommended to use a non-intercepting device. Protons at 70 MeV do not have the same energy deposition as heavy ions, but the p-LINAC provides a high ion current of 70 mA which leads to a comparable level of stress for any intercepting material. Instead of using solid material, the idea is to use residual gas as a source for secondary electrons.

By increasing the local pressure in the vacuum chamber from the  $5 \cdot 10^{-8}$  mbar operating pressure to  $5 \cdot 10^{-6}$  mbar the omnipresent beam loss due to collisions of the beam ions with residual gas, can be exploited to create ionized gas particles which emit enough secondary electrons for a usable signal. The non-intercepting approach is described below.

### 3.3.1. Working Principle

The non-invasive BSM prototype (for a sketch see figure 3.10) is based on secondary electrons (SEs), which are freed by collisions with the residual gas within the Field-Box. The whole beam path is an interaction zone, where SEs are created.

All electrons are accelerated upwards by a homogeneous electrostatic field of up to 5.0 kV/mm. About  $\sim 0.1\%$  of those electrons can be extracted through a slit in the top plate of the Field-Box. To reduce the divergence of the SEs two apertures separated 70 mm from each other are used. The apertures can be remotely adjusted between 0.1 mm and 1 mm opening.

Behind the apertures, there are two energy sensitive  $90^\circ$  filters, the cylindrical electrostatic Energy Analyzer with a bending radius of 30 mm. A second similar element bends the SEs beam back in the original direction, to keep it strictly in the vertical axis. Depending on the applied driving potential the applied voltages for the opposite cylinder segments are  $\pm 5.5$  kV. A third aperture is placed 10 mm behind the edge of the second analyzer to force a point-to-point focusing from the second to the third aperture.

Drifting 90 mm the SEs reach an RF driven resonant deflector coupled to the accelerator master oscillator. At the RF Deflector each electron is deflected in dependence to its time of arrival. The time information (relative time of arrival equals relative time of creation at the bunch) is changed into a spatial one (angle of deflection). Two deflectors are available: one is operating at 36 MHz for long bunches and the other one for short

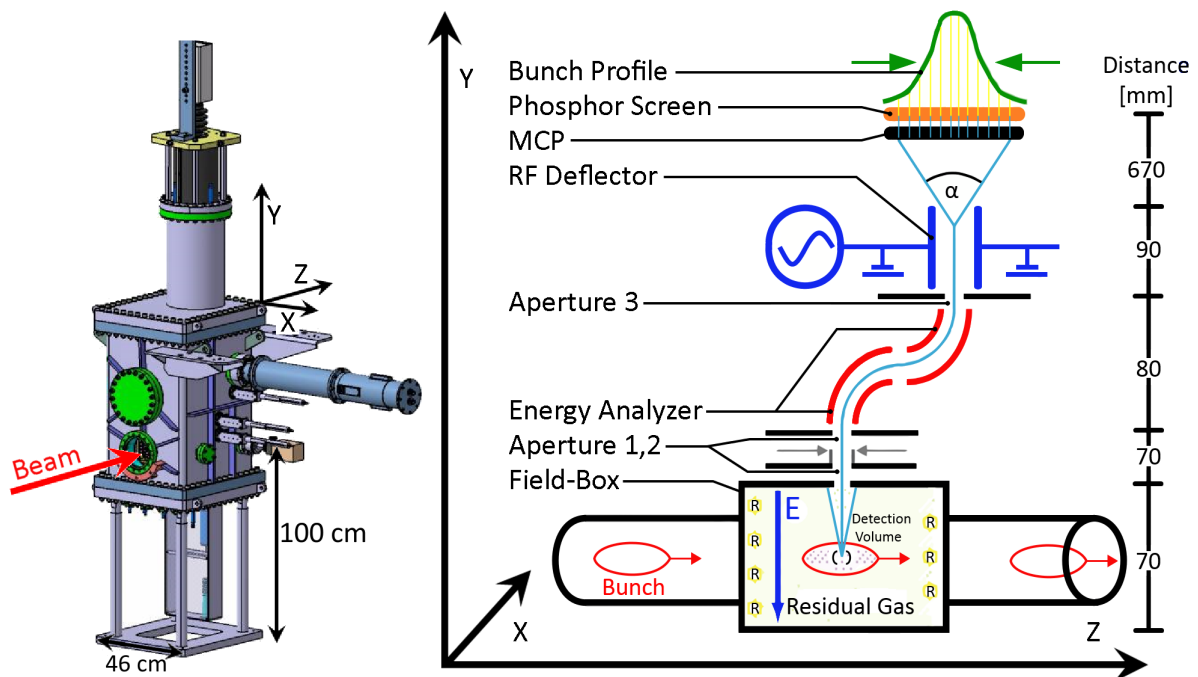


Figure 3.10.: Schematic illustration (right) of the non-intercepting BSM prototype. The 3D image (left) depicts the non-intercepting BSM vacuum chamber with a  $45^\circ$  perspective shift.

bunches at the third harmonic with 108 MHz.

Both deflectors are 800 mm long parallel wires, where the deflecting end corresponds to  $\lambda/4$  length of the standing wave for maximal field amplitude. The maximum power applicable is 100 W at 36 MHz and 50 W at 108 MHz with 6 ms pulse duration.

The deflected SEs, after a 670 mm flight, interact with an amplifying Micro Channel Plate (MCP) Detector with an effective diameter of 77 mm. The induced electron avalanche escapes the MCP back and hits a P47 phosphor screen. The illuminated spots on the phosphor screen are electronically processed by a CCD-Camera and for data analysis. In order to focus the SEs on the MCP Detector the deflector also acts as an electrostatic Einzel lens by a common DC voltage of maximum 6000 V on the deflector's plates.

### 3.3.2. The Field-Box

The Field-Box is the first module of the BSM. Its design is based on Ionization Beam Profile Monitors [74], which basically consist of two rectangular capacitor plates (see Figure 3.11). The Field-Box has the tasks to extract the created secondary electrons from the bunch and avoid distortions of the electron trajectories and to affect the continuing beam operation as less as possible.

To achieve a proper extraction a high voltage of maximum  $-31$  kV is applied to the lower of the two  $170$  mm  $\times$   $55$  mm capacitor plates. With a distance of 70 mm between the two plates a maximum electric field of 440 kV/m can be achieved.

In the center of the upper plate a 2 mm thick (in beam direction) and 28.5 mm long

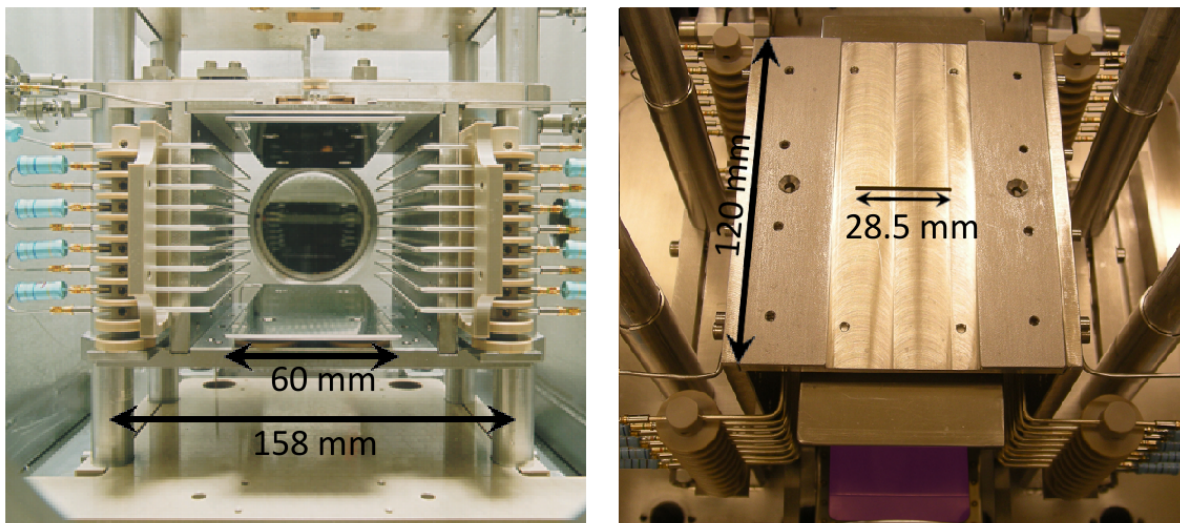


Figure 3.11.: Front view (left) of the Field-Box with its side strips to level the electric field, suppression grid not yet installed as the picture was taken. Top view (right) of the Field-Box. The exit slit is clearly visible and the suppression grid (purple) is also installed.

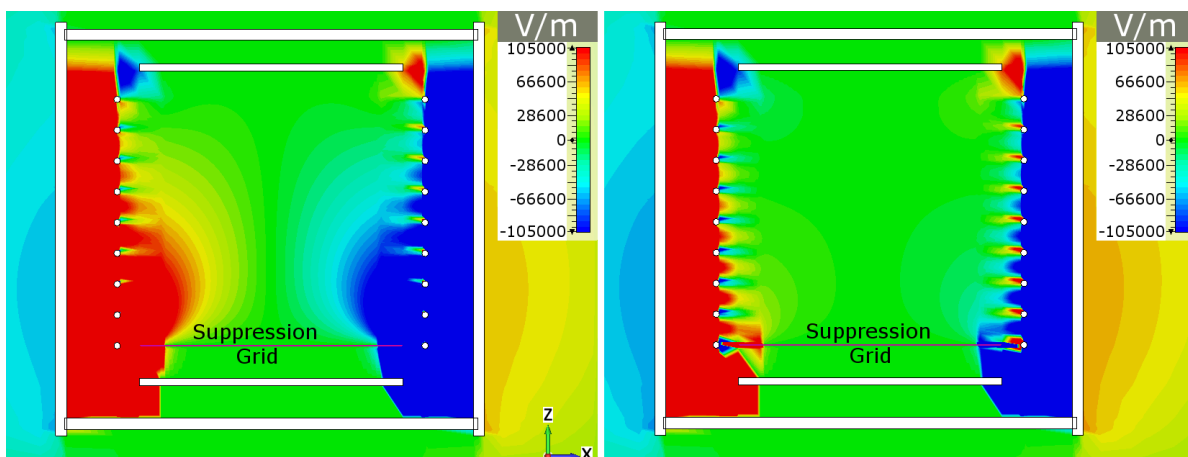


Figure 3.12.: CST based  $E_x$ -field distribution of the old circuit (left). The strips close to the bottom do not match the subsequently attached suppression grid. The new circuit (right) with better matching. Both pictures have the same color coding.

slit is located where the electrons are extracted. The vertical edge (the  $zy$  plane) of the Field-Box has to be shielded from the exterior. By attaching additional equidistant wires at the vertical edges and proportionally reducing the applied voltage, a far more homogeneous field distribution is achieved.

Due to a suppression grid, for better operation mounted above the bottom plate, the original wire shielding does not match the geometry any longer, fields created by the large potential difference between the grounded housing and the high voltage wire extend themselves into the interior and lead to a distortion (see fig. 3.12 left). The new wire setup based on CST calculations, is properly matched to the suppression grid and the field distortions are avoided (see fig. 3.12 right). Therefore proper extraction for further imaging properties of the SEs is guaranteed.

As a diagnostics tool it is highly recommended that the BSM is not disturbing the ongoing accelerator operation. By passing the BSM, the ion beam experiences the driving potential of the Field-Box and is therefore deflected. Based on CST calculations a  $U^{28+}$  beam at 11.4 MeV/u and  $-31$  kV applied voltage leads to an angle of deflection of  $\alpha = 120$   $\mu$ rad.

The angle  $\alpha$  is determined as follows:  
with  $v_z = 0.155 c$  at 11.4 MeV and  $v_y = 1.6 \cdot 10^{-4} c$  for a proton beam the angle  $\alpha$  is about 1 mrad. For heavy ions the effect decreases due to the lower-charge-to-mass ratio. For  $U^{73+}$  the angle is still about 300  $\mu$ rad.

While operating the BSM the beam deflection leads to a significant beam loss at the entrance of the SIS18. By attaching two extra electrodes with the opposite polarity this influence can be neutralized. With the help of a CST calculation (see fig. 3.13) a proper design of the compensation electrodes was developed. Due to the limited insertion space left in the BSM vacuum chamber and due to a barrier-free 55 mm diameter passage for

safe beam operation rather exotic keyhole shaped electrodes were picked (see figure 3.14 left). The angle of deflection is proportional to the averaged exposed  $E_y$ -component, therefore the  $E_y$ -component integrated along the beam trajectory determines the compensation effectiveness as follows:

$$f = \frac{\int E_y(z) (\text{compensated}) \cdot dz}{\int E_y(z) (\text{uncompensated}) \cdot dz} \quad (3.6)$$

According to CST calculations (see fig. 3.14 right) the compensation level achieved is up to 99% within a 30 mm diameter and almost everywhere above 90% in the regarded area within a 50 mm diameter. Beam based tests showed no detectable beam deflection at the SIS18 or any other disruptive effect behind the BSM.

Another error source is the stability of the applied voltage. The FUG power supply has a maximum voltage of  $-35$  kV and maximum current output of 100 mA. It has a stability of 10 V, but only a limited speed to react if some fast induced disturbance occurs. Such a disturbance might be the beam gas interaction. Gas atoms hit by the beam get ionized and lose one electron (SE) or more. Those positive charged ions will travel to the bottom because they are attracted by the negative voltage. Depending on

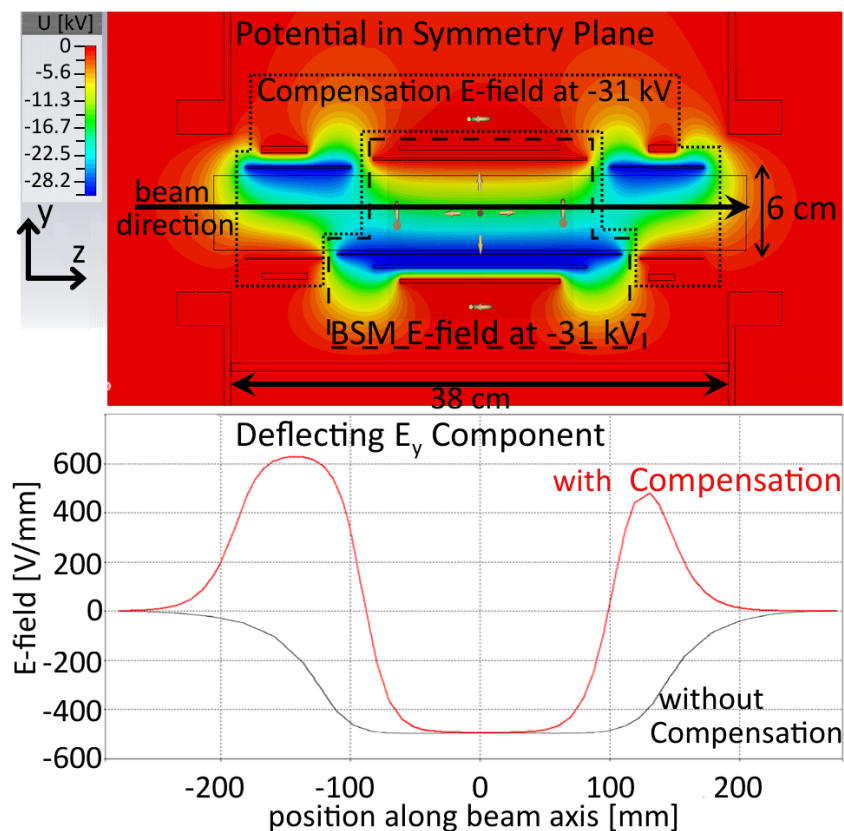


Figure 3.13.: On the left side CST simulation of the potential distribution along the beam axis. Right side the electric field in vertical direction along the central beam trajectory with extra electrodes (red) and Field-Box only (black).

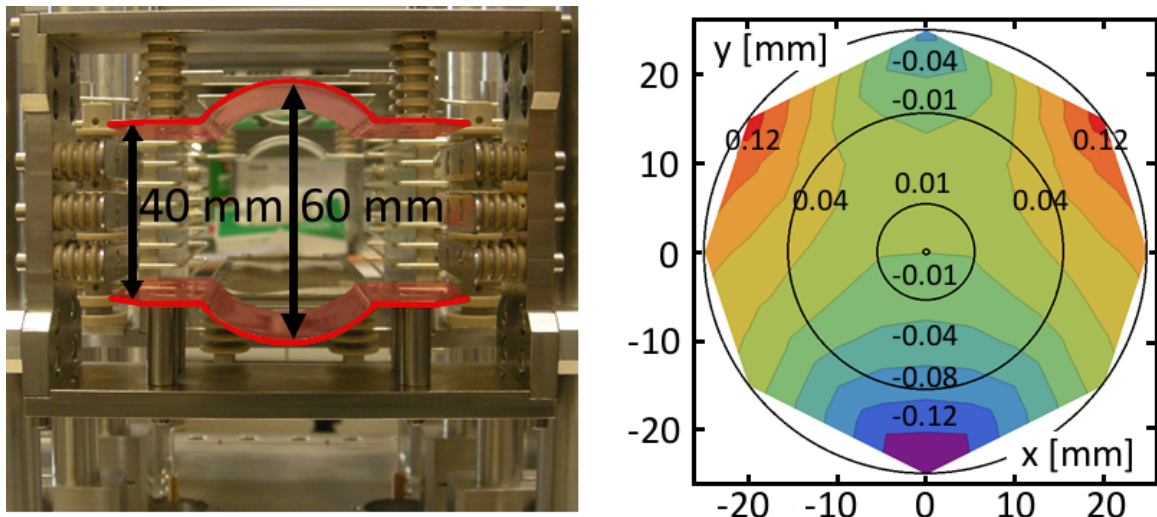


Figure 3.14.: On the left side a picture of a compensation electrodes (red) with its bended shape. Right image shows a contour plot of the deflection residuals defined by eq. 3.6 in absolute values depending on the  $xy$  position.

their kinetic energy, those ions will hit the bottom plate and create a lot of secondary electrons which leads to voltage drop. The amount of negative charges located on the plate can be calculated by the following equation:

$$Q = C \cdot U = \epsilon \cdot \frac{U}{d} \approx 1 \cdot \frac{U}{d} \quad (3.7)$$

At a typical operating voltage  $U = -25$  kV,  $d = 70$  mm and  $A = 0.00935$  m<sup>2</sup> the bottom plate is charged with about  $Q = 3340$  C or  $2 \cdot 10^{22}$   $e$ . In comparison a  $U^{73+}$ , 2 mA and 100  $\mu$ s long macro pulse consists only of  $17 \cdot 10^9$  ions. Even if each ion ionizes one atom, each ionized atom has to create  $4.7 \cdot 10^8$  electrons to force a voltage drop of just 1 V on the bottom plate, therefore any voltage drop is negligible.

The majority of the secondary electrons in the Field-Box do not contribute to the bunch signal. They hit the housing or the top plate. Through the impact the electrons emit X-ray radiation which creates a strong background. A method to reduce the X-ray intensity is to mount a suppression grid (90% transmission, meaning 10% of the total area is occupied by the meshes) and trap the SEs between the grid and the bottom plate (see fig. 3.15) via an additional potential. For the Field-Box the additional potential is fixed by electronic circuit to one-tenth of the applied voltage (3 kV at 30 kV). Virtually all electrons originating from the bottom are trapped, only the electrons emitted by the grid meshes themselves contribute to the X-rays. The background and especially the X-rays will be investigated in section 4.3.4.



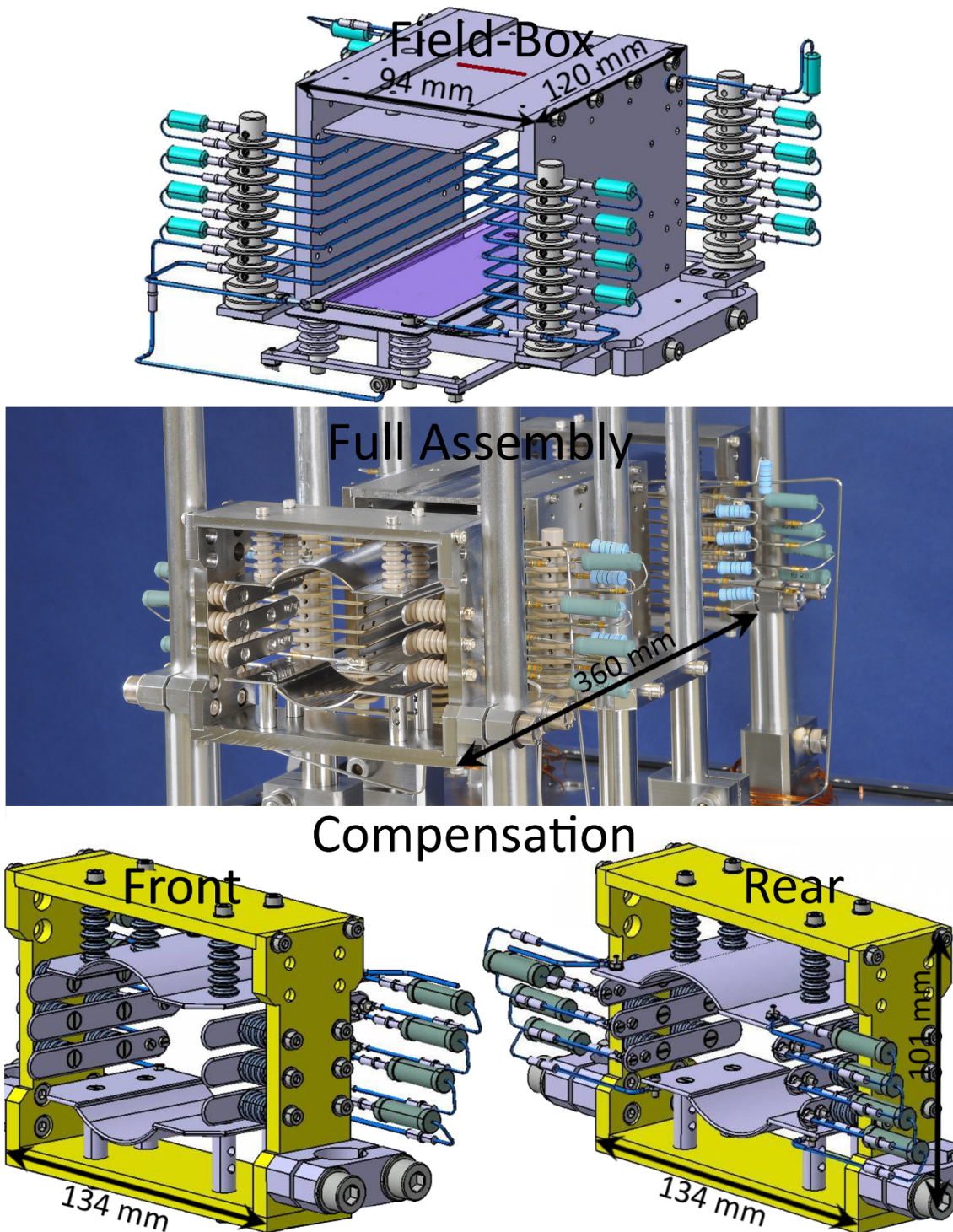


Figure 3.15.: 3D plots of the Field-Box (upper image) with purple indicated suppression grid and the two compensation electrodes (lower image). A picture of the full assembly is depicted in the middle. The resistors are necessary the smoothing of the E-field through the wires or fines.

### 3.3.3. Electron Beam Coordinates

Due to historical reasons the nomenclature of the electron optical system is derived from the utilized electron beam, created by the Field-Box. Henceforth a different coordinate system is used to avoid confusion caused by the original designations. The new coordinates use the electron beam as a reference, instead of the ion beam. The coordinates are transformed as follows:

$$\text{ion beam horizontal: } x_{\text{old}} \Rightarrow y_{\text{new}}, \text{ electron beam long side} \quad (3.8)$$

$$\text{ion beam vertical: } y_{\text{old}} \Rightarrow z_{\text{new}}, \text{ electron beam propagation} \quad (3.9)$$

$$\text{ion beam propagation: } z_{\text{old}} \Rightarrow x_{\text{new}}, \text{ electron beam narrow side} \quad (3.10)$$

Figure 3.16 illustrates the origin of the new coordinate system. The direction of the long side of the Field-Box extraction slit is designated to the  $y$  direction, as the narrow side is designated to the  $x$  direction. The old vertical axis is the direction of propagation of the electron beam, hence the new  $z$  direction.

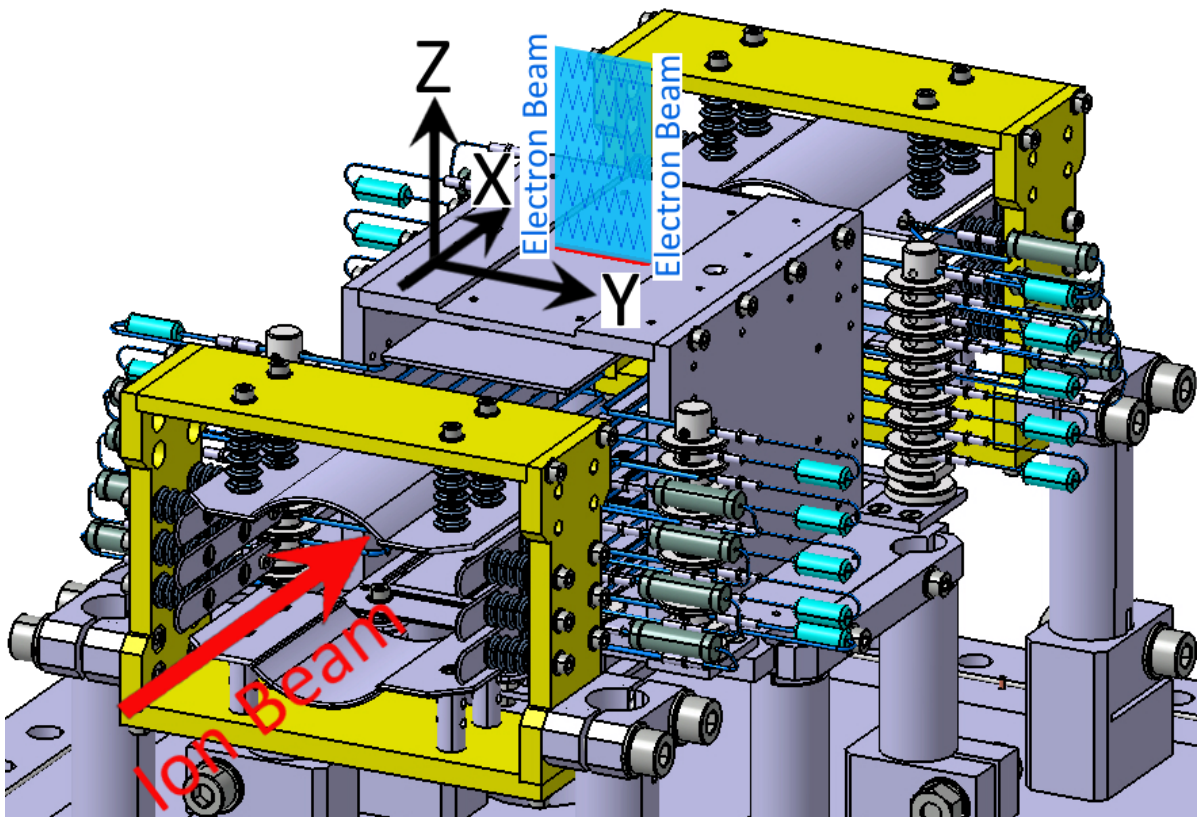


Figure 3.16.: Definition of the new coordinates with respect to the electron beam [75].

### 3.3.4. Apertures and Energy Analyzer

For imaging properties the BSM includes a sophisticated aperture and energy analyzer system. The apertures are responsible for the transverse properties of the electron beam and restrict the detection area within the Field-Box. The Energy Analyzer (EA) is responsible for the longitudinal properties and is restricting the detection depth (replacement for the absent thin wire see chap. 3.2.1).

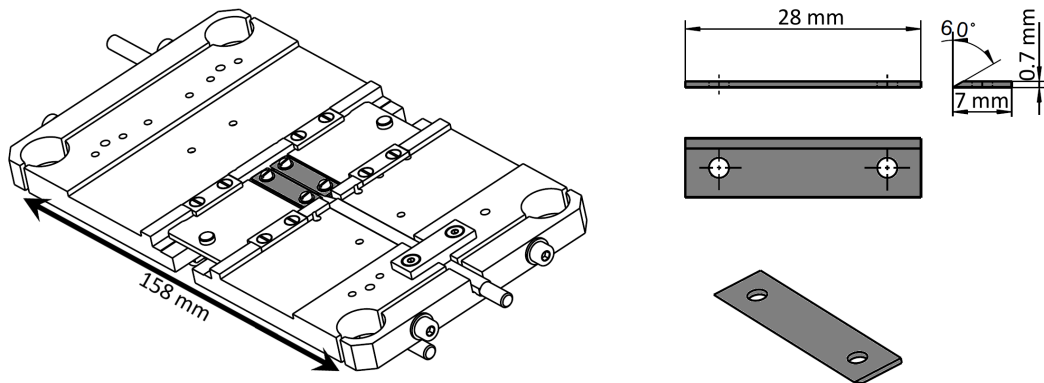


Figure 3.17.: XY Aperture module viewed from above with gray marked X Aperture blades [76].

The BSM has five apertures. There are three apertures along narrow side of Field-Box extraction slits (called X Apertures for the electron beam) and two apertures along the broad side of the extraction slit (called Y Apertures). The X Apertures can be remotely opened and closed between 0.1 and 1.0 mm for aperture 1 and 2 (see fig. 3.17) and between 0.2 and 2.0 mm for aperture three. The location of the center is fixed and is not adjustable.

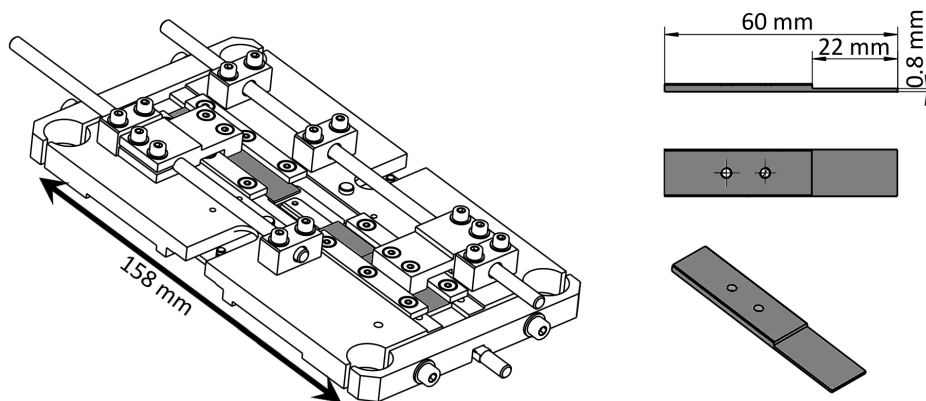


Figure 3.18.: XY Aperture module viewed from below with gray marked Y Aperture blades [77].

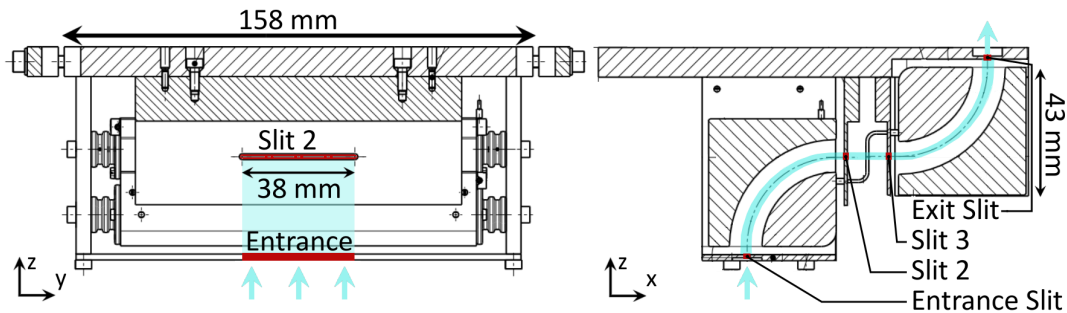


Figure 3.19.: Energy Analyzer module, on the left in electron beam direction the exit slit (red) of first 90° section. Cross section through both 90° cylinder segments with electron path (blue) [78].

The 0.7 mm thick aperture blades are sharpened to give a minimal front surface for any electron scattering within the passage gap. The first X Aperture is directly behind the extraction slit of the Field-Box and the second X Aperture 70 mm after the first one (see fig. 3.20).

The Y Apertures have a different design. The aperture blades are 0.8 mm thick and not sharpened (see fig. 3.18). The two Y Apertures are located directly above the X Aperture so that the X Aperture will stop most of the scattered electrons. Each y-blade is controlled individually and can be set from 0 to 25 mm. This allows scans of different areas of the field box or just to adapt if the center of the ion beam is displaced and again analyze the beam center.

The Energy Analyzer is responsible for sorting out electrons with the wrong kinetic energy, restricting the detection volume within the Field-Box. Basically it is a 120 mm long quarter cylinder with an inner radius  $r_1 = 25$  mm and an outer radius  $r_2 = 36$  mm (see fig. 3.19). The inner wall is charged with a positive voltage of up to  $U_{r1} = +6000$  V and the outer wall with a negative voltage up to  $U_{r2} = -6000$  V. The electric field is calculated as follows:

$$E(r) = \frac{U_{r1} - U_{r2}}{r \cdot \ln(r_2/r_1)} \quad (3.11)$$

For an electron traveling through the analyzer the centrifugal force  $F_c = \frac{mv^2}{r}$  has to equal the electric force  $F_e = -E(r) \cdot e$ . The electron velocity for the central trajectory is calculated as:

$$v = \sqrt{\left(\frac{2 \cdot U_a \cdot e}{m_e}\right)} \quad (3.12)$$

The acceleration voltage  $U_a$  depends on the vertical location of the ion beam and the applied Field-Box voltage  $U_0$ . If a secondary electron is emitted in the middle of the Field-Box then is  $U_a = 1/2 U_0$ . The total voltage applied to the EA is calculated as:

$$U_{\text{total}} = U_0 \cdot \ln(r_2/r_1) = U_{r1} - U_{r2} \quad (3.13)$$

For  $U_0 = 31$  kV  $U_{r1}$  has to equal 5658 V and  $U_{r2}$  has to equal  $-5658$  V for the central trajectory of the electron originating from the middle of the Field-Box.

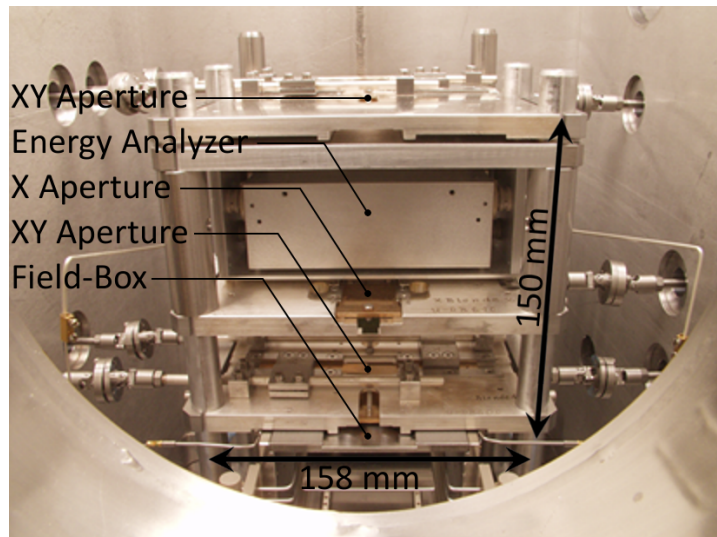


Figure 3.20.: Picture of the three aperture modules and the Energy Analyzer straight above the Field-Box (still visible below) inside of the BSM vacuum chamber. The mechanic clutches for the aperture control are installed on the chamber wall [79].

To achieve an almost ideal field distribution each opening of the two analyzers  $90^\circ$  modules is upgraded with an additional aperture plate with a  $2 \times 38$  mm slit. The apertures are located 2.75 mm in front and behind the quarter cylinder to force the effective  $\vec{E}$ -field edge to match the cylinder edge.

The apertures are inducing an electron trajectory offset after the first analyzer module of about 0.17 mm which doubles after the second module [80]. This offset has to be compensated by shifting the second module location. A proper matching of the electron trajectory with the geometric center of the EA is necessary to keep the electrons on 0 V potential. The distance  $D$  between the second X and third X Aperture, with ideal trajectory at  $r_0$  within the EA, fulfills the following equation [81]:

$$D = \frac{r_0}{\sqrt{2}} \cdot \frac{\cos(\sqrt{2} \cdot 90^\circ) + 1}{\sin(\sqrt{2} \cdot 90^\circ)} \quad (3.14)$$

Equation 3.14 yields  $D = 10.51$  mm which is satisfied by the aperture design (see [80]). This leads to a point-to-point focusing (see [82]) between the two X Apertures. Electrons with the same energy but an offset at the X2 Aperture will exit the optical system at the X3 Aperture with the identical offset.

The EA is designed to avoid electron scattering on charged planes due to its generous design. Electrons with a deviating kinetic energy will be deflected and stopped outside of the EA at the third X Aperture or at the additionally fixed apertures.

### 3.3.5. RF Deflector

The RF Deflector is the centerpiece of the BSM. Here the time information of the SEs is converted into a spatial distribution, but there is also the focusing acting and the electron beam steering in direction of deflection.

The RF Deflector is driven in a resonant mode to achieve the necessary high E-field variation far below 200 ps (head to tail bunch length  $\approx 2$  ns). Working as a cavity the RF Deflector is driven in phase to the accelerator RF at 36 MHz. The conductor length within the deflector is 2.08 m and wound up into a 800 mm housing.

The active end of the cavity consists of two plates which are 18 mm away from each other, where the electron beam is traveling through (see fig. 3.21). This enables a deflection of the electrons with the maximum E-field strength for the applied RF power, due to its  $\lambda/4$  design.

The angle of deflection is limited by the deflector's shell. For the focusing property this conductive shell is needed to achieve an Einzel lens behavior of the deflector's electrode layout. In the shell, there are two windows for electron beam passage. The maximum angle allowed by the RF Deflector blades and the window edges is  $3^\circ$ . The applied maximum RF power is 100 W at a duration of 6 ms, which is fully sufficient due to maximum heavy ion LINAC macro pulse length of 5 ms.

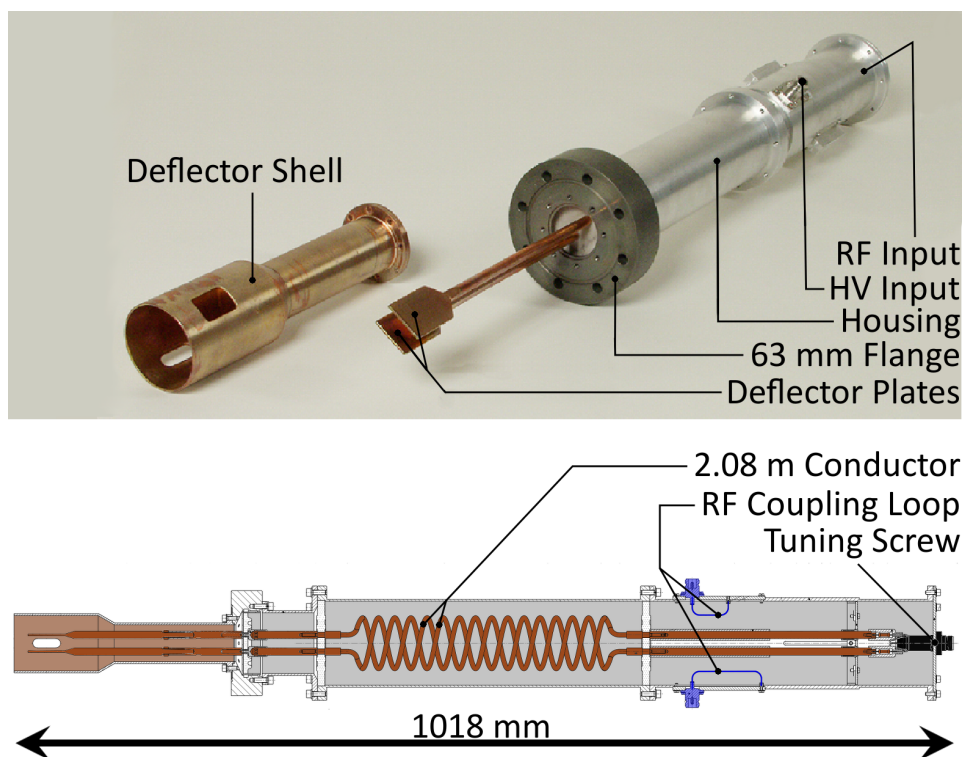


Figure 3.21.: Picture of the RF Deflector and the cross-section with the coiled cavity inside [83].

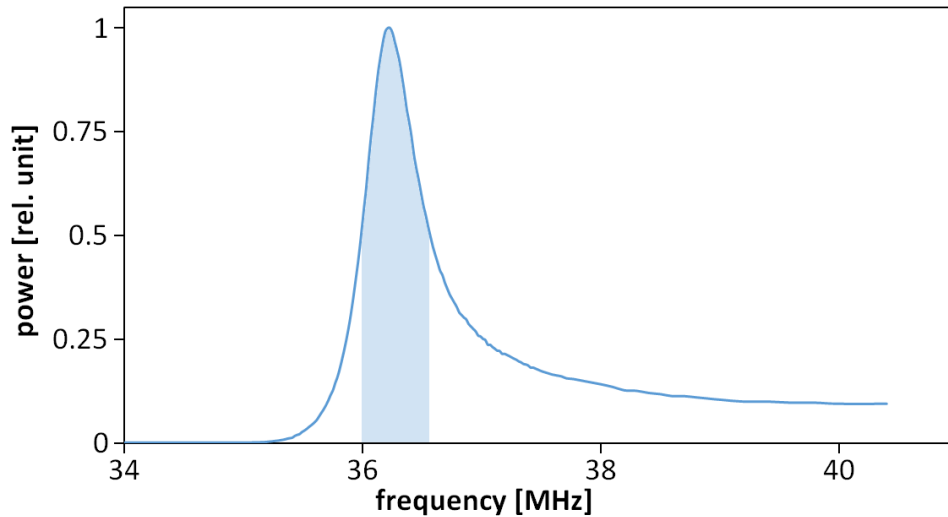


Figure 3.22.: Measurement of the resonance curve of the 36 MHz Deflector. The stored power in the resonator and the bandwidth  $B$  (blue area) over the frequency are depicted.

The quality factor of the RF Deflector is necessary to calculate the deployed field strength while using it as a high frequency deflector. By obtaining the resonance curve (see pic. 3.22) one can calculate the quality factor with:

$$Q = \frac{f_0}{B} = \frac{f_0}{f_1 - f_2} \quad (3.15)$$

Where  $f_0$  is the resonance frequency,  $f_1$  the low  $-3$  dB frequency,  $f_2$  the high  $-3$  dB frequency and  $B$  the bandwidth. The measured frequencies for  $f_1$  and  $f_2$  are 35.99 MHz and 36.57 MHz, respectively. With an  $f_0$  of 36.22 MHz this leads to  $Q \approx 62.5$ .

The Einzel lens ability is achieved through an electrostatic potential of up to  $-7$  kV applied to both blades. Together with the grounded deflector shell an Einzel lens field distribution is accomplished (see fig. 3.23). The Einzel lens focusing quality is decisive

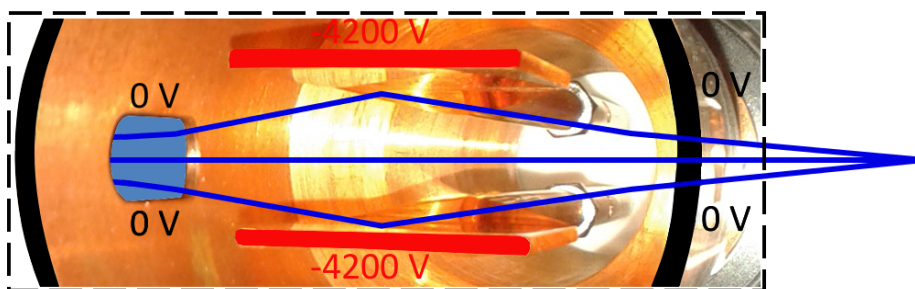


Figure 3.23.: Illustration of the deflector blades and shell acting as an Einzel lens, focusing the electron beam.

for the BSM resolution, but will be later discussed in detail.

Analog to the Einzel lens an electrostatic potential can be equally applied to both deflector plates, but to achieve a constant steering effect the blades need a potential with different polarity of a total value of maximal  $\pm 1000$  V. With the steering voltage electron beam trajectory tilts might be compensated, at least for the  $x$  direction (deflection) which could restrict the usable area of the MCP detector, if reaching the MCP not at the geometric center.

### 3.3.6. MCP and Phosphor Assembly

The Micro Channel Plate (MCP) and Phosphor Assembly is a common amplifier-imaging system for the deflected electrons.

In principle an MCP is based on thin channels traversing a thin circular plate of insulator material. The channels are evenly distributed on the whole surface like pores with a typical diameter of about  $10\ \mu\text{m}$  and they are  $20\text{--}30\ \mu\text{m}$  apart from each other which leads to a channel to surface ratio of 0.3. Approximately 30% of the particles drop into a channel. The channels have a typical tilt angle to the surface of  $10^\circ$ .

The surface plate is coated with a conductive material. The channel inside is coated with a semi conductive material with high electron density. The MCP front (input side) and MCP back have a potential difference ( $\leq 1000$  V), which will force any electron within the channel to the MCP back. If an electron coming from the deflector enters a channel it will hit the inner wall, due to the tilt angle.

By hitting the wall additional electrons will be created which will be forced by the electric gradient to the MCP back and hit the opposing inner wall. This process repeats itself several times. The maximum gain is up to a thousand electrons from a single incoming electron. The principle is quite similar to a dynode system in a photomultiplier. The created electrons are further accelerated by another voltage and hit a phosphor screen. The phosphor molecules will be excited by the electrons and will emit visible photons which can be detected by an optical camera system.

The BSM uses a chevron Hamamatsu F2226 24P MCP, which means two plates are mounted in one assembly. This design further increases the possible net gain by a factor

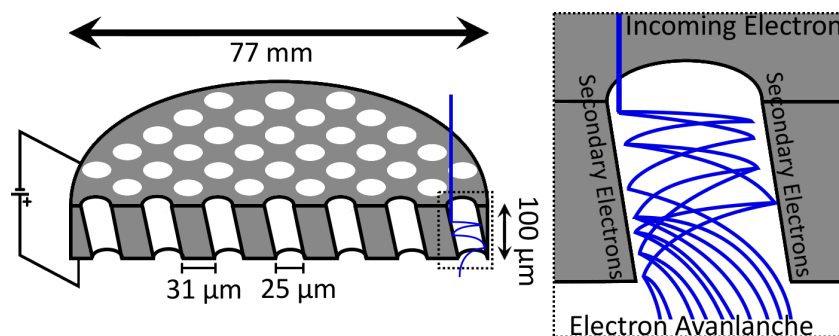


Figure 3.24.: Schematic of an MCP. A single electron is multiplied several times inside the channel.



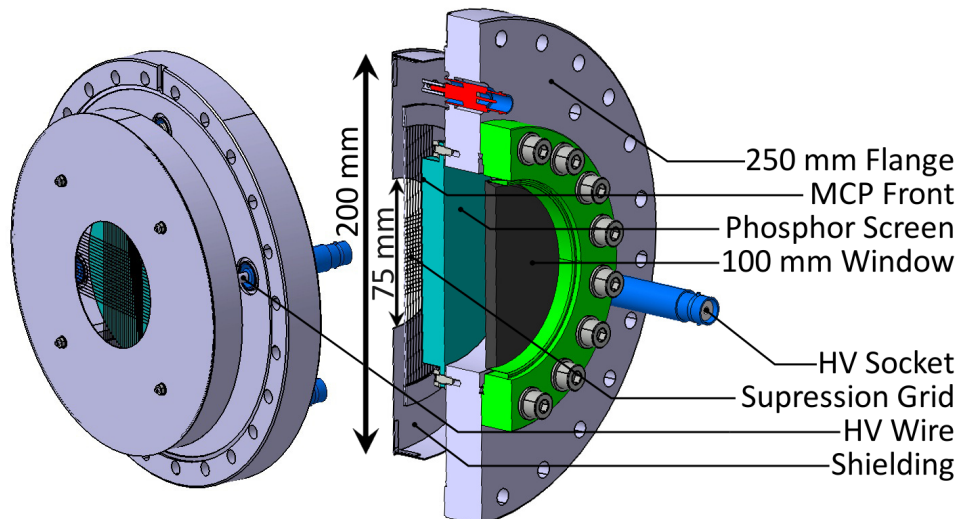


Figure 3.25.: A 3D model of the whole MCP assembly with high voltage connections and shielding of an MCP (image from [84]).

of 100. The effective area of the circular plate is 77 mm in diameter and has a total assembly diameter of 123 mm [85]. The channel diameter is 25  $\mu\text{m}$  with a 31  $\mu\text{m}$  pitch and 8° tilt angle [85].

The high voltage supply wires are close to the MCP's front, which can lead to deflection of incoming electrons. This is highly undesirable and countered with a shielding plate (see figure 3.25). Now the supply wire can only affect the area close to the surface of the MCP. Strong electron deflection is avoided.

The phosphor screen, used for signal illumination, is a P-46. The MCP output electrons can be accelerated with an extra voltage up to 4000 V. Due to a coating the minimal voltage is 2000 V, otherwise the electrons will get stuck in the coating and not illuminate any spot on the phosphor screen. The phosphor emission spectrum has its intensity maximum at a wavelength of 530 nm and has a decay time (10% intensity left) of 300 ns [85], which is fast in comparison with other available phosphor screens and allows even macro pulse structure analysis (duration  $\approx$  100  $\mu\text{s}$ ).

### 3.3.7. CCD Camera

The MCP assembly is responsible for the amplification and illumination of the electron distribution. In order to resolve the bunch shape out of the spatial distribution digital data acquisition is necessary. For this purpose a CCD based PCO 12 Bit SensiCam is focused on the Phosphor Screen.

The CCD camera has  $640 \times 480$  pixels at a chip size of  $6.4 \times 4.8$  mm [86]. The chip itself is cooled down to -12 °C to achieve a low readout noise of 4  $e^-$  RMS [86]. The quantum efficiency is high with 65% in the visible range. The exposure time can be varied from 500 ns to several seconds if necessary. The camera works with auto trigger

and an external trigger which is better suited to match the macro pulse with a short exposure time for higher signal intensity.

The camera is remotely controlled through an optical fiber by PCO software. The software allows direct averaging over several images ( $n = 2 \dots 256$ ) and the pixel readout can be chosen (binning) from  $1 \times 1$  to  $8 \times 8$ , which means how many pixel are read out together, which leads to a reduction of the read out noise of  $\sqrt{n}$  for  $n$  bonded pixels.

A small draw back is the smaller resolution due to the loss of image dots. A trade-off between both advantages is a  $2 \times 2$  binning, which is also used for most of the measurements presented in this thesis.

Another feature is the contrast and pseudo color option. The presented image brightness can be adjusted as well as the brightness progression. This allows to assign the full monitor screen brightness (gray values) to a narrow band of small intensity values, which will greatly increase the visibility of low signal. The assignment of pseudo colors increases the contrast even further (see fig. 3.26). This means that blue indicates for example low intensity and red to white high intensity with the other colors in between. This option makes it possible to recognize even finest structures on the phosphor screen by the bare eye.

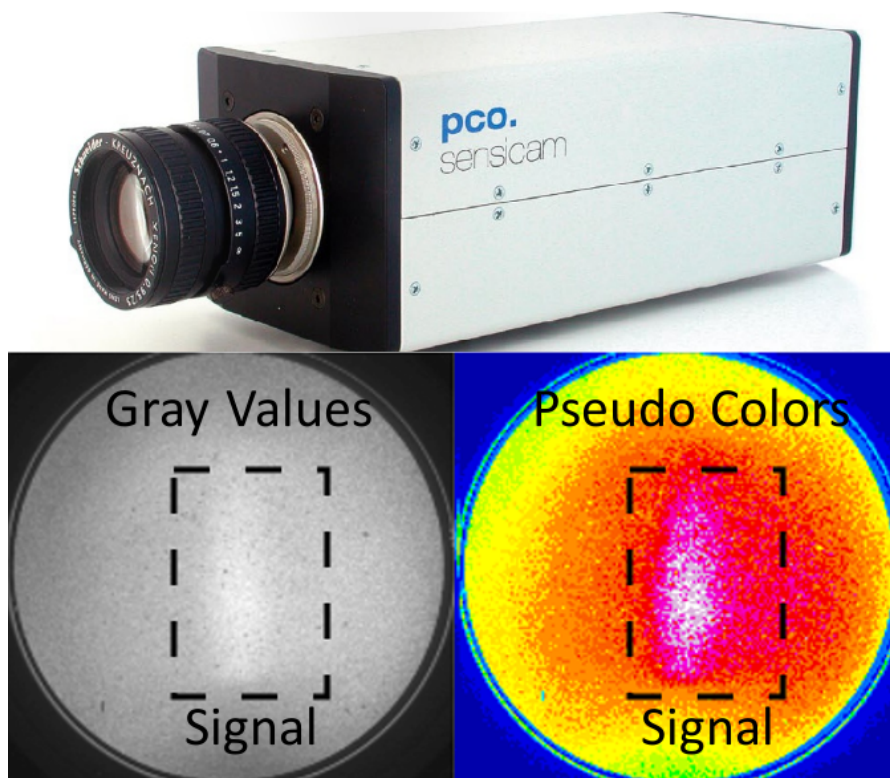


Figure 3.26.: Depicted is an actual measurement taken by the PCO SensiCam in gray values and pseudo colors (image from [86]). Note the far enhanced detectability of a signal with pseudo colors.

## 4. BSM Measurements

The non-intercepting BSM was introduced in the preceding chapter. The following chapter will present successful bunch shape measurements and background investigations. Furthermore it will investigate the susceptibility of the BSM on different parameter settings, like gas pressure, MCP voltage and ion beam settings. Finally it will be shown that longitudinal emittance determination is possible with a series of measurements.

### 4.1. BSM in Operation

The operation of the BSM is quite demanding. For a proper profile measurement several settings have to meet the ion beam parameters: higher initial ion beam currents require lower signal gain, shifts of the vertical beam position force the BSM electron optics to be readjusted. All these procedures aim to enhance the signal-to-background ratio and to reduce the signal noise. Usually it is not possible to sufficiently manipulate the beam properties by changing the accelerator setting, due to the lack of available beam diagnostic or just because the ongoing accelerator operation does not allow for it. Nevertheless it is shown that the device can cope with different settings of the beam parameters.

#### 4.1.1. Data Acquisition and Post Processing

The signal acquisition and post processing is a necessary process in order to obtain useable data from the BSM. The primary signal is a spatial distribution of SEs amplified by an MCP Detector. A CCD Camera system takes digital pictures of the back panel of the MCP Detector and allows image post processing which yields the actual information measured by the BSM.

The longitudinal bunch profile typically has a total length of  $\pm 30^\circ$  of the accelerator RF. For 108 MHz this corresponds to  $\sim 1.5$  ns. The imaging phosphor of the MCP Detector has a decay time of 300 ns (see sec. 3.3.6). In addition the CCD Camera system has a minimal exposure time of 1  $\mu$ s (see sec. 3.3.7). A dedicated investigation of a single bunch is extremely challenging. In addition the small SEs yield per single bunch forces the BSM to determine the profiles via the averaging of several thousand bunches within a macro pulse of typical  $\tau \sim 100$   $\mu$ s in the TK, in order to achieve a sufficiently good signal.

To adjust the electronic circuits as well as the CCD Camera with the macro pulse timing, the accelerator infrastructure provides several trigger events with known time position in relation to the macro pulse. The BSM is usually triggered by "Event 20" [87],

which is set 180  $\mu\text{s}$  ahead of the rising edge of the macro pulse. Figure 4.1 illustrates this issue. A short pulse, "Event 20", precedes the transformer voltage signal [88] induced by the macro pulse ( $U_{\text{trafo}} \propto I_{\text{pulse}}$ ). With a manually set delay the exposure time of the camera is set to cover the full duration of the macro pulse with an extra 10  $\mu\text{s}$  in front and behind the pulse. A not matching exposure time will only decrease the signal quality, therefore the delay between trigger and the beginning of the exposure is mandatory.

The electric circuits, like the amplifier for the RF Deflector, are driven in a 6 ms long triggered pulsed mode. The comparatively long duration time of the amplifier does not have any negative effects on the measurement procedure. On the other hand the pulsing is necessary to avoid overheating of the circuit. Also 6 ms duration allows BSM operation with a similar macro pulse length which other accelerator sections are capable of in contrast to the TK.

The BSM data acquisition forces the user to follow several post processing steps which are illustrated in fig. 4.2. The CCD Camera provides a digitized image of the phosphor screen attached to the MCP Detector. The information is contained in the detected spatial distribution of the SEs. In case of a bunch profile measurement the spatial distribution has to be projected over the RF Deflector's sweep axis. The image intensity averaged over the sweep axis yields a first profile plot (see fig. 4.2 upper part). This preliminary profile is afflicted with background and statistical noise, degrading the quality of the measurement. With an auxiliary measurement the quality can be improved by ensuring a measurement with an absent bunch signal (closed apertures). This background determination has to be compared with the bunch measurement to adjust the intensities to each other. If the background plot is matching the intensity of the primary measurement, then the background can be subtracted. The new profile

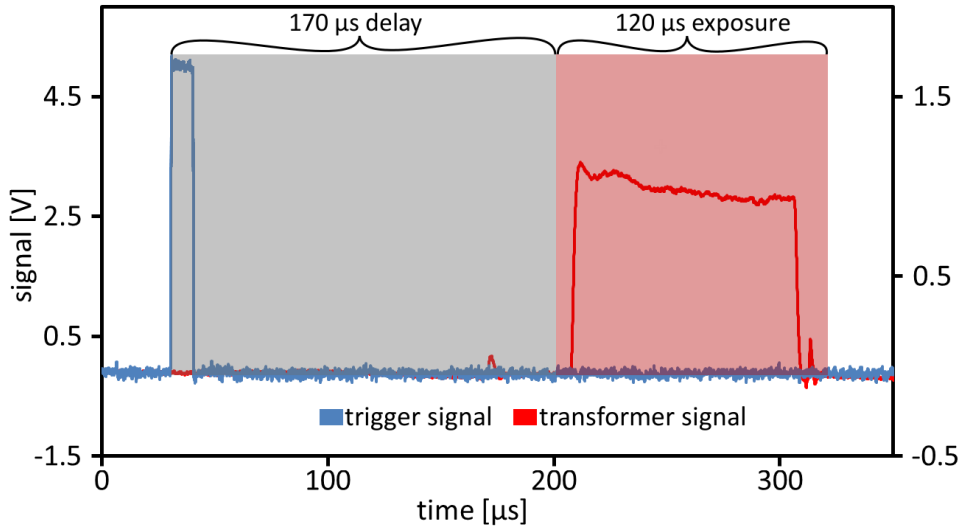


Figure 4.1.: An exemplary picture of the macro pulse and trigger structure with extra labeled delay and exposure time of the imaging CCD Camera.

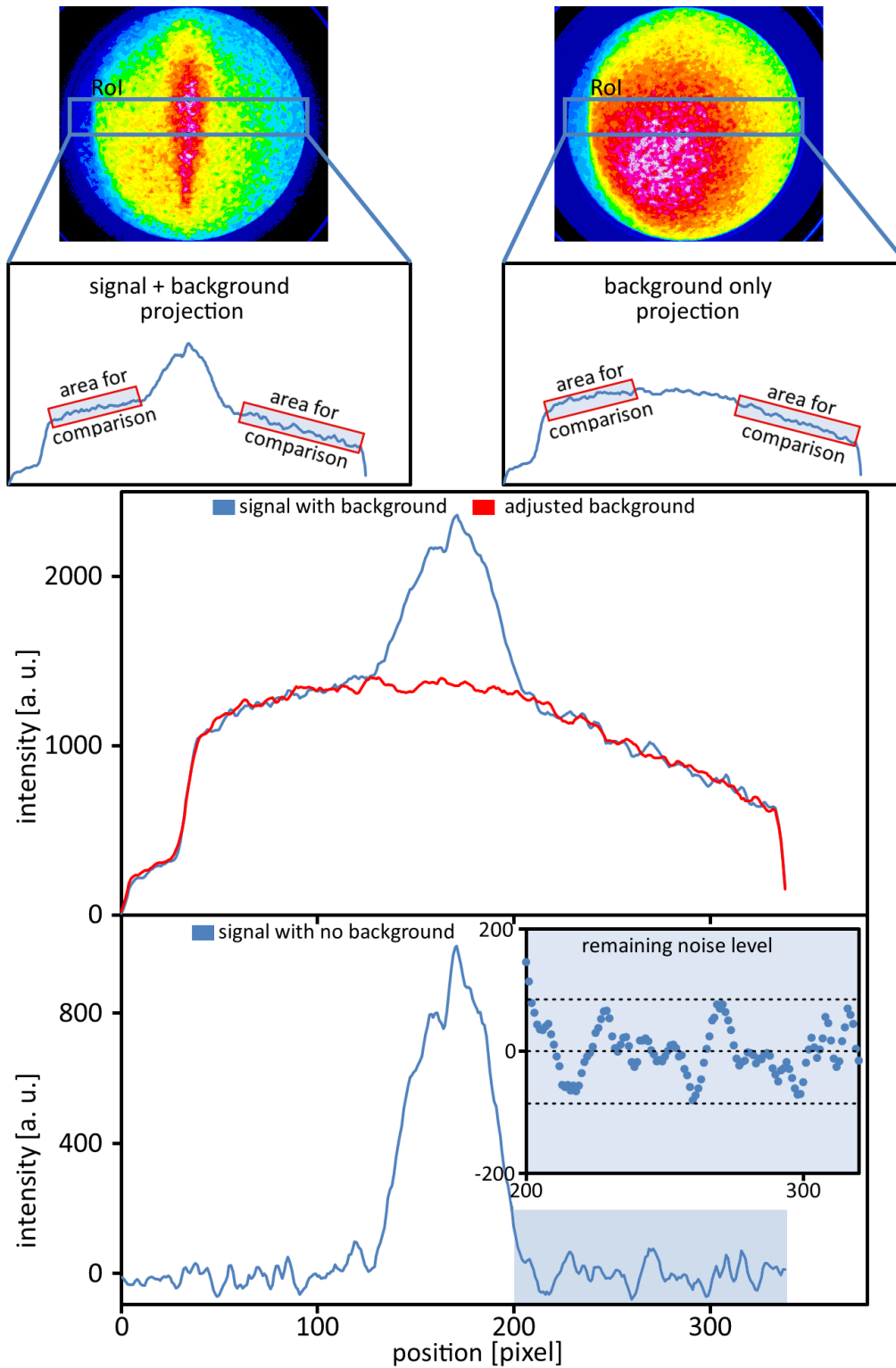


Figure 4.2.: Illustration of the post processing procedure to obtain a bunch profile measurement from the image data. With a second measurement the background can be subtracted. The signal and noise remains.

plot is almost background free because a minor background contribution of the bunch signal itself (scattered SEs) can not be excluded. Although the signal quality has been improved, there is still statistical noise remaining (camera read-out noise, MCP dark current, phosphor screen fluctuations) which limits the sensitivity of the BSM for low intensity measurements or increases the total amount of single bunches necessary to obtain a proper profile measurement.

#### 4.1.2. Phase Calibration

The Phase Calibration is essential for the proper operation of the BSM. To gain access to the time structure of the obtained data, at least a second measurement, related to the first measurement, is necessary to analyze the time structure by post-processing.

The measured particle distribution is created by an alternating E-field, deflecting the SEs in dependence on their time of arrival at the two capacitive plates of the RF Deflector (see sec. 3.3.5). The RF Deflector is coupled to the master oscillator of the accelerator and driven by the same frequency. The master oscillator RF can be shifted by a delay with an accuracy up to  $0.3^\circ$  for 36 MHz. The phase matching of the RF Deflector to

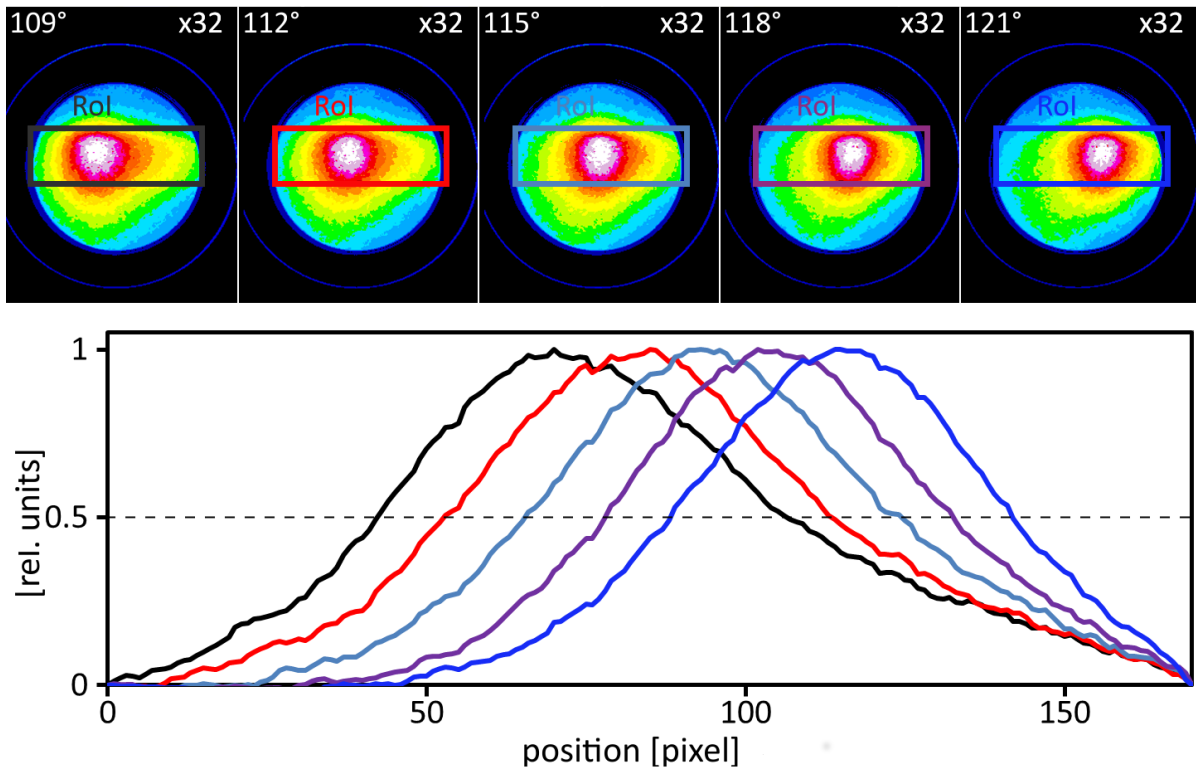


Figure 4.3.: Several profile measurements with a different RF Deflector phase setup leads to the phase calibration to obtain the time structure of the bunch. Beam setting:  $\text{Ni}^{28+}$ ,  $I = 0.9 \text{ mA}$ ,  $\tau_{\text{pulse}} = 145 \text{ }\mu\text{s}$ , 32 shots, Field-Box  $-24 \text{ kV}$ , MCP 1800 V, EA  $\pm 4400 \text{ V}$ ,  $p = 5 \cdot 10^{-6} \text{ mbar}$ ,  $P_{\text{RF}} = 100 \text{ W}$ .

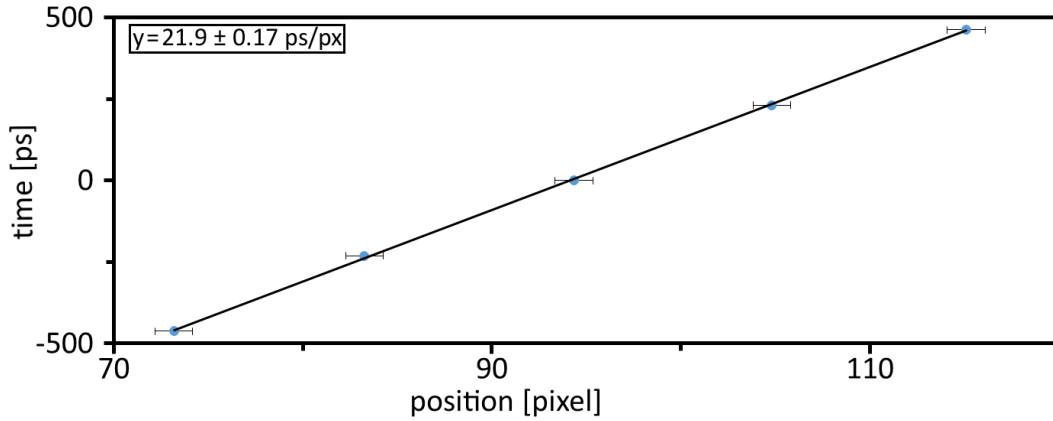


Figure 4.4.: Depicted are the profile centers of fig. 4.3 with the allocated relative time. The regression curve leads to the phase calibration.

the actual bunch RF phase is necessary for proper function of the device. The phase matching has to be redone every time the accelerator setting has changed.

Due to the use of a sinusoidal frequency instead of a sawtooth, the SE beam has to interfere with the deflector's alternating E-field in the linear realm at  $\pm 30^\circ$  around the zero-crossing of the RF. Otherwise measurement distortions will occur which cannot be undone. For proper matching the center of the spatial distribution has to be shifted to the middle of the MCP Detector and should stay there, while the applied RF power is increased. The increasing RF power will show any mismatch. For any mismatch, the phase has to be readjusted.

If the relative RF phase of the bunch center is known, a second measurement with the same setting, but a different RF phase setting has to be done. This additional measurement is used for the phase calibration by determining the location of the center of at least two profiles. In addition the relative phase (equals the relative time) is assigned to the location of the profile centers. The offset between the two profile centers yields the necessary time information for the profile width. Usually more than two profiles are used for a higher precision of the calibration. Figure 4.3 depicts 5 phase shifted profiles. Due to intensity cutting, at the right side of the MCP Detector, only measurement points above 50% threshold are used for the center determination. By reducing the angle of deflection, by lowering the RF power, the cutting can be avoided for the disadvantage of a reduced detector width.

Figure 4.4 depicts a phase calibration using the obtained centers from figure 4.3. The regression curve leads to the phase calibration. In this case the calibration corresponds to  $21.9 \pm 0.17$  ps/px for an applied RF power of 100 W or  $48.7 \pm 0.38$  ps/mm with a pixel size of 0.45 mm. For shorter bunches an even higher phase calibration can be achieved by using the 108 MHz Deflector, which allows higher field gradients, while deflecting.

### 4.1.3. Imaging Properties of the BSM

The RF Deflector has a secondary function as an electrostatic Einzel lens. This feature is necessary to compensate for the electron beam divergence, while the SEs are imaged on the MCP surface. It is of great importance to investigate the imaging properties of the BSM. Not only is the Einzel lens setup vital. There is a whole set of parameters which has to be considered. The first one is the voltage setup of the Field-Box which forms the initial divergence of the SE beam together with the aperture system of 7 adjustable apertures. Another parameter is the voltage applied to the Energy Analyzer. The influence of the ion beam parameters is also of importance, but it is not accessible for most experiments and the BSM is capable of adapting to most of the ion beam presets. For the reason of only investigating the focusing properties the primary function of the RF Deflector is disabled (zero RF power), no time information of the bunch width is present or of interest for this measurement series.

The Field-Box is fixed to  $-22$  kV and the Energy Analyzer is fixed to  $\pm 4000$  V. These two values are the result of an iterative optimization of the overall image intensity on the MCP phosphor assembly without changing another parameter like MCP gain or residual gas pressure. If the vertical ion beam position changes, it is necessary to optimize these two parameters again.

The focus width of the SE beam was investigated for three different X Aperture setups: 1.0 mm, 0.5 mm and 0.2 mm. Both Y Apertures were fixed to  $\pm 5$  mm. For each aperture setup the applied lens voltage has been varied from 3300 V to 4800 V with an 100 V step size, except for the last measurement. For each particle distribution the RMS values were determined and plotted in fig. 4.5. All three aperture settings show two linear branches.

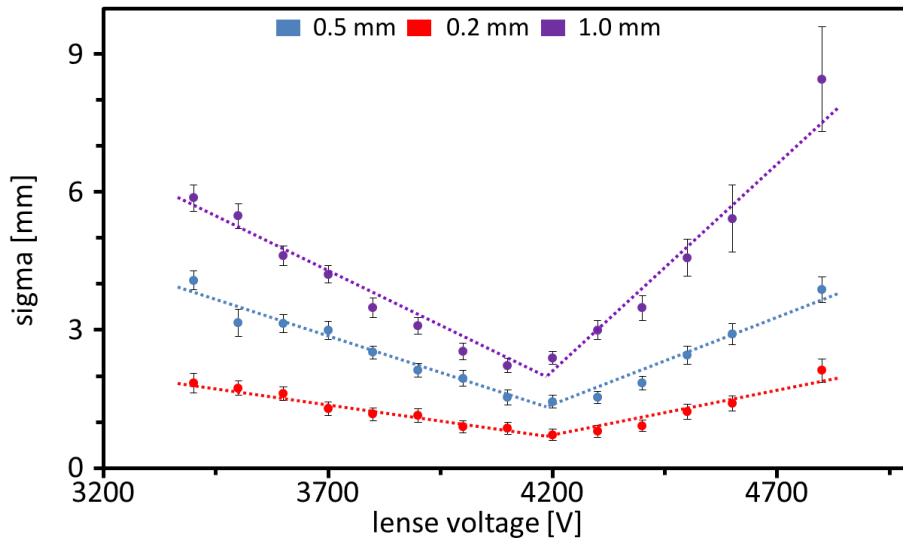


Figure 4.5.: Depicted is the focus width for different aperture settings depending on the lens voltage. Beam setting:  $U^{73+}$ ,  $I = 0.2$  mA,  $\tau_{\text{pulse}} = 145$   $\mu$ s, 16 shots, Field-Box  $-22$  kV, MCP 1600 V,  $p = 5 \cdot 10^{-6}$  mbar.



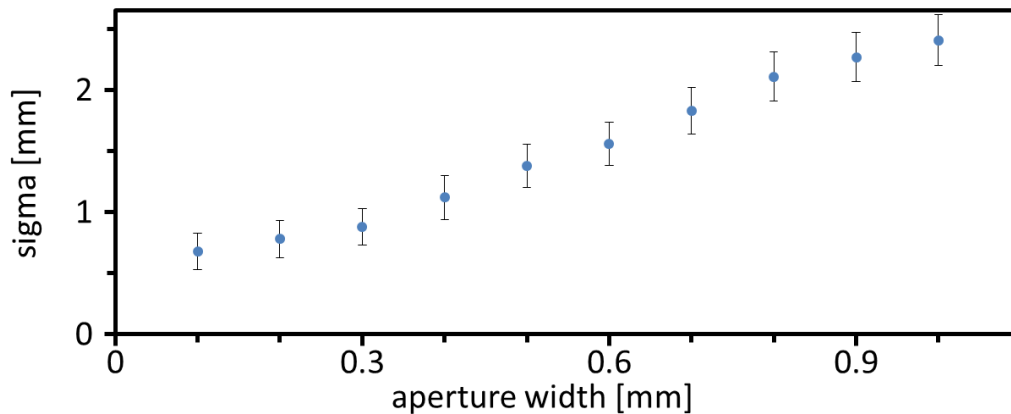


Figure 4.6.: Depicted are the optimal focuses for different aperture settings. Beam setting: see fig. 4.5.

This agrees with a similar electron optic of a commercial wire based BSM [89]. The optimal focus voltage is between 4100 V and 4300 V. For the different settings (1.0 mm, 0.5 mm, 0.2 mm) a minimum focus width of  $2.4 \pm 0.14$  mm,  $1.38 \pm 0.14$  mm and  $0.79 \pm 0.13$  mm is obtained, respectively. Even if the optimal voltage is not matched, the Einzel lens setup does not have a high sensitivity. A voltage band of 200 V is available with only a minor deviation of a  $\pm 10\%$  of the focus width.

A second measurement with variable X Aperture setting from 0.1 mm to 1.0 mm and a fixed voltage of 4200 V was done (see fig. 4.6). At 0.1 mm aperture setting the focus width is even smaller with 0.67 mm. Due to the immensely reduced signal intensity, this value is more of theoretical use. For big aperture settings ( $< 0.8$  mm) the curve flattens, the fixed aperture in the interior of the Energy Analyzer or the Field-Box contributes more and more to the electron beam shaping. Therefore the maximum electron beam width is restricted by these fixed internal apertures.

#### 4.1.4. Phase Resolution and Absolute Time Resolution

The effective phase resolution and therefore the absolute time resolution depends on two factors. One is the image resolution of the obtained spatial resolution, the focus width. Another one is the phase calibration which determines the time amount allocated to the image resolution in mm. Both values together yield the time resolution.

If the values from section 4.1.2 and section 4.1.3 are taken, a time resolution of  $37 \pm 6.3$  ps is achieved or a phase resolution below  $0.5^\circ$  at 36 MHz. This resolution usually is sufficient for bunch lengths of 1 ns (head to tail). Longer bunches are also quite likely in the middle of the transfer channel (TK) at GSI, due to long beam transport (55 m) and due to the momentum spread. For these long bunches the used RF power (100 W) on the RF Deflector would be too high to fit all the deflected SEs on the MCP surface. Typically the applied power is decreased down to 30 W for such long bunches, leading to a lower phase calibration and reducing the time resolution by

a factor of 1.8.

In principle the achieved time resolution is derived from the actual phase resolution for a specific frequency. If the applied RF is changed to a higher harmonic (to 108 MHz e.g.), the phase resolution of the device stays the same, but the time resolution will increase by a factor of three. Typically each accelerator complex has its characteristic RF frequencies. The FAIR p-LINAC has an RF of 325 MHz, here the phase resolution might yield to an achievable time resolution of 4.3 ps. This gives a strong hint about the possible performance of a new non-intercepting Bunch Shape Monitor for FAIR.

## 4.2. BSM Measurements

The essential stages of the measurement preparations were explained. The basic performance of the BSM was derived from the preceding section and the time resolution was considered sufficiently for extensive bunch shape analysis. The following section will present recent bunch shape measurements and parameter studies as well, to demonstrate the feasibility and the full spectrum of applications of the BSM.

### 4.2.1. Bunch Profile Measurement

The longitudinal bunch profile is an indicator for the quality of the phase matching of the different LINAC sections [90]. Therefore it is beneficial, especially while the LINAC is put into operation, to analyze the bunch shape. Many numeric beam evaluation programs use a Gaussian bunch shape for the purpose of a fast and stable calculation. In operation most certainly the bunch structure deviates from the Gaussian shape for several reasons, like machine phase mismatching or non-linear effects or space charge effects [91].

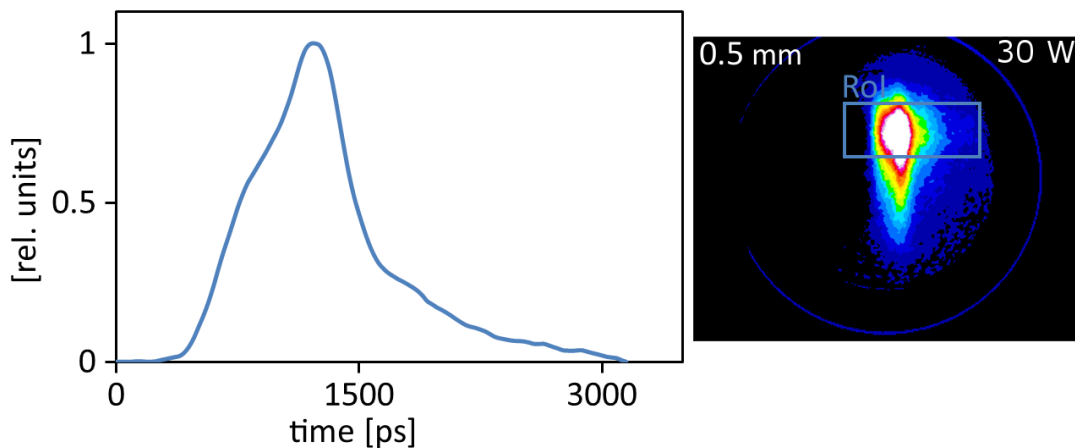


Figure 4.7.: Depicted is a non-Gaussian bunch profile and the related MCP distribution. Beam setting:  $U^{28+}$ ,  $I = 1.6$  mA,  $\tau_{\text{pulse}} = 95$   $\mu\text{s}$ , 32 shots, Field-Box  $-24.5$  kV, MCP 1400 V,  $p = 1 \cdot 10^{-5}$  mbar.

Using the BSM different bunch profiles with non-Gaussian distribution were obtained. Figure 4.7 depicts the profile after background subtraction. The rising edge shows a second structure at 1100 ps, while the top is thinner than a Gaussian shape. Also very prominent is the long tail of the bunch which indicates particles which are possibly out of the realm of longitudinal phase focusing (RF bucket). Some of these bunch distortions were predicted (see theory section 2.5.3). For further discussion of any results the different approaches for analyzing the obtained profile have to be considered.

Figure 4.8 shows four different numeric methods: Gaussian fit, multiple Gaussian fit (impulse fit), logarithmic normalized distribution (LND) and the standard deviation through numeric integration of the data. To some extent it makes sense to assume a Gaussian distribution and try to fit a Gaussian curve to the data, because many numeric beam calculation codes are based on Gaussian profiles. A quite similar approach is an impulse fit which consists of several sub curves of Gaussian shape. The envelope of all single curves yields the complex obtained profile. A third possibility is a logarithmic normalized distribution. The last variant is the standard deviation (SD) for an arbitrary distribution, which provides a virtual width (note: in the strict mathematical sense the SD only provides the profile width for a Gaussian distribution) for the given profile and a center of the profile. The SD can be considered as a numeric integration of distribution with the necessary weighting for the variance or the center of gravity for each data point.

All four methods are separately displayed in fig. 4.8 with their distinct SD, the center of gravity  $x_c$  and the numerical values adjusted  $\chi^2$  and adjusted coefficient of determination  $R^2$  as a degree of the fit quality which take the degrees of freedom into account. The single Gaussian fit (1) provides a good approximation of the peak structure of the profile and of the rising edge. The falling edge is acceptable until the occurrence of the bunch tail which is almost completely neglected by the fit algorithm. The obtained profile width  $SD = 336.5 \pm 7.8$  ps is too small if compared to the actual distribution and the occupied area. Also the center  $x_c = 1171.8 \pm 7.5$  ps is shifted wrongly to the left.

The multiple Gaussian fit (2) consists of three sub curves (dashed curves), due to the two major deviations from the single Gaussian (rising flank bump and the bunch tail). The multiple Gaussian achieves an exceptional good accordance due to the 10 free parameters available (3 each single Gaussian plus the offset). The center of gravity  $x_c = 1261.1 \pm 30.8$  ps obtained by combining and weighting the centers of each single Gaussian. The exceptional high error of  $\Delta x_c = 30.8$  ps is the consequence of the high error of the third sub curve of  $\Delta x_{c3} = 51$  ps; the location of this sub curve is obviously highly sensitive to the starting parameters due to its location in the profile tail and therefore, the lack of good characteristic points for the fit. The profile width  $SD = 459.8 \pm 17.3$  ps is obtained by numeric integration of the envelope of all three sub curves analog to the SD for an arbitrary distribution. It might be possible to treat the three Gaussian as separated functional descriptions for further analysis, but preliminary analysis has indicated that there is no physical meaning of the sub curves (slightly different beam setup yields completely different sub curves). Nevertheless the multiple Gaussian fit is suited for profile smoothing and the reconstruction of unintentional truncated data points. The logarithmic normalized distribution (LND) following [92] is

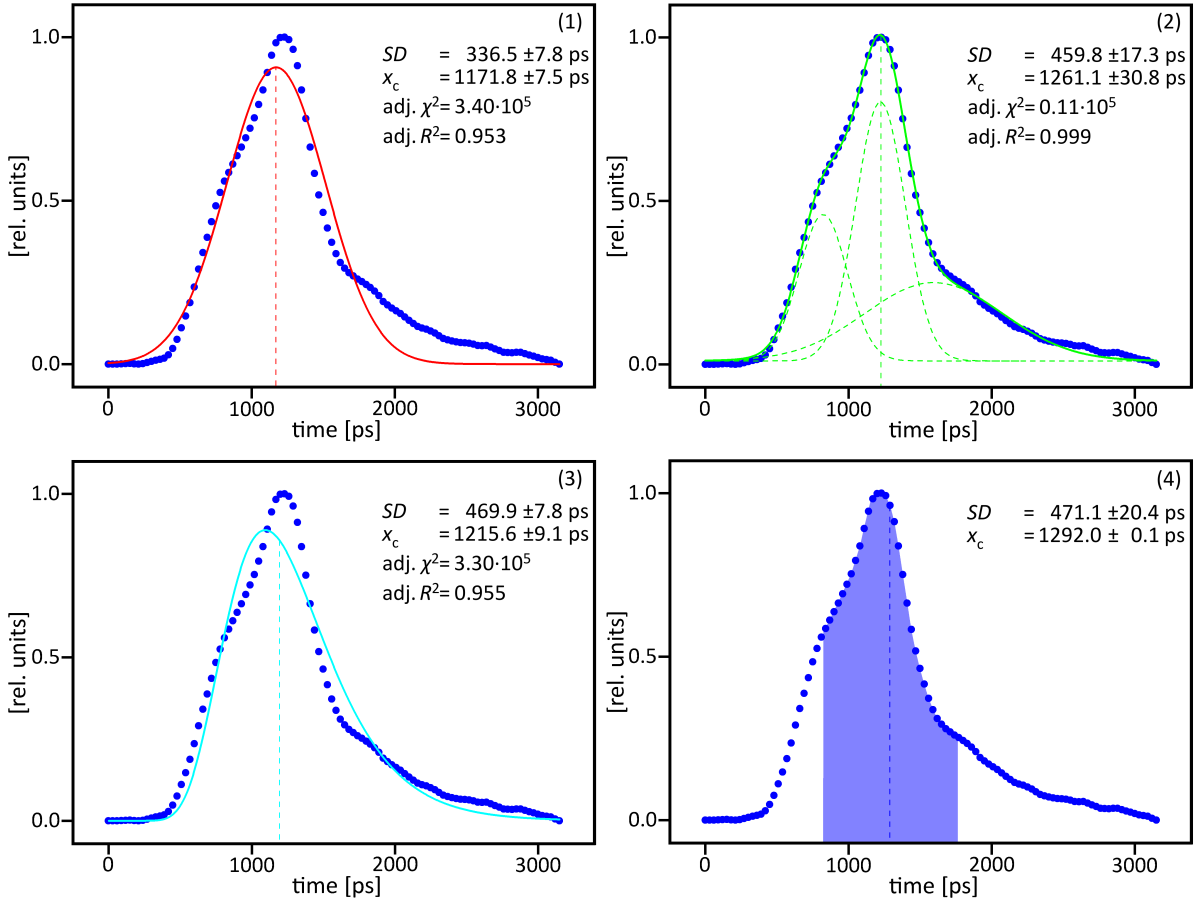


Figure 4.8.: Four different approaches for profile analysis: single Gaussian (1), multiple Gaussian (2), logarithmic normalized distribution (3) and standard deviation (4). Beam setting: see fig. 4.7.

defined as:

$$f(x) = \frac{A}{2\pi\sigma x} e^{-\frac{\left(\ln \frac{x}{x_c}\right)^2}{2\sigma^2}}, \quad (4.1)$$

where instead of  $\mu$  the location of the center  $x_c$  is used as a parameter which is by  $\mu = \ln x_c$  related to each other. Also  $\sigma$  is not the standard deviation, which is for the LND defined as:

$$\sqrt{\text{Var}(f(x))} = e^{\left(\ln(x_c) + \frac{\sigma}{2}\right)} \cdot \sqrt{e^{(\sigma^2)} - 1}. \quad (4.2)$$

The LND (3) resembles the peak structure almost as good as the single Gaussian, but in strong contrast to the latter, the LND follows the bunch tail quite well which yields significantly bigger values for the profile width  $SD = 469.9 \pm 7.8$  ps than the single Gaussian. The center  $x_c = 1215.6 \pm 9.1$  ps is still shifted to the left if compared with the multiple Gaussian fit.

The last variant is the SD for arbitrary distributions which is basically a numerical

integration of the profile:

$$\sqrt{\text{Var}(f(x_i))} = \sqrt{\sum_i^n \left( (x_i - x_c)^2 \frac{f(x_i)}{\sum_i^n f(x_i)} \right)}, \quad (4.3)$$

whereby the center of gravity  $x_c$  is obtained as follows:

$$x_c = \sum_i^n \left( x_i \cdot \frac{y_i}{\sum_i^n y_i} \right). \quad (4.4)$$

The SD has the drawback of high susceptibility of baseline fluctuations which strongly contributes due to the  $(x - x_c)^2$  dependance of the numerical integration and it makes no statement of the actual profile shape. The obtained center  $x_c = 1292.0 \pm 0.1$  ps is the most right center of all methods, also the profile width  $SD = 471.1 \pm 20.4$  ps is the biggest. The rather big  $\Delta SD = \pm 20.4$  is the consequence of the high susceptibility of fluctuations. On the other hand the  $\Delta x_x = 0.1$  ps is the smallest.

To judge the quality of the specific fits, the numeric values  $\chi^2$  and  $R^2$  are used. The multiple Gaussian provides a high adjusted coefficient of determination  $R^2 = 0.999$  and a 30 times smaller adjusted sum of the squared errors  $\chi^2 = 1.1 \cdot 10^4$  than the other two fits. On the one hand, it is not possible to directly obtain the profile width by using the values provided by the three sub Gaussians. It is only possible to obtain the profile width by numeric integration (see equation 4.3) of the resulting envelope, just like the SD for any other arbitrary distribution. Therefore, including the absence of physical meaning of the sub curves, there is no true advantage of the multiple Gaussian fit over the SD for an arbitrary distribution. For further profile investigations the SD will be preferred over the multiple Gaussian fit.

In contrast to the multiple Gaussian, the single Gaussian and the LND directly yield a profile width. The numeric quality of the LND is slightly better than the single Gaussian's with  $R_{\text{LND}}^2 = 0.955$  to  $R_{\text{Gauss}}^2 = 0.953$  and  $\chi_{\text{LND}}^2 = 3.30 \cdot 10^5$  to  $\chi_{\text{Gauss}}^2 = 3.40 \cdot 10^5$ .

If one fit has to be preferred, it has to be the LND. Nevertheless the difference is only marginal. More important are the provided results of each method. The LND yields systematically bigger values for the profile width because it takes the profile tail into account. In addition, if compared with the multiple Gaussian and the SD for arbitrary distributions, the LND yields very similar results. Further profile evaluations will use the single Gaussian, LND and SD for arbitrary distributions.

### 4.2.2. Aperture Variation Profiles

The aperture setup is crucial for the obtained resolution of the bunch profile. A small aperture setting leads to a higher resolution, but the signal intensity of the obtained profile will decrease. With high resolution it is necessary to average over more macro pulses for a single profile measurement which leads to a longer acquisition time.

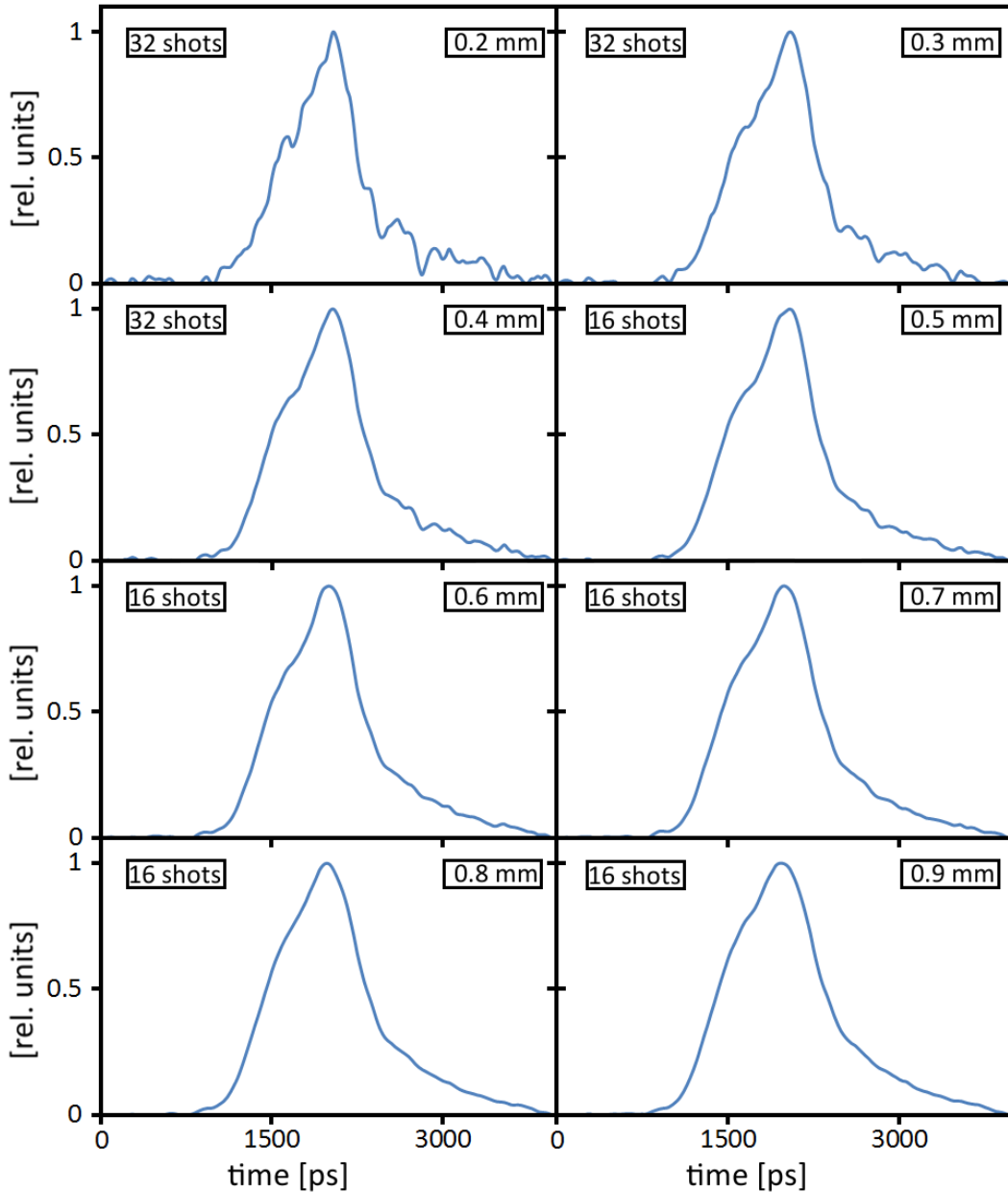


Figure 4.9.: Depicted are bunch profiles obtained with different X Aperture setup. Beam setting: see fig. 4.7.

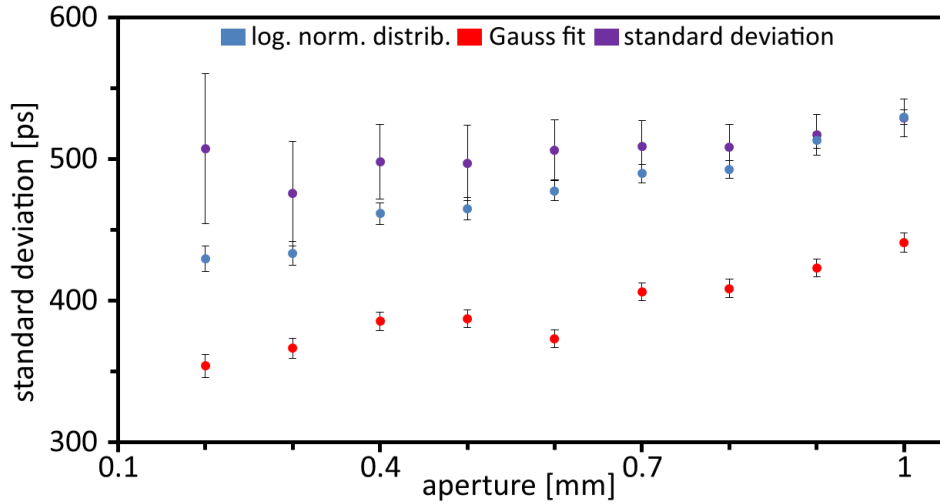


Figure 4.10.: Depicted are RMS profile widths obtained with different X Aperture setup for three analyzing models. Beam setting: see fig. 4.7.

For primary measurements the acquisition time is below one minute due to the high allocated repetition rate (1-5 Hz). As parasitic secondary user of the accelerator, the necessary time can easily exceed 10 or 20 minutes. While operating the BSM a proper compromise between resolution and acquisition time has to be found.

The aperture dependence of the obtained profile was investigated. For the presented profile in 4.2.1, a series of measurements was executed. The beam and BSM setup is basically the same except for the X Aperture opening width. The X Apertures were varied from 0.2 mm to 1.0 mm in 0.1 mm step size while the RF Deflector is in operation. The averaging grade was adjusted for each measurement (see the number of shots in fig. 4.9).

Figure 4.9 depicts the obtained profiles for different aperture setups. It can be seen that from 0.2 mm to 0.9 mm the dips in the profile are vanishing, especially in the rising edge and the bunch tail. But on the other hand the noise level decreases which can be seen at the baseline of the obtained profiles. For 0.2 and 0.3 mm setting the baselines at the beginning of the profiles fluctuate, due to the low event rate (see fig. 4.11 for intensity). For higher signal intensities this effect vanishes almost completely. Furthermore, it is not clear whether the additional structures in the rising edge are due to noise or higher resolution and therefore true bunch structures.

Figure 4.10 depicts the obtained profile width for different analyzing approaches: variance, Gaussian and logarithmic normalized distribution. All three methods show the same trend of increasing profile widths with increasing aperture opening due to broadening of the profile image on the MCP Detector. It has also been seen that the variance is strongly susceptible to low signal intensities with high noise level, as the 0.2 mm measurements proves with its high error. Although it should be in the range of the 0.3 mm measurement the SD obtains almost the biggest profile of the whole series here with  $507 \pm 53$  ps (max  $529 \pm 13$  ps at 1.0 mm), as the other methods strongly indicate. There

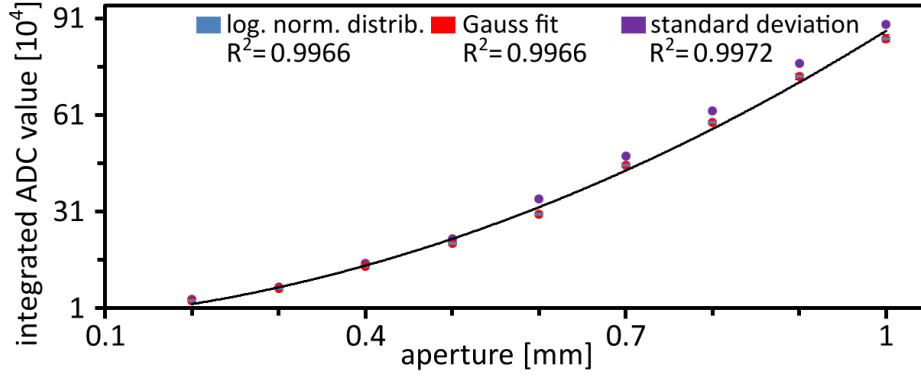


Figure 4.11.: Depicted is the obtained signal intensity for different X Aperture setups, errors are smaller than spot size. Beam setting: see fig. 4.7.

is again a big gap between the Gaussian and the LND. The Gaussian shows systematically smaller values although the behavior of the two series are remarkably similar. This indicates that the Gaussian fit is still suited for qualitative analysis of different setups.

Figure 4.11 shows the obtained signal level as integrated ADC values of the CCD Camera. The values match a parabolic fit as the high adjusted coefficient of determination  $R^2$  values indicate. The quadratic relation is expected due to the filtering of the spatial dimension in  $x$  direction and the additional filtering in  $z$  direction as a product of the interworking of the X Aperture and Energy Analyzer. The SD shows the most counts for each measurement where the Gaussian and the LND show almost identical values. The obtained average deviation of the intensity value predicted by the parabolic fits are  $\Delta I_{\text{Gauss}} = 4.2\%$ ,  $\Delta I_{\text{LND}} = 5.1\%$  and  $\Delta I_{\text{SD}} = 4.0\%$ .

It can be assumed that a resolution below 80 ps at 0.5 mm is sufficient for bunch shape investigation with quite high intensity levels for the given phase calibration (36 ps/px). In addition, the measurement exemplarily shows the advantage of a fit if there is a low signal-to-noise ratio present.

### 4.2.3. Single Macro Pulse Measurements

All of the precedingly presented measurements are multiple shot measurements which means that one obtained profile is averaged over several macro pulses (typical 8-32 pulses) depending on the beam setting. Another meaningful test of the reliability of the BSM are single macro pulse measurements. The obtained profile lengths should change only within a small margin. This time only the bunch length, not its shape, is of interest due to the low signal intensity. For this purpose ten measurements were done with the same beam setting and BSM setup comparable to 4.2.2.

Figure 4.12 shows the different obtained profile lengths for three analyzing methods. Here only the relative changes for each method are of interest, because the systematic differences between the methods have been covered already. Most of the profile lengths are within a small margin around the average for each series (dashed colored line) of  $\pm 20$  ps for the two fits and  $\pm 50$  ps for the SD. The bigger error and fluctuations of



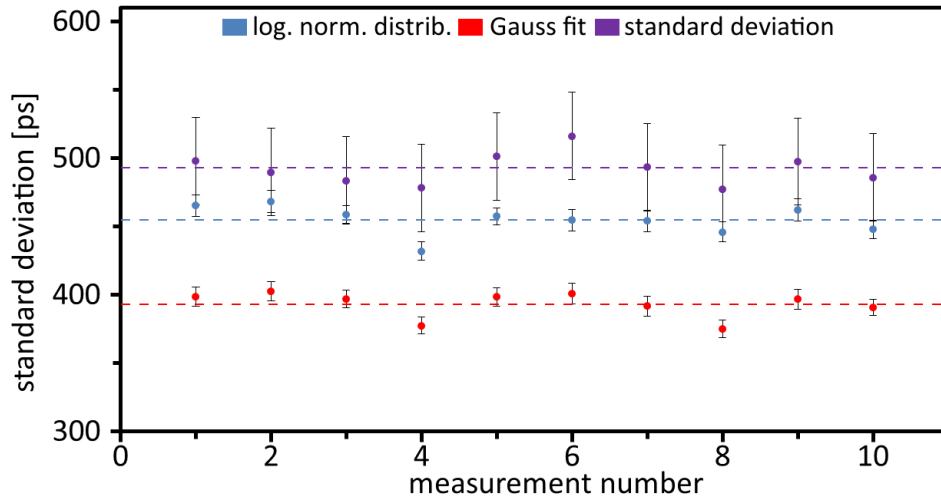


Figure 4.12.: Depicted is the profile length for single shot measurements for three different analyzing methods. Beam setting: see fig. 4.7, X Aperture setting 0.5 mm.

the SD are not surprising due to the high susceptibility of the statistic moment for high noise present at single shot measurements. The typical phase stability is about  $\Delta\phi = \pm 1^\circ$  @ 108 MHz [93]. Measurement four does not match the criterion. Another important insight is that all three methods follow the same trend over the course of the ten measurements although they do not provide the same absolute values.

For further investigation of the quality of the obtained data the relative location in phase (@ 36 MHz) of the center of gravity for each measurement is depicted in fig. 4.13. Again most of the measurements are within a tight margin less than  $\pm 0.2^\circ$  besides

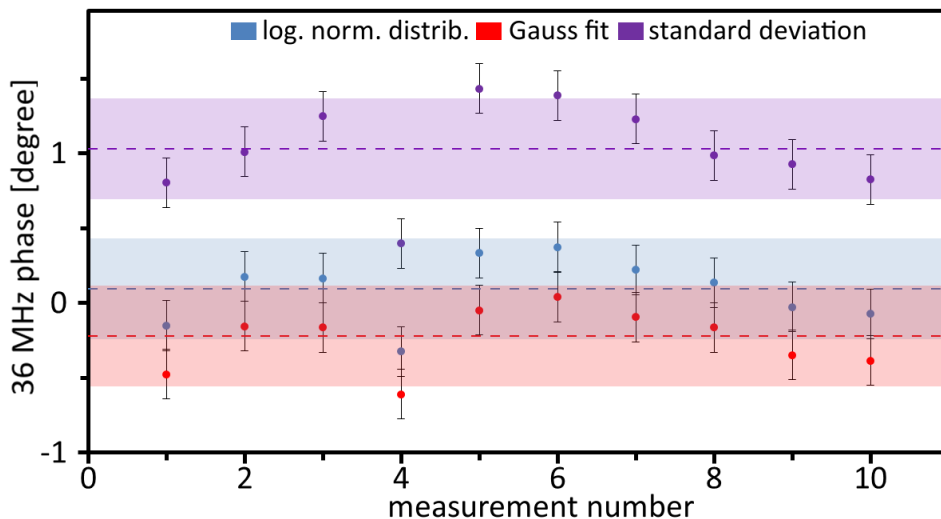


Figure 4.13.: Depicted is relative phase location of the bunch center.

measurement four. The accuracy of this measurement is determined by the delay used for the phase shift ( $\pm 0.166^\circ$ ), the other errors resulting from the different analyzing methods are negligible. The deviation of measurement four is even more stressed here and the different methods again show a similar trend. The LINAC RF stability of  $\Delta\phi = \pm 1^\circ @ 108 \text{ MHz}$  [93] is displayed as the colored strip around the average phase values (dashed colored lines). It is likely that the accelerator RF control is responsible for the deviation of measurement four.

The detection of RF phase errors of the LINAC shows the capability of the BSM of a macro pulse investigation which aims to detect bunch fluctuations within a single macro pulse. Such measurements are very useful for a better understanding of the LINAC.

#### 4.2.4. Vertical Beam Profile

The BSM is not only able to measure the longitudinal, but also the vertical beam profile. This is possible with a multiple step measurement by varying the accepted kinetic energy of the Energy Analyzer. Done in a systematic manner the obtained signal

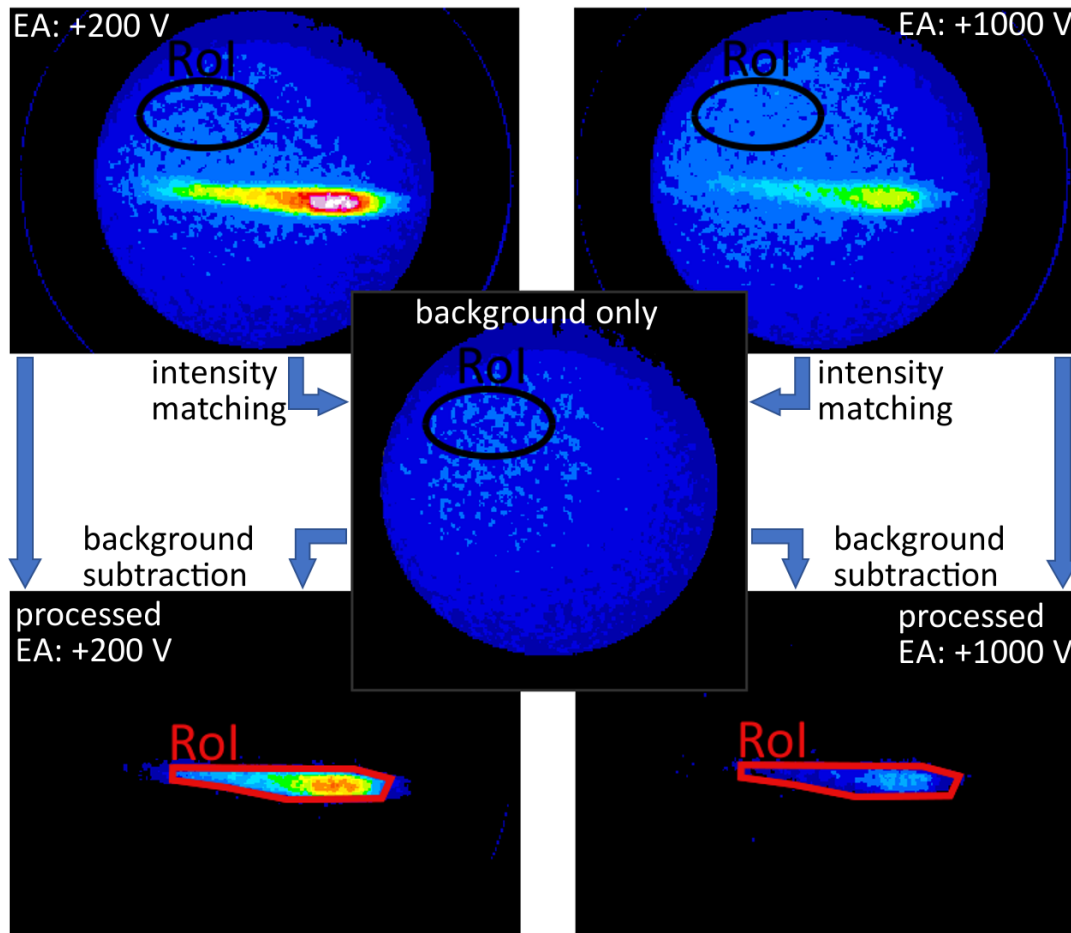


Figure 4.14.: Illustration of the specific steps to execute a vertical profile measurement.

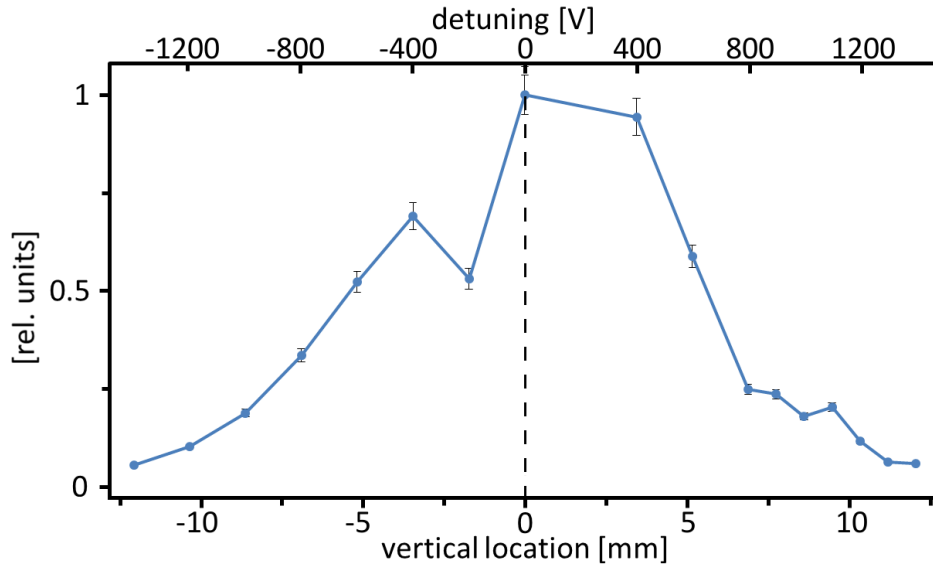


Figure 4.15.: Vertical beam profile obtained through variation of the Energy Analyzer voltage from  $-1400$  V to  $+1400$  V. Beam setting: see fig. 4.7, RF Deflector off. The depicted errors are the result of the intensity analysis of section 4.2.2.

intensity at the MCP Detector will reflect the vertical ion distribution of the beam. For transverse profile measurements there are several other devices available to make a comparative measurement to judge the feasibility of the BSM, at least for the vertical profile measurement.

The beam setting is stated in chapter 4.2.1, but this time the RF Deflector is switched off. The Energy Analyzer has a default setting of  $\pm 4000$  V which will be detuned from  $-1400$  V to  $+1400$  V corresponding to  $\pm 12.4$  mm vertical scan range around the beam center at the vertical position 4 mm lower than the beam pipe.

The measurement series is started from the maximum at 4000 V of the Energy Analyzer in 200 V or even 100 V step size. For each measurement the intensity level of the line focus is taken, where most of the SEs hit the MCP Detector. Also the initial beam intensity is taken into account by comparing and matching the background and signal level of each measurement. After the background is subtracted, one spot of the vertical profile is obtained by counting the obtained SEs in the Region of Interest (RoI) (illustrated in fig. 4.14). Now the Energy Analyzer is further detuned for the next measurement. Most of this process is executed by post processing the data of the digital MCP Detector images.

The obtained profile is depicted in fig. 4.15 and normalized to its maximum due to the lack of an ion current based calibration for the profile. A second measurement (see fig. 4.16), taken by a profile grid [94] is available for comparison. Unfortunately the location of the closest grid is 6 m upstream from the BSM. Nevertheless the two measurements can be checked for similarities in their shape. The beam is just drifting from the grid to the BSM.

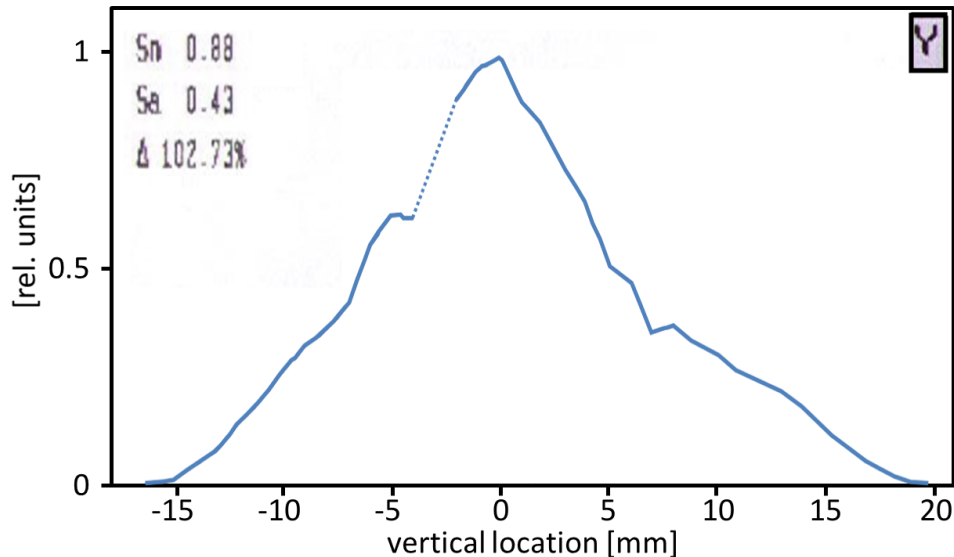


Figure 4.16.: Comparative vertical profile obtained 6 m upstream from the BSM location.

At  $-5$  mm both profiles show a small gap, as both figures show a fast dropping edge till 7 mm and the maximum is almost at the same location. The grid suffered a broken wire, indicated by the dotted line. Although not identical, the two profiles still look alike, and allow a positive judgment on the reliability of the BSM.

### 4.3. BSM Parameter Studies

Profile measurements taken by the BSM demand high effort during the measurement process due to the time sweep process of the device by the RF Deflector. The deflection of the SEs deteriorates the signal intensity due to the dispersion of the SEs on a bigger area of the MCP Detector surface. Further parameter studies like background contribution and signal intensity are required for further performance improvements.

#### 4.3.1. Ion Beam Intensity

The BSM is based on the creation of SEs liberated by the beam ions. The liberation process itself is a wide topic which is beyond the scope of this thesis. Still the dependance of the BSM on the ion current can be investigated by changing the accelerator ion current and monitoring the difference in the obtained data.

The ion current for  $U^{28+}$  was changed from  $75 \mu\text{A}$  to  $1.6 \text{ mA}$  and the intensity levels at the MCP Detector were measured. Due to the current restriction at the ion source, the actual beam current at the BSM location will strongly deviate. For low current settings ( $< 100 \mu\text{A}$ ) the level can change about several tens of percent from one macro pulse to another. For higher currents ( $> 500 \mu\text{A}$ ) a few percent are regular. Regarding this error source an averaging of 16 shots per measurement is taken. For the analysis two values

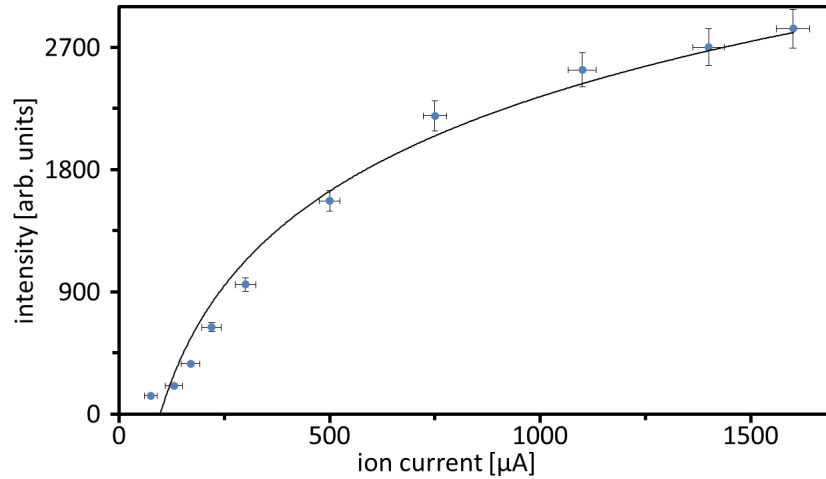


Figure 4.17.: Obtained average SE signal intensities in dependence on the ion current. A non-linear global behavior is seen. Beam setting: see fig. 4.7, RF Deflector off, 16 macro pulses per measurement.

are taken, the mean background intensity and the mean signal intensity of the line focus like for the vertical profile (RF Deflector off).

Figure 4.17 depicts the obtained intensities. A logarithmic regression indicates a strong saturated signal. The MCP Detector might show saturation after reaching a certain threshold, due to improper usage. Due to the line focus, the achieved intensity can be too high on the concerning MCP surface. A second measurement, with the RF Deflector in operation, is executed to avoid MCP saturation. Due to the partial low currents only the mean intensity of the SE distribution is taken.

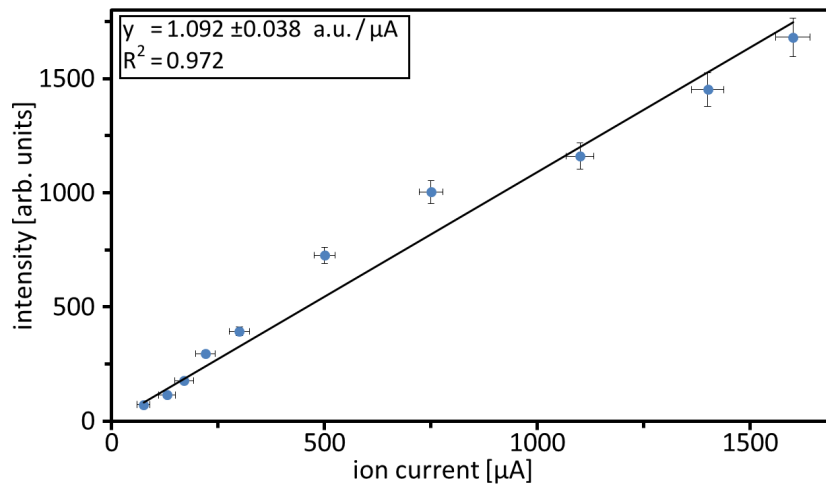


Figure 4.18.: Second signal intensity measurement. The RF Deflector is in operation. A global linear behavior is visible. Beam setting: see fig. 4.7, RF Deflector 10 W, 16 macro pulses per measurement.

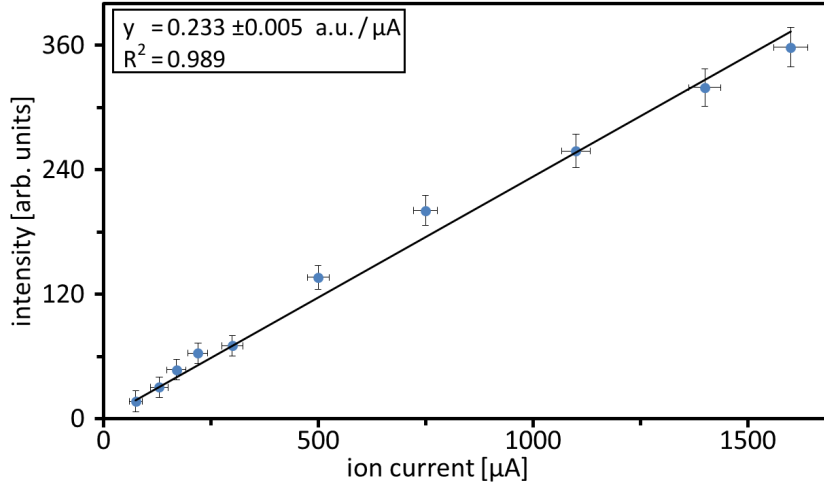


Figure 4.19.: Average intensity level of the non-signal occupied area of the MCP Detector. A linear progression is obtained.

With a lower global intensity level the obtained data ( see fig. 4.18) is in good accordance with a linear regression. The global intensity for the second measurement is therefore below the local saturation threshold of the MCP Detector.

A third measurement investigates the background dependence on the ion current. Figure 4.19 depicts the mean intensity of the MCP surface which is not covered by signal SEs. Due to the nature of the background and the bigger MCP surface the obtained mean intensities are significantly smaller. The data points also show linear behavior, but of a different gradient, indicating that the background is not mostly a result of misguided or scattered SEs all over the MCP Detector. A different process is responsible.

### 4.3.2. MCP Saturation Effects

The MCP gain is based on electrons (also charged particles or X-rays) hitting the inner wall of a micro channel and liberate additional electrons located in the semiconductive coating of the wall (high electron density see sec. 3.3.6). The escaping electrons experience the voltage and are also forced towards the channel wall to liberate more electrons. The process can be seen as an electron avalanche which grows exponentially with the applied voltage and the initial amount of electrons entering the detector channels as long as there are enough electrons available in the channel coating. If overstrained with too many initial electrons or by depleting the electron density within the channel, the MCP net gain will only slightly increase with the applied voltage. Saturation is the consequence and can occur globally for the whole MCP or locally in a few channels within a distinct area of the MCP Detector. Space charge effects at the exit might also cause voltages drops in the micro channels [95]. Therefore the saturation properties have to be investigated to avoid wrong operation of the MCP.

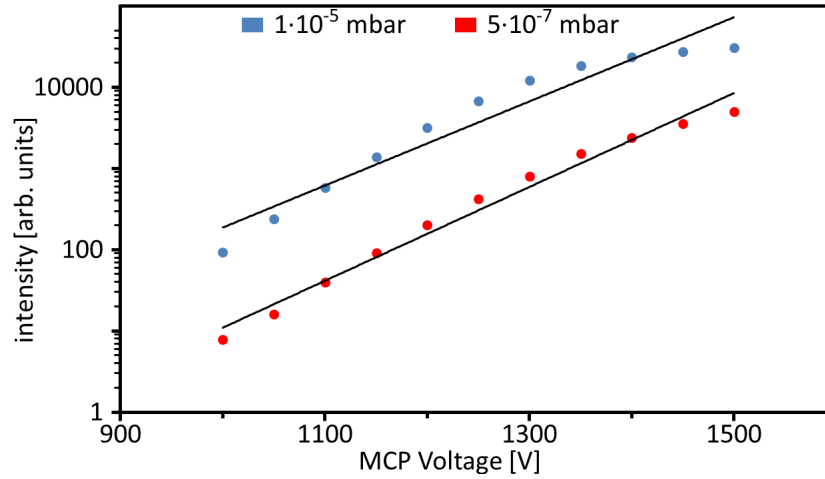


Figure 4.20.: Depicted is the averaged SE intensity versus the applied MCP voltage and two exponential fits. Intensity errors are below the dot size. Beam setting:  $N^{7+}$ ,  $I = 6.2$  mA,  $\tau_{\text{pulse}} = 145$   $\mu\text{s}$ , Field-Box  $-22$  kV, EA  $\pm 4000$  V, 32 shots, X Aperture 0.5 mm.

Two different measurement series were done. For both series the MCP voltage was changed from 1000 V to 1500 V and the signal intensity as well as the background level was analyzed. The aperture setup and accelerator setup is fixed for both measurements (see fig. 4.20).

In figure 4.20 the averaged intensity of the line focus of SEs is depicted for  $5 \cdot 10^{-7}$  and  $1 \cdot 10^{-5}$  mbar (upper limit for the TK). In addition to both measurements an exponential regression is plotted as it is expected for the MCP gain over voltage. In

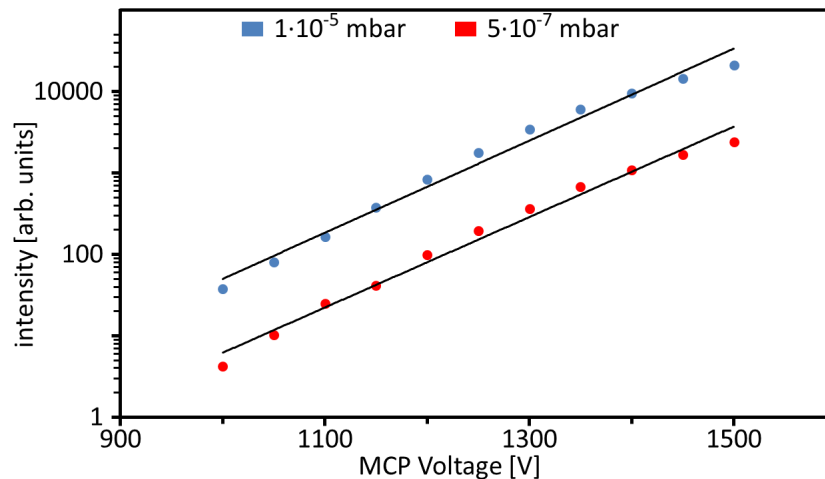


Figure 4.21.: Depicted is the average intensity of the non SEs covered MCP Detector surface versus the MCP voltage and two exponential fits. Intensity errors are below the dot size. Beam setting: see fig. 4.20.

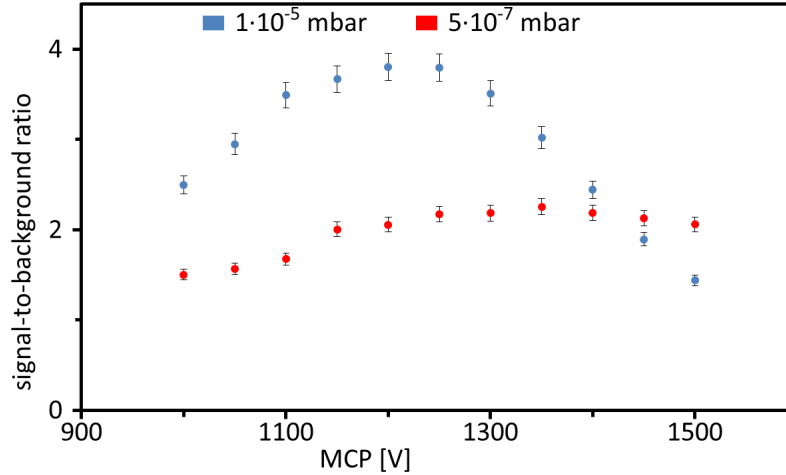


Figure 4.22.: Shown is the signal-to-background ratio calculated with the data from fig. 4.20 and fig. 4.21.

the logarithmic representation the gradient of a straight line represents the exponent. Both measurements have different gradients. The high pressure series (blue) has an average deviation of 47% from the exponential regression. Especially for higher MCP voltages the intensity increases far less than expected by the regression which indicates saturation. The low pressure series (red) shows better agreement with the exponential regression and has a smaller average deviation of 22%, but the overall intensity level is lower due to the lower gas pressure.

Although the origin of the background is not fully understood, it is highly recommended to choose an MCP setup which does not prefer the background gain over the SE signal gain. It has to be clarified whether the MCP itself is responsible for background or not.

Figure 4.21 shows a similar measurement series where the non SE covered MCP surface is investigated. Again blue represents high pressure and red low pressure with an exponential regression. The obtained average deviations from the exponential regression are smaller before (27% high pressure, 17% low pressure) and both series share almost the same gradient, indicating that the background is only amplified by the MCP Detector. Another important fact is that both measurements show no saturation over the entire range.

For a high resolution of the BSM or single shot measurements the signal-to-background ratio has to be maximized. The data from fig. 4.20 and fig. 4.21 are taken to calculate this ratio which is depicted in fig. 4.22. The ratio for the high pressure starts on a higher level than the low pressure measurement and achieves a maximum between 1200 V and 1250 V. Due to the saturation of the MCP for high intensities the ratio drops below the low pressure measurement at 1350 V. The low pressure measurement starts at a ratio below 2 and stays above 2 between 1150 V and 1500 V. The influence of the MCP voltage for the low pressure ratio is only marginal in strong contrast to the high pressure measurement.



The MCP investigation suggests high gas pressure together with low MCP gains. With a different beam setup the settings have to be adapted, but as a preset these values are of huge importance.

### 4.3.3. Macro Pulse Measurement

The operation of the MCP Detector is essential for a good signal-to-background ratio as chapter 4.3.2 has shown. If saturation occurs, the signal-to-background ratio will decrease. Preliminary measurements indicated that the saturation occurs over the course of the macro pulse. Therefore it is important to investigate if the MCP works properly over the whole period of a macro pulse shot.

The data acquisition uses a CCD Camera to digitize the illumination of the MCP Detector. The camera is triggered by an event provided by the accelerator 180  $\mu\text{s}$  ahead of each macro pulse shot (duration 95  $\mu\text{s}$ ). The exposure time of the camera can be set to reasonable 10  $\mu\text{s}$  and the delay is progressively shifted from 180  $\mu\text{s}$  to 280  $\mu\text{s}$  with 10  $\mu\text{s}$  step size leading to a histogram like image of the macro pulse structure. The average SE signal intensity for each measurement is determined. The result is compared with a different macro pulse measurement taken by current transformer [96] close to the BSM's location. This kind of measurement only provides qualitative analysis of the macro pulse structure. A current-to-intensity calibration would be necessary for quantitative analysis. Due to the low image intensity acquired by a short exposure time, the image averaging is set to 64 shots per image.

Figure 4.23 shows the results of the stepwise measurement. The 95  $\mu\text{s}$  preset for the macro pulse duration is in agreement with the read off value of almost 100  $\mu\text{s}$ . Another

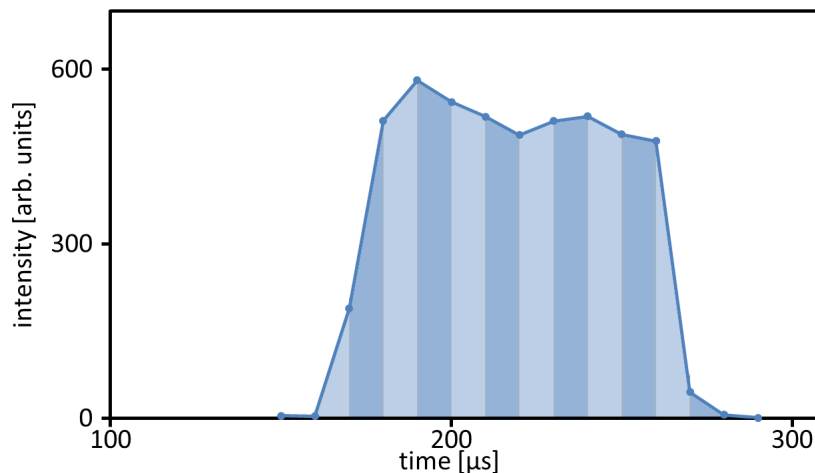


Figure 4.23.: Depicted is the macro pulse measurement done by delay sweeping and short CCD Camera exposure time (10  $\mu\text{s}$ ), indicated by the colored area below the plot.

Beam setting:  $U^{28+}$ ,  $I = 0.2 \text{ mA}$ ,  $\tau_{\text{pulse}} = 95 \text{ } \mu\text{s}$ , Field-Box  $-24.5 \text{ kV}$ , EA  $\pm 4000 \text{ V}$ , 64 shots, X Aperture 0.5 mm.

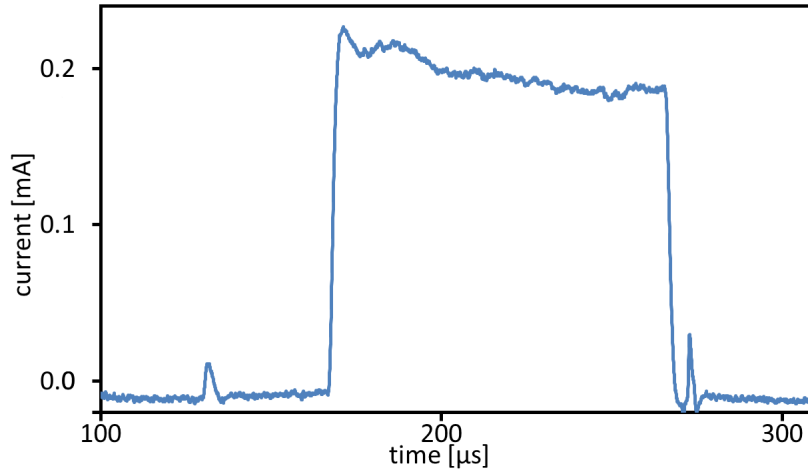


Figure 4.24.: Macro pulse measurement obtained by current transformer located in TK5. Parameters: see 4.23.

important statement is the maintaining of the signal level over the full duration of the pulse. Preliminary measurements with a poor MCP setup showed a strong decline of the intensity level up to 90% during the macro pulse presence. The result can also be compared with a measurement taken by a transformer seen in fig. 4.24. The transformer measurement confirms the 95  $\mu\text{s}$  preset perfectly, but it clearly shows a steeper rising and falling edge. This is expected because the edge rise time is shorter than the 10  $\mu\text{s}$  exposure time.

The macro pulse analysis can also be used to test the CCD Camera system for reliability. Another measurement is done, a single image is taken with an exposure time equaling the pulse duration. The integrated intensity of one full macro pulse image by the CCD Camera should equal the manually integrated intensity of the stepwise taken macropluse image to confirm proper function of the camera system. The combined intensity of each short exposure measurement is  $I_{\text{series}} = 4876 \pm 154$  a.u., of the one shot single measurement is  $I_{\text{single}} = 4833 \pm 120$  a.u.. Although not completely equal, the deviation is well within the error bars.

#### 4.3.4. Background Investigation with Absent Bunch Signal

The Background presence is a strong handicap for further performance increases of the BSM. Experimental experience indicated that the background is not susceptible to electric fields (suppression grid, steering voltage). This leads to the assumption that ionizing radiation is responsible for the majority of the background. An experimental setup with closed apertures will examine the background dependance on the applied voltage to the Field-Box. The high voltages of up to 35 kV are in the typical range of X-ray tubes. It is almost certain that accelerated electrons, hitting the Field-Box interior, generate X-rays.

Figure 4.25 depicts the average background intensity obtained on the MCP Detector

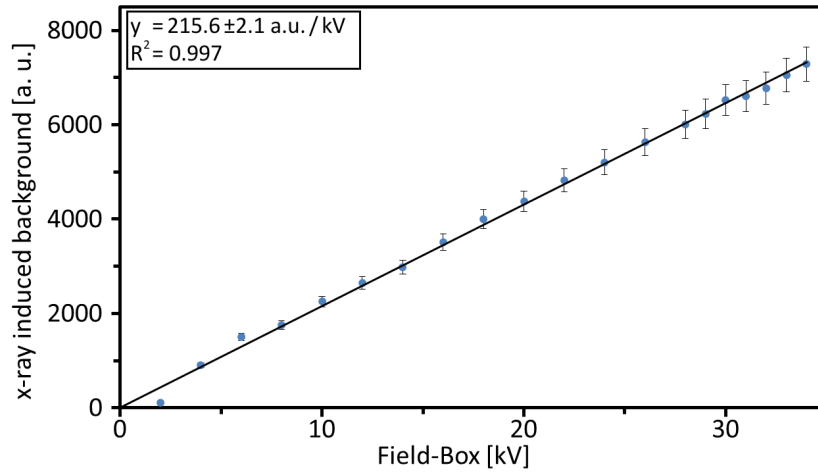


Figure 4.25.: Average background intensity of the MCP Detector in dependence of the Field-Box driving potential. Due to closed apertures SE contribution can be dismissed. Beam setting:  $U^{28+}, I = 0.2 \text{ mA}, p = 1 \cdot 10^{-6} \text{ mbar}, \tau_{\text{pulse}} = 145 \text{ }\mu\text{s}, 16 \text{ shots}, \text{MCP} = 1600 \text{ V}, \text{apertures closed}.$

without the presence of any bunch signal. All apertures are closed to guarantee a signal free measurement. The applied voltage is varied from 2 kV up to 34 kV, which also proves the electric strength of the Field-Box. A linear regression is also drawn to check the background relation with the voltage. Most of the values agree with the linear regression. The obtained data supports the X-ray major contribution to the background, because of the linear behavior and the drop to almost zero for low voltages.

A measurement depicted in figure 4.25 suggests that almost the entire background depends on the creation of X-ray within the Field-Box. Another measurement series is

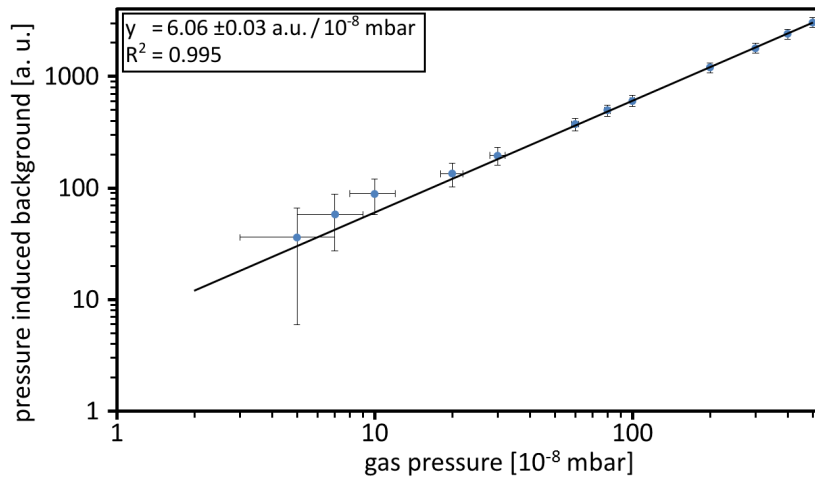


Figure 4.26.: Average background intensity of the MCP Detector in dependence of the gas pressure in the BSM. Beam setting: see 4.25.

done by keeping the apertures closed and changing the gas pressure within the Field-Box. The gas pressure determines the amount of beam gas collisions and therefore a linear relation with the obtained background is expected. The Field-Box voltage is fixed to 20.5 kV. Again a linear behavior of the background can be determined following fig. 4.26. The X-ray pressure relation should be even stronger. If the gas pressure is too low, only a few beam gas collisions occur any longer. For good vacuum level ( $p < 10^{-7}$ ) the background level should go to zero.

### 4.3.5. Background Investigation with Bunch Signal

The presence of strong background with the absence of a bunch signal was demonstrated. The dependence on the pressure and the Field-Box voltage was shown. The bunch signal itself is expected to be strongly related to the gas pressure due to the increasing beam gas impacts within the Field-Box, creating more SEs. For better BSM performance in operation it is of great interest to determine the signal-to-background ratio depending on the gas pressure.

Figure 4.27 depicted the average obtained background with opened apertures and bunch signal. The results are almost identical with fig. 4.26, supporting the minor contribution of any misguided SEs or any bunch signal correlated effect. The background again shows a linear behavior in double logarithmic scale.

Figure 4.28 shows the average intensity level induced by the bunch signal on the MCP Detector. The obtained intensity is consistently higher than for the background and also grows linearly with the pressure which is supported by the linear regression plotted in the figure. For small pressure values the intensity drops to almost zero. It seems that the pressure affects the background intensity in the same manner as the signal. Due to focusing of the SEs the intensity of the signal is higher where the background is

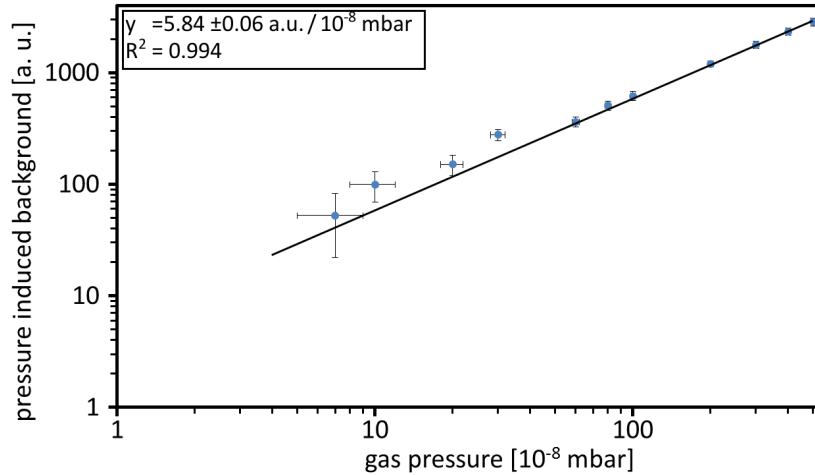


Figure 4.27.: Background determination with opened apertures. Beam setting:  $U^{28+}, I = 0.2$  mA,  $\tau_{\text{pulse}} = 95$   $\mu$ s, Field-Box  $-24.5$  kV, EA  $\pm 4000$  V, MCP = 1500 V, 16 shots, X Aperture 0.5 mm.

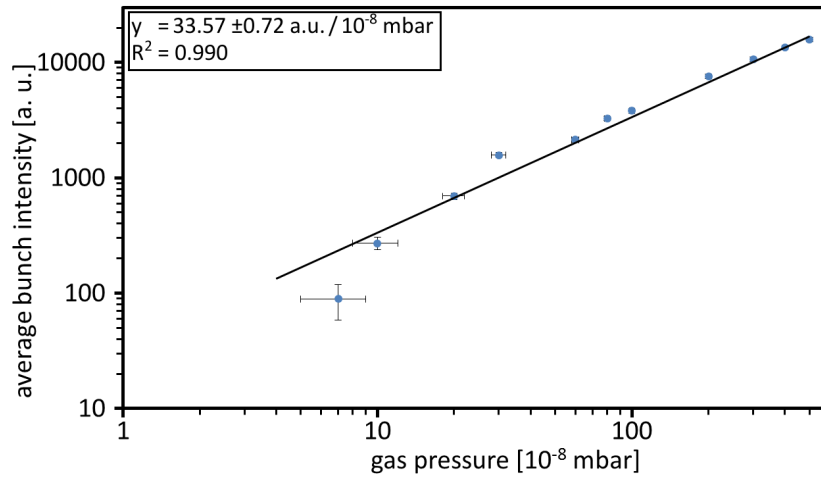


Figure 4.28.: Depicted is the average bunch induced signal versus the pressure. Parameters: see 4.27.

distributed over the whole detector surface.

For easy operation the ratio between the bunch signal and the background is of great importance. Figure 4.29 depicts the result of the simple division of the data of fig. 4.28 by the data of fig. 4.27. Instead of the signal peak the average signal level is used to determine the ratio. This approach is far more robust to produce reliable results, because of a reduced influence of the different BSM setups on the outcome.

Figure 4.29 depicts the signal-to-background ratio, which quickly rises from 1.7, at low pressure ( $p < 1 \cdot 10^{-6}$  mbar), to its maximum of about 6.4, at  $p = 8 \cdot 10^{-7}$  mbar and maintains this high ratio with a minor decrease till  $p = 5 \cdot 10^{-6}$  mbar. Therefore, for a good signal-to-noise ratio high pressure are recommended.

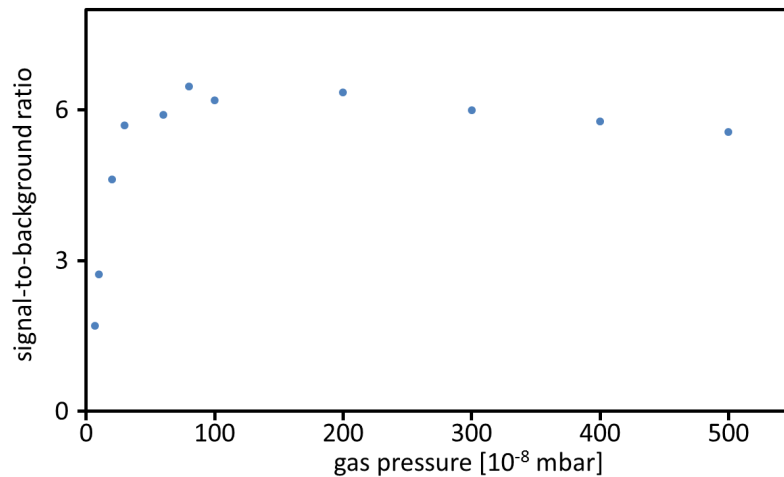


Figure 4.29.: Depicted is the ratio of the average bunch signal and the average background of the MCP Detector. Beam setting: see 4.28.

## 4.4. Choice of Parameters

The preceding chapters introduced several parameter studies for the BSM. The resolution as well as the signal quality dependencies on the BSM parameters were determined. The contribution to signal intensity and background of ion beam, gas pressure and MCP Detector was investigated. For a proper and fast BSM operation the choice of parameters have to be optimized.

The parameter studies demonstrated that a matching initial parameter choice is crucial for a successful bunch shape determination. Several parameters show a not trivial so optimum within the adjustable range, easily leading to a strong deterioration of the signal quality of a factor of 10. Wrong adjustment of only two parameters can completely prevent proper matching while in operation.

The outcome can be summarized as follows:

- A better signal-to-background ratio is achieved by increasing the pressure rather than the beam current.
- The beam current should not exceed 2 mA, better is below 1 mA to avoid high background.
- The applied voltage to the MCP Detector should not exceed 1500 V to prevent saturation of the device.
- An X Aperture preset of 0.5 mm is a good trade-off between signal intensity and spatial resolution.
- Background is not induced by SE, but primary by X-rays.

## 4.5. Emittance Measurement

The non-intercepting BSM proved its reliability on several occasions and is suited for advanced tasks. Although measuring solely the bunch length, the BSM is able to perform more sophisticated measurements. With the help of a longitudinal focusing element systematic bunch length manipulation can be executed which allows modest longitudinal emittance determination. The approach is similar to a quadrupole variation for the transverse emittance [97].

### 4.5.1. Experimental Setup

The GSI heavy ion LINAC consists of different accelerator sections. The front end consists of the ion sources and the RFQ and two IH tanks, the poststripper section of five Alvarez tanks. The final section consists of 15 single gap resonators (SGR) which can accelerate an uranium beam up to 13.5 MeV/n before it enters the TK. In principle an SGR works as a single pill box cell which has to match the bunch phase for acceleration or deceleration. If the SGR's zero crossing matches the bunch center, the gap voltage can be used for focusing or defocusing (depending on the polarity) of the bunch structure instead of acceleration or deceleration.

The SGR is set with a phase probe to detect any unwanted bunch shifts at the probe's location. Then the applied gap voltage will be increased systematically in a small step size of 0.1 V up to 10 V of the control value. To obtain the actual gap voltage in the SGR10 the calibration:  $U_{\text{control}} * 0.12 \text{ MV/V}$  [98], is used. For the bunch manipulation SGR10 was used which is located 55 m upstream from the BSM in TK5 DK1. The gap voltage was increased from 0.53 MV to 0.99 MV, the applicable maximum due to a control unit malfunctioning for higher voltages. With preliminary measurements the transition of the focal point through the location of the BSM was tested in advance.

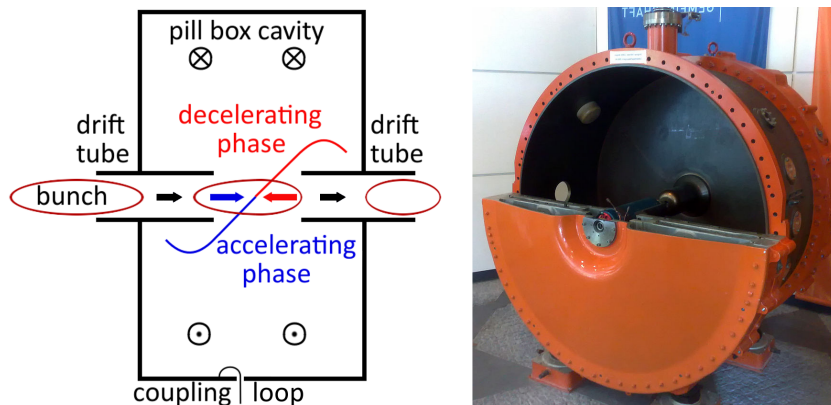


Figure 4.30.: A sketch of the cross section of a single gap resonator in bunching mode, indicated by the shortened bunch at the drift tube exit. On the right a picture of an obsolete GSI single gap resonator is shown.

### 4.5.2. Bunch Profile Variation

Figure 4.31 depicts the systematic bunch shape manipulation for selected parameters. For each obtained profile, 32 single measurements were taken to ensure a low influence off other accelerator parameters, like current fluctuations between the macro pulses. The profiles are presented in an absolute scale for a better judgment of the profile alterations.

The weakly bunched profiles ( $U < 0.7$  MV) show a clear merged two peak structure with a long tail ( $\sim 2$  ns), contributing half of the overall profile length ( $\sim 4$  ns). With increased bunching power the tail is affected the most. It interferes with a far bigger

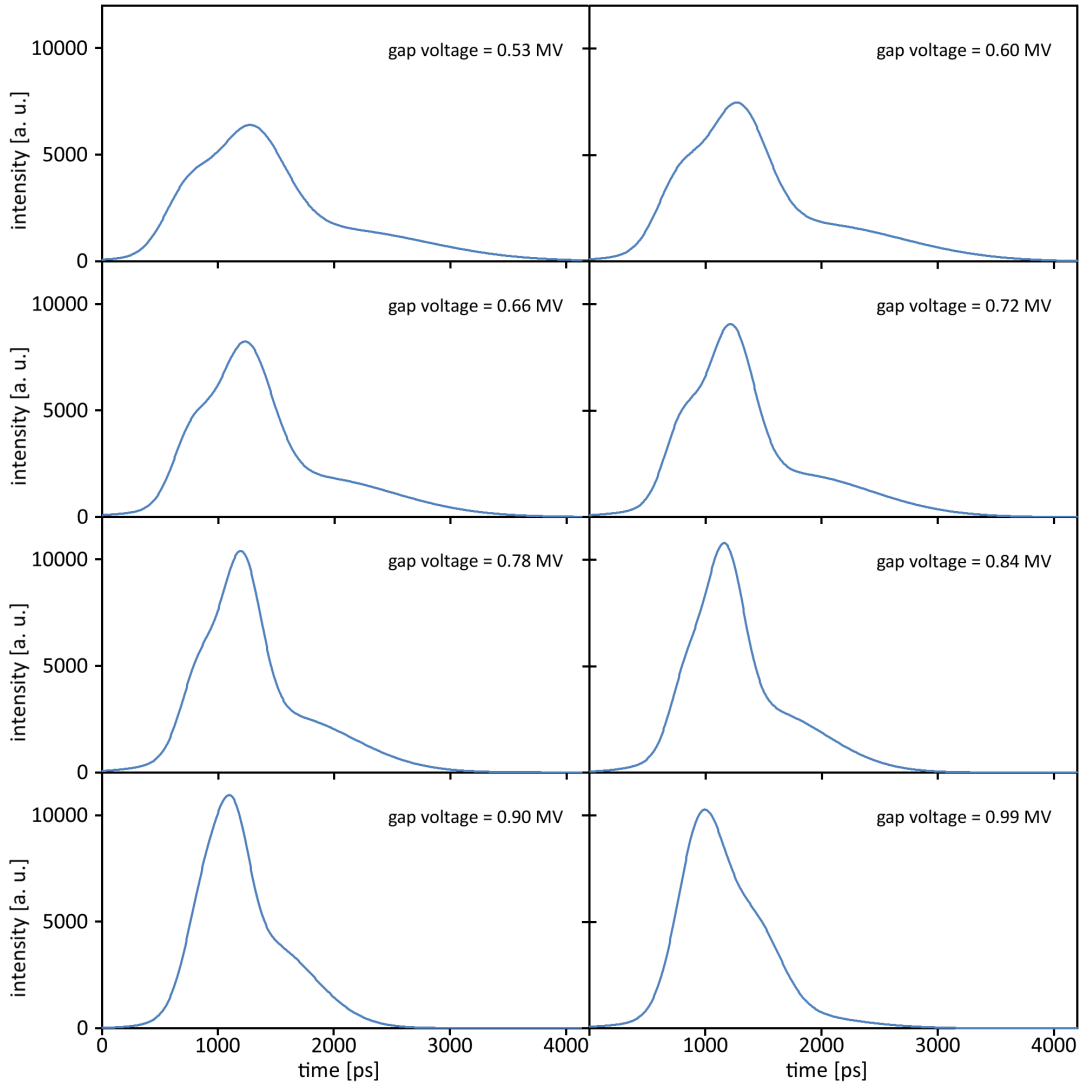


Figure 4.31.: Depicted are the bunch profiles manipulated by the SGR10 as a buncher. Beam setting:  $U^{28+}$ ,  $I = 1.6$  mA,  $\tau_{\text{pulse}} = 95$   $\mu$ s, 32 shots, Field-Box  $-24.5$  kV, MCP 1400 V,  $p = 1 \cdot 10^{-5}$  mbar, X Aperture 0.5 mm, RF Deflector  $P = 30$  W.



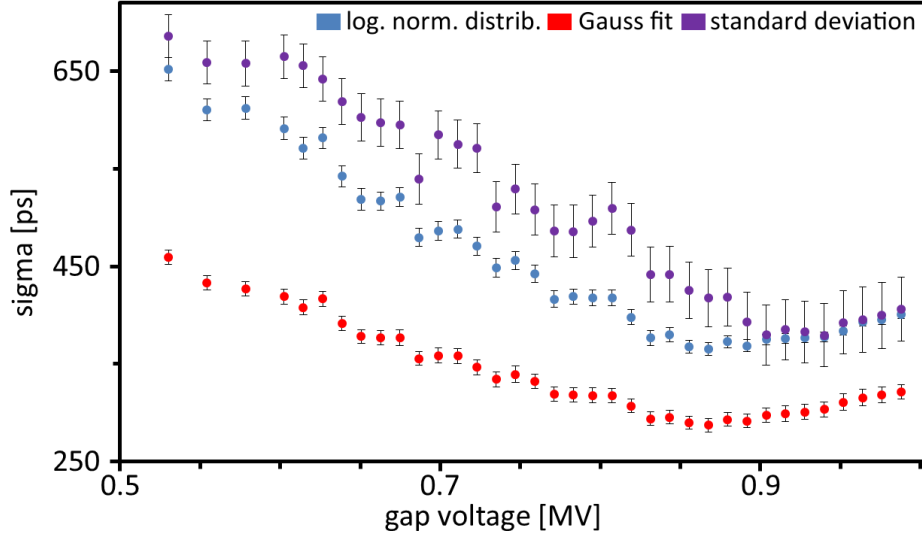


Figure 4.32.: Depicted is the obtained RMS width of manipulated bunch profiles.

E-field in the buncher gap due to its big delay in relation to the bunch center, where the gap voltage is just building up. The peak structure will be affected more moderately. It is located close to the zero crossing of the bunching phase leading to smaller E-fields interfering with this bunch segment.

For high bunching voltages ( $U > 0.8$  MV) the two-peak-structure merges into a single peak and the tail forms a shoulder. For highest voltages ( $U > 0.9$  MV) the peak structure is already broadening, where the tail is not completely shifted into the center. This behavior, where the peak is already in transition, but not the tail, indicates a complicated momentum distribution (fraying of the phase space distribution see sec. 2.5.3). This kind of bunch can not be completely prepared for injection into the SIS18. For optimal injection the bunch segments need different bunching parameters. The ions in the tail are not only displaced, but also carry a big momentum discrepancy picked up over their run through the LINAC.

The obtained profiles were analyzed with three different methods: Gaussian fit, LND fit and SD for arbitrary distribution (numerical integration of the whole distribution). In foresight of the emittance determination a Gaussian fit based analysis would be preferred, but the complicated profiles make a multiple variant analysis mandatory to allow an estimation of the systematic error through the improper use of a Gaussian fit.

Figure 4.32 depicted the result of the different methods. All three plots show decreasing profile widths along the increasing gap voltage until a minimum is reached. The Gaussian fit gives the smallest profile widths and obtains a minimum RMS profile width of  $287.4 \pm 6.7$  ps for a gap voltage  $U = 0.86$  MV. The LND fit results in significantly larger profile widths, but still smaller than the SD. The LND fit obtains its minimum of  $365.1 \pm 5.9$  ps also at  $U = 0.86$  MV, where the SD results in a minimum of  $377.3 \pm 32.4$  ps at  $U = 0.94$  MV. The more the bunch tail is taken into account, the more the minimum is shifted to higher gap voltages. Also an asymmetry is determined between the rising

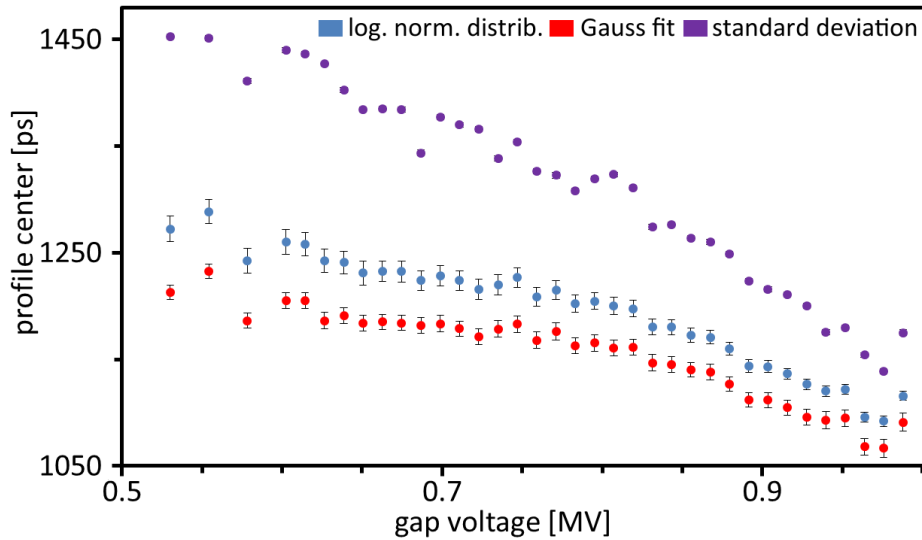


Figure 4.33.: Depicted is the location of the center of the manipulated profiles for cross checking with fig. 4.32 for any anomalies. For the SD (purple) the error bars are smaller than the plot point. Parameters: see 4.31.

and falling edge of the LND fit and SD. This is due to the bunch tail and its assumed momentum discrepancy. For the Gauss fit such an asymmetry is not visible.

All three methods show good agreement in the profile progression over the course of the measurement besides their already stated systematic differences (see 4.2.1) and are able to detect even smallest profile variations. In addition the fits deliver more stable results, whereas the SD tends to produce larger fluctuations.

Another point is the coincidence of small series of a few profiles, which form a pattern in each of the three models (the third profile at 0.53 MV). These consistent patterns indicate the significance of these obtained deviations and they can be excluded as mathematical artifacts due to the analyzing method. It can be assumed that the accelerator itself is the source for these non trend-conform bunch profile variations.

Several times the profile width changes only by a small margin (3 or 4 consecutive profiles), which is not in good agreement with the trend. This series might be a result of the sensitivity of the SGR control unit. Using small step sizes the control deviation is below the threshold to determine a new equilibrium between the control response and the given actual value. This leads to a non-adjusted gap voltage, while acquiring the next measuring point. With further progression the selected voltage jump increases until the control deviation is big enough between selected and given voltage to force a reaction of the control unit. In addition an occasional freezing of the SGR control screen has been observed, indicating a malfunctioning.

Figure 4.33 depicts the profile center for each analysing model. The Gaussian fit and the LND fit deliver quite similar results. The LND fit takes the bunch tail into account, leading to an on average 30 ps delayed bunch center. The standard deviation results in a further delayed bunch center by up to 200 ps. The progression of the bunch center is

also more irregular for the SD than for the two fits. Although there are still agreements between the two fits and the SD (like measuring point 3), the standard deviation shows a more unique shape. On the other hand the two fits show a small shift of the center, while the gap voltage increases until a voltage of  $U = 0.9$  MV. Beyond this value the two fits show a comparable behavior like the SD due to a strong contribution of the bunch tail to the peak structure.

The presence of a non negligible bunch center shift over the course of the measurement indicates an imperfect matching of the SGR10 phase. But the complicated spatial structure of the bunch and more so the presumed momentum structure interfere with the task of a perfect phase match. Nevertheless no anomalies have been detected, underlining the reliability of the obtained data for a longitudinal emittance determination.

### 4.5.3. Parabolic Fit

To determine the longitudinal emittance a mathematical approach is used. Many beam transport codes like TRANSPORT, MAD or MIRCO use linear transformation to calculate the beam properties at a given location. The process can be described by the following matrix:

$$\begin{pmatrix} \sigma_{55}(s_1) & \sigma_{56}(s_1) \\ \sigma_{56}(s_1) & \sigma_{66}(s_1) \end{pmatrix} = \begin{pmatrix} R_{55} & R_{56} \\ R_{65} & R_{66} \end{pmatrix} \cdot \begin{pmatrix} \sigma_{55}(s_0) & \sigma_{56}(s_0) \\ \sigma_{56}(s_0) & \sigma_{66}(s_0) \end{pmatrix} \cdot \begin{pmatrix} R_{55} & R_{56} \\ R_{65} & R_{66} \end{pmatrix}^T \quad (4.5)$$

Where  $\boldsymbol{\sigma}(s_0)$  consists of the longitudinal Twiss Parameters:

$$\alpha(s_0) = -\frac{\sigma_{56}}{\epsilon}, \quad (4.6)$$

$$\beta(s_0) = \frac{\sigma_{55}}{\epsilon}, \quad (4.7)$$

$$\gamma(s_0) = \frac{\sigma_{66}}{\epsilon}, \quad (4.8)$$

defining the incident beam properties at location  $s_0$ ,  $\mathbf{R}$  describes the beam transfer from  $s_0$  to  $s_1$ , which finally yields the outgoing beam properties at  $s_1$ . The beam properties  $\boldsymbol{\sigma}(s_0)$  have to be known as well as the drift  $L$  and focusing properties described by  $\mathbf{R}$  in order to solve the linear equations. If  $\boldsymbol{\sigma}(s_0)$  is not known, it is possible to obtain the beam properties through variation of the beam transportation parameters, like the focusing strength  $K$  of a quadrupole or a buncher and measuring the outgoing corresponding profile width of the beam or bunch.

The measurement of the bunch length  $x_{\text{rms}}$  is inserted into the following equation:

$$x_{\text{rms}}^2(s_1) = \sigma_{55}(s_1) \quad (4.9)$$

$$= L^2 \sigma_{55}(s_0) \cdot K + 2(L\sigma_{56}(s_0) + L^2\sigma_{56}(s_0)) \cdot K + \sigma_{55}(s_0) + 2L\sigma_{56}(s_0) + L^2\sigma_{66}(s_0) \quad (4.10)$$

Equation 4.9 and 4.5 for  $\sigma_{55}(s_1)$  are equal for the thin lens approximation [99].

Equation 4.9 consists of the unknown values of  $\sigma_{55}(s_0)$ ,  $\sigma_{56}(s_0)$  and  $\sigma_{66}(s_0)$ , therefore at least three measurements are necessary to determine  $\sigma(s_0)$ . For higher accuracy and for an error estimation more measurements are recommended.

The obtained redundant system of equations can either be solved by a least square fit or by linear regression, but for a parabola fit the beam waist (location of the parabola fit's vertex) should have been obtained for solving the fit with sufficient precision. The obtained data from chapter 4.5.2 allows the usage of the parabola fit due to the executed measurement of the beam waist for each analyzing model.

For the parabola fit the following expression with the fit parameters  $a, b$  and  $c$  is used:

$$y(K) = a(K - b)^2 + c = aK^2 - 2abK + ab^2 + c \quad (4.11)$$

comparison with equation 4.9 yields:

$$\begin{aligned} a &= L^2\sigma_{55}(s_0) \\ -ab &= L\sigma_{55}(s_0) + L^2\sigma_{56}(s_0) \\ ab^2 + c &= \sigma_{55}(s_0) + 2L\sigma_{56}(s_0) + L^2\sigma_{66}(s_0) \end{aligned}$$

Due to the chosen parameterization of the fit parameters and with a look at equation 4.11 they can be interpreted as:

- Parameter  $a$  corresponds to the parabola gradient.
- Parameter  $b$  is the location of the parabola vertex or beam waist.
- Parameter  $c$  is the offset of the curve from zero.

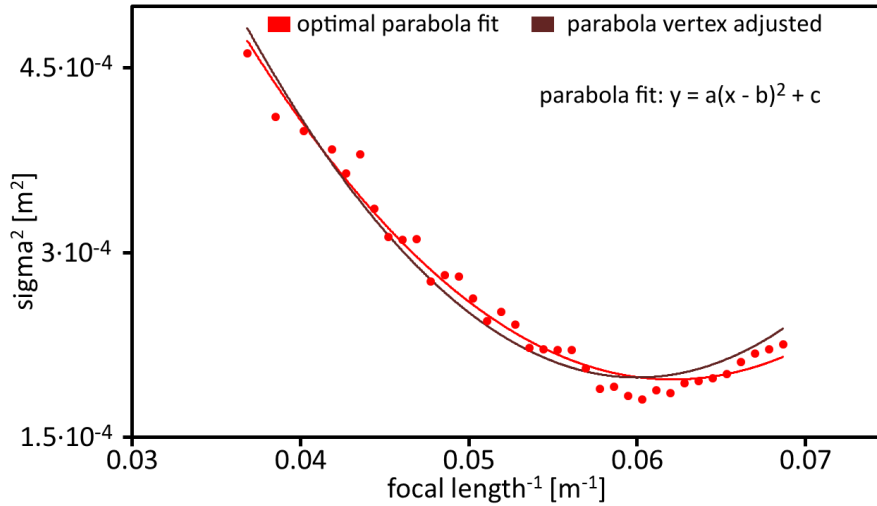


Figure 4.34.: Depicted is the parabola fit for the squared profile widths of the Gaussian fit series from fig. 4.32. For better subsequent analysis all scales are in m or derivatives of m.

The allocation of the parameters to geometric plot characteristics based on the measurements of fig. 4.32 is a big advantage for a stable and reliable solution based on the parabola fit.

Figure 4.34 introduces the squared profile widths  $x_{\text{rms}}^2$  obtained by the Gaussian fit and two corresponding parabola fits. The light red is the least square fit, where the dark red one has a manually fixed vertex position. In order to obtain the emittance in a proper physical dimension all units were represented as a spatial dimension (meter<sup>n</sup>). The fit was executed with OriginPro 9.1™. By obtaining the parameters  $a, b$  and  $c$  the emittance and the matrix elements can be determined as follows:

$$\sigma_{55}(s_0) = \frac{a}{L^2}, \quad (4.12)$$

$$\sigma_{56}(s_0) = -\frac{a}{L^2} \left( \frac{1}{L} + b \right), \quad (4.13)$$

$$\sigma_{66}(s_0) = \frac{1}{L^2} \left( ab^2 + c + \frac{2ab}{L} + \frac{a}{L^2} \right) \text{ and} \quad (4.14)$$

$$\epsilon = \sqrt{\det \boldsymbol{\sigma}(s_0)} = \sqrt{\sigma_{55}(s_0) \sigma_{66}(s_0) - \sigma_{56}^2(s_0)} = \frac{\sqrt{ac}}{L^2} \quad (4.15)$$

The results as well as the errors resulting from fig. 4.34 are summarized in table 4.5.3. Figure 4.35 depicts the least square fit for each analyzing method (Gauss, LND, SD), except for the SD. For the SD parabola fit only a fixed parameter  $b$  has given an acceptable location of the vertex. Taken from table 4.5.3 all three models yield comparable values. As expected both fits for Gauss model result in the smallest values for the emittance within a 10% margin between each other and a fit error of the same magnitude.

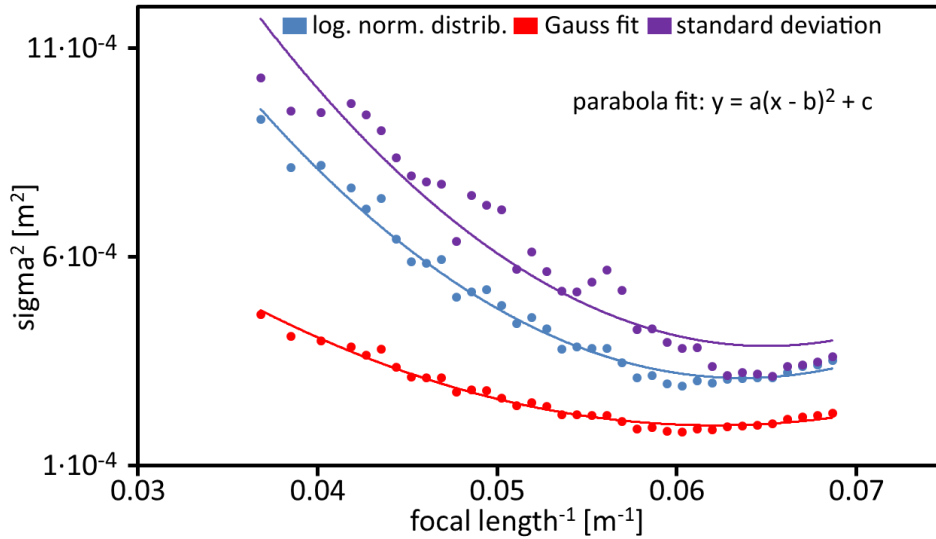


Figure 4.35.: Depicted are the least square fits for LND, Gauss and SD obtained from fig. 4.32.

parameter	Gauss		LND		SD
	best	vertex	best	vertex	vertex
$y = a(x - b)^2 + c$					
a [m <sup>4</sup> ]	0.431	0.529	0.897	1.034	0.988
b [m <sup>-1</sup> ]	0.062	0.060	0.064	0.062	0.065
c [m <sup>2</sup> ]	$1.97 \cdot 10^{-4}$	$1.98 \cdot 10^{-4}$	$3.10 \cdot 10^{-4}$	$3.16 \cdot 10^{-4}$	$3.87 \cdot 10^{-4}$
adj. $\chi^2$	$1.40 \cdot 10^{-10}$	$2.20 \cdot 10^{-10}$	$6.10 \cdot 10^{-10}$	$7.35 \cdot 10^{-10}$	$4.28 \cdot 10^{-9}$
fit errors					
a [m <sup>4</sup> ]	0.026	0.018	0.054	0.027	0.050
b [m <sup>-1</sup> ]	$5.8 \cdot 10^{-4}$	0	$6.7 \cdot 10^{-4}$	0	0
c [m <sup>2</sup> ]	$2.71 \cdot 10^{-6}$	$3.34 \cdot 10^{-6}$	$6.31 \cdot 10^{-6}$	$5.95 \cdot 10^{-6}$	$1.59 \cdot 10^{-5}$
results					
$\epsilon$ [keV/u ns]	$1.42 \pm 0.14$	$1.61 \pm 0.19$	$2.61 \pm 0.28$	$2.84 \pm 0.28$	$3.0 \pm 0.33$
$l_{s0}$ [ps]	$255 \pm 28$	$283 \pm 27$	$368 \pm 40$	$395 \pm 37$	$386 \pm 40$
$\Delta E/E$ [keV/u]	$22.5 \pm 2.7$	$24.2 \pm 2.8$	$32.8 \pm 3.9$	$34.4 \pm 4.0$	$35.1 \pm 4.1$

#### 4.5.4. Emittance Measurements Conclusion

The results for the emittance determination based on the bunch profile analyzing model vary between 1.42 keV/u ns for the Gaussian fit data and 3.0 keV/u ns for the standard deviation based data. All these values miss a reference value of  $\sim 0.85$  keV/u ns [100]. But the reference value is a mere approximation due to the small comparability of the two completely different beam setups. Therefore the obtained values seem reasonable for a first estimation.

The errors resulting from the fit are in the range of 10% of the total value for all five parabolic fits, where the Gaussian fit based data delivers the smallest absolute values, as well as the smallest fit errors. This is highly expected due to the omission of the bunch tail by the Gaussian fit model. But it is also clear that the obtained emittance is not valid for the whole beam. Of more importance is the error obtained through the invalid use of a Gaussian fit for non-Gaussian bunch profiles. The bigger emittance values for the other models give a good approximation of the obtained systematic error. An error of almost plus 100% seems possible, if the emittance value determined by the SD model is considered.

Nevertheless the presented results were obtained with only little beam preparation, due to low priority and little time. With an optimized beam profile an emittance determination as shown above will provide more reliable results.

# 5. Particle Tracking Simulations

Although comprehensive knowledge has been gathered about the BSM, some important quantities are non-accessible by experimental means, such as the longitudinal propagation pattern of the SEs in the interior of the device. Furthermore the SE distribution on the MCP Detector surface reveals considerable shifts in its center of gravity which are not expected or accessible to manipulations of the BSM parameters. With the design of a detailed finite-element model, these occurrences can be investigated and unexpected crosstalk or misalignment of the BSM sections can be investigated.

## 5.1. The AMaze Modules

The AMaze 3D [101] finite-elements software is a modular script based program with an optional user interface to solve static field distributions and track particles in three or two dimensions.

The AMaze 3D software is separated in several modules: Geometer [102] and MetaMesh [102] for mesh creation which provides the finite-element structure, the HiPhi [103] static solver for electric fields and the OmniTrack [104] particle tracker which imports or creates a particle distribution and tracks the trajectories through the simulation volume with respect to acting forces and the geometric boundaries.

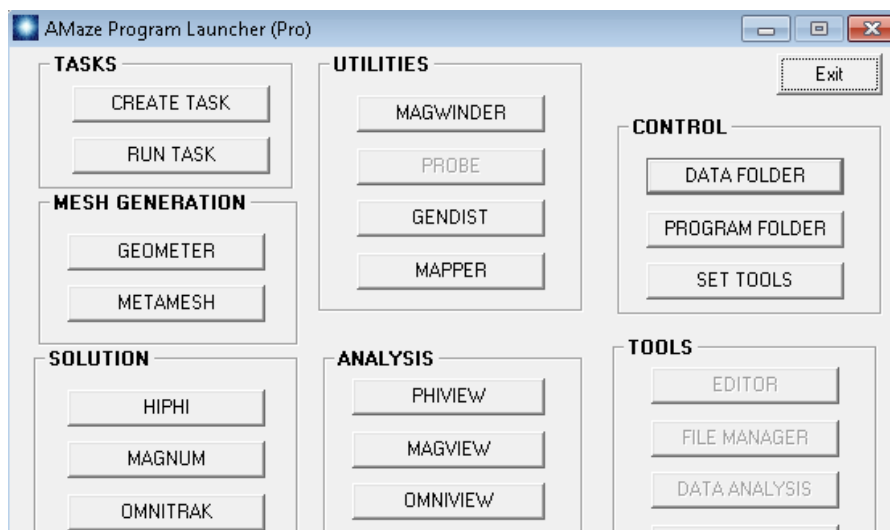


Figure 5.1.: Screen shot of the AMaze selection screen for the different modules.

### 5.1.1. Geometer and MetaMesh

As the AMaze program uses finite-elements the user has to import or create a raw file with the spatial information of all the geometric parts taken into account for the future field distribution and particle tracking operation. If a 3D model [105] of the device is available it can be imported. However, due to its level of detail, like screw holes or small pins, it is too time-consuming even for high performance computer to create a mesh file with the desired smoothness in foresight to the HiPhi field solver.

The available 3D model was used as a template for a new file created with the AMaze utility Geometer which is reduced to its fundamental geometric shapes. Figure 5.2 shows a visualization of the source file which will be used to create the finite-elements file. Each element of the 3D model which will be assigned to a specific electric potential, has to be a separate object of the model, indicated by the different colors. The well known side strips (see sec. 3.3.2) of the Field-Box are a good example for this color coding.

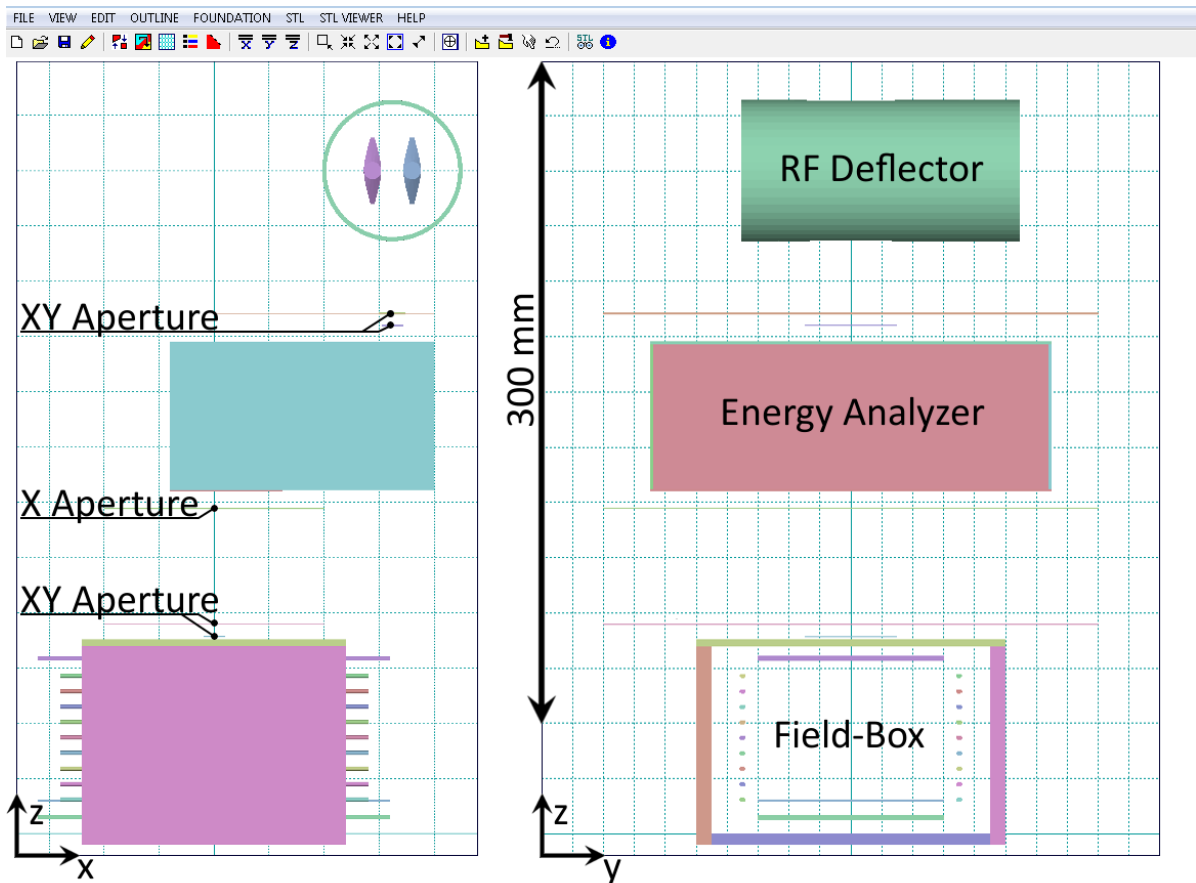


Figure 5.2.: Screen shot of the for MetaMesh designed 3D model created by the AMaze utility Geometer.



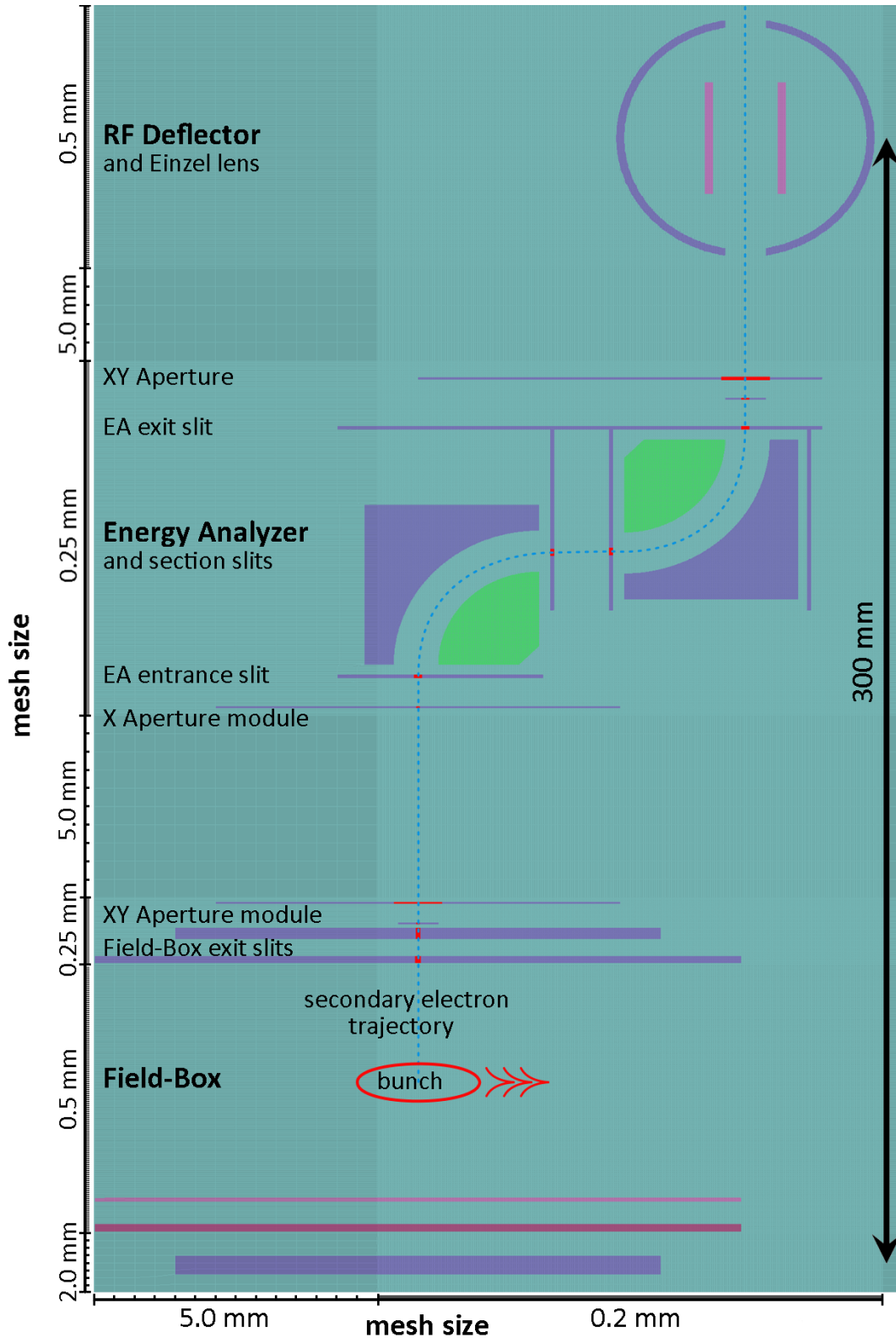


Figure 5.3.: Cross section of the MetaMesh finite-elements model of the BSM. The red areas indicate apertures within the different sections for the SE trajectory. The presented model has a 1.0 mm X Aperture and 10 mm Y Aperture setup. The mesh size is varied as indicated by the scales.

The challenge in creating a discrete model of a real object is to align the edges of the object with the model, where it is crucial, like the small X Apertures of the BSM. A good as possible match is pursued for reliable results in the subsequent tracking mode. For a small mesh size this is not an issue, but typically a global mesh size in sub mm range will blow up the computational effort to an unacceptable limit. The consequence is to keep the mesh size as big as possible and adjust it, where a higher level of detail is necessary. This may need some iteration steps to succeed. The adjusted mesh sizes are displayed in fig. 5.3.

Afterwards the MetaMesh model is checked for its accuracy. If everything is in agreement with the requirements, the model is ready for the HiPhi field solver. The displayed finite-elements model consists of extensive 57.492.384 element cells.

### 5.1.2. HiPhi

HiPhi is capable of calculating electrostatic fields in 3D systems either as dielectric or conductive solutions (see [103]). The HiPhi solver has many abilities:

- using conformal hexahedron meshes
- using unique structured submeshes, allowing multi CPU calculations
- dynamic memory allocation, allowing a large number of mesh cells (> 100 million)

For this thesis the dielectric solver is used, meaning that all objects in the code are considered as ideal dielectrics (zero conductivity). The fields are given by the Poisson equation

$$\nabla \cdot (\epsilon_r \nabla \phi) = -\frac{\rho}{\epsilon_0}, \quad (5.1)$$

where  $\phi$  is the potential,  $\rho$  is the space charge density (for static case e.g.  $\rho = 0$ ),  $\epsilon_r$  is the relative permittivity and  $\epsilon_0$  the electric constant. HiPhi will solve the Poisson equation for each node in the mesh system and will compare it to an approximation based on the neighbor nodes. The difference is called residuum. To obtain a reliable numeric approximation of the real field distribution the residuum has to be minimized.

To calculate the field solution, first the earlier created mesh file has to be selected. Then the utility screen opens, where the most important parameters can be adjusted (see fig. 5.4).

- DUNIT determines the dimension of the basic geometric unit and has to be the same as in the mesh file (here mm).
- MAXCYCLE determines the maximum amount of iterative calculations before the program stops, if the preset residuum is not reached.
- RESTARTGET determines the desired calculation residuum, averaged over the whole mesh. It can be considered as a numerical error. For reliable results  $< 1 \cdot 10^{-6}$  is recommended.

- OMEGA is the over-relaxation factor used to correct potential errors during the calculation. If not assigned, HiPhi automatically picks values which vary per iteration cycle following the Chebyshev's inequality [106].
- BOUNDARY determines the boundary condition [107] at the edge of the mesh. If not assigned, the default is opened boundary condition.
- SUPERPOSITION is used to scale the interpolation factor between two HiPhi solution files. Default setting is off.
- REGION PROPERTIES determine whether the region has a potential, is vacuum (apertures for instance), an electric conductor or has a space charge density. Only one property per region may be assigned. Most regions have an assigned potential or are grounded. The simulation volume is a region of itself.

The utility program creates the used command script. By opening the script file advanced commands can be inserted or the file can be checked.

The left side of fig. 5.5 shows the input script for the HiPhi calculations. More information can be obtained from the script file such as the name of the mesh file (BSM10Spalt) or the DUnit in the chosen scale ( $1 \cdot 10^3$  mm = 1 m). The Parallel

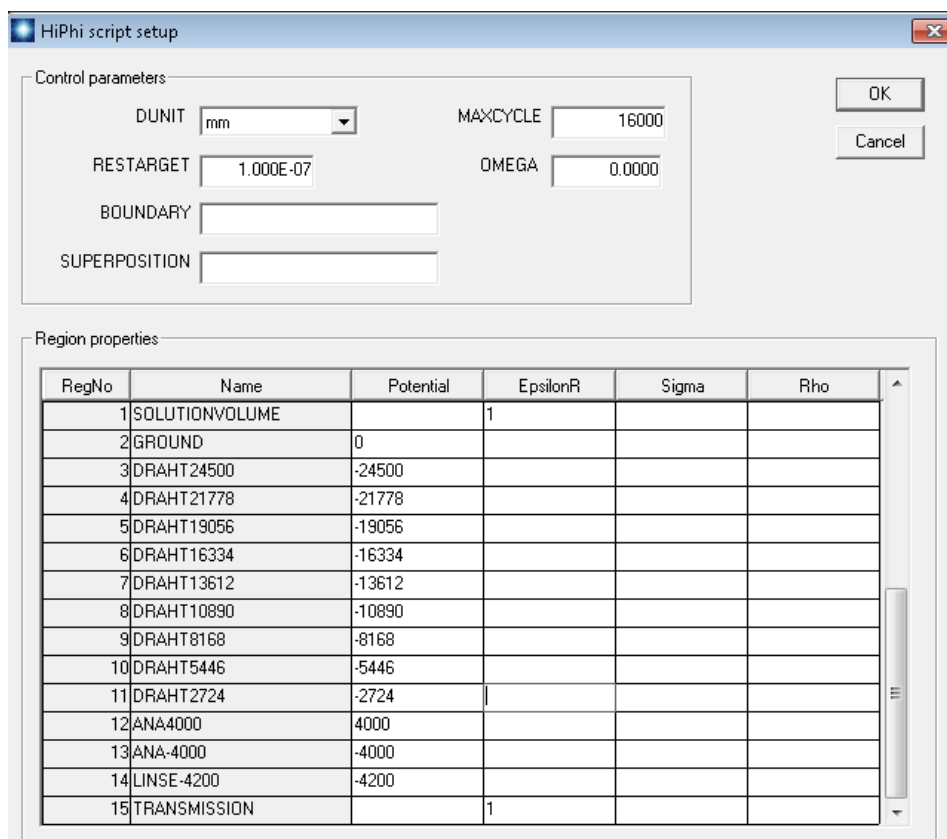
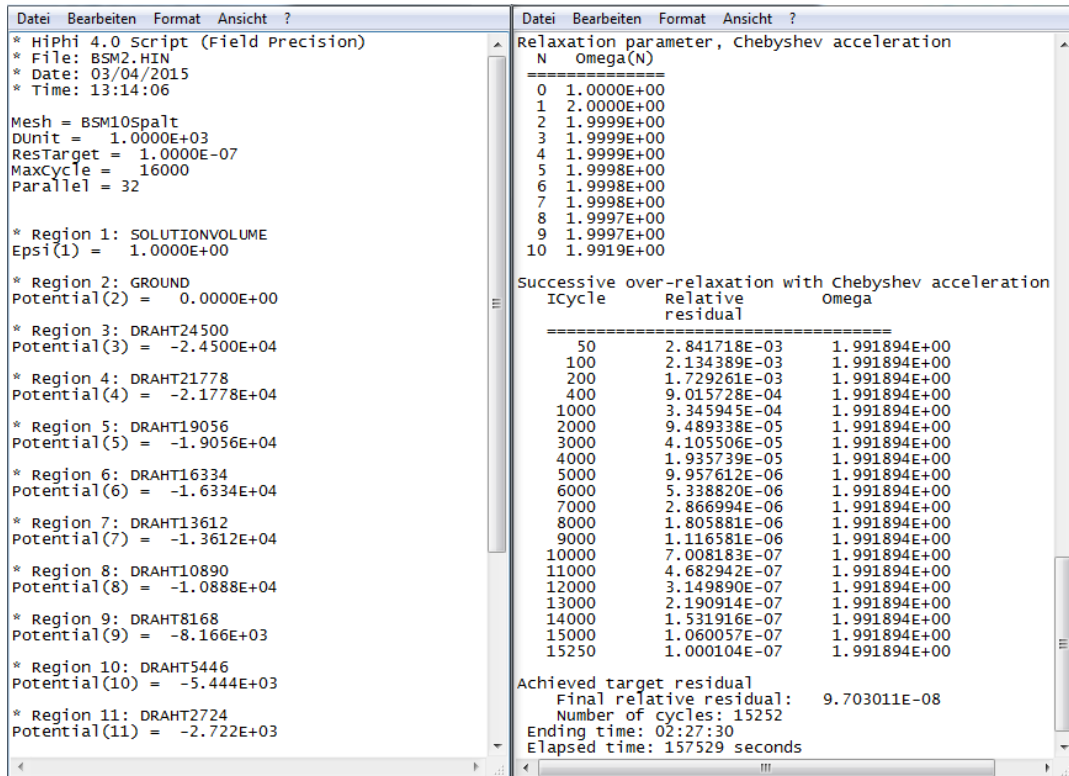


Figure 5.4.: Screen shot of the HiPhi utility program to create the input script file.



```

Datei Bearbeiten Format Ansicht ?
* HiPhi 4.0 Script (Field Precision)
* File: BSM2.HIN
* Date: 03/04/2015
* Time: 13:14:06

Mesh = BSM10Spalt
Dunit = 1.0000E+03
ResTarget = 1.0000E-07
MaxCycle = 16000
Parallel = 32

* Region 1: SOLUTIONVOLUME
Epsi(1) = 1.0000E+00

* Region 2: GROUND
Potential(2) = 0.0000E+00

* Region 3: DRAHT24500
Potential(3) = -2.4500E+04

* Region 4: DRAHT1778
Potential(4) = -2.1778E+04

* Region 5: DRAHT19056
Potential(5) = -1.9056E+04

* Region 6: DRAHT16334
Potential(6) = -1.6334E+04

* Region 7: DRAHT13612
Potential(7) = -1.3612E+04

* Region 8: DRAHT10890
Potential(8) = -1.0888E+04

* Region 9: DRAHT8168
Potential(9) = -8.166E+03

* Region 10: DRAHT5446
Potential(10) = -5.444E+03

* Region 11: DRAHT2724
Potential(11) = -2.722E+03

Relaxation parameter, Chebyshev acceleration
N Omega(N)
-----
0 1.0000E+00
1 2.0000E+00
2 1.9999E+00
3 1.9999E+00
4 1.9999E+00
5 1.9998E+00
6 1.9998E+00
7 1.9998E+00
8 1.9997E+00
9 1.9997E+00
10 1.9919E+00

Successive over-relaxation with Chebyshev acceleration
Icycle Relative residual omega
-----
50 2.841718E-03 1.991894E+00
100 2.134389E-03 1.991894E+00
200 1.729261E-03 1.991894E+00
400 9.015728E-04 1.991894E+00
1000 3.345945E-04 1.991894E+00
2000 9.489338E-05 1.991894E+00
3000 4.105506E-05 1.991894E+00
4000 1.935739E-05 1.991894E+00
5000 9.957612E-06 1.991894E+00
6000 5.338820E-06 1.991894E+00
7000 2.866994E-06 1.991894E+00
8000 1.805881E-06 1.991894E+00
9000 1.116581E-06 1.991894E+00
10000 7.008183E-07 1.991894E+00
11000 4.682942E-07 1.991894E+00
12000 3.149890E-07 1.991894E+00
13000 2.190914E-07 1.991894E+00
14000 1.531916E-07 1.991894E+00
15000 1.060057E-07 1.991894E+00
15250 1.000104E-07 1.991894E+00

Achieved target residual
Final relative residual: 9.703011E-08
Number of cycles: 15252
Ending time: 02:27:30
Elapsed time: 157529 seconds

```

Figure 5.5.: Screen shot of the for HiPhi script input (left) and log (right) file with information about the calculation process.

command is an advanced command which allocates 32 CPUs to the calculation which decreases the amount of time by a factor of ten. There are several more commands which can be found in the HiPhi manual [103].

The right side of fig 5.5 shows the log file of the HiPhi calculation. For the first ten steps the Omega parameter is displayed. In the columns below the progress for an even number of iteration is displayed as well as the automatically chosen Omega. The calculation either stops for a sufficient small residual or if the maximum cycles are reached (preset 16000). After 15252 cycles and almost 44 hours, the residual target is reached with  $9.7 \cdot 10^{-8}$ .

If there is no sophisticated mesh file used (no extensive details and smart choice of mesh size), the necessary amount of cycles can easily increase tenfold, which is not acceptable any longer in order to investigate several different settings within a matter of weeks. A less restrictive residual target is not an option either. These results have high numeric errors (residual  $\sim 1 \cdot 10^{-4}$  for 20.000 cycles) leading to field distributions which are wrong. The obtained field distribution will be discussed in a subsequent section.

### 5.1.3. OmniTrack

OmniTrack is a comprehensive 3D simulation software for charged-particle optics, such as particle accelerators, ion sources, microwave sources, electrostatic and magnetostatic lenses [104]. The results can be displayed in 2D or 3D with the optional post processing. The following features are included:

- combine different calculated fields in one 3D file
- precise interpolation to planes and material surfaces for lens investigation
- standardized particle file format (txt format) which allows easy creation and alteration of particle input files
- 2D and 3D orbit representation
- particle filtering by charge, mass position or energy for the result representation
- easy export of the results for further use with optional software
- OmniTrack can track particles even outside the given HiPhi solution volume by using a Ballistic Mode [104] for drift calculations if the bigger volume is defined.

By using OmniTrack again a utility program is used to create the script file (see fig. 5.6). In the script file additional information can be obtained, like the integration time (Dt: 1E-12, 1 ps) or the solution volume boundaries in mm (−120, −100, −10) (90, 100, 300). For figure 5.7 the particle tracking is terminated at the center of the Einzel lens at  $z = 300$  mm, although the particles do not hit an obstacle.

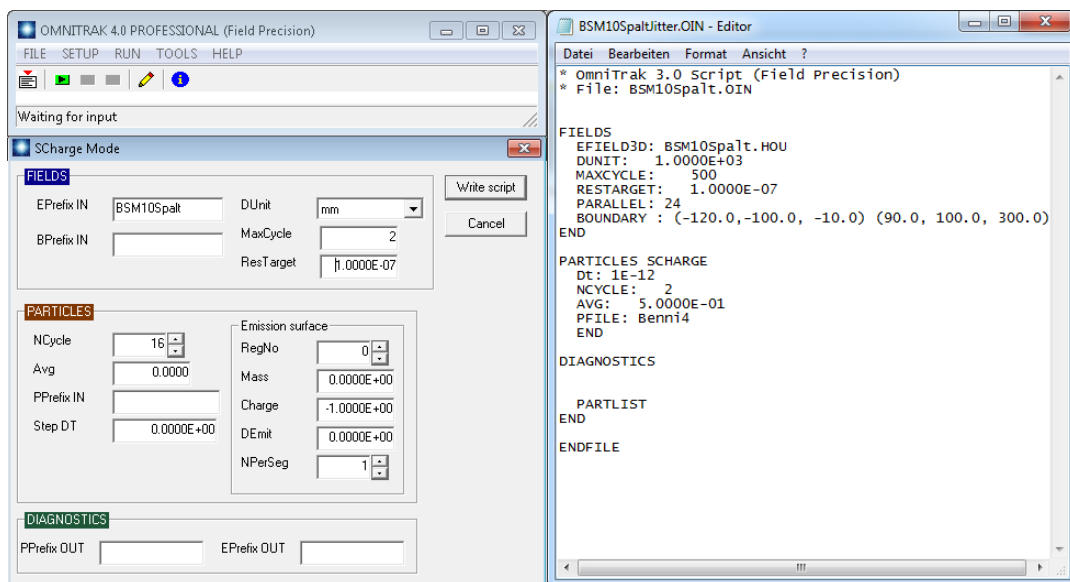


Figure 5.6.: Screen shot of the OmniTrack utility programm (left) and the script file (right) used as input.

```

Datei Bearbeiten Format Ansicht ?
Boundaries for orbit integrations
(User defined values)
  XMin: -1.200000E+02  XMax:  9.000000E+01
  YMin: -1.000000E+02  YMax:  1.000000E+02
  ZMin: -1.000000E+01  ZMax:  8.800000E+02
Line 13:
Line 14: PARTICLES SCHARGE

===== START PARTICLES SECTION =====

----- Reading commands -----
Line 15:  Dt: 1E-12
Line 16:  NCYCLE:  2
Line 17:  AVG:   5.0000E-01
Line 18:  PFILE: Benni4
0 -1 0 -0.138 -4.2923 49.3505 0 0 1 1e-11
0 -1 0 -0.1136 2.0428 49.7779 0 0 1 1e-11
0 -1 0 -0.0464 1.1008 49.4212 0 0 1 1e-11
0 -1 0  0.0816 -2.0379 49.3278 0 0 1 1e-11
0 -1 0  0.0248 1.9026 49.5225 0 0 1 1e-11
0 -1 0 -0.0959 4.3154 49.5249 0 0 1 1e-11
0 -1 0  0.0032 -4.4967 49.5426 0 0 1 1e-11
0 -1 0 -0.0172 2.134 49.5675 0 0 1 1e-11
0 -1 0  0.062 0.1707 49.6617 0 0 1 1e-11
0 -1 0 -0.0607 -2.9061 49.4096 0 0 1 1e-11
0 -1 0 -0.0417 -4.191 49.3307 0 0 1 1e-11
0 -1 0 -0.0769 -1.9235 49.395 0 0 1 1e-11
0 -1 0 -0.0415 0.7651 49.6972 0 0 1 1e-11
0 -1 0 -0.0827 3.4554 49.7929 0 0 1 1e-11
0 -1 0 -0.0004 2.3758 49.768 0 0 1 1e-11
0 -1 0  0.1904 2.7007 49.3287 0 0 1 1e-11
0 -1 0  0.0953 3.316 49.6353 0 0 1 1e-11
0 -1 0 -0.1096 -1.7211 49.7008 0 0 1 1e-11
0 -1 0  0.1474 4.0876 49.3158 0 0 1 1e-11
0 -1 0  0.0154 -4.1621 49.704 0 0 1 1e-11
0 -1 0 -0.0972 -2.8171 49.3798 0 0 1 1e-11
0 -1 0 -0.1754 4.0279 49.305 0 0 1 1e-11
0 -1 0 -0.1289 -4.3876 49.726 0 0 1 1e-11
0 -1 0 -0.0275 -3.7969 49.4598 0 0 1 1e-11
0 -1 0  0.2462 -1.5047 49.7085 0 0 1 1e-11
0 -1 0 -0.1754 -0.5802 49.3108 0 0 1 1e-11
0 -1 0 -0.0844 0.7247 49.4111 0 0 1 1e-11
0 -1 0  0.1032 -4.6207 49.74 0 0 1 1e-11

```

Figure 5.7.: Screen shot of the OmniTrack log file. The first 28 of 1000 particles are shown.

The solution volume can also be extended over the limits of the field solution to track particles which have a long drift to a remote location. This feature is very useful to keep the field simulation detailed where it is necessary and still track the particles over a longer course. The assumed focal length of the electrostatic lens is about 550 mm. The solution volume has a total length of 420 mm in the same direction, where the lens is located at position  $z = 300$  mm. Therefore providing a field solution for the whole volume would blow up the calculation effort by a factor of three. On the other hand, at a distance at about the lens diameter the electron trajectory is almost free of any force.

The compound approach has an acceptable accuracy and saves a lot of calculation time.

For the BSM simulation an external simple particle distribution is used. For a quick and reliable investigation of the ion optics of the BSM randomly distributed initial particles are used with no kinetic energy. An extract of the 1000 particles can be observed in the OmniTrack log file depicted in fig. 5.7 after line 18.

- The first column shows the particle mass (0 indicates electron).
- The second column determines the charge ( $-1$  means  $1 e$ ).
- The third column determines the initial kinetic energy in eV (0, no kinetic energy).
- The next three columns determine the initial  $x$ ,  $y$  and  $z$  coordinates in mm. Note that the initial volume has an edge length of  $0.6 \text{ mm} \times 10 \text{ mm} \times 0.5 \text{ mm}$ .
- Another three columns determine the relative momentum in  $x$ ,  $y$  and  $z$  direction. The program expects a non-zero ratio (here 0, 0, 1), but with no kinetic energy the initial momentum is still zero.

Line 24: PARTLIST

Particle Tables - Initial and Final Parameters

Position Table								
No	xi	yi	zi	xf	yf	zf	Time	Distance
1	-1.380000E-01	-4.292300E+00	4.935050E+01	-8.551734E+01	-5.204479E+00	3.000000E+02	5.463854E-09	3.044628E+02
2	-1.136000E-01	2.042800E+00	4.977790E+01	-8.158525E+01	2.386585E+00	3.000000E+02	5.497114E-09	3.042063E+02
3	-4.640000E-02	1.100800E+00	4.942120E+01	-8.367191E+01	1.262979E+00	3.000000E+02	5.485364E-09	3.049258E+02
4	8.160000E-02	-2.037900E+00	4.932780E+01	-8.232701E+01	-2.501867E+00	3.000000E+02	5.505053E-09	3.058345E+02
5	2.480000E-02	1.902600E+00	4.952250E+01	-8.155613E+01	2.229092E+00	3.000000E+02	5.507495E-09	3.053065E+02
6	-9.590000E-02	4.315400E+00	4.952490E+01	-8.343042E+01	5.130925E+00	3.000000E+02	5.483754E-09	3.045405E+02
7	3.200000E-03	-4.496700E+00	4.954260E+01	-8.166185E+01	-5.506112E+00	3.000000E+02	5.504066E-09	3.051596E+02
8	-1.720000E-02	2.134000E+00	4.956750E+01	-8.186741E+01	2.502556E+00	3.000000E+02	5.501538E-09	3.049850E+02
9	6.200000E-02	1.707000E-01	4.966170E+01	-7.964950E+01	1.455489E-01	3.000000E+02	5.526222E-09	3.054761E+02
10	-6.070000E-02	-2.906100E+00	4.940960E+01	-8.391605E+01	-3.547448E+00	3.000000E+02	5.481839E-09	3.048555E+02
11	-4.170000E-02	-4.191000E+00	4.933070E+01	-8.423177E+01	-5.108118E+00	3.000000E+02	5.480371E-09	3.050431E+02
12	-7.690000E-02	-1.923500E+00	4.939500E+01	-8.431597E+01	-2.355216E+00	3.000000E+02	5.477941E-09	3.047742E+02
13	-4.150000E-02	7.651000E-01	4.969720E+01	-8.108991E+01	8.695674E-01	3.000000E+02	5.506003E-09	3.047286E+02
14	-8.270000E-02	3.455400E+00	4.979290E+01	-8.087156E+01	4.093708E+00	3.000000E+02	5.505275E-09	3.044080E+02
15	-4.000000E-04	2.375800E+00	4.976800E+01	-7.972379E+01	2.794467E+00	3.000000E+02	5.521083E-09	3.049729E+02
16	1.904000E-01	2.700700E+00	4.932870E+01	-8.046173E+01	3.192344E+00	3.000000E+02	5.528796E-09	3.065617E+02
17	9.530000E-02	3.316000E+00	4.963530E+01	-7.921194E+01	3.928487E+00	3.000000E+02	5.532963E-09	3.057453E+02
18	-1.096000E-01	-1.721100E+00	4.970080E+01	-8.217105E+01	-2.127264E+00	3.000000E+02	5.492261E-09	3.042987E+02
19	1.474000E-01	4.087600E+00	4.931580E+01	-8.134995E+01	4.869230E+00	3.000000E+02	5.518237E-09	3.062690E+02
20	1.540000E-02	-4.162100E+00	4.970400E+01	-7.998737E+01	-5.092480E+00	3.000000E+02	5.519226E-09	3.051348E+02

Momentum Table								
No	px1/moc	py1/moc	pz1/moc	Tf(ev)	pxf/moc	pyf/moc	pzf/moc	Tf(ev)
1	0.000000E+00	0.000000E+00	0.000000E+00	0.000000E+00	-3.127268E-03	-3.141109E-03	1.645569E-01	6.877517E+03
2	0.000000E+00	0.000000E+00	0.000000E+00	0.000000E+00	-1.215791E-03	2.500106E-04	1.629486E-01	6.740142E+03
3	0.000000E+00	0.000000E+00	0.000000E+00	0.000000E+00	-2.406692E-03	-2.058403E-04	1.644133E-01	6.862127E+03
4	0.000000E+00	0.000000E+00	0.000000E+00	0.000000E+00	-5.673143E-04	-2.042998E-03	1.651748E-01	6.925064E+03
5	0.000000E+00	0.000000E+00	0.000000E+00	0.000000E+00	-4.520574E-04	1.800693E-04	1.641386E-01	6.837958E+03
6	0.000000E+00	0.000000E+00	0.000000E+00	0.000000E+00	-2.434213E-03	1.491905E-03	1.638811E-01	6.818663E+03
7	0.000000E+00	0.000000E+00	0.000000E+00	0.000000E+00	-4.749377E-04	-4.115918E-03	1.644509E-01	6.868105E+03
8	0.000000E+00	0.000000E+00	0.000000E+00	0.000000E+00	-8.662811E-04	3.104889E-04	1.639128E-01	6.819439E+03
9	0.000000E+00	0.000000E+00	0.000000E+00	0.000000E+00	1.095886E-03	-7.444509E-04	1.634978E-01	6.785409E+03
10	0.000000E+00	0.000000E+00	0.000000E+00	0.000000E+00	-2.237895E-03	-2.493336E-03	1.646072E-01	6.879570E+03
11	0.000000E+00	0.000000E+00	0.000000E+00	0.000000E+00	-2.020746E-03	-3.434407E-03	1.649964E-01	6.913079E+03
12	0.000000E+00	0.000000E+00	0.000000E+00	0.000000E+00	-2.744008E-03	-1.777128E-03	1.645207E-01	6.872255E+03
13	0.000000E+00	0.000000E+00	0.000000E+00	0.000000E+00	-3.873920E-04	-3.929164E-04	1.633684E-01	6.774373E+03
14	0.000000E+00	0.000000E+00	0.000000E+00	0.000000E+00	-4.628667E-04	1.047228E-03	1.628495E-01	6.731939E+03
15	0.000000E+00	0.000000E+00	0.000000E+00	0.000000E+00	7.421518E-04	4.512943E-04	1.629194E-01	6.737547E+03
16	0.000000E+00	0.000000E+00	0.000000E+00	0.000000E+00	1.265808E-03	6.025425E-04	1.650131E-01	6.910964E+03
17	0.000000E+00	0.000000E+00	0.000000E+00	0.000000E+00	1.623359E-03	9.542779E-04	1.634612E-01	6.782842E+03
18	0.000000E+00	0.000000E+00	0.000000E+00	0.000000E+00	-1.504910E-03	-1.888177E-03	1.634279E-01	6.780672E+03
19	0.000000E+00	0.000000E+00	0.000000E+00	0.000000E+00	3.463032E-04	1.399651E-03	1.650633E-01	6.915172E+03
20	0.000000E+00	0.000000E+00	0.000000E+00	0.000000E+00	4.208246E-04	-3.797233E-03	1.636284E-01	6.799413E+03

Figure 5.8.: Picture of the tabular formatting particle diagnostic output in the OmniTrack log file. Note: all particles are terminated latest at  $z_f = 300 \text{ mm}$ .

- The last column determines the current in A. For small values the program tracks every particle only once with these parameters.

The trajectories can be observed with OmniView. If the command Partlist [104] is used in the script file, OmniTrack will create additional output in the log file concerning the initial coordinates ( $x_i$ ,  $y_i$  and  $z_i$ ) and final coordinates ( $x_f$ ,  $y_f$  and  $z_f$ ) of each particle and the initial and final momenta in a tabular formatting similar to the particle distribution.

## 5.2. Particle Tracking

The preceding section presented the capabilities and details of the AMaze program. Concerning numeric errors, a precise implementation of the simulation was achieved and should yield reliable results. The numeric residual is a factor of 10 higher than recommended (see 5.1.2). The alignment of the sections is manually checked and the geometric mesh size is driven at certain locations to 0.2 mm to guarantee smooth field progression within the ion optic sections with bent surfaces. Nevertheless the results have to be checked for anomalies.

The following section will discuss the results obtained with a simple initial electron distribution. The electrons have no kinetic energy at the beginning and are randomly distributed. A different more complex electron distribution will be introduced in a succeeding section.

### 5.2.1. Field Distribution and Cross Talk

The HiPhi field solution file is checked by the OmniView [104] utility for any anomalies. Figure 5.9 shows the color-coded potential plot. For a quick test of the quality of the solution the homogenous electric field within the Field-Box is investigated.

The potential distribution is uniform and smooth within the Field-Box, which can be seen in the even thickness of the potential layers and the absence of any disturbances between the different layers for almost the complete geometric length of the Field-Box. Also, there are only minor potential deviations from zero in the open space above the Field-Box. These observations indicate a reliable field solution obtained by HiPhi, which are also in agreement with CST based calculations of the Field-Box (see 3.3.2).

Most of the path of the SEs is free of a potential outside of the Field-Box. All electric fields out of the ion optic devices are shielded for one exception: the area close to the EA.

The back panels of the outer cylinders of the EA are not separated from the exterior by a housing. Therefore the high voltage applied to these elements strongly affects the surrounding area. The color coding of fig. 5.9 indicates a potential zone of  $\sim -1000$  V (slightly yellow) till the housing of the Field-Box. Also the effect forms an undesired field pattern at the Field-Box exit, see fig. 5.10 for more details. The unshielded other EA cylinder shows a milder behavior, due to its orientation and proximity to the mechanical structure of the second X Aperture. The aperture mount is made of metal and has a



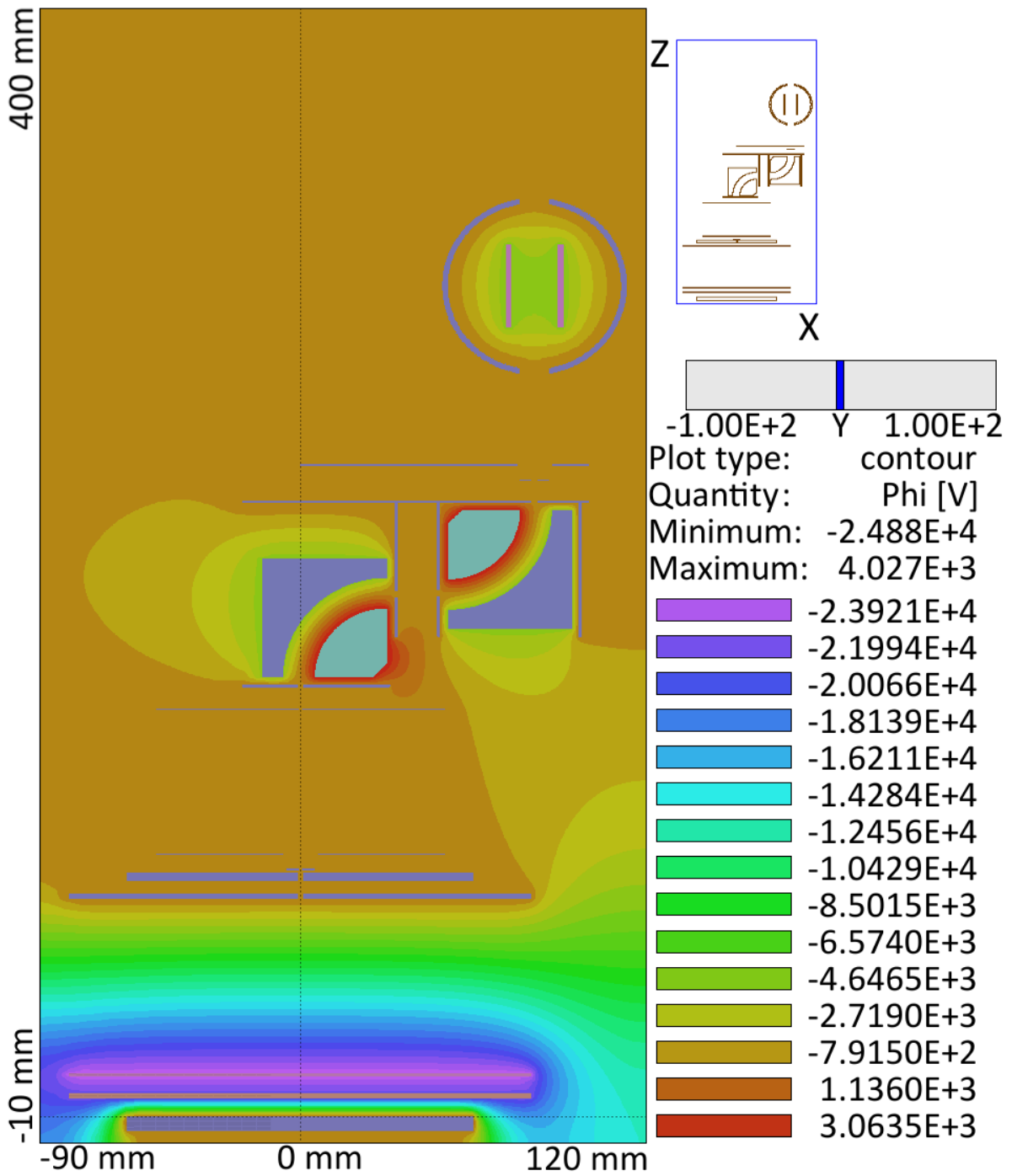


Figure 5.9.: Cross section ( $xz$  plane) of the potential distribution. Different colors indicate the potential level.

significant surface area. Due to the fact that the aperture mount is grounded, it acts as a shielding. Unfortunately, this is only partly the case for the right cylinder element.

It is likely that this field pattern will influence the SE, where the SEs are supposed to drift freely. A second potential plot with rescaled color coding will reveal the magnitude of influence of the unshielded cylinder element. Figure 5.10 depicts a cutout of the preceding field solution with a different scaling. Instead of presenting potentials from  $-24$  kV to  $+4$  kV the plot limit is readjusted from  $-50$  V to  $50$  V. Higher voltages are represented with plain white areas. This rescaling allows a far better judgment of the field pattern close to the electron trajectory (dashed line). With higher details the field pattern is visible. According to the plot, close to the middle between the two apertures, the electron trajectory experiences a potential of  $-30$  V before it drops back to almost zero at the second X Aperture.

This field pattern leads to an applied electric field of about  $2000$  V/m in perpendicular direction of the electron trajectory. Although being only shortly exposed to this field, the electrons will experience a considerable shift in this direction at the MCP Detector, as preliminary experiments showed. Usually the shift is compensated with a voltage

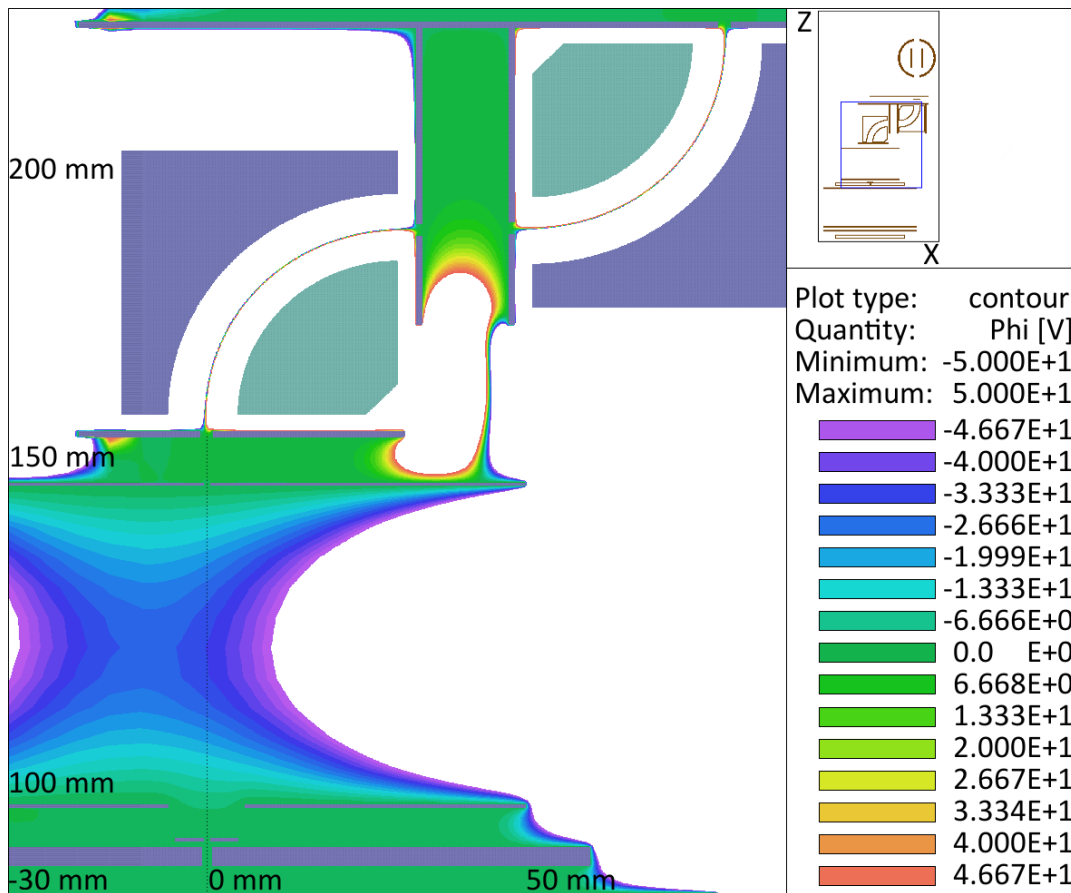


Figure 5.10.: Cutout of fig. 5.9 with rescaling of the displayed potential limits. The dashed line indicates the electron trajectory.

difference applied to the lens pads for electron steering.

Another interesting observation gives the EA (see fig. 5.10). Within the 90° bending a slim path with a potential of zero is formed. The ideal trajectory has to see no potential changes, while passing the EA to maintain the electron beam properties [108]. According to the plot the ideal trajectory is slightly shifted from the center of the entrance slit (see dashed line in fig. 5.10). The same is the case for the exit slit of the EA. The offset is in the range of 0.5 mm. Due to the field pattern of the EA (see sec. 3.3.4), which goes with  $E(r) \propto \frac{1}{r}$ , the field distortion should be small for 0.5 mm deviation and is only detected in the entrance area.

### 5.2.2. SE Trajectories

The preceding section presented the field solution. The next step is to check the actual trajectories plotted in the solution volume for any anomalies.

Figure 5.11 shows the trajectories of one out of ten electrons while traveling through the BSM. The initial electron distribution is a simple ensemble within a volume of  $0.5 \times 10 \times 0.5$  in mm<sup>3</sup> and 1000 electrons are randomly put into the volume. The BSM setting is -24.5 kV applied to the Field-Box and  $\pm 4000$  V applied to the EA. The aperture setup is still 1.0 mm for the X Aperture and  $\pm 10$  mm for the Y Apertures.

The initial coordinates are carefully picked to ensure a high probability for the electrons to get through the BSM to receive a good statistic for later investigations. For the taken distribution of 1000 particles 852 get through. This value of 852 will vary about  $\pm 30$  particles depending on the initial distribution.

The trajectories of the electrons are uniform and compact. Only a few electrons are stopped by the slits and apertures until they reach the EA. Preliminary MIRKO [109] based electron beam calculations showed the presence of two transverse foci within the two 90° bending of the EA [108]. To check this fig. 5.11 provides a closer look to this specific section (blue framed area). The formation of two focuses is clearly visible.

The same MIRKO calculations predicted an inflation of the electron beam divergence after leaving the EA. At the X3 Aperture, 10 mm behind the exit slit of the EA, several electrons are stopped, as the higher divergence is leading to an opening cone towards the electrostatic lens. Approximately at the center of the lens the divergence is compensated and a focused beam is formed.

For the three different X Aperture settings (1.0 mm, 0.6 mm, 0.2 mm) the trajectory shapes are similar, although with a smaller aperture setting, the electron beam is more filtered and an overall more dense image of the trajectories is obtained. This makes it harder to judge the behavior of the electron beam by just looking at the trajectory plot.

Another observation is the stopping of some electrons at the non-adjustable slits between the 90° cylinder segments. These slits are only installed for field forming properties. The dimensions are picked generously (2 mm  $\times$  38 mm) [110] to avoid electron beam loss. The unintended filtering of electrons could limit the beam shaping possibilities for big aperture settings ( $> 0.5$  mm). This phenomenon is not expected by the MIRKO calculations. MIRKO uses a beam envelope representing the particle ensemble which is determined by the aperture setting. This implies that only particles which get through

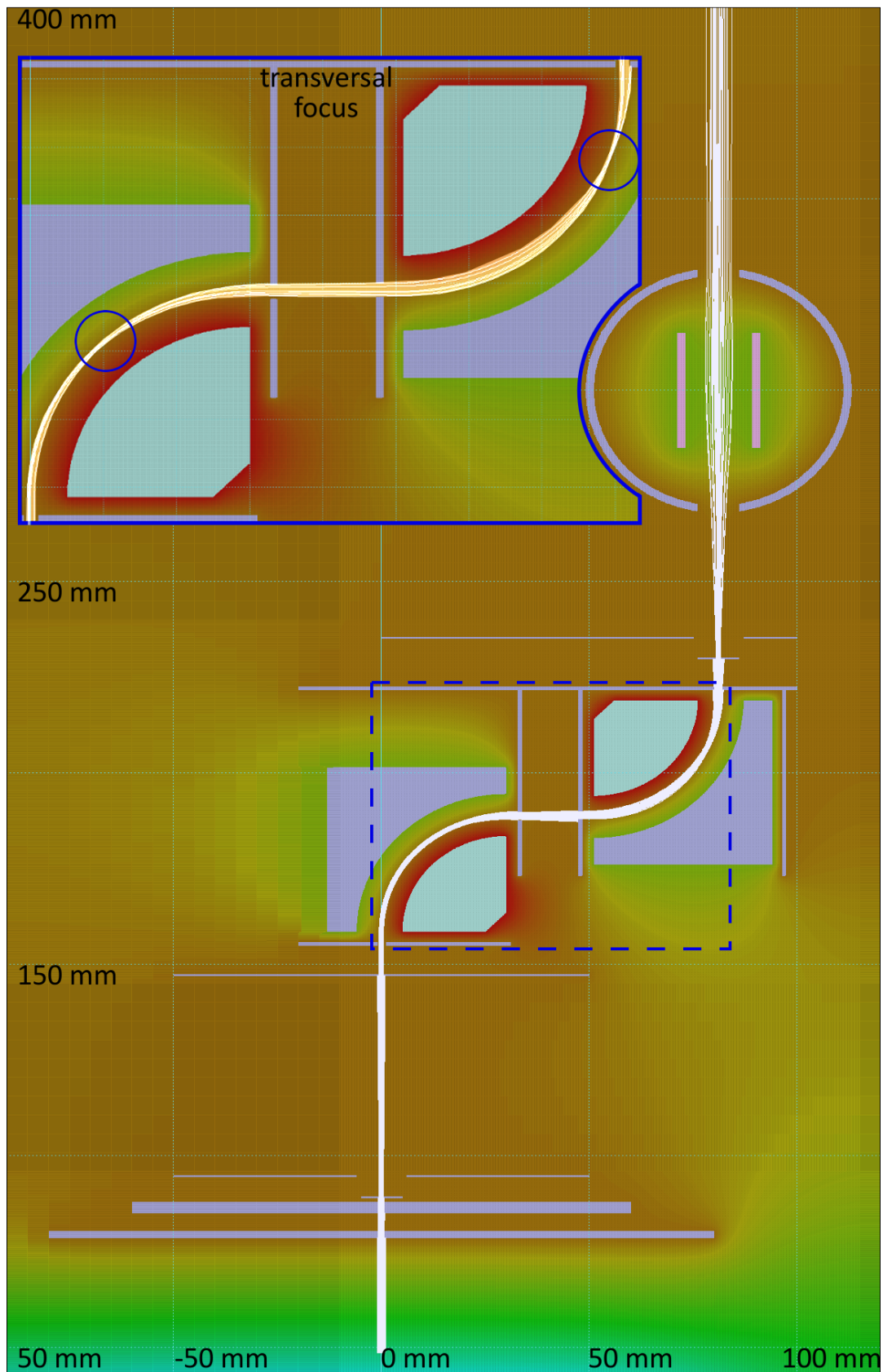


Figure 5.11.: Trajectories of a simple ensemble tracked through the simulation volume. For better orientation the potential solution is also displayed.

will be covered by the calculation. Therefore, a loss of any particle at an unexpected location can not be obtained by MIRKO.

The impact of the unexpected filtering of the slits declines with a smaller aperture setting until it completely vanishes. More important is that no electrons are lost on an active surface (high voltage applied) within the EA or the lens. High energy electrons stopped by a high voltage surface might lead to uncontrolled creation of additional electrons. According to the tracking simulation the BSM design is preventing this.

### 5.2.3. Longitudinal Structure of the Electron Beam

The reason for the simulation is the electron path and its longitudinal structure. Neither of these issues are directly accessible through experimental means.

The longitudinal structure or time structure of the electrons is responsible for a so far not treated reduction of the absolute time resolution of the BSM. Secondary electrons created in the same vertical bunch plane should arrive at the same moment at the RF Deflector. Therefore they should be detected under the same angle of deflection on the MCP Detector. This is the ideal case. In reality the electrons have a time structure while traveling through the BSM and arrive at slightly different time spots at the RF Deflector.

Electrons created on a lower vertical plane (closer to the high voltage bottom plate) have a higher kinetic energy after leaving the Field-Box. Electrons created on a higher vertical plane (closer to the exit slit) have a lower kinetic energy compared to an electron created in the bunch center. In addition, these three samples have to cover different distances to arrive at the RF Deflector, due to a different path through the EA and their initial offset. Past the RF Deflector the time structure is irrelevant, the time information has been converted into a spatial one. All together the time of arrival at the RF Deflector is depending on several parameters.

In order to obtain the time of arrival the electrons are tracked from their starting point till the middle of the RF Deflector. All incoming electrons are terminated here. This investigation was executed for three aperture setups to compare the results which are listed in table 5.1.

Table 5.1.:

X Aperture [mm]	$N$	$x_i$ [mm]	$y_i$ [mm]	$z_i$ [mm]	$\Delta t_\sigma$ [ps]	$\Delta t_{\max}$ [ps]
1.0	23057	$\pm 0.22$	$\pm 8.98$	$\pm 0.67$	$\pm 27.1$	$\pm 128$
0.6	8235	$\pm 0.14$	$\pm 8.98$	$\pm 0.39$	$\pm 16.4$	$\pm 78$
0.2	799	$\pm 0.04$	$\pm 8.93$	$\pm 0.13$	$\pm 5.2$	$\pm 24$

For each aperture setup the amount  $N$  of evaluated particles, the maximum initial range  $x_i$  of the evaluated particles in the X Aperture direction, the maximum initial range  $y_i$  of the particles in the Y Aperture direction, the maximum initial range  $z_i$  of the particles in the potential plane, the RMS value of the time of arrival  $\Delta t_\sigma$  and the

complete time interval  $\Delta t_{\max}$  between the first and last electron arriving are given. The average total run time the electrons take to travel is about  $t_{\text{run}} \approx 5.5$  ns.

For the 1.0 mm setup a rather big time interval of  $\Delta t_{\max} = 128$  ps is obtained. On the other hand the RMS value  $\Delta t_{\sigma}$  is 27.1 ps. This indicates that only a few particles have a large deviation in their time of arrival. The vast majority arrives within a much tighter margin, and therefore with a determined optical resolution of  $> 100$  ps (see sec. 4.1.4) which is not a critical contribution to the total resolution.

For the other aperture setups the pattern remains: a large  $\Delta t_{\max}$  in contrast to a much smaller  $\Delta t_{\sigma}$ . For the 0.2 mm setup  $\Delta t_{\sigma}$  is about 5 ps, which is again not critical compared to the best optical resolution of 37 ps (see sec. 4.1.4). A  $\Delta t_{\sigma} < 5$  ps is even sufficient for future BSM designs with a resolution target of 10 ps.

The  $x_i$ ,  $y_i$  and  $z_i$  results represent the analyzing volume  $xyz$  of the BSM for the given setup. Due to the fixed Y Aperture ( $\pm 10$  mm) the  $y_i$  is not of great interest and only changes only marginally with a different X Aperture setting. This a consequence of the reduced amount of particles and strongly indicates a decoupling of the  $y$  plane from the  $x$  plane.

The BSM acceptance behaves like a step function, therefore the  $x_i$ ,  $y_i$  and  $z_i$  values are min-to-max intervals like  $\Delta t_{\max}$ . For the different X Aperture settings the  $x_i$  quotients of 0.22 mm to 0.14 mm and 0.14 mm to 0.04 mm follow quite exactly the expected values based on the aperture settings (1.0 mm to 0.6 mm, 0.6 mm to 0.2 mm). Also remarkable: for the 0.2 mm setup the  $x_i$  value is below the thickness of the tungsten wire (0.1 mm) used in wire based BSMs. The  $z_i$  values also correspond to the aperture settings.

If the  $\Delta t_{\sigma}$  and  $\Delta t_{\max}$  are compared, both values correspond to the aperture setting, too. Although the time structure has to be determined by particle tracking, the variation through different settings can be predicted.

By simply allocating a potential to the obtained  $z_i$  values an energy acceptance can be determined for the EA for the given setup. The distance between the bottom plate and the top plate of the Field-Box is 68 mm (see sec. 3.3.2) with an applied voltage of  $-24.5$  kV, which corresponds to 360 V/mm. For the different aperture settings one obtains an energy resolution of  $\pm 241$  V,  $\pm 140$  V and  $\pm 48$  V, respectively.

The value  $N$  shows the amount of arriving particles and therefore indicates how the aperture influences the signal intensity. The amount of particles  $N$  follows a  $1/x^2$  relation due to the reduction of the acceptance in  $x$  and  $z$  direction at the same time by only changing the X Aperture setup and confirms the results obtained by measurements (see sec. 4.2.2).

#### 5.2.4. Lens Focusing Properties

The AMaze program allows the tracking of particles even beyond the limits of a provided field solution file. After leaving the geometric borders of the solution file the particles are treated by the ballistic mode, they drift force free until they reach a specified plane for termination. Also it is possible to implement diagnostic planes to obtain information about the particles parameters while crossing the plane.

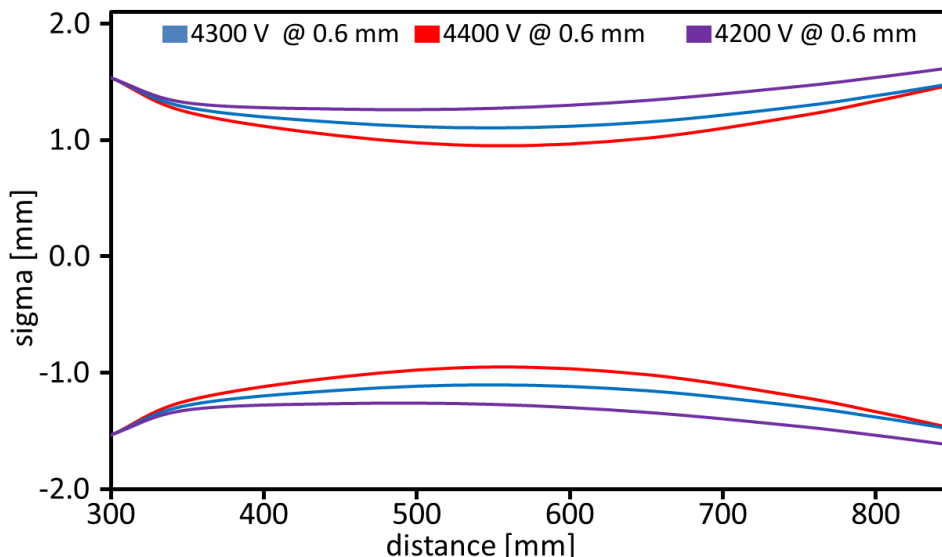


Figure 5.12.: Plot of the RMS envelope of electron beam width in  $x$  direction for different voltage settings of the Einzel lens with 0.6 mm X Aperture setup.

The provided HiPhi solution file covers the area around the Field-Box till the RF Deflector. By using the ballistic mode and diagnostic planes the focusing properties of the electron beam for different aperture settings and applied voltages can be investigated and compared with the experimental results.

Figure 5.12 exemplarily provides the envelope for three different voltages applied to the Einzel lens (4200 V, 4300 V and 4400 V). The plot starts at 300 mm where the center of the Einzel lens in  $z$  direction is located. At position 859 mm the surface of the MCP Detector is located where the particles are terminated and the statistical evaluation of the final  $x$  coordinates yields the focus width. At 300 mm, 350 mm, 450 mm, 650 mm, 750 mm, 800 mm and 830 mm additional diagnostic planes are implemented, providing the necessary  $x$  coordinates of each particle to obtain the beam envelope in the gap between lens and MCP.

Surprisingly no setup is able to adjust the beam waist on the detector. This observation is also persistent for the two other aperture setups. The best result is obtained at 4300 V, with only marginal lesser results for 4200 V and 4400 V. With a closer look at the electron beam progression for the applied voltages the results are checked. For 4400 V the beam envelope is focused stronger and the beam waist is narrowed if compared with the 4300 V setting. For 4200 V only a pseudo beam waist develops close to the lens due to lower focusing strength and boundary effects of the lens. This behavior is expected, if the applied voltage is increased, the focusing strength should increase as well. For even higher potentials the focusing on the MCP gets worse.

Further simulation results as well as the experimental results for different setups are displayed in tab. 5.2. For all results the applied focusing voltage is listed,  $N$  the amount of evaluated particles out of 1000,  $\sigma_{\text{sim}}$  the obtained RMS  $x$  width at the MCP Detector of

the evaluated particles,  $\sigma_{\text{exp}}$  the experimental result for comparison and the full  $x$  range of the calculated particle distribution. The simulation provides systematically smaller RMS  $x$  widths in comparison to the experimental results. One exception are the thick marked  $\sigma_{\text{exp}}$  values, where the experimental results are obtained with a 0.5 mm aperture setting instead of the 0.6 mm of the simulation, due to the lack of experimental results.

Another observation is the stringent shift of the optimal focusing voltage to slightly higher voltages for the simulation results. This occurrence may result out of the use of a simple ensemble which forms a better shaped electron beam, leading to different imaging properties.

Besides the small deviation from the experimental results the simulation is in good accordance with the measurements and demonstrates the utility of the BSM model for detailed investigation of the ion optics of the device. Further investigations (see sec. 5.3) will check the dependance of the results on the initial electron distribution.

Table 5.2.:

X Aperture [mm]	Voltage [V]	$N$	$\sigma_{\text{sim}}$ [mm]	$\sigma_{\text{exp}}$ [mm]	100% (sim.) [mm]
1.0	4200	866	$\pm 2.24$	$\pm 2.39$	$\pm 7.08$
1.0	4300	858	$\pm 2.03$	$\pm 2.99$	$\pm 7.84$
1.0	4400	817	$\pm 2.29$	$\pm 3.47$	$\pm 9.89$
0.6	4200	493	$\pm 1.64$	$\pm \mathbf{1.44}$	$\pm 3.81$
0.6	4300	493	$\pm 1.49$	$\pm \mathbf{1.53}$	$\pm 4.75$
0.6	4400	493	$\pm 1.50$	$\pm \mathbf{1.84}$	$\pm 5.45$
0.2	4200	56	$\pm 0.64$	$\pm 0.72$	$\pm 1.29$
0.2	4300	56	$\pm 0.61$	$\pm 0.79$	$\pm 1.32$
0.2	4400	56	$\pm 0.62$	$\pm 0.92$	$\pm 1.47$

### 5.2.5. Lens Aberrations

The simulation indicates a not optimal operation of the Einzel lens. The initial lens design has foreseen the usage of the lens with 1 mm or smaller pinhole instead of apertures with several millimeters broad gap (Y Aperture setting:  $\pm 10$  mm). Therefore the lens susceptibility for shifts of the  $y$  coordinates will be investigated.

For a detailed investigation a new HiPhi field solution file is created which is dedicated only to the Einzel lens. For the focusing properties the potential distribution of the  $xz$  cross section of the lens is responsible. If the distribution significantly changes with the  $y$  coordinate a non-optimal operation cannot be avoided.

Figure 5.13 depicts the HiPhi solution file for nine different picked  $y$  locations of the  $xz$  cross section. The color coding is identical for each plot. Figure 5.14 depicts the potential values taken from the center of the  $xz$  cross section (indicated by a red dot in each plot) along the  $y$  direction. According to figure 5.14 the potential distribution changes dramatically from the open end of the lens shell ( $y = -15$  mm) to the closed



end ( $y = 15$  mm). At  $y = -15$  mm the Einzel lens potential has a value of  $-3730$  V in contrast to the middle of the lens ( $y = 0$  mm) with about  $-4050$  V. The potential further decreases to a minimum of  $-4080$  V at  $y = 4.3$  mm and at  $y = 15$  mm the potential is still below  $-4040$  V.

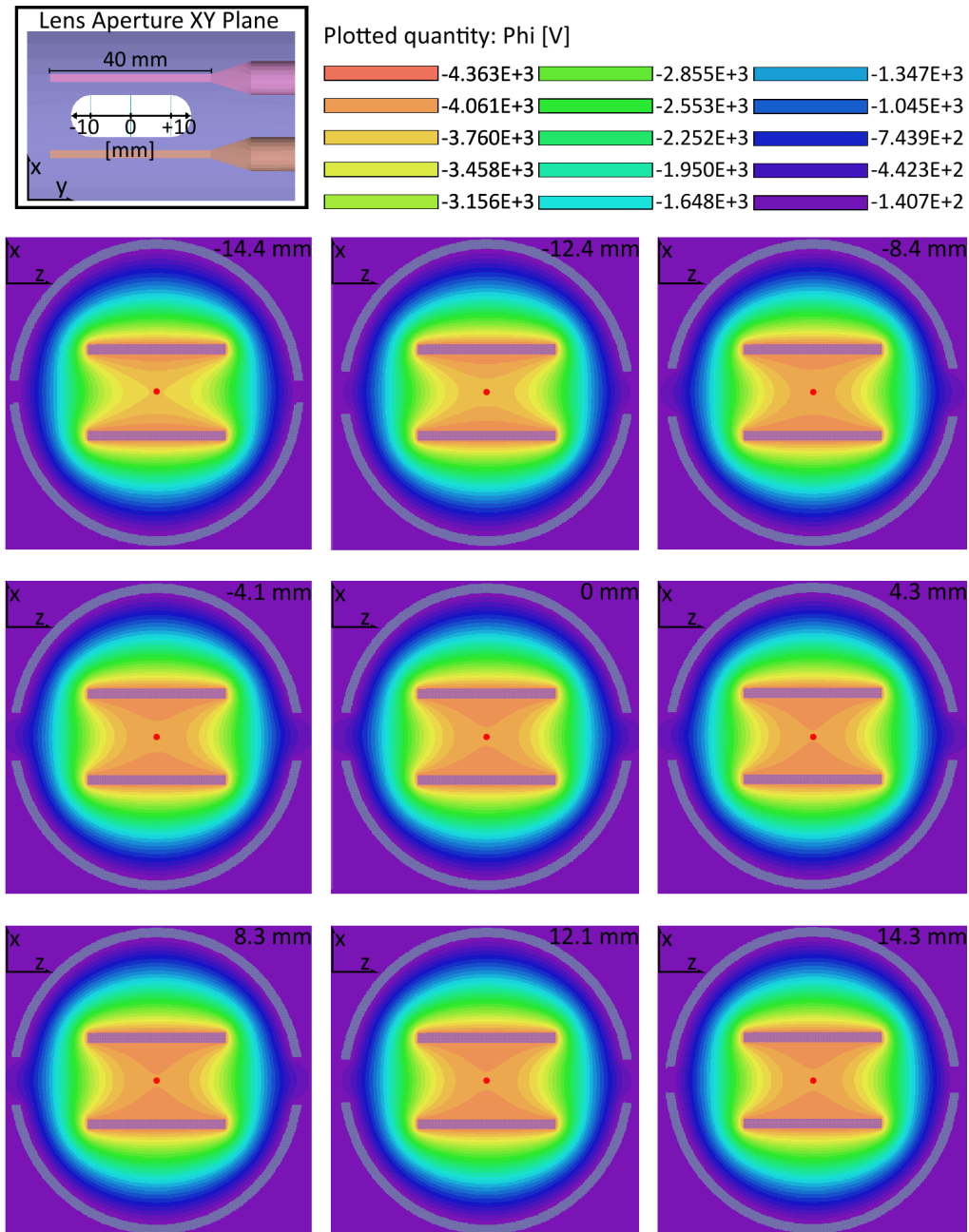


Figure 5.13.: Potential distribution plots of the  $xz$  cross section of the electrostatic Einzel lens for different locations along the aperture length in  $y$  direction. The color coding for each image is identical. The red dots indicate the center.

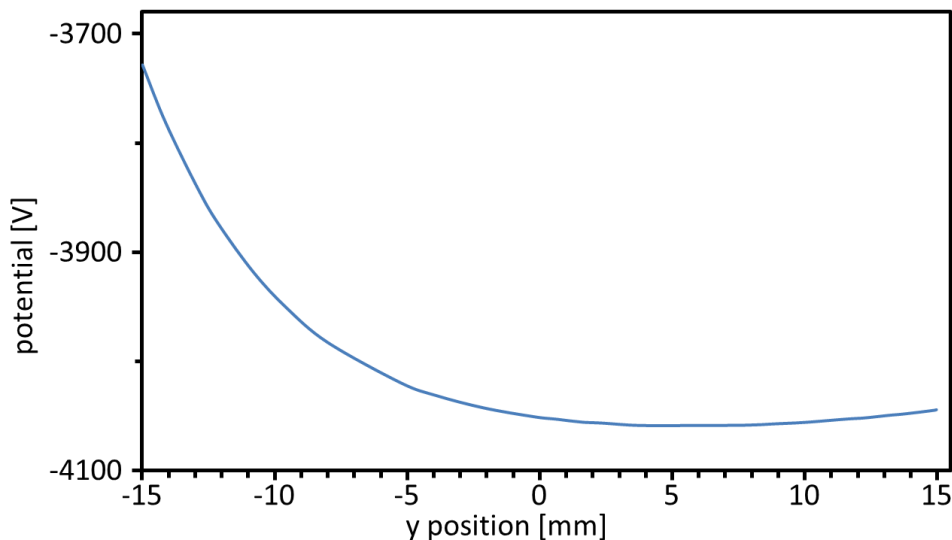


Figure 5.14.: Depicted is the potential distribution in the central axis (along the red dots of fig. 5.13) of the Einzel lens in  $y$  direction.

In direction of the opening of the lens shell the potential and therefore focusing strength strongly decreases. In the other direction it stays within a 2% margin. If the Y Apertures are opened symmetrically, the Einzel lens will produce different focal lengths depending on the location of  $y$  parameter of any electron in the  $xz$  plane. This should be detectable by checking the particle distribution along the  $y$ -axis on the MCP surface.

The lens does not only have different focusing strengths along the  $y$ -axis, but there is also an electric force along the  $y$ -axis induced by the asymmetric shape (open end of the shell, rods of the high voltage panels). The resulting electric force strongly increases the beam divergence in  $y$  direction, as preliminary tracking plots indicated. With detailed investigation, it is evident that the lens is the origin of the extra divergence.

Figure 5.15 provides the tracked electron distribution on the MCP Detector with an actual MCP Detector image obtained by the BSM for comparison. A brief approximation of the  $y$  location of the particles, where they entered the Einzel lens is also provided (dashed red lines) to estimate the electron beam divergence in  $y$  direction. For the simple ensemble (no transverse momenta) the beam divergence in  $y$  direction should be moderate. The electron beam increases from the lens to the MCP to almost 50 mm. The initial broadening of the electron beam till the lens is 2 mm. Without the additional effect of the lens, the total width of  $\sim 16$  mm would be expected (6 mm in 860 mm) at the MCP Detector. The highest particle density is located at  $y_f = -5.0$  mm. If these particles are retraced, they originate at  $y_i \approx 0.0$  mm, where most of the particles enter the lens. Also, if equidistant endpoints on the MCP Detector are picked, the related  $y_i$  origins are not equidistant (see fig. 5.15). In both  $y_i$  directions the divergent electric force on the particles increases.

The progression of the focus width along the  $x$  direction follows the obtained results

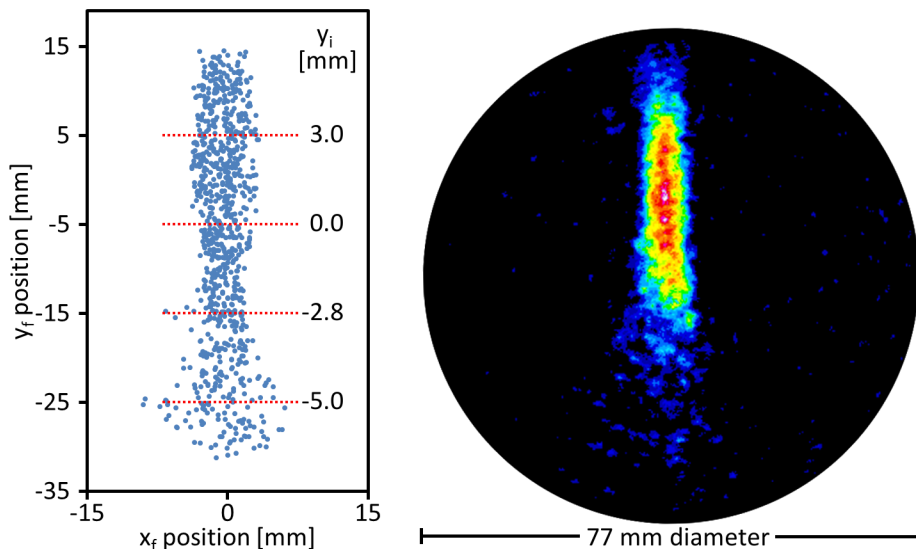


Figure 5.15.: Blue spots in the left image indicate the point of arrival of a single tracked electron on the MCP Detector. The dashed lines indicate the origin of the tracked particle in the  $y$  plane at the lens entrance ( $y_i$ ). On the right side a measurement in pseudo colors is shown for comparison. Setup: 1.0 mm X Aperture,  $\pm 10$  mm Y Aperture,  $-4200$  V applied lens voltage,  $-24.5$  kV Field-Box,  $\pm 4000$  V EA, no RF power.

from fig. 5.13. For  $y$  coordinates below  $y_i < 0$  mm the focusing strength continuously decreases leading to a steady broadening of the  $x$  distribution on the MCP Detector. For values  $y_i < 0$  mm the changes in the focusing strength are only marginal and therefore only a small change in the focus width is obtained. The comparison with the MCP image shows remarkable similarities. The differences in the potential distribution serves as a satisfying explanation of these fish like line focus shapes observed on the MCP Detector. During measurements the lens aberration was minimized with an offset of the Y Apertures of a few millimeters.

### 5.3. An Ensemble Generated by the Ion Beam

The following section introduces a far more complex and realistic electron ensemble and will study the obtained results. It is of great importance to understand the extend of impact of a complex electron ensemble on the simulation outcomes and whether the results of the preceding chapter are still meaningful or not. Otherwise it is unavoidable to put much more resources and time into future simulations.

The actual liberated electron behavior follows a double differential cross section and is still subject of scientific research. For the complex electron ensemble used in this section a simpler approach is used based on [111].

The electron ensemble is randomized in energy and angle based on the relative prob-

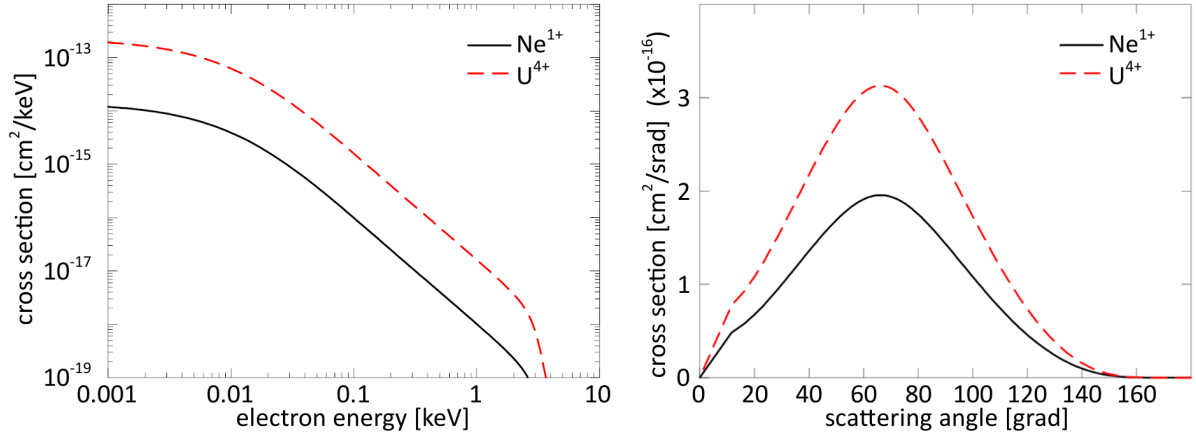


Figure 5.16.: Cross section of ion impact induced electrons for a 1.4 MeV/u beam hitting residual N<sub>2</sub> gas. The left plot shows single differential cross section  $\frac{d\sigma}{dE}$  as a function of the kinetic energy  $E$  in keV and the right plot shows the single differential cross section  $\frac{d\sigma}{d\Omega}$  of the emission angle in degree ( $0^\circ$  means in beam direction)(figure from [111]).

abilities obtained from the cross sections depicted in fig 5.16. The plots provide data for an U<sup>4+</sup> beam at 1.4 MeV/u. The typical beam energies used for the BSM are 11.4 MeV/u, therefore slight adjustments were carried out by means of other ion target interactions for higher energies. For example, the maximum cross section of the emission angle moves closer to  $90^\circ$  for higher energies [111]. These adjustments are carried out with great caution.

Table 5.3.:

Energy [eV]	0-1	1-2	2-4	4-8	8-16	16-32	32-100
Probability	0.0874	0.0819	0.1322	0.1735	0.20222	0.1783	0.1441

To use AMaze tracking module the continuous distribution has to be used to create a discrete distribution with individual angles and energies. For this task specific energy intervals are picked. The relative occupied area of these intervals give the probability for a picked energy. The results are listed in tab. 5.3. Energies above 100 eV are neglected due to their small contribution.

For the emission angle a similar approach is used. The angle cross section plot of fig. 5.16 is again divided in several intervals to obtain the relative probabilities for the picked angle range. Table 5.4 provides the probabilities for the angle ranges.

Table 5.4.:

$\phi$ [deg]	0-20	20-40	40-60	60-80	80-100	100-120	120-140	> 140
Prob.	0.0147	0.0926	0.1810	0.2484	0.2294	0.2294	0.0673	0.0168

With both distributions available, first the emission angle of one electron is binned by a program, then the energy is binned, too, based on relative probabilities. In addition the orientation around the beam axis is completely randomized, because only the angle between ion beam and liberated electron is defined. Finally the location of the particle within the volume is randomized, too. This algorithm is reproduced, to create an ensemble of the desired quantity. The simulation setup is as follows: Field-Box  $-24.5$  kV, EA  $\pm 4000$  V, Lens  $4200$  V, X Aperture  $0.6$  mm, Y Aperture  $\pm 10.0$  mm, initial volume  $xyz$  ( $2 \times 20 \times 1.8$ )  $\text{mm}^3$ ,  $360000$  particles.

First the change of the analyzing volume of the BSM is checked. Due to the angular distribution of the complex ensemble the BSM acceptance does no longer behave like a step function. For comparison the RMS values for each energy are listed in tab. 5.5. The obtained acceptance in  $x$  direction shows a significant increase. The angular distribution of the particles strongly increases the acceptance in  $x$  direction which is the most restricted axis by the BSM aperture design.

A simple estimation by the geometric parameters (relation of aperture width to the travel distance) yields the angle acceptance. For an  $0.6$  mm X Aperture setting and a traveling distance of  $300$  mm an angle of  $3/1000$  is obtained ( $0.17^\circ$ ). The corresponding kinetic energy is  $0.1$  eV in  $x$  direction at  $11$  keV. This indicates that even an energy of  $1$  eV significantly affects the angle acceptance of the electron optical system of the BSM. For further investigations the  $x_i$  starting coordinate and the momentum  $p_x$  in this direction are compared.

Figure 5.17 depicts the different initial coordinates sorted from small to large and their related initial momenta for the identical particle order. The starting coordinate  $x_i$  and starting momentum  $p_x$  show an inversely proportional correlation. If the  $x_i$  coordinate is shifted further to negative values, the momentum  $p_x$  gets bigger to compensate the negative offset by orientating the particles back to the geometric center of the analyzing volume at  $x = 0$ . By using the equation  $E = \frac{p^2}{2m_e}$  ( $m_e$  electron rest mass) the corresponding kinetic energy can be obtained. According to figure 5.17 the maximum kinetic energy in  $x$  direction is  $E_{\text{kin}} \approx 1.6$  eV ( $p_{x_i} = 0.00253 m_e c$ ). For the correlation of the  $y_i$  coordinates with the  $p_y$  a similar behavior occurs. With a spatial offset the

Table 5.5.:

Energy [eV]	N	$\sigma_{x_i}$ [mm]	100% $x_i$ [mm]	$\sigma_{y_i}$ [mm]	100% $y_i$ [mm]	$\sigma_{z_i}$ [mm]	100% $z_i$ [mm]
1	491	$\pm 0.37$	$\pm 0.79$	$\pm 2.65$	$\pm 5.45$	$\pm 0.18$	$\pm 0.39$
2	431	$\pm 0.46$	$\pm 0.96$	$\pm 2.75$	$\pm 5.64$	$\pm 0.17$	$\pm 0.37$
4	449	$\pm 0.49$	$\pm 0.96$	$\pm 3.06$	$\pm 6.04$	$\pm 0.17$	$\pm 0.36$
8	400	$\pm 0.53$	$\pm 0.98$	$\pm 3.43$	$\pm 6.53$	$\pm 0.17$	$\pm 0.38$
16	293	$\pm 0.54$	$\pm 0.90$	$\pm 4.43$	$\pm 7.24$	$\pm 0.18$	$\pm 0.39$
32-100	129	$\pm 0.47$	$\pm 0.75$	$\pm 4.78$	$\pm 8.18$	$\pm 0.18$	$\pm 0.40$
all	2193	$\pm 0.47$	$\pm 0.99$	$\pm 3.33$	$\pm 8.18$	$\pm 0.17$	$\pm 0.42$

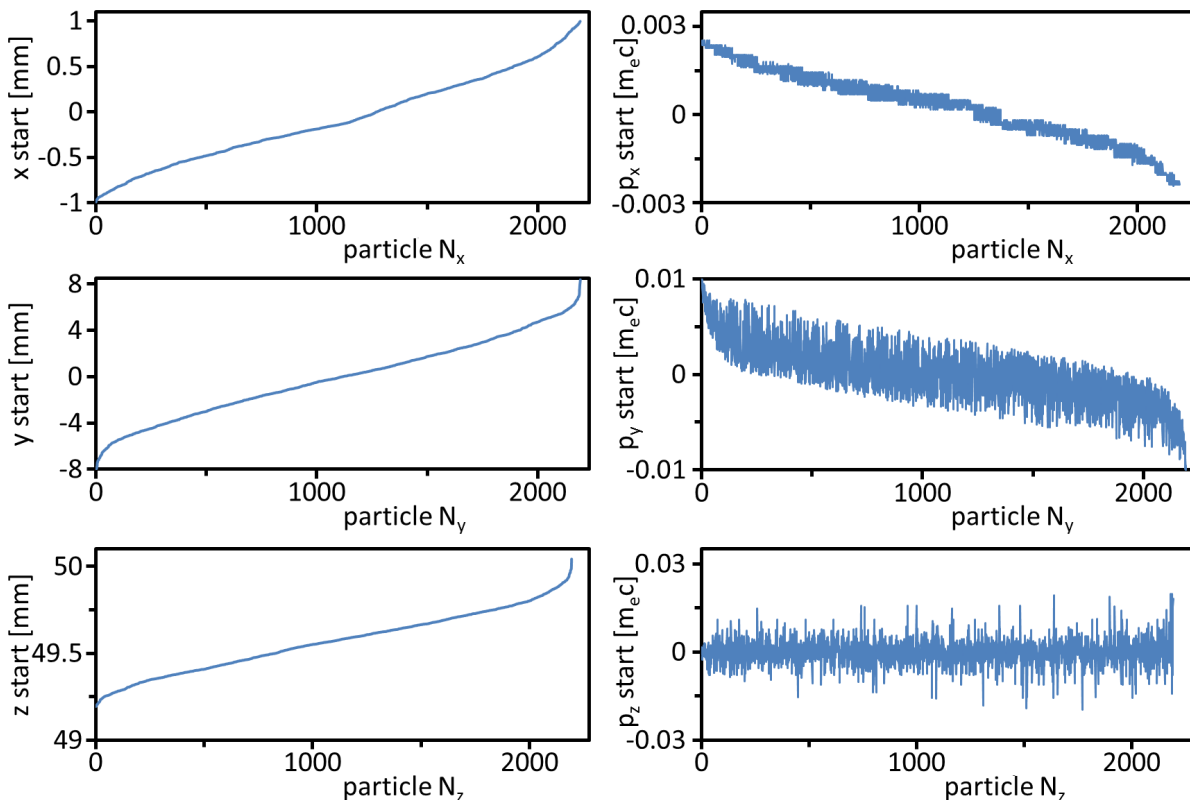


Figure 5.17.: For each set of initial coordinates the ensemble is sorted from small to large. The related momenta for each identical particle order is depicted on the right side for comparison.

starting momentum is directed back to the center. Due to the more generous design of Y Apertures the correlation is not as strict as for the  $x$  direction. Particles with a small offset can have a momentum in the offset's direction, which will increase the offset and the electrons still pass. The obtained momentum range  $p_y$  is 3 times larger than in  $x$  direction. The maximum energy is  $E_{\text{kin}} \approx 24.5$  eV ( $p_{yi} = 0.0098 m_{ec}$ ).

A special case is the acceptance in  $z$  direction. The initial kinetic energy can only increase the kinetic energy of the electron in  $z$  direction while leaving the Field-Box. Electrons starting with a kinetic energy in opposite direction of the driving potential will first be stopped and then leave the Field-Box with an energy corresponding to the potential of the stopping location. Therefore, the  $z$  acceptance can only increase in the upper direction, pointing to lower potentials.

For example the additional energy of 100 eV will enlarge the total  $z_i$  range about 0.23 mm. If an electron only has a slight tilt in any other than the  $z$  direction, the particle will be filtered. In fact the probability of a 100 eV electron emitted with the right angle is very small ( $P \approx 0.024\%$ ), indicating only 1 of 4000 of these electrons will pass. Indeed even the 100%  $z_i$  range only slightly increases from  $\pm 0.39$  mm to  $\pm 0.42$  mm. If the  $z_i$  values for smaller energies are chosen, the difference almost vanishes. The acceptance does not increase significantly because statistics prevent this from happening.

Table 5.6.:

Energy [eV]	N	$\sigma_{xf}$ [mm]	$\sigma_{yf}$ [mm]	$\Delta t_\sigma$ [ps]	$\Delta t_{\max}$ [ps]
1	491	$\pm 1.60$	$\pm 11.80$	$\pm 17.1$	$\pm 45.5$
2	431	$\pm 1.73$	$\pm 12.39$	$\pm 20.9$	$\pm 51.3$
4	449	$\pm 1.72$	$\pm 14.95$	$\pm 21.9$	$\pm 52.5$
8	400	$\pm 1.85$	$\pm 19.74$	$\pm 25.1$	$\pm 59.9$
16	293	$\pm 1.88$	$\pm 25.35$	$\pm 33.1$	$\pm 64.3$
32-100	129	$\pm 2.06$	$\pm 28.63$	$\pm 45.5$	$\pm 115.4$
all	2193	$\pm 1.76$	$\pm 17.68$	$\pm 25.7$	$\pm 115.4$

The changes of the analyzing volume, due to a more realistic and complex ensemble, are considerable in case of the  $x$  direction, but how do the start conditions affect the lens focusing and the time resolution? Table 5.6 provides the data of the particles arriving at the MCP Detector and the obtained time jitter when passing the center of the RF Deflector. For the 0.6 mm aperture setup the RMS focus width increases from 1.49 mm to 1.76 mm, which is well within the margin of error of the obtained experimental value of  $x_\sigma = 1.6 \pm 0.18$  mm. For lower energies the obtained focus width moves closer to the simple ensemble. For higher energies the focusing decreases ( $\pm 2.06$  mm for 32-100 eV), but the high energies do not contribute much due to their low number.

The RMS time of arrival of the evaluated particles arriving at the RF Deflector is  $\Delta t_\sigma = 25.7$  ps. This increase compared to the  $\Delta t_\sigma = 16.7$  ps (see tab. 5.1) is a result of low influence of starting conditions on results in  $z$  direction. If the linear prediction from sec. 5.2.3 is used based on the increased  $x_i$  range, a twice as big  $\Delta t_\sigma$  could have been the result. A  $\Delta t_\sigma$  of 25.7 ps is still not critical in comparison to the optical time resolution of  $> 100$  ps for the 0.6 mm aperture setup.

The obtained particle distribution on the MCP Detector is depicted in fig 5.18 together with the MCP image already displayed in fig. 5.15. In addition an extra set of plots shows the distribution for low initial energies (1-2 eV), moderate initial energies (4-8 eV), and high initial energies (16-100 eV). The distributions filtered by their energies still look alike, besides the width in the  $y$  direction. This indicates that the different energies are similarly treated by the lens aberration. The complex more realistic ensemble shows considerable deviation from the simple approach. Although the complex ensemble is more accurate, the simple ensemble is still good enough to predict how different settings or even design changes will affect the BSM performance and easily provides a factor of 10 better statistic.

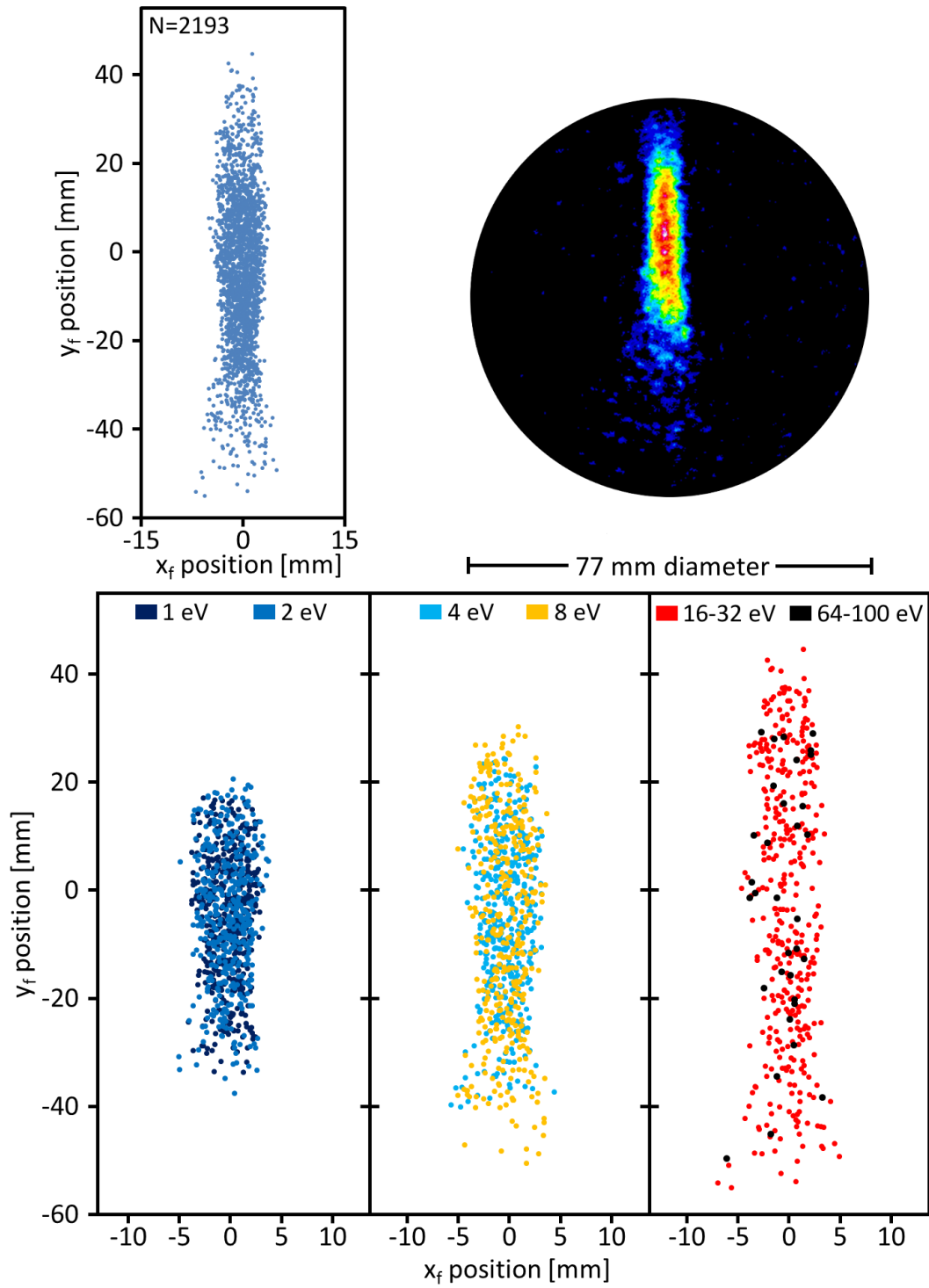


Figure 5.18.: Depicted is the particle distribution detected on the MCP surface. The lower plots show the same distribution for the different initial kinetic energies of the particles.



## 6. Conclusion

In the framework of this thesis, a prototype of a non-intercepting Bunch Shape Monitor (BSM) was developed at the heavy ion LINAC at GSI. The purpose was to obtain a diagnostics tool with a resolution below 100 ps [112], which clearly outstrips phase probes at low  $\beta \approx 0.15 c$ . It was also attempted to prove the feasibility of such a device for the planned proton-LINAC at FAIR (sec. 1.1) with a necessary resolution of 10 ps [113].

Early investigation of materials put into a 11.4 MeV/u heavy ion beam (sec. 3.2.2) indicated very high thermal stress. Therefore, a non-intercepting approach for a BSM was pursued. The design (sec. 3.3.1) is utilizing secondary electrons which are created by beam gas interaction within the Field-Box. By applying a homogenous driving potential up to  $-31$  kV, an electron beam is formed which carries the time structure. With a sophisticated electron optical system, the electron beam is imaged on a micro channel plate and phosphor screen based assembly which is logged by a low noise CCD Camera. Hereby, the electron beam is deflected by an RF Deflector working in resonance at 36 MHz in order to transform the time information (relative time of arrival) into a spatial distribution on the detector which finally yields the longitudinal bunch structure.

To compensate the undesired influence of the driving potential on the ion beam, extra electrodes, with the same applied potential, were designed and accommodated in the existing BSM housing (sec. 3.3.2). Razorblade like apertures were installed to avoid electron scattering within the aperture gap (sec. 3.3.4). After substantial beam based measurements (sec. 4), the whole device was subject to numerical simulations (sec. 5) to investigate the evolution of the electron beam within the BSM and to explain electron optical aberrations.

The BSM was used to measure non-Gaussian bunch profiles (sec. 4.2.1). Due to the complex shape, different approaches were followed to execute a quantitative and qualitative investigation of the obtained profiles (see fig. 4.8). Hereby, a standard Gaussian fit, a logarithmic normalized distribution (LND) and a numerical integration, resembling the mathematical standard deviation (SD), were used. Each approach showed distinctive quantitative results, but also comparable qualitative results. The achieved time resolution of  $37 \pm 6.3$  ps (sec. 4.1.4) exceeds the necessary resolution of 100 ps. The corresponding phase resolution for 37 ps is below  $0.5^\circ$  at 36 MHz. A 108 MHz RF Deflector is also available which will increase the applicable resolution by a factor of three, if the phase resolution is maintained. The BSM's reliability was proven under different setups, as single shot measurements (sec. 4.2.3), variations of the electron optical apertures (sec. 4.2.2) and ion beam current variations (sec. 4.3.1). Despite of wide parameter and intensity variations, the BSM provided constant and reliable results.

Hereafter, parameter studies were executed to investigate the signal-to-background ratio, the signal and the background intensity dependencies. A proper operation of the MCP Detector proved to be crucial for high signal-to-background ratios due to the swift and sudden emerge of a detector saturation (sec. 4.3.2). By reducing the applied voltage below a threshold of  $U_{\text{MCP}} = 1500 \text{ V}$ , in most cases saturation can be avoided. The source of the MCP background was traced back to X-rays created by the Field-Box (sec. 4.3.4). Finally, a set of initial parameters for safe operation was presented in section 4.4.

As part of advanced measurements, a Single Gap Resonator (SGR) in rebuncher mode (sec. 4.5.1), was used to investigate the bunch transformation under systematic manipulation of the focusing power of the SGR. Again the single Gaussian, LND and SD were used for quantitative and qualitative analysis, yielding remarkable similar qualitative results for the bunch profile progression (sec. 4.5.2). The parabolic fit  $y = a(x - b)^2 + c$  was used for each obtained set of the profile series (sec. 4.5.3). Based on linear transformations, the determination of the fit parameters  $a$ ,  $b$  and  $c$  allows to obtain the longitudinal emittance of the ion beam. Depending on the analyzing method, the parabolic fit provided results from  $\epsilon_{\text{Gauss}} = 1.42 \pm 0.14 \text{ keV/u ns}$  to  $\epsilon_{\text{SD}} = 3.0 \pm 0.33 \text{ keV/u ns}$ . The obtained emittance values fell short of a reference value  $\epsilon_{\text{ref}} = 0.85 \pm 0.14 \text{ keV/u ns}$  (sec. 4.5.4) which was obtained for a complete different LINAC setup. This outcome is still satisfying due to the lack of a well suiting model to analyze strongly deformed bunch profiles.

A numerical simulation, using the modular AMaze finite-elements software (sec. 5.1), was developed. The tracking of the trajectory of single particles allowed the investigation of the electron beam within the electron optical system. A strict reduction of the numeric error of the static field-solver down to  $9.7 \cdot 10^{-8}$  (sec. 5.1.2) together with detailed examination of the field distribution, proved that the simulation yields reliable results (sec. 5.2.1). The observation of the particle trajectories (sec. 5.2.2) demonstrated the necessity of sufficient shielding of the active components to avoid accumulation of additional electron beam divergence. The tracking of the time of flight to reach the center of the RF Deflector of the up to 90,000 particles yielded a time spread  $\tau_{\sigma} \approx 5.2 \text{ ps}$  (sec. 5.2.3) which slightly contributes to the time resolution of 37 ps. A different, more complex initial ensemble yielded a 50% bigger time spread (sec. 5.3) which is still not critical. Also a more detailed simulation of the field distribution of the RF Deflector, used as an Einzel lens, showed the strongly changing focusing strength of the device over the aperture's long side (sec. 5.2.5), leading to imaging errors and therefore decreasing the achievable resolution.

The foreseen performance goals of  $1^\circ$  phase resolution and at least a time resolution of 100 ps have been achieved. Furthermore, the device proofed to be applicable as a diagnostics tool, due to its non-interference with the ongoing LINAC and Synchrotron operation. In addition, the BSM surpasses the expectations, due to the demonstration of an emittance measurement and the execution of single shot measurements. The latter might lead to the investigation of possible RF power degradation in the LINAC structure

during a macro pulse. Also the numerical simulations allowed access to the time structure of the electron beam, validating the obtained time resolution and allowing predictions of the resolution limits of the non-intercepting design. Another subject is the improper operation mode of the Einzel lens. The device is foreseen for a pinhole only usage. If these optical aberrations are fixed, a higher performance of the device can be achieved.

## 6.1. Outlook

Remote operation of the BSM will become available soon [114]. A suitable user interface is about to be finished, allowing the regular operation of the BSM by non-specialized personnel in the main control room of the GSI facility. Together with sufficient beam preparation frequent proper and correct longitudinal emittance measurements will deepen the understanding of LINAC structure.

Still, some problems have not been treated within the scope of this thesis. As preliminary calculations showed [115], high beam current ( $I > 5$  mA) induced space charge forces are the source for significant image distortion of the detected signal. Due to the use of beam currents  $I < 2$  mA for the presented measurements, these disturbing effects are not an issue. However, the subject remains, as high current machine measurements are of great interest. The reduction of the ion current by selecting a lower populated charged state with the foil strippers [116] is a possibility. In this way the high current beam propagates through the LINAC structure and is filtered subsequently, providing reliable results of the high current LINAC operation.

A dedicated solution for space charge induced effects is still desirable. As an additional homogeneous magnetic field within the Field-Box might guide the secondary electrons on a spiral path out of the beam tube. But at the exit slit of the Field-Box the diverting magnetic fields have to be compensated. By reducing the aperture width of the Field-Box exit slits, at the expense of the signal intensity, this negative influence can be minimized. Nevertheless, it is already a task to further decrease the necessary aperture width to obtain a higher time resolution. The combined efforts might yield synergies.

A possible approach to reduce the necessary aperture width is the compression of the not focused plane of the electron beam (see fig. 5.18). Already a gentle compression—no real focusing is necessary—can increase the signal intensity on the MCP Detector by about a factor of two or three. A device for manipulating the electron beam in this plane is already available and only needs brief adjustments.

A more extensive approach might be the application of a gas jet as virtual indestructible thin wire to serve as a more localized source for secondary electrons. This might allow intensity growths without feeding the X-ray generation, which is responsible for most of the background (sec. 4.3.4).



# Bibliography

- [1] O. Kester, "Status of the FAIR Facility", IPAC'13, Shanghai, May 2013, TUXB101, p. 1085, <http://www.JACoW.org>
- [2] P. Spiller et al., "Status of the FAIR SIS100/300 Synchrotron Design", PAC07, Albuquerque, June 2007, TUPAN014, <http://www.JACoW.org>
- [3] Green Paper, "The Modularized Start Version", FAIR Committee, Darmstadt, October 2009, <http://www.fair-center.de>
- [4] L. Groening et al., "Status of the FAIR 70 MeV Proton LINAC", LINAC'12, Tel-Aviv, September 2013, THPB034, p. 927, <http://www.JACoW.org>
- [5] M. Winkler et al., "The Status of the Super-FRS In-Flight Facility at FAIR", October 2008, Nuclear Instruments and Methods in Physics Research Section B: Beam Interactions with Materials and Atoms
- [6] O. Kester, private communication, GSI Helmholtzzentrum für Schwerionenforschung
- [7] R. Toelle et al., "HESR at FAIR: Status of Technical Planning", PAC07, Albuquerque, June 2007, TUPAN024, <http://www.JACoW.org>
- [8] K. Peters, "Status of FAIR and PANDA", IWHSS 2013, Erlangen, July 2013, <https://indico.cern.ch>
- [9] S. Litvinov et al., "The Alternative Ion-Optical Mode of the Recuperated Experimental Storage Ring", PAC09, Vancouver, May 2009, FR5REP118, <http://www.JACoW.org>
- [10] GSI, "GSI Geschichte-Ein Forschungslabor für Alle", Über uns/Geschichte, Darmstadt 2010, <https://www.gsi.de/start.htm>
- [11] P. J. Spiller et al., "Status of the FAIR Synchrotron Projects SIS18 and SIS100", IPAC'14, Dresden, June 2014, <http://www.JACoW.org>
- [12] GSI, High Current Ion Sources, [https://www.gsi.de/de/work/-fairgsi/linac\\_operations/ion\\_sources/sources/ion\\_sources.htm?nr=%2Fproc%2Fself%2F%27](https://www.gsi.de/de/work/-fairgsi/linac_operations/ion_sources/sources/ion_sources.htm?nr=%2Fproc%2Fself%2F%27)

- [13] C. Muhle et al., "Development of the Penning Ionization Gauge Source for Higher Current", Review of Scientific Instruments, Volume 69, Issue 2, June 2009, <http://www.JACoW.org>
- [14] R. Keller, "Multicharged Ion Production with MUCIS in GSI", Sci. Rep. 1987, 1988
- [15] H. Reich et al., "Metal Vapor Vacuum Arc Ion Source Development at GSI", Rev. Sci. Instrum., Volume 71, 2000,
- [16] GSI, MUCIS, [https://www.gsi.de/work/fairgsi/linac\\_operations/ion\\_sources/sources/ion\\_sources.htm](https://www.gsi.de/work/fairgsi/linac_operations/ion_sources/sources/ion_sources.htm)
- [17] L. Dahl, "The Low Energy Beam Transport System of the New GSI High Current Injector", Linac'00, Monterey, August 2000, MOD15, <http://www.JACoW.org>
- [18] H. Vormann et al., "Straight Injection of an Intense Uranium Beam into the GSI High Current RFQ", IPAC'14, Dresden, June 2014, THPME006, <http://www.JACoW.org>
- [19] W. Barth, "HSI-Frontend Upgrade", GSI Scientific Report 2009, Darmstadt, March 2010, <http://www.JACoW.org>
- [20] U. Ratzinger, "Status of the 36 MHz LINAC Cavities for the GSI High Current Injector", PAC'99, August 1999, New York,
- [21] P. Forck et al., "Measurements with a Novel Non-Intercepting Bunch Shape Monitor at the High Current GSI-LINAC", DIPAC'05, Lyon, June 2005, <http://www.JACoW.org>
- [22] GSI, HSI, [https://www.gsi.de/work/fairgsi/linac\\_operations/linac/unilac/high\\_current\\_injector.htm](https://www.gsi.de/work/fairgsi/linac_operations/linac/unilac/high_current_injector.htm)
- [23] GSI, Gasstripper, [https://www.gsi.de/work/-fairgsi/linac\\_operations/linac/unilac/gasstripper.htm](https://www.gsi.de/work/-fairgsi/linac_operations/linac/unilac/gasstripper.htm)
- [24] J. Klabunde, "The High Charge State Injector For GSI", LINAC'92, Ottawa, August 1992, TH1-02, <http://www.JACoW.org>
- [25] GSI, Poststripper, [https://www.gsi.de/work/fairgsi-/linac\\_operations/linac/unilac/poststripper.htm](https://www.gsi.de/work/fairgsi-/linac_operations/linac/unilac/poststripper.htm)
- [26] S. Yaramishev, et al., "Investigations of the Beam Matching to the GSI-Alvarez DTL Under Space Charge Conditions", LINAC'04, Lübeck, August 2004, <http://www.JACoW.org>
- [27] P. Forck, private communication, 2014
- [28] GSI, Beam Transfer Line, [https://www.gsi.de/work/fairgsi-/linac\\_operations/linac/unilac/beam\\_transfer\\_line.htm](https://www.gsi.de/work/fairgsi-/linac_operations/linac/unilac/beam_transfer_line.htm)

- [29] GSI, SIS 18 - Injection, [https://www.gsi.de/work/-fairgsi/linac\\_operations/linac/unilac/sis\\_18\\_injection.htm](https://www.gsi.de/work/-fairgsi/linac_operations/linac/unilac/sis_18_injection.htm)
- [30] GSI, ESR, <https://www.gsi.de/gsiwork/beschleuniger/esr.htm>
- [31] P. Spiller, "Status of the FAIR Synchrotron Projects SIS18 Upgrade and SIS100", IPAC'14, Dresden, June 2014, [http://accelconf.web.cern.ch/-AccelConf/IPAC2014/talks/weoba01\\_talk.pdf](http://accelconf.web.cern.ch/-AccelConf/IPAC2014/talks/weoba01_talk.pdf)
- [32] T. P. Wangler, "RF Linear Accelerators", Wiley-VHC, 2008, p. 97
- [33] Spektrum der Wissenschaft, "Cockcroft-Walton-Beschleuniger", Akademischer Verlag Heidelberg, 1998
- [34] Spektrum der Wissenschaft, "Vor fünfzig und vor hundert Jahren", Akademischer Verlag Heidelberg, June 1996, p. 97
- [35] G. Otto, private communication, GSI Helmholtzzentrum für Schwerionenforschung
- [36] O. Boine-Frankenheim, "Basic Course on Accelerator Optics", lecture, GSI, Darmstadt, 2004, <http://web-docs.gsi.de/~boine/vorlesung/skript/ss04.pdf>
- [37] GmbH, Firma Kress, Biebergemünd Wirthheim, Germany, <https://www.Firma-kress.de>
- [38] T. P. Wangler, "RF Linear Accelerators", Wiley-VHC, 2008, p. 232
- [39] P. Blewett, "Linear Accelerator Injection for Proton Synchrotrons", Symposium in High-Energy Accelerators and Pion Physics, CERN, Geneva, 1956, p. 162
- [40] J. Pfister, "Entwicklung und Anwendung schneller Strahldiagnose für Ionenstrahlen", doctoral thesis, IAP Goethe University, Frankfurt, June 2010, p. 10
- [41] D. Warner et al., "CERN Heavy-Ion Facility Design Report", report, CERN, Geneva, April 1993, p. 24
- [42] U. Ratzinger, "Effiziente Hochfrequenz-Linearbeschleuniger für leichte und schwere Ionen", postdoctoral thesis, IAP Goethe University, Frankfurt, 1998
- [43] R. Tiede, "Simulationswerkzeuge für die Berechnung hochintensiver Ionenbeschleuniger", doctoral thesis, IAP Goethe University, Frankfurt, June 2009, p. 6
- [44] U. Ratzinger, "A Coupled RFQ-IH Cavity for the Neutron Source FRANZ", LINAC'12, Tel-Aviv, September 2012, THPB008, p. 858
- [45] U. Amaldi et al., "Cluster: a High Frequency H-mode Coupled Cavity LINAC for Low and Medium Energies", Nucl. Instr. Meth. A
- [46] G. Clemente, "The Room Temperature CH-DTL and its Application for the FAIR Proton Injector", doctoral thesis, IAP Goethe University, Frankfurt, 2007

- 
- [47] R. Tiede, "Simulationswerkzeuge für die Berechnung hochintensiver Ionenbeschleuniger", doctoral thesis, IAP Goethe University, Frankfurt,, June 2009, p. 7
- [48] J. Liouville, "Note sur la Théorie de la Variation des constantes arbitraires", Journal de Mathématiques Pures et Appliquées 3 (1838),p. 342-349
- [49] J. Pfister, "Entwicklung und Anwendung schneller Strahldiagnose für Ionenstrahlen", doctoral thesis, IAP Goethe University, Frankfurt, June 2010, p. 26
- [50] M.P. Stockli, "Measuring and Analyzing the Transverse Emittance of Charged Particle Beams", proceeding, BIW'06, Batavia, May 2006, p. 25-62
- [51] O. Kester, "Physik und Technik von Ionenquellen", lecture script, IAP Goethe University, Frankfurt, September 2007
- [52] F. Hinterberger, "Physik der Teilchenbeschleuniger und Ionenquellen", Springer-Verlag, November 2007, p. 220
- [53] T. Sieber, "Entwicklung von 4-Rod und IH-Radio-Frequenz-Quadrupol (RFQ)-Beschleunigern für radioaktive Ionenstrahlen bei REX-ISOLDE und MAFF", doctoral thesis, Faculty of Physics, University Munich, May 2001
- [54] R. Tiede, "Simulationswerkzeuge für die Berechnung hochintensiver Ionenbeschleuniger", doctoral thesis, IAP Goethe University, Frankfurt, June 2009, p. 11-15
- [55] R. Tiede, "Simulationswerkzeuge für die Berechnung hochintensiver Ionenbeschleuniger", doctoral thesis, IAP Goethe University, Frankfurt, June 2009, p. 39-52
- [56] R. Tiede, private communication, 2015
- [57] M. Almalki, "Simulation data p:LINAC", private communication, 2015
- [58] P. Forck, "Lecture Notes on Beam Instrumentation and Diagnostics", JUAS, Archamps, March 2012, p. 103-123, <https://indico.cern.ch>
- [59] J. D. Jackson, "Classical Electrodynamics", John Wiley & Sons (1962), p. 381 <https://archive.org/details/ost-physics-jackson-classicalelectrodynamics>
- [60] M. Almalki, "Beam Position Monitor System for the Proton LINAC for FAIR", doctoral thesis, IAP Goethe University, Frankfurt, December 2015
- [61] P. Forck, "Lecture Notes on Beam Instrumentation and Diagnostics", JUAS, Archamps, March 2012, p. 105, <https://indico.cern.ch>
- [62] P. Forck, "Lecture Notes on Beam Instrumentation and Diagnostics", JUAS, Archamps, March 2012, p. 106, <https://indico.cern.ch>



- [63] A. V. Feschenko, Topical Workshop on Bunch Shape Measurements, ESS, Lund, February 2013
- [64] E. S. McCrory et al., "Use of an INR-style Bunch Length Detector in the Fermilab LINAC", proceedings LINAC'92, Ottawa, August 1992, p. 662
- [65] GSI, Poststripper Accelerator, [https://www.gsi.de/work/fairgsi/-linac\\_operations/linac/unilac/poststripper.htm](https://www.gsi.de/work/fairgsi/-linac_operations/linac/unilac/poststripper.htm)
- [66] Wikipedia, "Thermal Conduction", [https://en.wikipedia.org/wiki/Thermal\\_conduction#Fourier.27s\\_law](https://en.wikipedia.org/wiki/Thermal_conduction#Fourier.27s_law)
- [67] Wikipedia, "Stefan–Boltzmann law", [https://en.wikipedia.org/wiki/Stefan-Boltzmann\\_law](https://en.wikipedia.org/wiki/Stefan-Boltzmann_law)
- [68] C. R. Crowell, "The Richardson Constant for Thermionic Emission in Schottky Barrier Diodes", Solid State Electronics, New Jersey, April 1965, p. 395-399
- [69] M. Sapinski, "Beam Interaction with Thin Materials: Heat Deposition, Cooling Phenomena and Damage Limits", proceeding BIW'12, Newport News, April 2012, <http://www.JACoW.org>
- [70] C. P. Welsch et al., "An Ultra Low Energy Storage Ring at FLAIR", Nucl. Instrum. Meth. A 546(3) p. 405-417 (2005).
- [71] Wikipedia, "Nyquist–Shannon Sampling Theorem", [https://en.wikipedia.org/wiki/Nyquist\0T1\textendashShannon\\_sampling\\_theorem](https://en.wikipedia.org/wiki/Nyquist\0T1\textendashShannon_sampling_theorem)
- [72] C. Deibele, "Fast Faraday Cup with High Bandwidth ", US patent No 20050212503 A1, September 2005, <http://www.google.com/patents/US20050212503>
- [73] T. Milosic, "Feasibility Study on Longitudinal Phase-Space Measurements at GSI UNILAC Using Charged-Particle Detectors", doctoral thesis, TU Darmstadt, Darmstadt, December 2013,
- [74] P. Forck et al., "Minimal Invasive Beam Profile Monitors for High Intense Hadron Beam", IPAC'10, Kyoto, May 2010, TUZMH01, <http://www.JACoW.org>
- [75] C. Dorn et al., private communication
- [76] C. Dorn et al., LOBI Wiki, RnD-Projects, Bunchprofil-Monitor, [www-bd.gsi.de/dokuwiki/lib/exe/fetch.php?media=fair-rnd:rnd-projects:std-000-101.110.000\\_x-y\\_blende\\_2013-11-11.pdf](http://www-bd.gsi.de/dokuwiki/lib/exe/fetch.php?media=fair-rnd:rnd-projects:std-000-101.110.000_x-y_blende_2013-11-11.pdf)
- [77] C. Dorn et al., LOBI Wiki, RnD-Projects, Bunchprofil-Monitor, [www-bd.gsi.de/dokuwiki/lib/exe/fetch.php?media=fair-rnd:rnd-projects:std-000-101.101.000\\_x-y\\_blende\\_13-04-17.pdf](http://www-bd.gsi.de/dokuwiki/lib/exe/fetch.php?media=fair-rnd:rnd-projects:std-000-101.101.000_x-y_blende_13-04-17.pdf)

- [78] C. Dorn et al., LOBI Wiki, RnD-Projects, Bunchprofil-Monitor, [www-bd.gsi.de/dokuwiki/lib/exe/fetch.php?media=fair-rnd:rnd-projects:std-v01-101.251.000\\_energieanalysator\\_v01\\_2013-11-29.pdf](http://www-bd.gsi.de/dokuwiki/lib/exe/fetch.php?media=fair-rnd:rnd-projects:std-v01-101.251.000_energieanalysator_v01_2013-11-29.pdf)
- [79] P. Forck, private communication, 2015
- [80] S. Mehler, "Auslegung eines Systems zur Messung der zeitlichen Struktur eines gepulsten Schwerionenstrahls", diploma thesis, GSI, Darmstadt, June 1998, <https://www.gsi.de>
- [81] J. Großer, "Einführung in die Teilchenoptik", Teubner Verlag Stuttgart 1983
- [82] H. Wollnik, "Point-to-Point Focusing", Optics of Charged Particles, Academic Press Inc., London 1987, p. 61
- [83] C. Dorn et al., LOBI Wiki, RnD-Projects, Bunchprofil-Monitor, [www-bd.gsi.de/dokuwiki/lib/exe/fetch.php?media=fair-rnd:rnd-projects:std-000-101.301.000\\_36\\_mhz\\_deflector\\_2014-04-24.pdf](http://www-bd.gsi.de/dokuwiki/lib/exe/fetch.php?media=fair-rnd:rnd-projects:std-000-101.301.000_36_mhz_deflector_2014-04-24.pdf)
- [84] C. Dorn et al., LOBI Wiki, RnD-Projects, Bunchprofil-Monitor, [www-bd.gsi.de/dokuwiki/lib/exe/fetch.php?media=fair-rnd:rnd-projects:std-000-101.460.000\\_baugruppe\\_mcp\\_2013-12-03.jpg](http://www-bd.gsi.de/dokuwiki/lib/exe/fetch.php?media=fair-rnd:rnd-projects:std-000-101.460.000_baugruppe_mcp_2013-12-03.jpg)
- [85] Hamamatsu Photonics K.K., "MCP & MCP Assembly", data sheet, <http://www.datasheetarchive.com>
- [86] PCO AG, "Sensicam, Dicom Pro", manual, Kehlheim, Germany, [www.pco.de](http://www.pco.de)
- [87] P. Kainberger, CSCOF0 Wiki, TimingEventDefs, <https://www-acc.gsi.de/wiki/Frontend/TimingEventDefs>
- [88] P. Kainberger, "DTI-Pulsstrommesseinrichtung (Trafos)", documentation, GSI, Darmstadt, February 2001, [www-acc.gsi.de/data/documentation/eq-models/dti/gm-dti.pdf](http://www-acc.gsi.de/data/documentation/eq-models/dti/gm-dti.pdf)
- [89] A. V. Feschenko et al., "BSM with Three Replaceable RF Deflectors and Three Replaceable RF Electronic Channels for GSI and FAIR LINACs", design report, INR, Moscow, June 2014, private communication
- [90] A. V. et al., "Longitudinal Beam Parameter Study in the SNS LINAC", proceedings PAC'07, Albuquerque, June 2007, THOAAB01, p. 2608 <http://accelconf.web.cern.ch/AccelConf/p07/papers/thoaab01.pdf>
- [91] M. Galonska et al., "Computer Simulations of a High Current Proton Beam at the SILHI-LEBT", proceedings LINAC'06, Knoxville, August 2006, TUP089, p. 469, <https://www.gsi.de/>

- [92] E. Limpert et al., "Lognormal Distributions Across the Sciences: Keys and Clues", publication, BioScience No. 51, 2001, <http://stat.ethz.ch/~stahel/lognormal/bioscience.pdf>
- [93] W. Vinzenz et al., "RF System Development for the new 108 MHz Heavy Ion High-Energy LINAC at GSI", proceedings LINAC'14, Geneva, August 2014, TUPP058, p. 556, <http://accelconf.web.cern.ch/AccelConf/LINAC2014/papers/tupp058.pdf>
- [94] M. Witthaus et al., "SEM-Grid Prototype Electronics Using Current-Frequency-Converter", proceeding, DIPAC'11, Hamburg, August 2011
- [95] Hamamatsu Photonics K.K., "MCP Assembly", manual, Japan, September 2006, p. 6 [www.hamamatsu.com](http://www.hamamatsu.com)
- [96] H. Reeg et al., "Current Transformers for GSI's keV/u to GeV/u Ion Beam - An Overview", proceedings DIPAC'01, Grenoble, August 2001, PS08, p. 120-122
- [97] S. Skelton, "Multi-Quadrupole Scan for Emittance Determination at PITZ", script, DESY Zeuthen, Hamburg, September 2007, <https://www-zeuthen.desy.de/students/2007/doc/skelton.pdf>
- [98] W. Vinzenz, private communication, March 2015
- [99] H. Wiedemann, "Particle Accelerator Physics", Springer, Hamburg, July 2015, p.184
- [100] L. Groening, private communication, March 2015
- [101] Field Precision LLC, Albuquerque, USA, <http://www.fieldp.com/>
- [102] Field Precision LLC, "Metamesh", manual, Albuquerque, USA, <http://www.fieldp.com/manuals/metamesh.pdf>
- [103] Field Precision LLC, "HiPhi", manual, Albuquerque, USA, <http://www.fieldp.com/manuals/hiphi.pdf>
- [104] Field Precision LLC, "OmniTrack", manual, Albuquerque, USA, <http://www.fieldp.com/manuals/omnitack.pdf>
- [105] C. Dorn et al., RnD-Projects, Bunchprofil-Monitor, [www-bd.gsi.de/dokuwiki/doku.php?id=fair-rnd:rnd-projects:bunchprofilmonitor](http://www-bd.gsi.de/dokuwiki/doku.php?id=fair-rnd:rnd-projects:bunchprofilmonitor)
- [106] Wikipedia, Chebyshev's Inequality, [https://en.wikipedia.org/wiki/Chebyshev's\\_inequality](https://en.wikipedia.org/wiki/Chebyshev's_inequality)
- [107] Wikipedia, "Boundary Value Problem", [https://en.wikipedia.org/wiki/Boundary\\_value\\_problem](https://en.wikipedia.org/wiki/Boundary_value_problem)

- [108] S. Mehler, "Auslegung eines Systems zur Messung der zeitlichen Struktur eines gepulsten Schwerionenstrahles", diploma thesis, FH Wiesbaden, Darmstadt, June 1998
- [109] B. J. Franczak, "MIRKO", GSI,  
[https://www.gsi.de/work/fairgsi/primary\\_beams/system\\_planning/projekte\\_pbsp/mirko.htm](https://www.gsi.de/work/fairgsi/primary_beams/system_planning/projekte_pbsp/mirko.htm)
- [110] C. Dorn et al., LOBI Wiki, RnD-Projects, Bunchprofil-Monitor,  
[www-bd.gsi.de/dokuwiki/lib/exe/fetch.php?media=fair-rnd:rnd-projects:std-v01-101.251.012\\_herzogblende\\_1\\_2013-11-29.pdf](http://www-bd.gsi.de/dokuwiki/lib/exe/fetch.php?media=fair-rnd:rnd-projects:std-v01-101.251.012_herzogblende_1_2013-11-29.pdf)
- [111] M. Kraemer, "Drift Calculations Based on Binary Encounter Approximation", private communication, GSI, 2004
- [112] P. Forck et al., "Measurements with a Novel Non-Intercepting Bunch Shape Monitor at the High Current GSI-LINAC", proceeding, DIPAC'05, June 2005,  
<http://www.JACoW.org>
- [113] B. Zwicker et al., "Non-Invasive Bunch Shape Monitoring for High Current LINACs", GSI scientific report, Darmstadt, March 2012, <http://repository.gsi.de/record/52876>
- [114] M. Beck, "Bunch Shape Monitor Interface", diploma thesis, FH Wiesbaden, July 2015
- [115] P. Forck et al., "A Novel Device for Non-Intercepting Bunch Shape Measurements at the High Current GSI-LINAC", proceedings, EPAC'04, Lucerne, July 2004, TH-PLT030, <http://www.JACoW.org>
- [116] J. Glatz et al., "A High Duty Foil Stripper System in the Injection Line to the new Heavy Ion Synchrotron SIS at GSI", proceedings EPAC'96, Barcelona, July 1996,  
<http://epac.web.cern.ch>
- [117] C. Dorn et al., LOBI Wiki, RnD-Projects, Bunchprofil-Monitor,  
<http://www-bd.gsi.de/dokuwiki/doku.php?id=fair-rnd:rnd-projects:bunchprofilmonitor>





## A. Pictures of the BSM

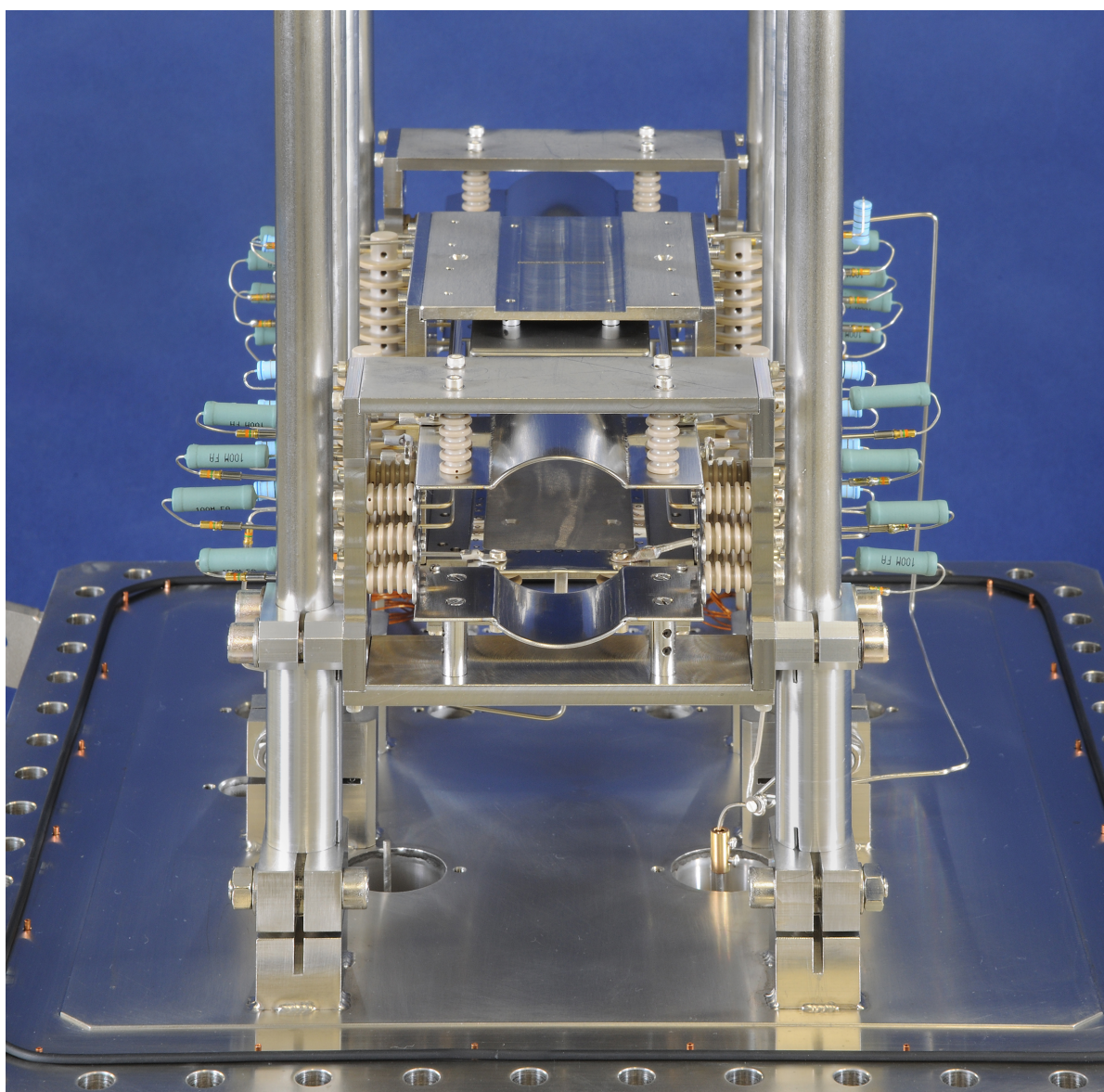


Figure A.1.: Picture of the full assembly of the Field-Box [35].

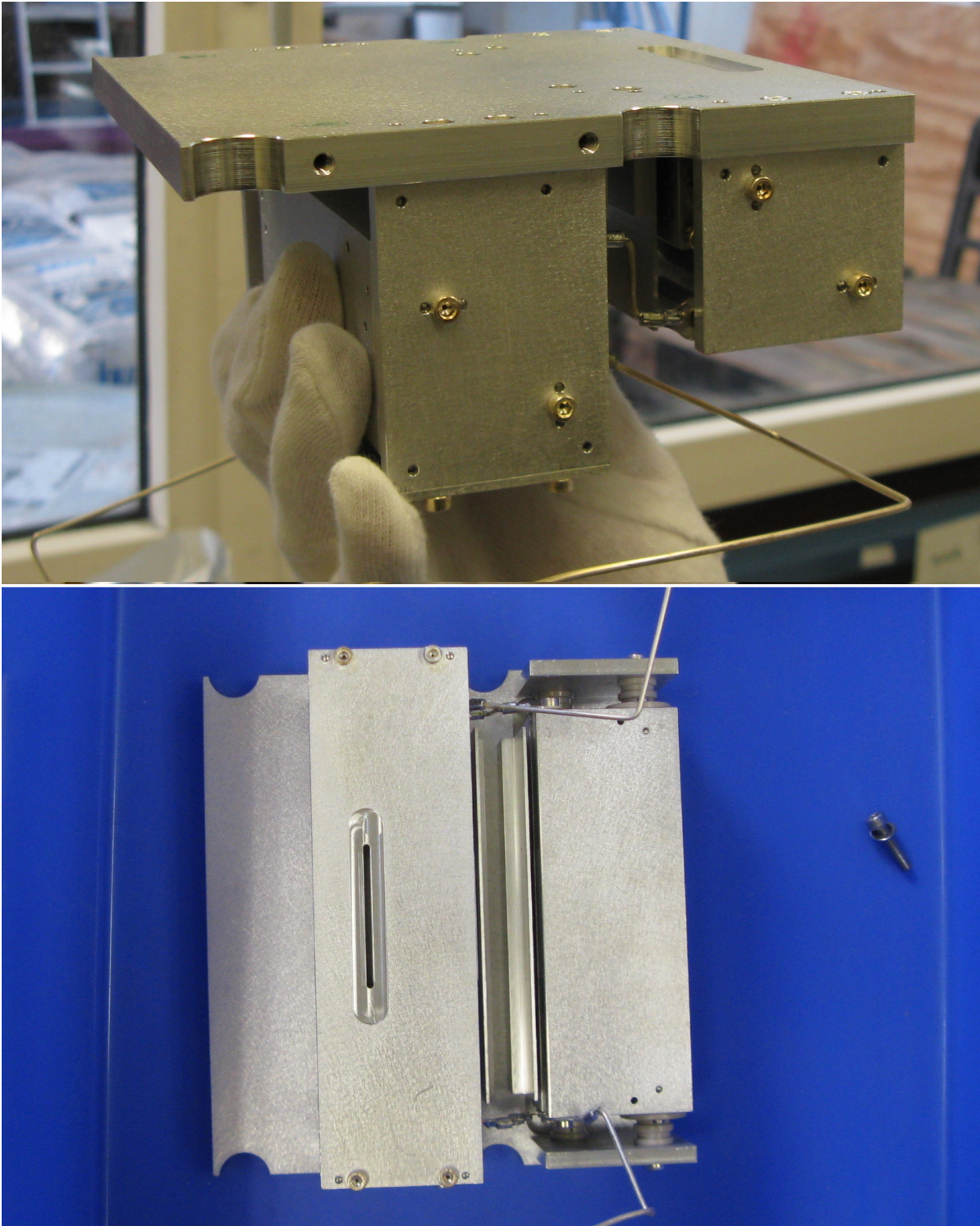


Figure A.2.: Pictures of the Energy Analyzer.



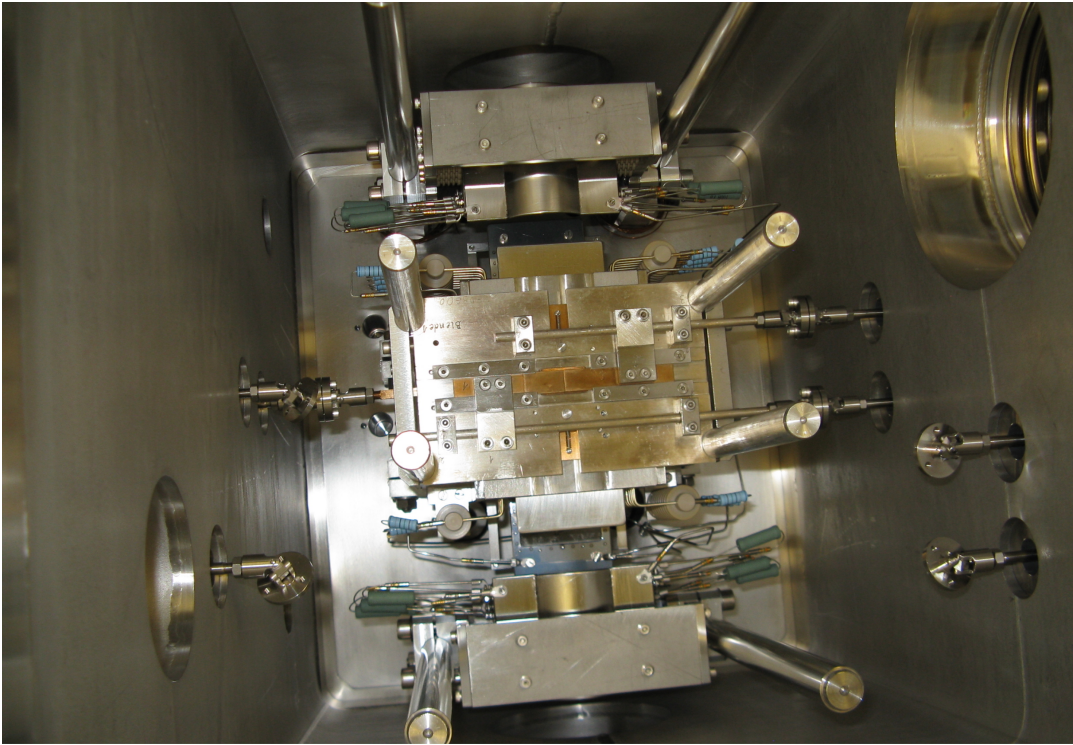


Figure A.3.: Insertion of an XY Aperture modul and the thick iron plate for the X-ray protection.

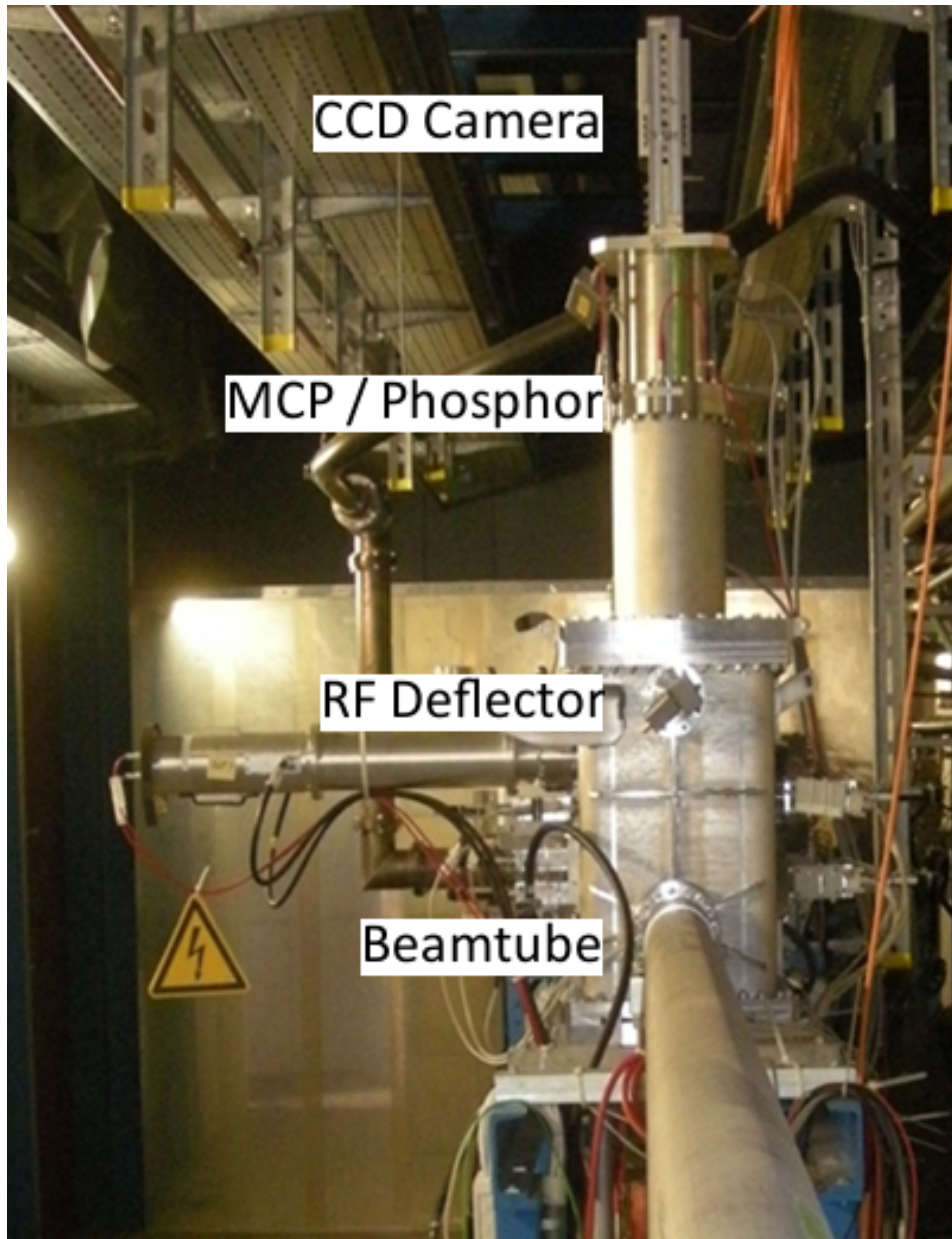


Figure A.4.: A picture of the BSM in the TK5 at GSI.

# B. Technical Drawings

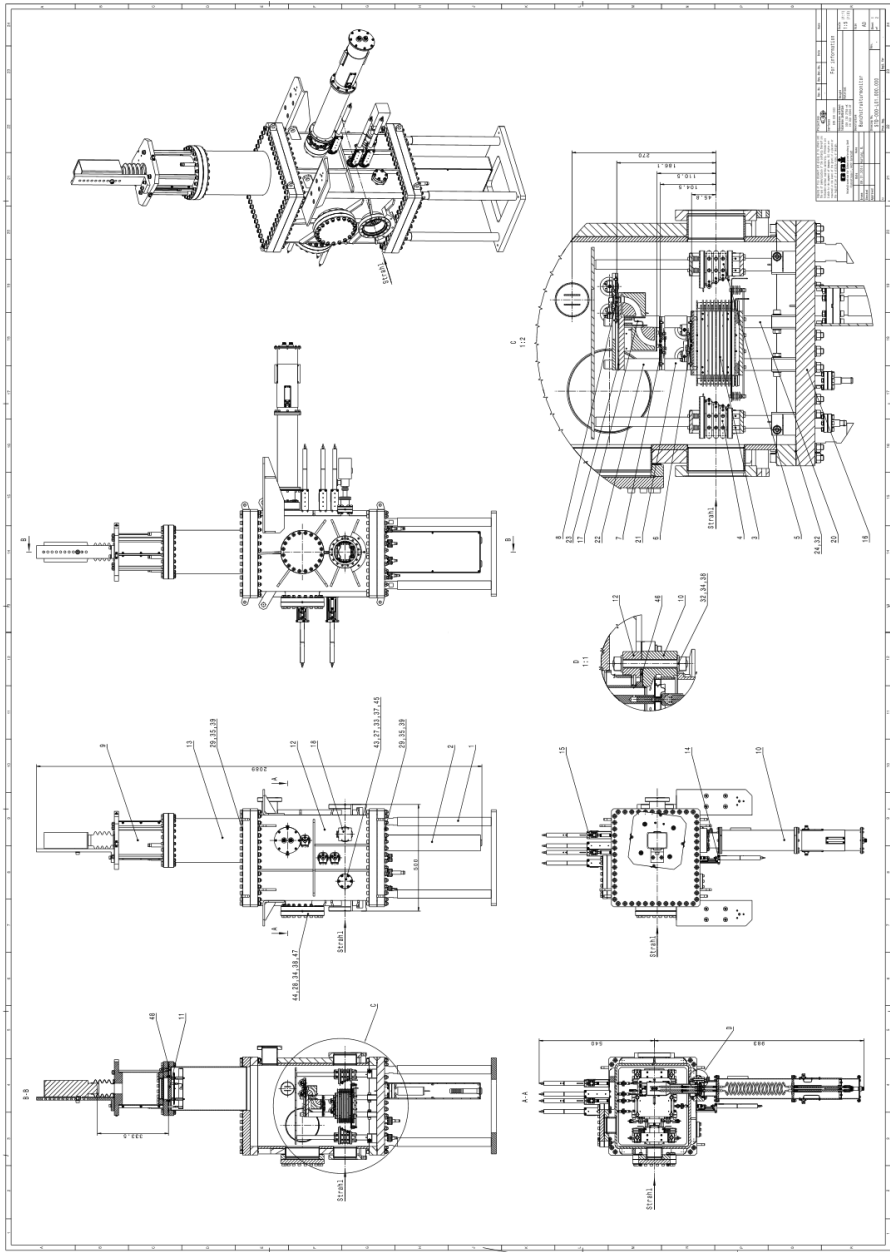


Figure B.1.: Technical drawing of the BSM [117].

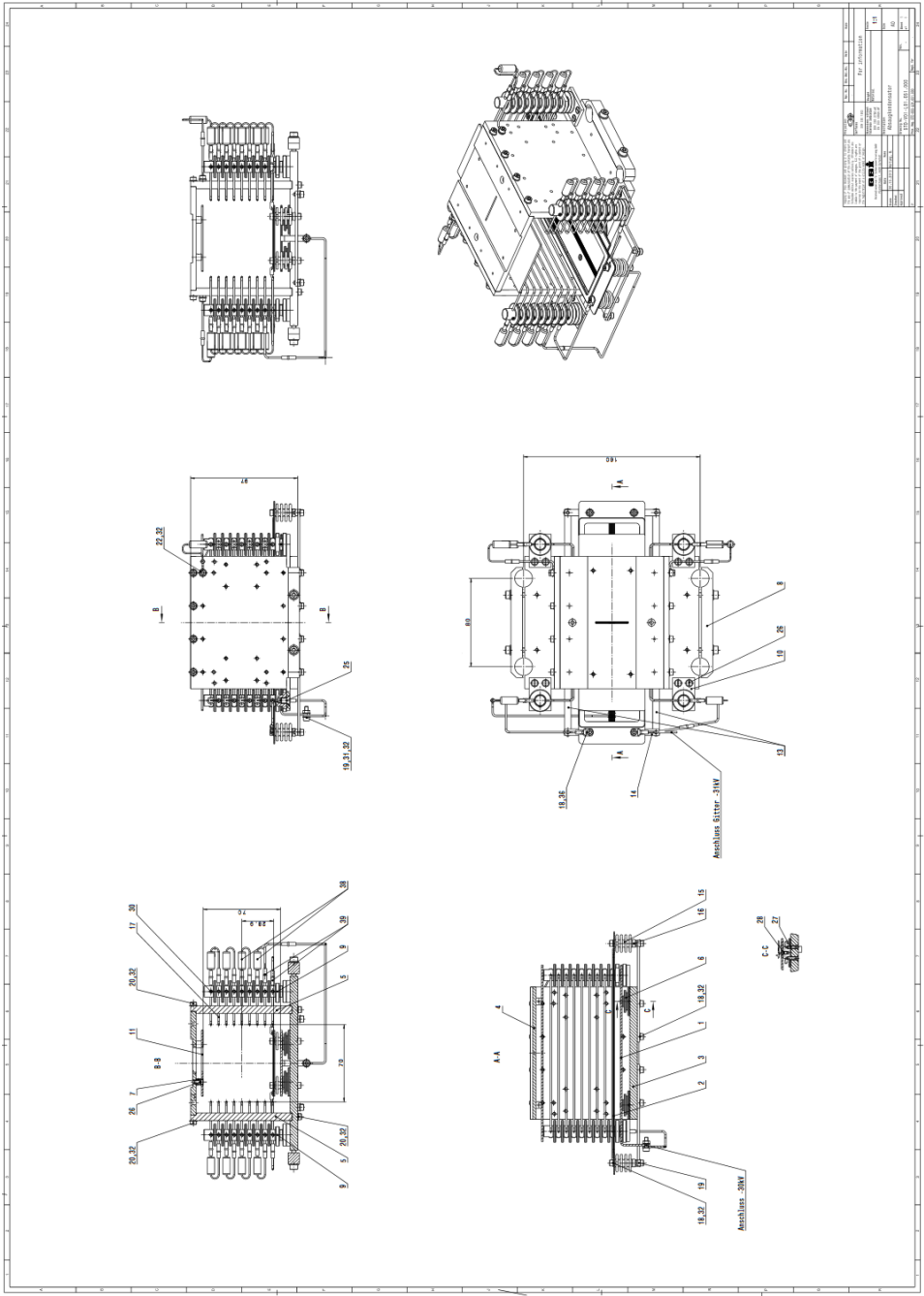


Figure B.2.: Technical drawing of the Field-Box [117].



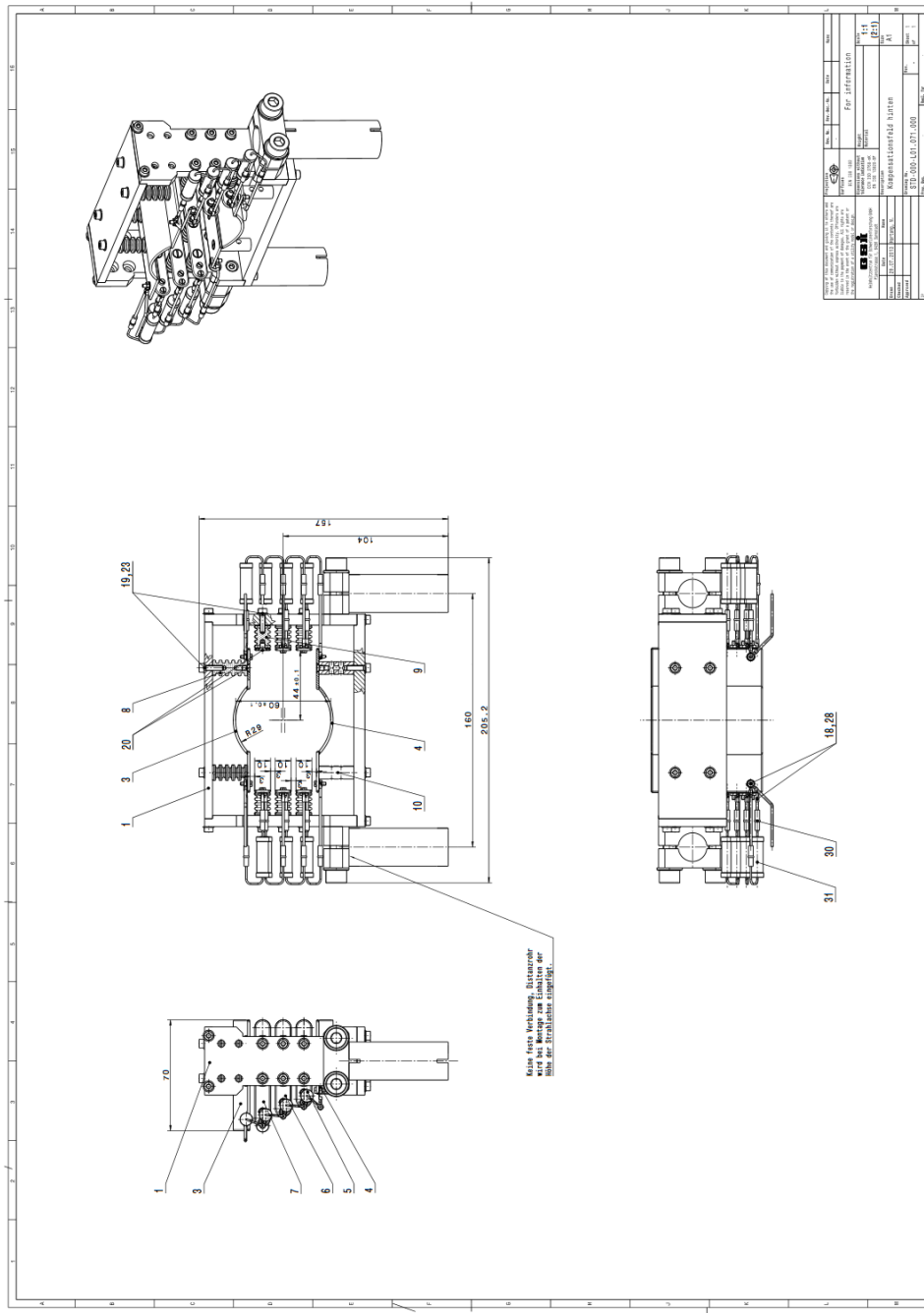


Figure B.4.: Technical drawing of the rear compensation electrode [117].

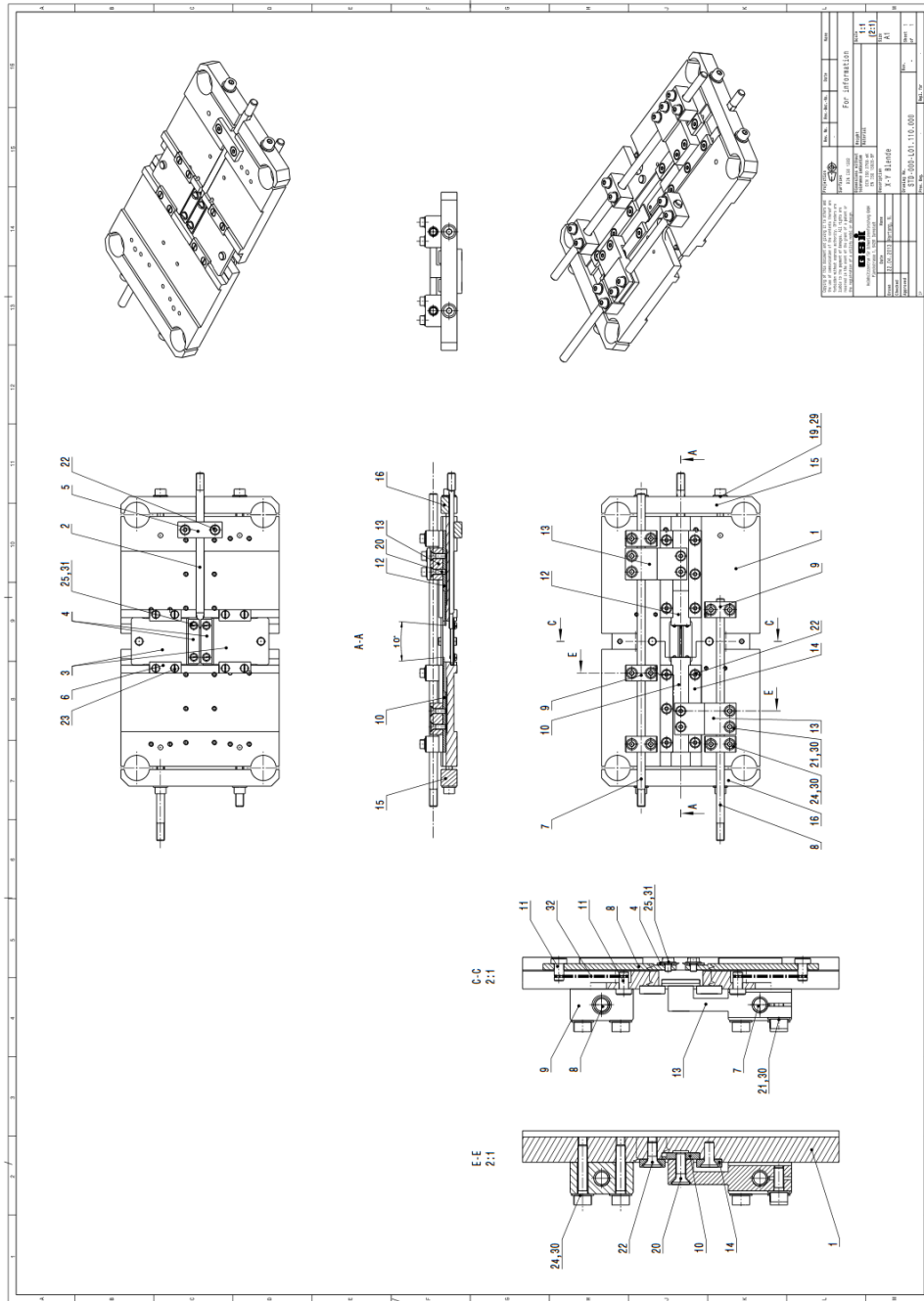


Figure B.5.: Technical drawing of an XY Aperture modul [117].

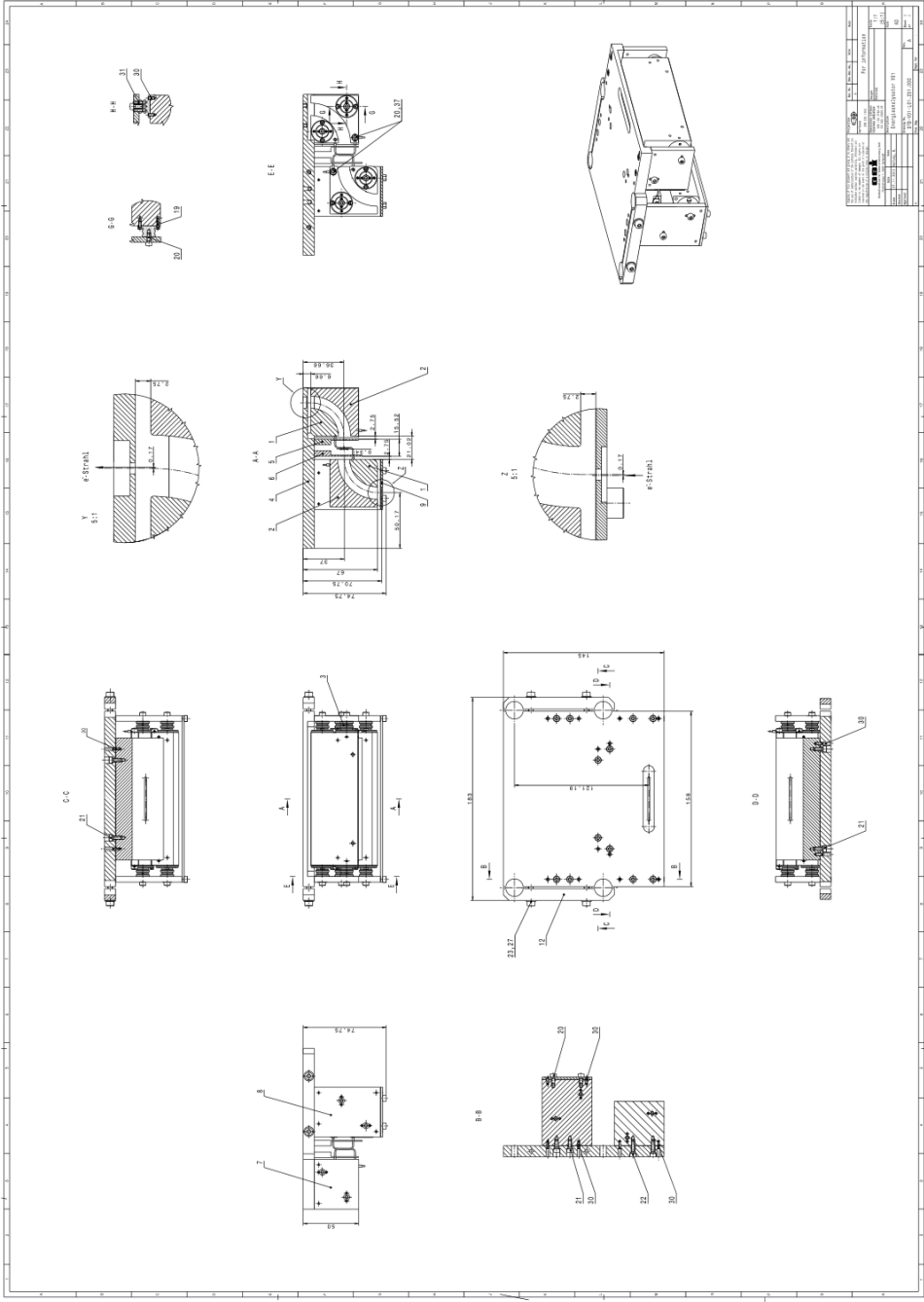


Figure B.6.: Technical drawing of the Energy Analyzer [117].



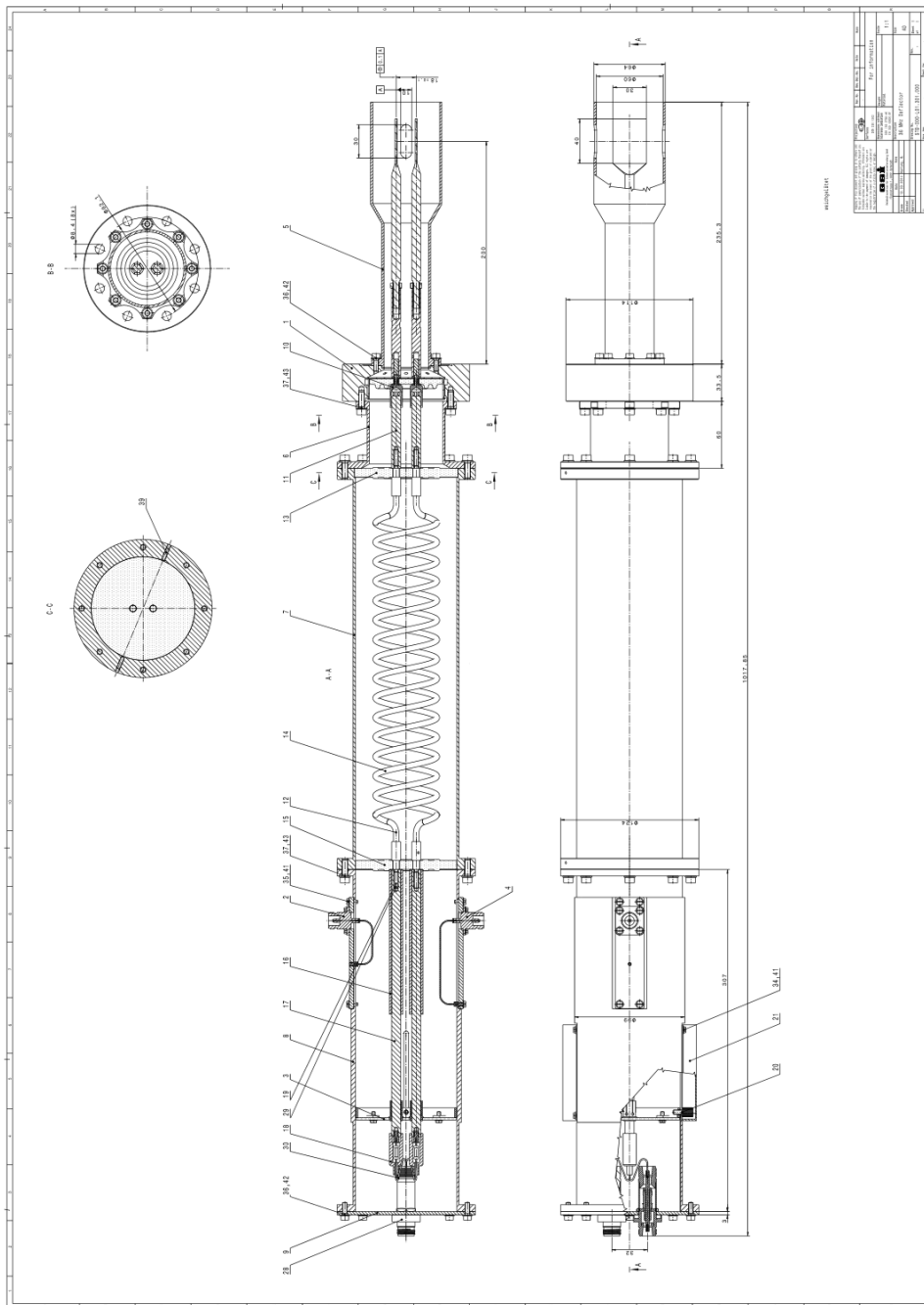


Figure B.7.: Technical drawing of the RF Deflector [117].

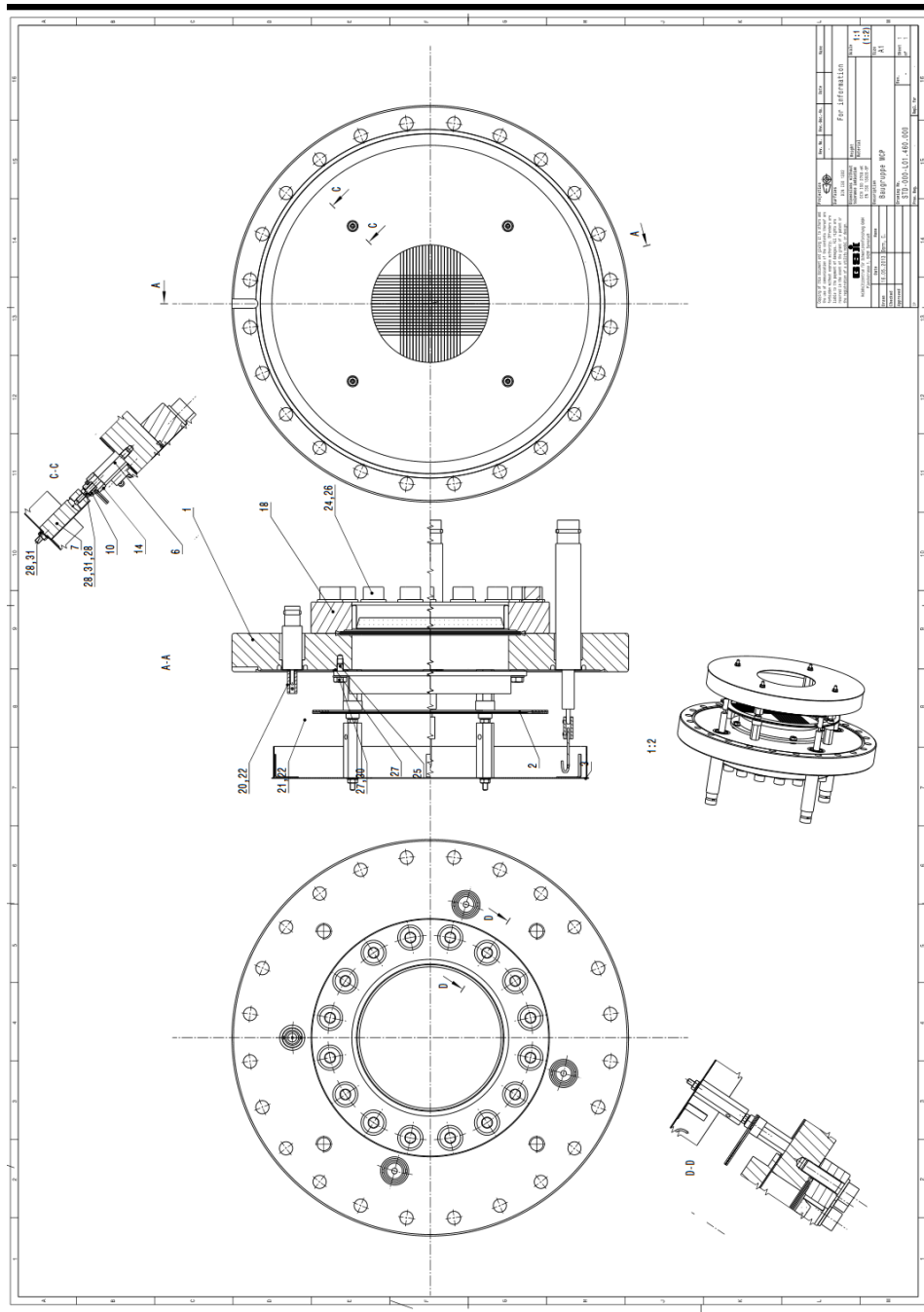


Figure B.8.: Technical drawing of the MCP mount [117].

## C. Miscellaneous



```
File Edit Format Run Options Windows Help
#!/usr/bin/env python
from random import *
from math import *
datei=open("BenniThermisch90000.txt", 'w')
y1=22
z1=2.0
x1=0.8
z=49.55
x=0.0
y=0.0
curr=1E-8/1000
#liste=[]
Teilchenzahl=range(90000)

for i in Teilchenzahl:
    dz=round(random()*z1-0.5*z1,4)
    dy=round(random()*y1-0.5*y1,4)
    dx=round(random()*x1-0.5*x1,4)
    #radius=sqrt(dz**2+dy**2)

    datei.write('0 -1 0 '+str(x+dx)+' '+str(y+dy)+' '+str(z+dz)+' 0 0 1 '+str(curr)+'\n')
    #liste.append(str(dx)+'/'+str(dy))
    #print i

print ('fertig')
datei.close()
```

Figure C.1.: Screenshot of the Python script to create a the thermal ensemble.

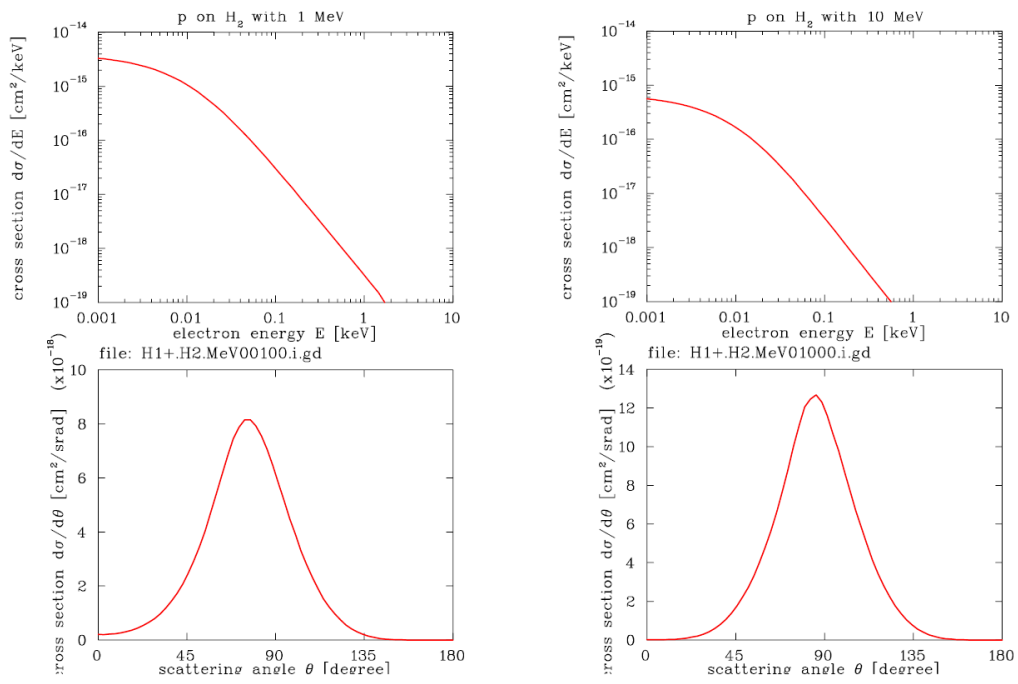


Figure 1: Single differential cross sections for  $H^+$  on  $H_2$ . Left: 1 MeV, Right: 10 MeV.

Figure C.2.: Simulations for the  $H^+$  cross section at 1 MeV and 10 MeV [111].

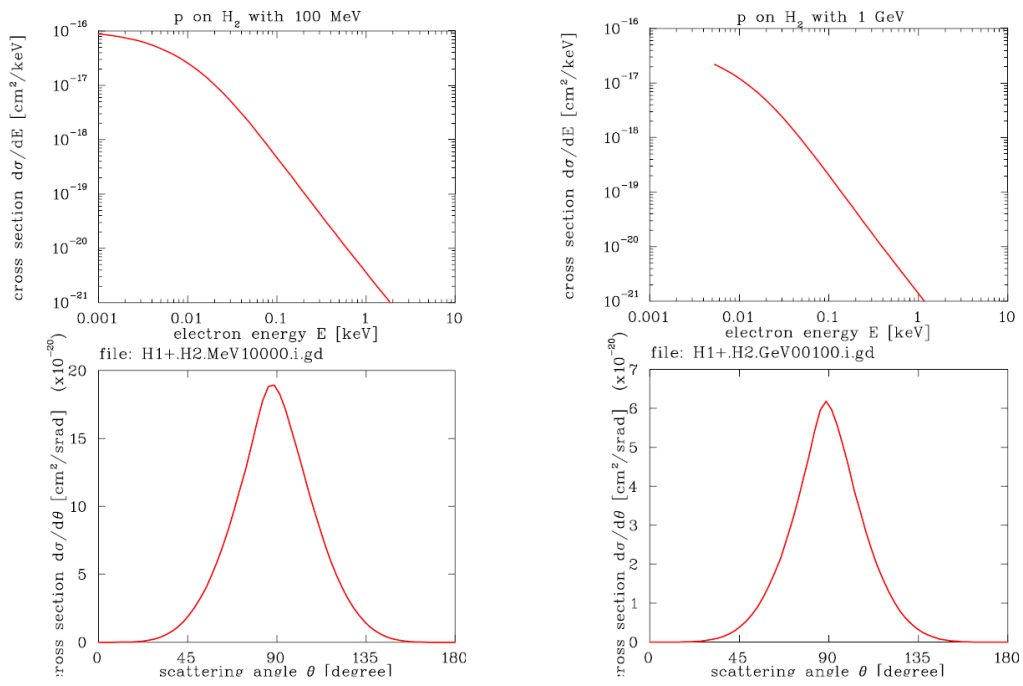


Figure 2: Single differential cross sections for  $H^+$  on  $H_2$ . Left: 100 MeV, Right: 1 GeV.

Figure C.3.: Simulations for the  $H^+$  cross section at 100 MeV and 1 GeV [111].

